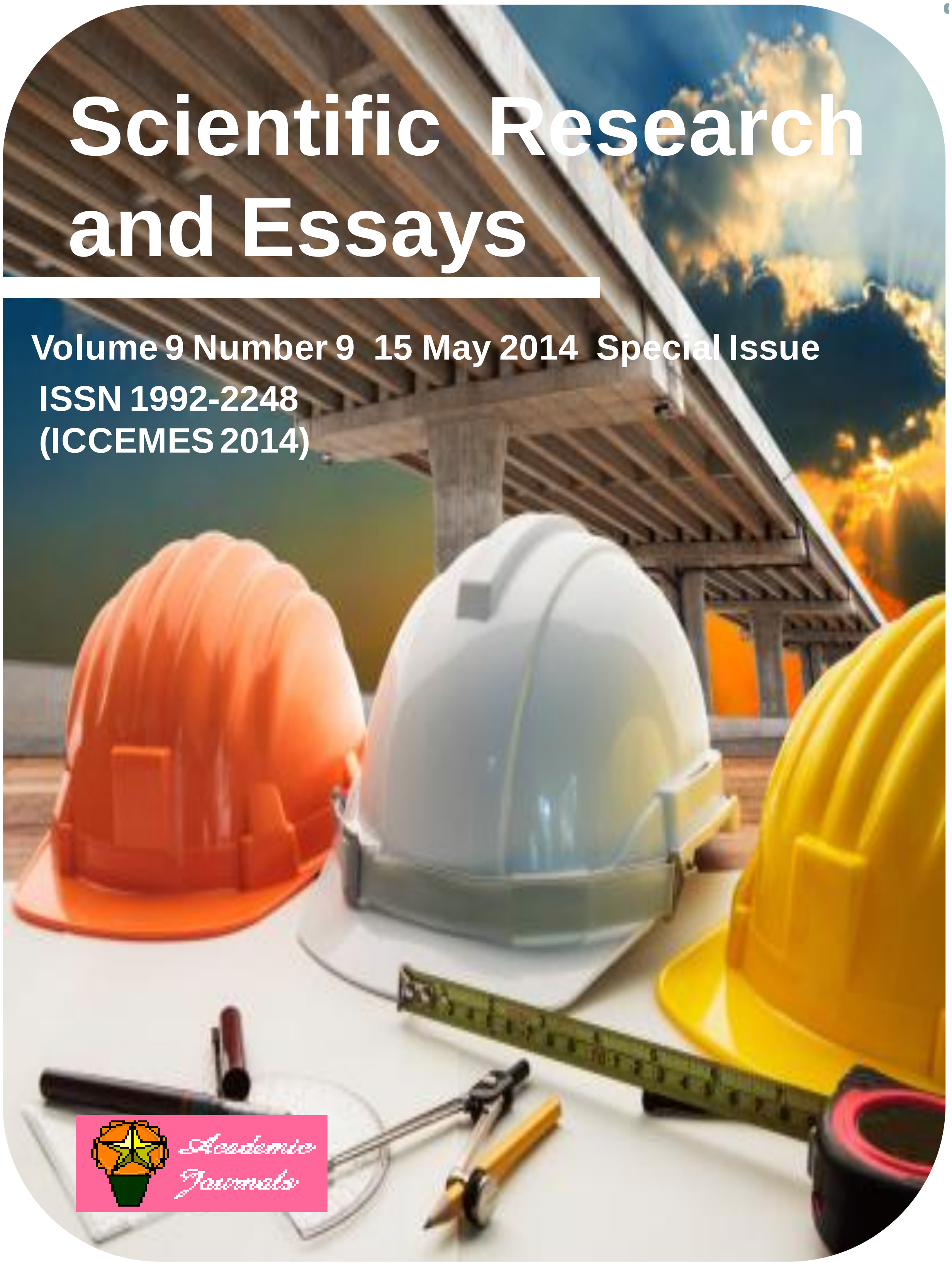

Scientific Research and Essays

Volume 9 Number 9 15 May 2014 Special Issue
ISSN 1992-2248
(ICCEMES 2014)

Academic Journals

ABOUT SRE

The **Scientific Research and Essays (SRE)** is published weekly (one volume per year) by Academic Journals.

Scientific Research and Essays (SRE) is an open access journal with the objective of publishing quality research articles in science, medicine, agriculture and engineering such as Nanotechnology, Climate Change and Global Warming, Air Pollution Management and Electronics etc. All papers published by SRE are blind peer reviewed.

Submission of Manuscript

Submit manuscripts as e-mail attachment to the Editorial Office at: sre@academicjournals.org. A manuscript number will be mailed to the corresponding author shortly after submission.

The Scientific Research and Essays will only accept manuscripts submitted as e-mail attachments.

Please read the **Instructions for Authors** before submitting your manuscript. The manuscript files should be given the last name of the first author.

Editors

Dr. NJ Tonukari
Editor-in-Chief
Scientific Research and Essays
Academic Journals
E-mail: sre.research.journal@gmail.com

Dr. M. Sivakumar Ph.D. (Tech).
Associate Professor
School of Chemical & Environmental Engineering
Faculty of Engineering
University of Nottingham
Jalan Broga, 43500 Semenyih
Selangor Darul Ehsan
Malaysia.

Prof. N. Mohamed El Sawi Mahmoud
Department of Biochemistry, Faculty of science,
King AbdulAziz university,
Saudia Arabia.

Prof. Ali Delice
Science and Mathematics Education Department,
Atatürk Faculty of Education,
Marmara University,
Turkey.

Prof. Mira Grdisa
Rudjer Boskovic Institute, Bijenicka cesta 54,
Croatia.

Prof. Emmanuel Hala Kwon-Ndung
Nasarawa State University Keffi Nigeria
PMB 1022 Keffi,
Nasarawa State.
Nigeria.

Dr. Cyrus Azimi
Department of Genetics, Cancer Research Center,
Cancer Institute, Tehran University of Medical Sciences,
Keshavarz Blvd.,
Tehran, Iran.

Dr. Gomez, Nidia Noemi
National University of San Luis,
Faculty of Chemistry, Biochemistry and Pharmacy,
Laboratory of Molecular Biochemistry Ejercito de los
Andes 950 - 5700 San Luis
Argentina.

Prof. M. Nageeb Rashed
Chemistry Department- Faculty of Science, Aswan
South Valley University,
Egypt.

Dr. John W. Gichuki
Kenya Marine & Fisheries Research Institute,
Kenya.

Dr. Wong Leong Sing
Department of Civil Engineering,
College of Engineering,
Universiti Tenaga Nasional,
Km 7, Jalan Kajang-Puchong,
43009 Kajang, Selangor Darul Ehsan,
Malaysia.

Prof. Xianyi LI
College of Mathematics and Computational Science
Shenzhen University
Guangdong, 518060
P.R. China.

Prof. Mevlut Dogan
Kocatepe University, Science Faculty,
Physics Dept. Afyon/ Turkey.
Turkey .

Prof. Kwai-Lin Thong
Microbiology Division,
Institute of Biological Science,
Faculty of Science,University of Malaya,
50603, Kuala Lumpur,
Malaysia.

Prof. Xiaocong He
Faculty of Mechanical and Electrical Engineering,
Kunming University of Science and Technology,
253 Xue Fu Road, Kunming,
P.R. China.

Prof. Sanjay Misra
Department of Computer Engineering
School of Information and Communication Technology
Federal University of Technology, Minna,
Nigeria.

Prof. Burtram C. Fielding Pr.Sci.Nat.
Department of Medical BioSciences
University of the Western Cape
Private Bag X17
Modderdam Road
Bellville, 7535,
South Africa.

Prof. Naqib Ullah Khan
Department of Plant Breeding and Genetics
NWFP Agricultural University Peshawar 25130,
Pakistan

Fees and Charges: Authors are required to pay a $550 handling fee. Publication of an article in the Scientific Research and Essays is not contingent upon the author's ability to pay the charges. Neither is acceptance to pay the handling fee a guarantee that the paper will be accepted for publication. Authors may still request (in advance) that the editorial office waive some of the handling fee under special circumstances.

Submission of a manuscript implies: that the work described has not been published before (except in the form of an abstract or as part of a published lecture, or thesis) that it is not under consideration for publication elsewhere; that if and when the manuscript is accepted for publication, the authors agree to automatic transfer of the copyright to the publisher.

Disclaimer of Warranties

In no event shall Academic Journals be liable for any special, incidental, indirect, or consequential damages of any kind arising out of or in connection with the use of the articles or other material derived from the SRE, whether or not advised of the possibility of damage, and on any theory of liability.

This publication is provided "as is" without warranty of any kind, either expressed or implied, including, but not limited to, the implied warranties of merchantability, fitness for a particular purpose, or non-infringement. Descriptions of, or references to, products or publications does not imply endorsement of that product or publication. While every effort is made by Academic Journals to see that no inaccurate or misleading data, opinion or statements appear in this publication, they wish to make it clear that the data and opinions appearing in the articles and advertisements herein are the responsibility of the contributor or advertiser concerned. Academic Journals makes no warranty of any kind, either express or implied, regarding the quality, accuracy, availability, or validity of the data or information in this publication or of any other publication to which it may be linked.

Scientific Research and Essays

Table of Contents: Volume 9 Number 9 15 May, 2014

ARTICLES

Research Articles

Risk analysis and assessment on construction operation based on human factors and empirical Bayesian theory 280
Kai-Chang Sun and Jian-Lan Zhou

Near-infrared spectra quantitative analysis for flue gas of thermal power plant based on wavelength selection 288
Hui Cao and Yan Zhou

Biogas production potential of transgenic *Vetiveria zizanioides* in mesophilic batch anaerobic digestion 293
Peipei Sun, Wudi Zhang, Fang Yin, Xingling Zhao, Jing Liu, Yubao Chen and Shiqing Li

Sustainable development of landscape environment of traditional Changzhen 297
Jia Yuanyuan, Lu Junfu and Qing Ling

Research on the transient radial force of the centrifugal pump 303
Wei Li, Weidong Shi, Zhongyong Pan, Xiaoping Jiang and Ling Zhou

Development of a method to detect infectious rotavirus and astrovirus by reverse transcriptase polymerase chain reaction (RT-PCR) with propidium monoazide (PMA) 311
Wei Yumei, Liu Tingting, Wang Jingqi, He Xiaoqing and Wang Zijian

Effect of Ozone fumigation on morpho-physiology and yield of field-grown rice in Pearl River Delta, China 315
Qiong Wang, Bilige Sude, Ming Dong, Yuan Shi, Chunmei Geng and Xiaoke Wang

Scientific Research and Essays

Table of Contents: Volume 9 Number 9 15 May, 2014

Design of indoor dust concentration monitor based on light scattering detection method 321
Li Tianhua and Wu Ying

Analysis of the shape of bearing push-extend reamed affecting the bearing capability of the pile of push-extend multi-under-reamed pile through the finite element method 325
Yongmei Qian, Xihui Wang and Guanghan Xu

Two-phase closed-loop system identification method based on the auxiliary model 331
Jie Jia, Jiao Cao, Yong Yang, Zhiteng Liu and Shuying Huang

Research on the topology control algorithm to maximize the Ad Hoc life cycle 336
Wenbo Zhang, Yongxin Feng, Xiaobo Tan and Lidong Fu

Hydrochemical characteristics of groundwater in Tongchuan City, China 343
Zhang Yuxi, Zhang Yuanjing and Liu Jingtao

Calculating cyan-magenta-yellow-black (CMYK) printer' gray component data based on polynomial modeling 352
Sun Bangyong, Liu Han and Zhou Shisheng

The reliability test assessment of three-parameter Weibull distribution of material life by Bayesian method 357
Xintao Xia, Yuanyuan Qin, Yinping Jin and Ming Qiu

Assessment for the quality of rolling bearing parts based on fuzzy theory 362
Xintao Xia, Yanyan Meng, Yantao Shang and Ming Qiu

Scientific Research and Essays

Table of Contents: Volume 9 Number 9 15 May, 2014

Air gap field-oriented vector control strategy for high-power electrically excited synchronous motor based on full-order flux linkage observer 367
Jing Shang, Xiaohong Nian and Kean Liu

A novel fusion algorithm for infrared image and visible light image based on non-subsampled contourlet transform 374
Yucheng Liu and Yubin Liu

Rural residents' acceptance towards a telehealth system: The integrative perspective of technology acceptance model and social cognitive theory 380
Chung-Hung Tsai

Safe and efficient mining technology for full-mechanized caving face of deep mine with capacity of ten million tons 384
Ma Liqiang, Sun Hai, Jin Zhiyuan, Wang Fei and Li Pan

Characterization of WPI-NaCas composite films modified by transglutaminase 391
Lei Qiao, Pan Jiazhen, Huang Zhiying, Bao Jianqiang and Xun Qiannan

Microarrays revealed general-key genes responsive to implantation of low-energy N+ ion beam in rice 400
Ya Huiyuan, Chen Qiufang, Wang Weidong and Jiao Zhen

Study on the warp and weft direction conductivity of anti-radiation knitted fabri 407
Zhu Xiao Yu

academicJournals

Vol. 9(9), pp. 280-287, 15 May, 2014
DOI: 10.5897/SRE2014.5902
Article Number: 3E9769244486
ISSN 1992-2248 © 2014
Copyright©2014
Author(s) retain the copyright of this article
http://www.academicjournals.org/SRE

Scientific Research and Essays

Full Length Research Paper

Risk analysis and assessment on construction operation based on human factors and empirical Bayesian theory

Kai-Chang Sun[1] and Jian-Lan Zhou[2]*

[1]College of Hydraulic and Environmental Engineering, China Three Gorges University, Yichang, Hubei, 443002 China.
[2]Automation College, Huazhong University of Science and Technology, Wuhan, Hubei, 430074 China.

Received 3 January, 2013; Accepted 2 March, 2013

This study was focused on the roles of human factors in construction accident and also dealt with the probabilities of fours levels of injury. We used an empirical Bayesian method and the human factors analysis and classification system framework to analyze the probability distributions of the severity of accidents of high risk operations in hydropower construction. Accident severity in four levels of injury was modeled: severe injury, one death, two deaths, and three deaths. The results show the behavior characteristics of workers and factors influencing their operation violations. The calculation of posterior distributions of the levels of injury enables us to rank the factors with respect to their risk of injury. The study revealed that lack of the ability to determine hazards is the direct reason in many accidents; resource management, inadequate supervision and supervisory violations also play important roles in the occurrence of accidents.

Key words: Empirical Bayesian analysis, human factors, work accidents, risk analysis and assessment.

INTRODUCTION

In the southwest China, there are numerous large-scale hydropower projects that have been built and put into operation. The construction projects are large-scale, with long construction period, and are extremely complex with high safety risks. At present, there are no systematic and thorough study on the hazards identification, risk evaluation and control management on the hydropower construction project at home and aboard. Though our country has built laws, technical specifications, and procedures, there are no related concrete contents of the construction safety hazards. On the other hand, strengthening the construction accident statistics work is an important part of the safety production. Construction accident statistics is the basic management work in the construction safety production. Statistical data are used to analyze the key factors of the accidents to obtain the cause and regulation of the accidents.

Hazard risk assessment involves many factors, which is a dynamic system with interaction factors. Therefore, the establishment of the evaluation indicator set must be scientific, rational and comprehensive. This study begins from the view of common hazard identification and

---

*Corresponding author. E-mail: zhoujl1999@163.com

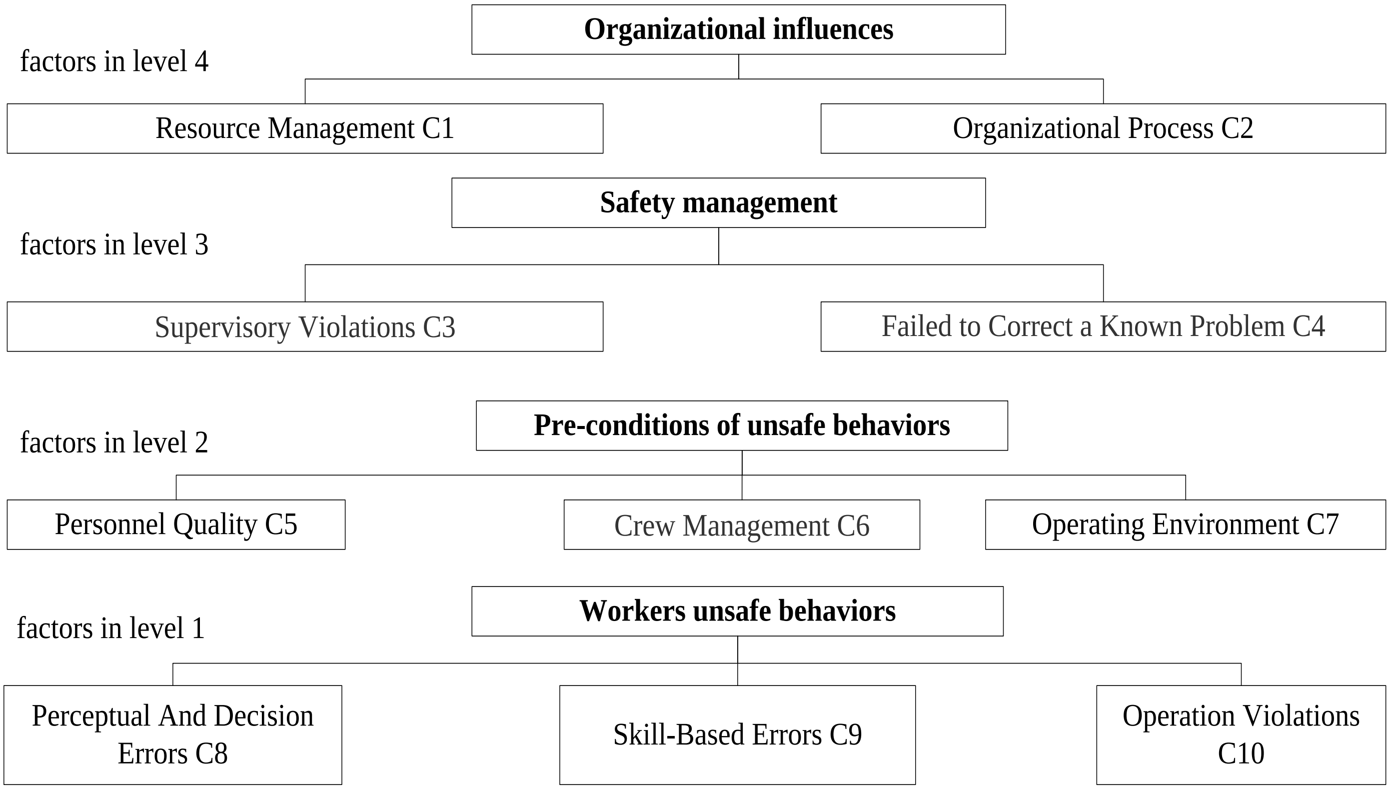

Figure 1. Four levels of the HFACS framework.

evaluation, takes into account the characteristics of construction safety hazard, and deeply analyzes the main factors influencing hazard risk assessment. On the basis of the human factors analysis and classification system framework (HFACS), we use classical Bayesian theory to calculate and sort the importance degree of the factors.

METHODOLOGY

Human factors analysis and classification system framework (HFACS)

The safety assessment structure model of high-risk operation and risk factors causing accidents are shown in Figure 1, which is also a HFACS framework (Wiegmann and Shappell, 1997, 2001). This study uses the HFACS framework to identify the kind of factors that are of most importance in the accidents.

The HFACS framework classified the human fault factors involved into four levels. L1 level factors were the focus of the past accident investigation, which are the personnel behavior mistakes causing the accident (i.e construction workers unsafe behaviors). This level can be further divided into four categories: decision-making mistake, skill-based errors, perception errors and violation operations. L2 level factors (precondition for unsafe behaviors-potential/obvious mistakes) refer to the obvious psychological or environmental factors' influence on L1 factors, such as operation environment that does not meet the required conditions and are more likely to cause accidents. L3 level factors (unsafe supervision-the potential mistakes) are the onsite supervision factors that lead to unsafe behaviors. L4 level factors (organizational influences-the potential mistakes) are described as the wrong decisions made by the high-level managers' influence on the low-level workers' behavior.

In HFACS framework, the higher level can influence the adjacent lower level. Adjusting and replacing some factors according to the characteristics of construction can strengthen the framework's independence and generality; and makes it possible to quickly identify the key factors in the whole system. The amendment HFACS framework is more in line with the actual hydropower construction project.

Statistical framework

There are two basic concepts in Bayesian statistics: the prior distribution and posterior distribution.

Prior distribution is a probability distribution of the overall distribution parameter θ. The fundamental idea of Bayesian School is that any statistical inference on the overall distribution of the parameter θ, in addition to samples provided by the information must also provide for a prior distribution. It is an indispensable element for making statistical inferences. They believe that the prior distribution does not need to have an objective basis, and can be partially or fully based on subjective belief (Shappell and Wiegmann, 2001); posterior distribution, according to the samples distribution and the prior distribution of the unknown parameters, with the method of conditional probability distribution to find out the conditional distribution of unknown parameters under the known samples. Because of this, distribution obtained after the sampling is called posterior distribution. The key of Bayesian inference method is that any inference must only rely on the posterior distribution, and no longer involve in sample distribution (de Lapparent, 2006).

The severity of the injury accident cases is divided into four levels: severe injury, one death, two deaths and three deaths. K indicates the mutually exclusive type of injury accident (that is, event space). $Y_{i,j}$ is the result of the accident type i leading to the injury type j, which is represented by an array of discrete random variable, $Y_i = \left(Y_{i,1}, \cdots Y_{i,k}\right)'$.

For all j=1, ..., K, $Y_{i,j}$ takes the value 1 if the severity of accident is the same with level j and the value 0 otherwise. A probability measure Pi on BY, the σ-algebra of the K elementary events, is associated with each other.

$P_{i,j} = P_i(Y_{i,j} = 1)$ is the probability that the accident i has an injury of type j. Therefore, we state that $Y_i | P_i \xrightarrow{id} M(1, P_i), P_i = (P_{i,i}, \cdots, P_{i,k})'$, where id stands for 'independently distributed': Y_i is distribution conditionally on Pi with a Multinomial probability distribution with parameter 1 and P_i (Leonard, 1977). The corresponding conditional probability density functions is then

$$f_{Yi|pi}(y_i) = \prod_{j-1}^{k} p_{i,j}^{yi,j}, \qquad p_{i,j} \in [0,1], \qquad y_{i,j} \in \{0,1\}. \tag{1}$$

Where $\sum_{j=1}^{k} p_{i,j} = 1$ and $\sum_{j=1}^{k} y_{i,j} = 1$

Because there are different accident configurations, understood as different circumstances and consequences, there are variations of the probabilities of the types of injury according to many factors. Due to the unpredictable nature of accident, for each accident i, P_i is random, and uses known accident model in line with the Bayesian analysis principle.

In a Bayesian context, the beliefs one can have about the family of distributions of probabilities of the types of injury are summarized through prior distributions. They represent the state of knowledge about the individual distributions of the types of injury before observing the sample $y = (y_1, \cdots, y_n)'$. For convenience, it is assumed that they all belong to the same family of probability distributions. A Dirichlet distribution is used because it can be mixed conveniently with the Multinomial distribution and it results in a Dirichlet posterior distribution. For all i= 1...n, $p_i \xrightarrow{id} D(\theta_{i,1}, \cdots, \theta_{i,k})$, where $\theta_{i,k} > 0, j = 1,..., K$, are shape parameters. The probability density function for the prior distribution is

$$\pi_{pi|\theta i}(p_i) = \frac{\Gamma(\sum_{i=1}^{K} \theta_{i,j})}{\prod_{j=1}^{K} \Gamma(\theta_{i,j})} \prod_{j=1}^{K} p_{i,j}^{\theta_{i,j}-1}, p_{i,j} \in [0,1], \theta_{i,j} > 0 \tag{2}$$

where Γ is the gamma function:

$$\Gamma(s) = \int_0^{\infty} e^{-x} x^{s-1} dx, \Gamma(s) = (s-1)\Gamma(s-1). \tag{3}$$

Using the conditional distribution (1) and the prior distribution (2), the joint distribution of (Yi, Pi) is defined:

$$\psi_{Yi,pi|\theta i|}(y_i, p_i) = \frac{\Gamma(\sum_{i=1}^{K} \theta_{i,j})}{\prod_{j=1}^{K} \Gamma(\theta_{i,j})} \prod_{j=1}^{K} p_{i,j}^{y_{i,j}+\theta_{i,j}-1}. \tag{4}$$

The marginal distribution of Yi is derived using (4) by integrating over Pi:

$$gY_i | \theta_i(y_i) = \frac{\Gamma(\sum_{j=1}^{K} \theta_{i,j})}{\prod_{j=1}^{K} \Gamma(\theta_{i,j})} \int_{[0,1]K} \prod_{j=1}^{K} p_{i,j}^{y_{i,j}+\theta_{i,j}-1} dp_{i,1\ldots} dp_{i,K}$$

$$= \coprod_{k=1}^{K} \left(\frac{\theta_{i,k}}{\sum_{j=1}^{K} \theta_{i,j}}\right)^{yi,k} \tag{5}$$

The posterior distribution of $p_i \mid y_i$ is obtained using the transition formula of Bayes:

$$h_{pi|yi,\theta i} = \frac{\psi Y_{i,pi|\theta i}(y_i, p_i)}{gY_i | \theta_i(y_i)}$$

$$= \frac{\Gamma(\sum_{j=1}^{K} \theta_{i,j} + y_{i,j})}{\prod_{j=1}^{K} \Gamma(\theta_{i,j} + y_{i,j})} \prod_{j=1}^{K} p_{i,j}{}^{y_{i,j}+\theta_{i,j}-1} \tag{6}$$

Where is a Dirichlet distribution:

$$p_i | y_i, \theta_i \xrightarrow{id} D(\theta_{i,1} + y_{i,1}, \cdots, \theta_{i,K+yi,K}). \tag{7}$$

Empirical Bayesian analysis is performed in two steps: first, estimate the unknown hyper parameters; secondly, compute the posterior distributions using the estimated parameters and analyze the results.

Estimation of hyper parameters

As stated above, before accident occurs, construction organizations attempt to improve the workers' safety consciousness, use safety equipment, strengthen safety supervision and management, and control the probability distribution of Pi of the severity of accident. Also, the construction environment and accident attributes will play different roles when the corresponding accident happens. From the statistical standpoint, it means that one can explain the values of the shape parameters of the distributions according to some exogenous factors.

Let $X_i \in X \subset R^p$ be a(p, 1) array of explanatory variables about observation i, and let $X = (X_1, \cdots, X_n)'$ be the full rank (n, p) matrix of explanatory variables about the observed sample. Let $\forall k = 1,..., K, \beta_k \in \Theta_k \subset R^p$ be a (p, 1) array of (unknown) weights measuring the causal effects of explanatory variables on the shape of the probability distribution through $\theta_{i,k} \cdot \beta_j$. Measure the effects of the explanatory variables x_i on the importance of the outcome j in the probability distribution of accident severity. $X, \Theta_1 \times \cdots \Theta_k$ are assumed to be compact subsets of R^p. In order to maintain consistency with the strict positivity of the shape parameters, it is assumed for the rest of the paper that:

$$\theta_{i,j} = \exp(x_i^{'}\beta_j) \quad (8)$$

The only available observation we have for an individual i is that severe injury, one death, two deaths and three deaths. In order to infer on the values of the unknown hyper parameters of the model, the marginal probability distributions of Yi, i = 1 . . . n, are used to build the sample log-likelihood function of observed yi, i = 1 . . . n:

$$\ell(\beta \mid y, x) = \prod_{i=1}^{n}\prod_{k=1}^{K}\left(\frac{\exp(x_i^{'}\beta_k)}{\sum_{j=1}^{K}\exp(x_i^{'}\beta_j)}\right)^{yi,k} \quad (9)$$

Looking at (9), we see there is no objective relationship between the value of the log-likelihood function and the values of the parameters as long as we do not set further identification restrictions. In fact, we must choose a benchmark outcome k^* which for $\beta_{k*} = 0$, and all the remaining estimable parameters are expressed as differences with respect to β_{k*}. The maximization of (9) with respect to the unknown parameters gives us asymptotically unbiased and efficient estimates we use to compute the posterior probability distribution of accident severity.

Analysis of result

Hyper parameters are interpreted in the sense of their causal influences on the shapes and moments of probability distributions of the types of accident. The posterior distribution represents the state of knowledge concerning pi after the observations have been combined with the prior information. Posterior distributions represent our updated beliefs about probability distribution of the types of accident after accidents happened.

The Bayesian estimator of the expected rate of an accident with injury of level j for individual i is given by the posterior mean of $p_{i,j}$ (Gwet, 2002b):

$$\mathrm{E}(p_{i,j}|y_i, \hat{\alpha}_i, \hat{\beta}_i) = \frac{\theta_{i,j} + y_{i,j}}{\sum_{k=1}^{K}(\theta_{i,k} + y_{i,k})}; \quad (10)$$

And the posterior variance of the distribution is

$$V(p_{i,j}|y_i, \hat{\alpha}_i, \hat{\beta}_i) = \frac{(\theta_{i,j} + y_{i,j})(\sum_{k=1}^{K}(\theta_{i,k} + y_{i,k}) - (\theta_{i,j} + y_{i,j}))}{(\sum_{k=1}^{K}(\theta_{i,k} + y_{i,k}))^2(1 + \sum_{k=1}^{K}(\theta_{i,k} + y_{i,k}))}. \quad (11)$$

MODEL CALCULATION AND ANALYSIS

Factors analysis

Select 59 accident cases occurring in the construction peak period of the Xiluodu project and the Xiangjiaba project. The accidents are not described as name but serial number from 1 to 59. The statistical process is to determine in turn whether the HFACS factors are the reasons causing these accidents. In the 59 accidents, there are 28 serious injuries, 27 cases with one person death, 3 cases with two persons death and 1 case with three persons death. According to the HFACS factors, we get descriptive statistics of the accident frequency, as shown in Table 1.

i) Resource management,
ii) Organizational process,
iii) Supervisory violations,
iv) Failed to correct a known problem,
v) Personal quality,
vi) Crew management,
vii) Operating environment,
viii) Perceptual and decision error,
ix) Skill-based errors,
x) Operation violations.

In Table 1, of the 59 cases, 47.46% severe injury, 45.76% one death, 5.08% two deaths, and 1.70% three deaths.

Super parameter calculation: Super parameter can be calculated by formula (12):

$$\theta_{i,j} = \exp(x_i^{'}\beta_{i,j}) \quad (12)$$

Let $x_i \in X \subset R^p$ be an array in the [p, 1] interval, x_i is the full rank matrix (n, p) of the explanatory variables of the observed samples and $\beta_{i,j}$ measures the influence of probability distribution of the explanatory variable x_i to the accident severity.

The value of $x_i^{'}$ is: $x_i^{'}$ =the sum of edge frequency of the factors in the accidents/1000. Where, the number of 1000 means that there are ten factors and the edge frequency is expressed as a percentage.

The edge frequency of the influence factors are given in Table 1. According to the inclusion relationship in Table 1, we can obtain the values of $x_i^{'}$, $\beta_{i,j}$ and $\theta_{i,j}$.(i=1,2,...,59; j=1,2,3,4). For example, $x_1^{'}$ corresponding to accident 1 is shown as follows:

$x_1^{'}$ =(55.93+67.8+62.71+52.54+74.58+62.71+50.85+40.68+83.05+66.10)/1000=0.62

The value of $\beta_{i,j}$ is:

$\beta_{i,j}$ =The sum of edge frequency of the factors corresponding to the injury type j in the accidents/1000.

For example, $\beta_{1,j}$ represents the sum of edge frequency of the factors corresponding to the injury type j in the accident 1. The values of $\beta_{1,j}$ in accident 1 are shown as follows:

Table 1. All HFACS factors' edge frequency.

Factors	Severe injury	One death	Two deaths	Three deaths	Edge frequency
(1)	50	42.31	7.69	0	44.07
Not (1)	45.45	48.49	3.03	3.03	55.93
(2)	52.5	40	5	2.5	67.8
Not (2)	36.84	57.9	5.26	0	32.2
(3)	54.55	40.91	4.54	0	37.29
Not (3)	43.24	48.65	5.41	2.7	62.71
(4)	45.16	51.61	3.23	0	52.54
Not (4)	50	39.29	7.14	3.57	47.46
(5)	60	33.33	6.67	0	25.42
Not (5)	43.18	50	4.55	2.27	74.58
(6)	54.54	40.91	4.55	0	37.29
Not (6)	43.24	48.65	5.41	2.7	62.71
(7)	40	53.33	6.67	0	50.85
Not (7)	55.17	37.93	3.45	3.45	49.15
(8)	54.17	45.83	0	0	40.68
Not (8)	42.86	45.71	8.57	2.86	59.32
9()	30	60	10	0	16.95
Not (9)	51.02	42.86	4.08	2.04	83.05
(10)	50	45	5	0	33.9
Not (10)	46.15	46.15	5.13	2.57	66.1
edge frequency	47.46	45.76	5.08	1.7	

$$\beta_{1,1} = (45.45+52.50+43.24+45.16+43.18+43.24+40.00+54.17+51.02+46.15)/1000=0.46$$

$$\beta_{1,2} = (48.49+40.00+48.65+51.61+50.00+48.65+53.33+45.83+42.86+46.15)/1000=0.48$$

$$\beta_{1,3} = (3.03+5.26+5.41+3.23+4.55+5.41+6.67+0+4.08+5.13)/1000=0.04$$

$$\beta_{1,4} = (3.03+2.50+2.70+0+2.27+2.70+0+0+2.04+2.57)/1000=0.02$$

The calculation of prior probability and posterior probability

Based on the results of the super parameter calculation, the formulas 2 and 6, we calculated prior probability and posterior probability of the 59 accidents.

Calculation results show the prior and posterior distribution of the accident samples. The difference among the prior distributions is not obvious, which indicates the researchers could not easily find out the occurring law of serious accidents based on the empirical prior distribution. But the posterior distribution makes up this shortage; it dramatically reflects the difference between the serious accidents and other accidents. For example, the number 32, 34, 39 and 46, their posterior distribution value is small, and the difference value between the posterior distribution and the prior distribution is negative, this feature shows that using Bayesian method to analyze the accident cause is feasible. According to the descending order of standard deviation, we get Table 2.

In accordance with the value of standard deviation, we sort the factors in descending order, and get the order of importance degree of the various factors in Table 2. It is the order of factors of the accident severity degree based on Bayesian theory under the new HFACS framework. To sum up the above 59 accidents, we may know the sample size is small, the accident is different from the experiment and is unrepeated, and the accident analysis is strong subjective. Such feature is suitable for the Bayesian statistical method.

The calculation and analysis of expectation

The expectation of each factor is shown in Table 3. We use the data in Table 3 to draw the broken line chart shown as Figure 2 for further analysis. We can draw the following conclusions from Figure 2: the expectations of severe injury accidents are almost over 0.3, “(5) personal quality”, “(3) supervisory violations”, “(6) crew

Table 2. The priori probability, posteriori probability and standard deviation of each factor by the descending order of standard deviation.

Factors	Priori probability	Posteriori probability	Standard deviations	
(8)	9.9676	16.8422	4.861076	1
(4)	9.9966	16.3475	4.490764	2
(6)	9.7212	15.9816	4.426771	3
(3)	9.6343	15.8303	4.381234	4
(10)	9.6773	15.7449	4.290441	5
Not (2)	9.6692	15.6051	4.197315	
(5)	9.5569	15.4921	4.19682	6
Not (9)	10.0507	15.9222	4.151777	
Not (7)	9.8722	15.7315	4.143151	
(1)	9.6939	15.5409	4.134453	7
Not (1)	10.1376	15.9145	4.084885	
Not (5)	10.0734	15.8378	4.076046	
(7)	10.0096	15.7677	4.071592	8
(2)	10.0717	15.8187	4.063743	9
Not (10)	10.0779	15.7525	4.012548	
Not (3)	10.1251	15.7021	3.943535	
Not (6)	10.0734	15.6121	3.916452	
(9)	9.4096	14.9054	3.886117	10
Not (4)	9.8817	15.0883	3.681622	
Not (8)	9.9245	15.0009	3.589557	

Table 3. The expectations of the influencing factors.

Factors	Severe injury	One death	Two deaths	Three deaths
(1)	0.3193	0.2982	0.1896	0.1793
(2)	0.3251	0.3089	0.1919	0.1839
(3)	0.3283	0.3026	0.1993	0.1875
(4)	0.3106	0.2924	0.1946	0.1852
(5)	0.3383	0.313	0.1951	0.1913
(6)	0.3279	0.2849	0.1914	0.1796
(7)	0.3009	0.3067	0.1944	0.1791
(8)	0.3283	0.2947	0.1908	0.1871
(9)	0.3194	0.3181	0.1833	0.1797
(10)	0.319	0.2561	0.1827	0.179

management", and "(8) perceptual and decision error", these four factors are prone to cause serious injured; the expectations of one death accidents evenly distribute on both sides of 0.3, the value of "(10) operation violations" is significantly lower than other factors, but the values of "(9) skill-based errors", "(5) personal quality" and "(2) organizational process" are relatively higher; in the cases of two deaths accidents, "(3) supervisory violations", "(4) failed to correct a known problem" and "(5) personal quality" most easily induce the accidents; and in the cases of three deaths accidents, "(5) personal quality", "(3) supervisory violations" and "(8) perceptual and decision error" most easily result in the accidents.

The calculation and analysis of variance

The posterior variance of each factor is shown in Table 4. We use the data in Table 4 to draw the posterior variance broke line chart of the accident severity of the factors, shown as Figure 3. We can draw the following conclusions from Figure 3: the posteriori variance of each factor to the four types of severity smoothly distributes at a mean value. The severe injury accidents and the one

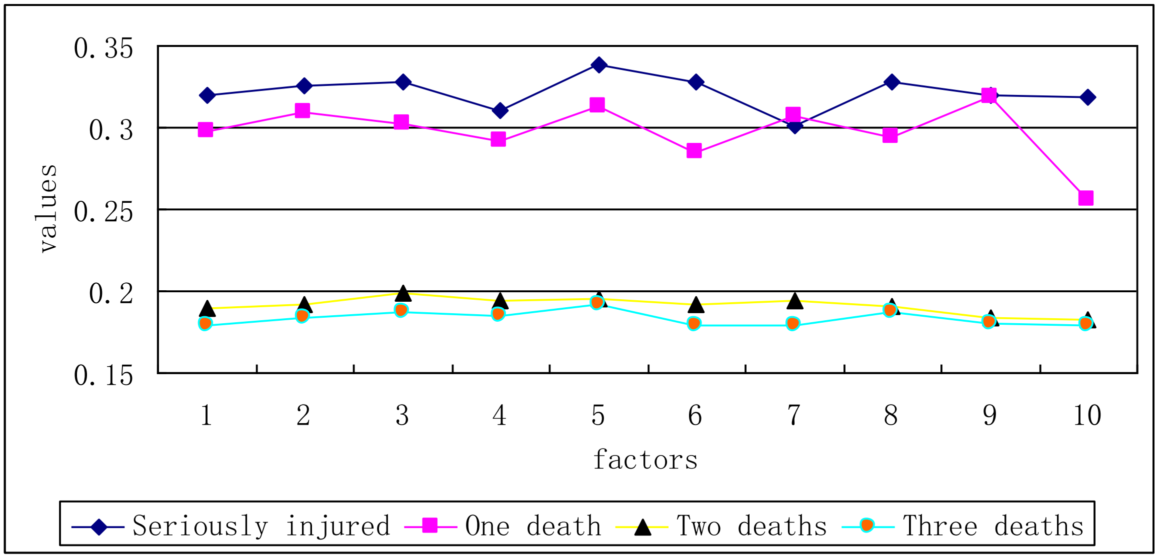

Figure 2. The expectation broke line chart of the ten factors causing the four types of accidents.

Table 4. The posterior variances of the influencing factors.

Factors	Severe injury	One death	Two deaths	Three deaths
(1)	0.0317	0.0308	0.0237	0.0224
(2)	0.0318	0.0305	0.023	0.0224
(3)	0.0323	0.0307	0.0234	0.0225
(4)	0.0311	0.0317	0.0229	0.0222
(5)	0.0329	0.0299	0.0238	0.0226
(6)	0.0322	0.0307	0.0233	0.0225
(7)	0.0305	0.0319	0.0233	0.0221
(8)	0.0321	0.0311	0.0226	0.0223
(9)	0.0298	0.0328	0.0243	0.0227
(10)	0.0317	0.0311	0.0234	0.0225

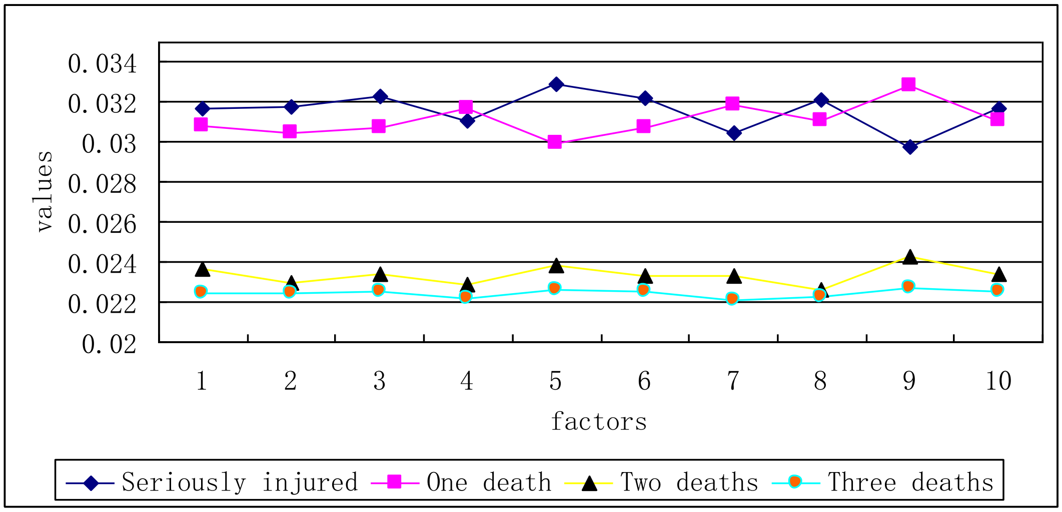

Figure 3. The variance broke line chart of the ten factors causing the four types of accidents.

death accidents are significantly different from zero in level 4%, and the two deaths accidents and the three deaths accidents are significantly different from zero in level 3%, which indicate the distribution consistency of accident severity of the samples is good.

Conclusion

Through the comparative analysis of the results calculated by the traditional statistical method and the Bayesian statistical method, we can find that the results calculated by the traditional statistical methods laid emphasis on the organizational and supervisory levels, and ignored the issue of workers. The results of Bayesian statistical method, however, appear more “humanization”. The proportion of the judgment and the physical state of the workers increases. We have referred in the above analysis that lack of the capacity of determining hazards is the direct reason in many accidents. It also conforms to China’s actual situation: lack of professional skills training of the workers, lower average educational level. Meantime, in the results of Bayesian statistical analysis, the proportions of resource management, inadequate supervision and supervisory violations are relatively higher, which indicates the defects of management rules and malfeasances of managers and supervisors play an important role in causing of accident. Such result is the same with it obtained by the classical statistical analysis.

So, Bayesian statistics method can learn from experience, combine historical information and sample likelihood function together, make a set of statistical method more flexible, more visual and easily understood than classical statistical method. Bayesian statistics method is widely used in the application of measurement model. Especially in the fewer samples, point estimate and interval estimate can get more accurate results than classical statistical method; secondly, we use Bayesian posterior distribution to take account of the losses caused by type one and type two errors, therefore it is more of practical than classical statistical method; in addition, in dealing with the problems of redundant parameters, Bayesian statistics method can directly integral off superfluous parameters in posterior density, which is far more convenient than classical statistical method.

Conflict of Interests

The author(s) have not declared any conflict of interests.

ACKNOWLEDGEMENT

This paper is supported by the national natural science fund project of China (50909045, 51079078).

REFRENCES

Gwet K (2002b). Inter-rater reliability: dependency on trait prevalence and marginal homogeneity. In: Statistical Methods for Inter-rater Reliability Assessment.

Leonard T (1977). A Bayesian approach to some multinomial estimation and pretesting problems, J. Am. Stat. Association 72:869-874.

de Lapparent M (2006). Empirical Bayesian analysis of accident severity for motorcyclists in large French urban areas. Accid. Anal. Prev. 38:260-268. http://dx.doi.org/10.1016/j.aap.2005.09.001; PMid:16280119

Shappell SA, Wiegmann DA (2001). Applying reason: the human factors analysis and classification system (HFACS). Hum. Factors Aerospace. 1:59-86.

Wiegmann DA, Shappell SA (1997). Human error analysis of post accident data: applying theoretical taxonomies of human error. Int. J. Aviat. Psychol. 7:67-81. http://dx.doi.org/10.1207/s15327108ijap0701_4

academicJournals

Vol. 9(9), pp. 288-292, 15 May, 2014
DOI: 10.5897/SRE2014.5903
Article Number: E4ED4ED44488
ISSN 1992-2248 © 2014
Copyright©2014
Author(s) retain the copyright of this article
http://www.academicjournals.org/SRE

Scientific Research and Essays

Full Length Research Paper

Near-infrared spectra quantitative analysis for flue gas of thermal power plant based on wavelength selection

Hui Cao[1] and Yan Zhou[2]*

[1]State Key Laboratory of Electrical Insulation and Power Equipment, School of Electrical Engineering, Xi'an Jiaotong University, Xi'an, 710049, China.
[2]School of Energy and Power Engineering, Xi'an Jiaotong University, Xi'an 710049, China.

Received 18 March, 2014; Accepted 20 March, 2014

This paper proposed a near-infrared (NIR) spectra quantitative analysis method for flue gas of thermal power plant based on wavelength selection. For the proposed method, the self-adaptive accelerated particle swarm optimization is presented for determining the most representative wavelengths of NIR spectral signals and is combined with partial least square for predicting the various contents of the real flue gas dataset. The proposed method chooses the current own optimal or the current global optimal as the reference state randomly and accelerated updates of the flight velocity by the reference state, then the particle state is updated based on the new velocity self-adaptively. The experimental results of a real flue gas dataset verified that the proposed method has higher predictive ability and could overcome the premature convergence.

Key words: Thermal power plant, fuel gas, near-infrared spectrum, wavelength selection, self-adaptive accelerated discrete particle swarm optimization.

INTRODUCTION

With regards to energy saving in a serious situation of coal and power energy shortages, using nature gas could decrease the power generation cost (Lee and Jou, 2012). The flue gas from the gas generating unit mainly consists of methane (CH_4), carbon monoxide (CO) and carbon dioxide (CO_2). The quantitative analysis of the flue gas could reflect the potential level of environmental pollution. The traditional chemical calibration analysis methods are usually time-expensive. Near-infrared (NIR) spectra is a fast nondestructive technique and has been widely used for analyte quantitative determination (Lillhonga and Geladi, 2011). Partial least square (PLS) is the most popular chemometric method and has been developed for quantitative analysis of NIR spectral data (Marcio et al., 2011). Since not all wavelengths in the spectrum are equally important model, the wavelength selection is the crucial step of NIR spectroscopy analysis. The most popular wavelength selection method is the uninformative variable elimination by PLS (UVE-PLS) and are better than the statistic-based wavelength selection methods (Centneret al., 1996). Moreover, wavelength selection could be deemed as a combinatorial problem, genetic algorithm (GA) and particle swarm optimization (PSO) combined with PLS are proposed for wavelength selection (Arakawa et al., 2011; Sorol et al., 2010). Nevertheless, GA and PSO may fall into the local minima.

---

*Corresponding author. E-mail: yan.zhou@mail.xjtu.edu.cn

In this paper, we proposed the self-adaptive accelerated particle swarm optimization (SAAPSO) to realize the wavelength selection of NIR spectral for building the analyte quantitative model.

THE PROPOSED METHOD

A wavelength selection method based on SAAPSO is presented for building the concentration prediction model of flue gas. Some notations would be explained beforehand. The number of particles in the population is *n* and the number of dimensions of each particle is *d*, namely, *d* equals the number of the total wavelengths. v_{ij}^{k} and x_{ij}^{k} are the velocity and the position of the *j*th dimension of the *i*th particle at generation *k*, where $i \in \{1, 2, \cdots, n\}$, $j \in \{1, 2, \cdots, d\}$ and *k* is an integer. Moreover, p_i and p_g are the best previous performing state of the *i*th particle and the global best state, respectively.

For SAAPSO, v_{ij}^{k} could be updated by $v_{ij}^{k+1} = w \cdot v_{ij}^{k} + a \cdot r_2 \cdot (p_c - x_{ij}^{k})$, where if $0 \le r_1 < f_c$, then $p_c = p_{ij}$, and if $f_c \le r_1 \le 1$, then $p_c = p_{gj}$, p_c is the reference state, r_1 and r_2 are both random number between 0 and 1, p_{ij} and p_{gj} are the positions of the *j*th dimension of p_i and p_g, respectively, f_c is the selection coefficient, *w* is the inertia factor and *a* is the acceleration factor. Then, x_{ij}^{k} could be updated by the formula (1):

$$x_{ij}^{k+1} = \begin{cases} p_{ij} & \rho < 1 \big/ \left(1 + \exp(-v_{ij}^{k+1})\right) \\ p_{gj} & \text{other} \end{cases} \tag{1}$$

where ρ is the random number between 0 and 1.

For wavelength selection, SAAPSO uses the binary coding to encode the location of each particle and each dimension represents a wavelength, where ‘1’ or ‘0’ indicates that the wavelength is selected or dropped, respectively. The velocity and location of each particle are initialized randomly, and then the prediction model is built by PLS with the selected wavelengths. In addition, the root-mean-squares error of cross-validation (RMSECV) is adopted as the fitness function. Aiming at minimizing the RMSECV, the optimal individual of SAAPSO is the solution of the problem after iterations.

For SAAPSO, the search space could be expanded and the acceleration factor would ensure the convergence rate. Furthermore, the new location determined self-adaptively would overcome the local optimum. In the next section, the experiments results could further verify the effectiveness of the proposed method.

EXPERIMENTAL RESULTS

To evaluate the effectiveness of the proposed method, a real dataset obtained by measuring the NIR spectra of the field flue gas is used in the experiments. The dataset are obtained during a combustion process and includes 106 samples and each sample consists of a spectrum for a mixture of CH_4, CO and CO_2 with the reference concentration obtained a gas chromatography (GC). The spectra were measured by a GASMET DX4000 Fourier transform infrared (FTIR) gas analyzer. The spectral wave number is 549.44~4238.28 cm^{-1} with a resolution of 7.72 cm^{-1}. Each spectrum contains 473 wavelengths. The concentration ranges of the three analytes are 0~0.4598 ppm, 0~0.4083 ppm and 0~0.3818 ppm, respectively.

In this study, PLS, UVE-PLS, GA combined with PLS (GA-PLS), PSO combined with PLS (PSO-PLS), the neighboring combined with PLS (NPSO-PLS) and SAAPSO combined with PLS (SAAPSO-PLS) are used for the concentrations of CH_4, CO and CO_2 in the gas dataset and compared the effectiveness of these models. The real dataset would be split into the calibration set and the validation set based on the Monte Carlo cross-validation, namely, 80% of the samples in the dataset are randomly selected as the calibration set and the other 20% are regarded as the validation set. To ensure the fairness of the experiment, the size of populations of GA-PLS, PSO-PLS, NPSO-PLS and SAAPSO-PLS were all set to be 30 and the number of iterations is 100. Although GA-PLS, PSO-PLS, NPSO-PLS and SAAPSO-PLS are initialized randomly, the initialization conditions of them are kept consistent for the experiments. For GA, the crossover probability and the mutation probability were set to be 0.7 and 0.05, respectively. For PSO-PLS and NPSO-PLS, two learning factors were both 1.7. For PSO-PLS, NPSO-PLS and SAAPSO-PLS, the inertia factors were all set to be 0.7. For NPSO-PLS, the number of neighbors of particle is 5. For SAAPSO-PLS, the selection coefficient is 0.5 and the acceleration factor is 2. Since these methods are based on PLS, the number of latent variables is determined according to the RMSECV with leave-one-out cross validation. For UVE-PLS, the latent variables are selected for each recalculation.

Similarly, for GA-PLS, PSO-PLS, NPSO-PLS and SAAPSO-PLS, the latent variables are re-determined at each iteration. The RMSECV for the calibration set, the root mean-squared error of prediction (RMSEP) for the validation set, the determination correlation coefficient (R^2), the cross-validation correlation coefficient calculated by with leave-one-out cross validation for the calibration set (R^2_{cv}), the squared correlation coefficient for the validation set (R^2_p), the number of latent variables (N_{lv}) and the compression ratio (*CR*) are used to assess and compare the predictive ability of the various models, where *CR* equals $\left(N_t - N_s\right) / N_t \times 100\%$, N_t is the number of total wavelengths and N_s is the number of the selected wavelengths. The experiments are implemented in MATLAB 7.0.4 on a personal computer with an Intel i5-2300 CPU and 3 GB of RAM.

The analytical results are summarized in Table 1. For SAAPSO-PLS, the predictive ability is higher and the compression ratio is largest all alone for different contents. For CH4, R^2 of SAAPSO-PLS are little less than those of UVE-PLS, GA-PLS, PSO-PLS and NPSO-PLS. For CO2, R^2 of SAAPSO-PLS are little less than those of PLS, GA-PLS, PSO-PLS, NPSO-PLS, R^2_{cv} of SAAPSO-PLS are

Table 1. Analytical results for flue gas dataset.

CH$_4$	**PLS**	**UVE-PLS**	**GA-PLS**	**PSO-PLS**	**NPSO-PLS**	**SAAPSO-PLS**
RMSECV	103.34	74.346	57.275	59.799	63.422	55.194
RMSEP	132.02	145.54	126.64	132.27	138.6	114.82
R^2	0.9975	0.9999	0.9998	0.9998	0.9998	0.9996
R^2_{cv}	0.9955	0.9957	0.9986	0.9985	0.9982	0.9987
R^2_p	0.9908	0.9907	0.9941	0.9912	0.9905	0.9942
CR(%)	0	57.505	46.723	50.74	47.569	82.241
N_{lv}	8	26	28	25	27	19

CO	**PLS**	**UVE-PLS**	**GA-PLS**	**PSO-PLS**	**NPSO-PLS**	**SAAPSO-PLS**
RMSECV	61.055	30.041	40.409	39.208	42.101	18.85
RMSEP	95.483	42.005	74.162	78.901	69.259	36.562
R^2	0.9993	0.9999	0.9994	0.9995	0.9991	0.9999
R^2_{cv}	0.9906	0.9977	0.9959	0.9961	0.9955	0.9991
R^2_p	0.9751	0.9954	0.9844	0.9826	0.9865	0.9963
CR(%)	0	82.875	53.066	46.934	48.203	84.355
N_{lv}	21	28	27	28	24	25

CO$_2$	**PLS**	**UVE-PLS**	**GA-PLS**	**PSO-PLS**	**NPSO-PLS**	**SAAPSO-PLS**
RMSECV	44.648	36.263	31.362	33.454	34.66	30.607
RMSEP	49.167	41.326	41.982	44.579	43.242	41.241
R^2	0.9996	0.9994	0.9996	0.9995	0.9996	0.9995
R^2_{cv}	0.9984	0.9989	0.9992	0.9991	0.9990	0.9991
R^2_p	0.9955	0.9970	0.9971	0.9965	0.9969	0.9970
CR(%)	0	76.321	52.854	48.203	51.163	78.647
N_{lv}	12	12	12	11	12	11

little less than those of GA-PLS and PSO-PLS and R^2_p of SAAPSO-PLS is only less than that of GA-PLS. The prediction accuracy of SAAPSO-PLS is higher.

Figure 1(a) to (c) show the scatter plots of measured value vs. predicted value of SAAPSO-PLS for CH$_4$, CO and CO$_2$ respectively. Because the data almost are positioned around the diagonal line, the prediction accuracy of SAAPSO-PLS model is high. Figure 1(d) and (f) show the iterations curves of GA-PLS, PSO-PLS, NPSO-PLS and SAAPSO-PLS for CH$_4$, CO and CO$_2$, respectively. At the beginning of iteration, SAAPSO-PLS would explore the new search area by the reference state determined randomly and the search efficiency would be limited in a certain extent. Nevertheless, because of including the acceleration mechanism, SAAPSO-PLS begins to converge after several iterations and has the fastest convergence rate overall. In summary, the experiments results verify that SAAPSO-PLS could be adopted for quantitative analysis of real NIR spectral data successfully and has a powerful predictive ability.

Conclusion

representative wavelengths and is combined with PLS for predicting the various contents of the real flue gas of thermal power plant. The proposed method has some advantages as follows. First, the prediction model of the various contents of flue gas dataset built by the proposed method is more accurate. Second, the proposed method explores new areas to avoid the premature convergence in a certain extent. Third, the proposed method accelerated finds the optimal solution with faster convergence speed. The experiments results verify that the predicative ability and the search performance of the proposed method.

Conflict of Interests

The author(s) have not declared any conflict of interests.

ACKNOWLEDGEMENT

This work is sponsored by National Natural Science Foundation of China (61375055), Program for New Century Excellent Talents in University (NCET-12-0447) and Fundamental Research Funds for the Central

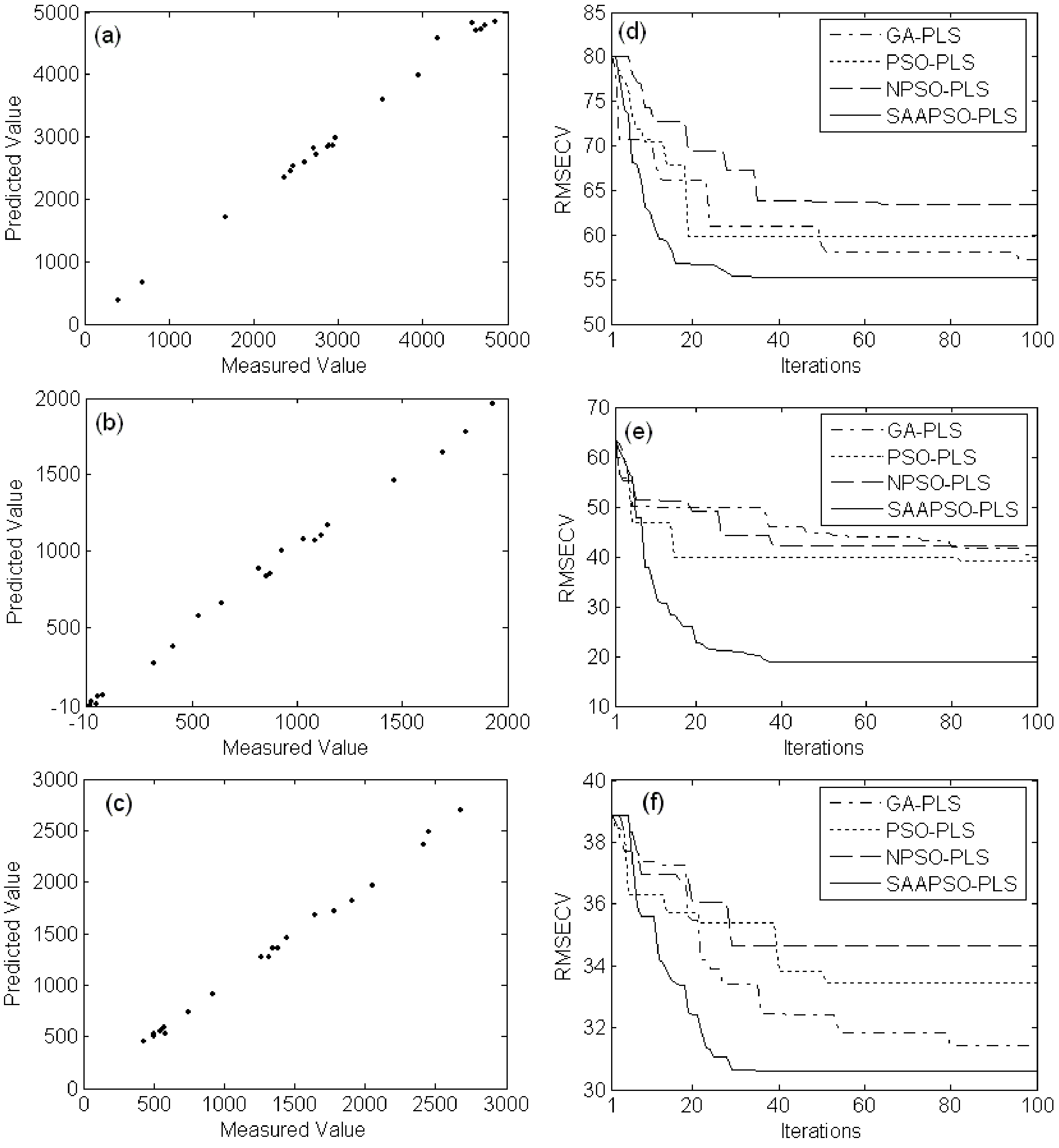

Figure 1. Scatter plot of measured value vs. predicted value and iterations curves for flue gas dataset.

In the paper, SAAPSO is presented for determining the University.

REFRENCES

Lee CL, Jou CJG (2012). Integrated methods to improve efficiency of furnace burning recovered tail gas. Int. J. Hydrogen Energy. 37(8):6620-6625. http://dx.doi.org/10.1016/j.ijhydene.2012.01.027

Lillhonga T, Geladi P (2011). Three-way analysis of a designed compost experiment using near-infrared spectroscopy and laboratory measurements. J. Chemometrics 25(4):193-20. http://dx.doi.org/10.1002/cem.1371

Marcio VR, Jamile BS, Maria FP, Leonardo SGT (2011). A novel approach for development of a multivariate calibration model using a

Doehlert experimental design: Application for prediction of key gasoline properties by near-infrared spectroscopy, Chemometrics and Intelligent Laboratory Systems 107(1):85-193.

Centneret V, Désiré-Luc M, Onno EN, Sijmen de J, Bernard MV, Cécile S (1996). Elimination of uninformative variables for multivariate calibration. Anal. Chem. 68(21):3851-3858. http://dx.doi.org/10.1021/ac960321m; PMid:21619260

Arakawa M, Yosuke Y, Kimito F (2011). Genetic algorithm-based wavelength selection method for spectral calibration. J. Chemometrics 25(1):10-19. http://dx.doi.org/10.1002/cem.1339

Sorol N, Eleuterio A, Santiago AB, Alejandro CO (2010). Visible/near infrared-partial least-squares analysis of Brix in sugar cane juice: A test field for variable selection methods, Chemometrics and Intelligent Laboratory Systems 102(2):100-109. http://dx.doi.org/10.1016/j.chemolab.2010.04.009

academicJournals

Vol. 9(9), pp. 293-296, 15 May, 2014
DOI: 10.5897/SRE2014.5904
Article Number: 625DAAB44490
ISSN 1992-2248 © 2014
Copyright©2014
Author(s) retain the copyright of this article
http://www.academicjournals.org/SRE

Scientific Research and Essays

Full Length Research Paper

Biogas production potential of transgenic *Vetiveria zizanioides* in mesophilic batch anaerobic digestion

Peipei Sun, Wudi Zhang*, Fang Yin, Xingling Zhao, Jing Liu, Yubao Chen and Shiqing Liu

College of Energy and Environmental Science, Yunnan Normal University Kunming 650092, China.

Received 3 January, 2013; Accepted 2 March, 2013

Transgenic *Vetiveria zizanioides* were anaerobic digested in a batch laboratory scale reactor at mesophilic conditions (30°C). Grinding and shearing, two kinds of processing methods were used. During total fermentation time of 80 days, the production potential of biogas were 310 mL/g·TS, 332 mL/g·VS in the grinding processing group and 322 mL/g·TS, 349 mL/g·VS in the shearing processing group. The results show that the shearing processing was slightly better than the grinding processing for transgenic *V. zizanioides* digestion.

Key words: Transgenic *Vetiveria zizanioides*, mesophilic, anaerobic digestion, biogas production potential.

INTRODUCTION

Vetiveria zizanioides (Linn.) Nash, also referred to as *Gramineae vetiveria*, is a tall tufted, perennial, scented grass with an abundant network of roots. It grows naturally in swamp areas of Northern India, Bangladesh, and is probably naturalized in many parts of Southeast Asia. *Vetiver* is both xerophytes and aquatic plants, and can be grown in very wide pH value environment and various types of soil (Xu, 1999). It is widely used in purifying water quality, water and soil conservation, improvement derelict land and desert land, weave handicraft, etc (Jiang et al., 2008). In addition, *vetiver* can be used as the raw material of essential oil extraction, a huge potential for development (Mao et al., 2008; Feng et al., 2009; Hu et al., 2006).

The biogas potential of the selected transgenic *V. zizanioides* in a batch anaerobic reactor was studied. The objective of this experiment was to assess the possibility of transgenic *V. zizanioides* as energy plant, to provide reference data for the construction of the biogas project using transgenic *V. zizanioides* as raw materials.

MATERIALS AND METHODS

Feedstock and Inoculums

The transgenic *Vetiveria zizanioides* for fermentation came from Dongchuan of Kunming in China, introduced for preventing or controlling flood and reinforcing dam, mature, about 2 m, and had air dried naturally. Blade was bar and of hard quality. Feedstock was grinded and cut into pieces, in order to make fermentation feedstock and inoculums contact fully. Stem and leaf of transgenic *V. zizanioides* were cut into less than 1 cm of small section in Shearing group, stem and leaf of transgenic *V. zizanioides* and were grinded into powder fineness less than 500 mesh in grinding group.

Inoculums were anaerobic activated sludge domesticated by our laboratory. The characteristics of the feedstock and inoculums were

*Corresponding author. Email: 786592293@qq.com

Table 1. The characteristics of the feedstock and inoculums.

Feedstock				Inoculum		
Grinding Group		Shearing group				
TS (%)	VS (%)	TS (%)	VS (%)	TS (%)	VS (%)	pH
94.42	93.29	93.11	92.32	8.08	50.38	6.5-7.0

TS: total solids, VS: volatile solids.

Table 2. TS, VS and pH value of fermentation liquid before and after fermented and TS, VS degradation rate of fermentation liquid.

Sorts	Treatment	TS (%)	VS (%)	pH	TS degradation rate (%)	VS degradation rate (%)
Grinding group	Before fermented	4.60	63.46	6.5	36.09	6.82
	After fermented	2.94	59.13	6.5		
Shearing group	Before fermented	4.88	67.88	6.5	23.57	12.89
	After fermented	3.73	59.13	7.0		
Control group	Before fermented	3.87	46.13	7.0	51.16	0.50
	After fermented	1.89	45.90	7.0		

TS: total solids, VS: (volatile solids)

shown in Table 1.

According to the total solid (TS) of feedstock and inoculums, experimental group, including grinding group and shearing group, was chosen (4%) as objective fermentation concentration, mass fraction of inoculums set (30%) to preparation. In order to eliminate the gas products of inoculums and get the net gas products of feedstock, the control group is necessary. Three groups of devices in each group were used for parallel comparison. Biogas production from the reactors was monitored daily by water displacement method. The volume of water displaced from the bottle was equivalent to the volume of gas generated. Methane content was judged by observing the flame color. The reactor was mixed manually by means of shaking and swirling once in a day. The reactor was operated at mesophilic conditions (30°C) using a constant temperature water bath.

RESULTS AND ANALYSIS

TS, volatile solid (VS) and pH value of fermentation liquid before and after fermented: TS, VS and pH value of fermentation liquid before and after fermented and TS, VS decompose rate of fermentation liquid show in Table 2.

Gas production rate

In this fermentation experiment, the grinding group lasted for 80 days, shearing group for 77 days, and control group for 13 days. The definite gas production quantity varying with fermentation time is shown in Figure 1.

Gas production rate varying with fermentation time was gotten by calculating, the result can be seen in Figure 2. Gas production rate reached 85% on the 42nd day in the grinding group, and on 49th day reached the same level in the shearing group. Hence when designing biogas project of transgenic *V. zizanioides* the HRT is suggested to be design for 45 day which is more reasonable and ensure the full decomposition of the raw materials, reduce the investment cost and shorten the payback time.

Analysis on gas production potential

Biogas production potential of transgenic *Vetiveria zizanioides* in anaerobic digestion were statistically analyzed, the results are as shown in Table 3. In order to further evaluate biogas production potential of transgenic *V. zizanioides*, we compared its potential with other materials fermented at the same temperature, and show the result in Table 4. Cellulose and hemicellulose content is high and matter of sugar and fat kind content is low in botanic fermentation material, which digested difficultly and had a long fermentation period. Similar to this kind of materials, the result of transgenic *V. zizanioides* fermentation to produce biogas appears ideal. From Table 3, compared with the traditional fermentation materials, dung and straws, TS gas production rate is 0.75 times of pig manure, and much better than straws. Compared with Eupatorium adenophorum Spreng, a kind of energy plant, the gas production potential is 4.86 times. Therefore, transgenic *V. zizanioides* is a very good methane fermentation raw materials and a good energy

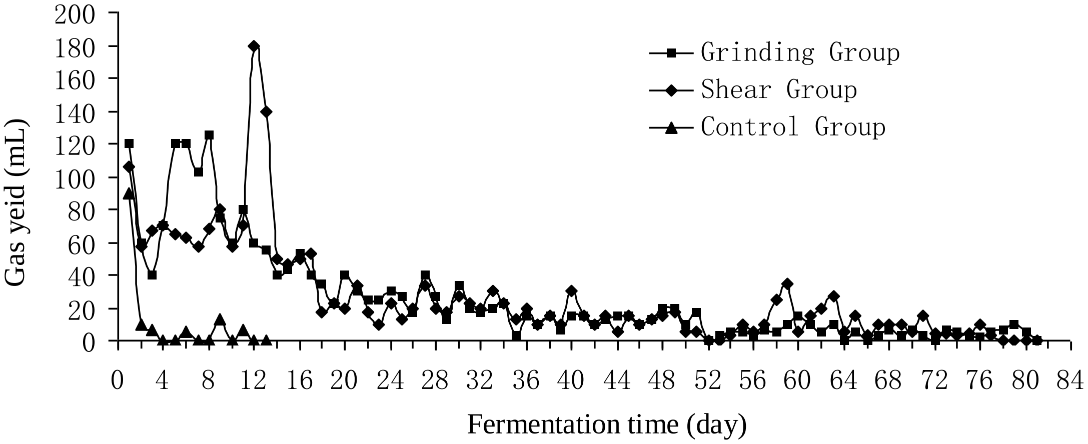

Figure 1. Curve of gas production varying with fermentation time.

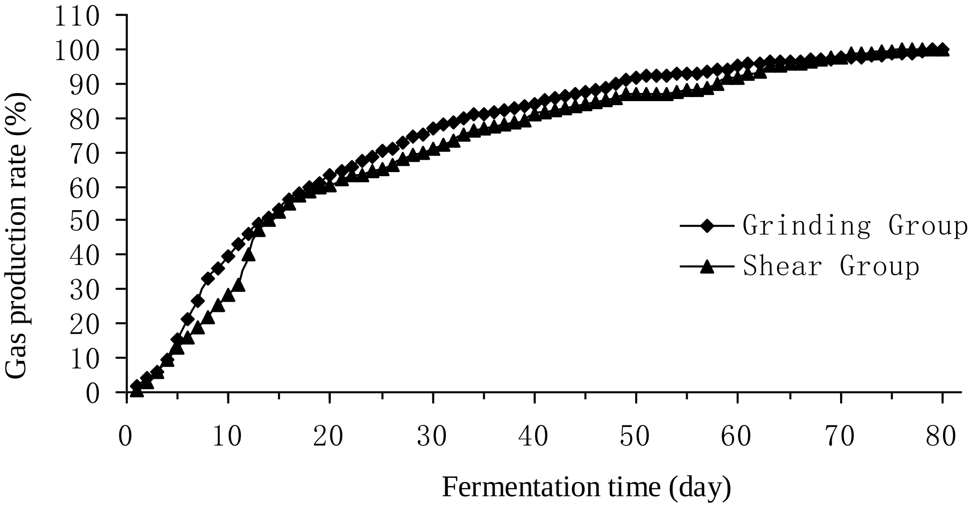

Figure 2. Curve of gas production rate varying with fermentation time.

Table 3. Biogas production potential of transgenic *Vetiveria zizanioides* in anaerobic digestion.

Sorts	**Net gas production (mL)**	**TS gas production rate (mL/g·TS)**	**VS gas production rate (mL/g·TS)**	**Tank volume gas production rate (mL/mL·d)**	**Raw material gas production (mL/g)**
Grinding Group	1950	310	332	0.06	293
Shearing Group	2000	322	349	0.06	300

TS: total solids, VS: volatile solids.

plant (Hu et al., 2008; Yang et al., 2011; Zhang et al., 2004).

Conclusion

In the experiment of anaerobic digestion to produce biogas by transgenic *Vetiveria zizanioides*, the production potential of biogas were 310 mL/g•TS and 332 mL/g•VS of the grinding processing group, and 322 mL/g•TS and 349 mL/g•VS of the shearing processing group. From the gas production and VS degradation rate two advantages can be judged that *vetiver* fermentation shearing processing is slightly better than the grinding processing.

Table 4. Gas production potential of different raw materials.

Fermentation material	Fermentation time (day)	TS gas production potential (mL/g·TS)	TS gas production potential multiple	Reference
Transgenic *Vetiveria zizanioides*	80	316	1.00	-
Vetiveria zizanioides	90	471	0.67	HU et al. (2008)
Pig dung	-	420	0.75	ZHANG et al. (2004)
Wheat straw	70	207	1.53	FENG et al. (2009)
Bean straw	70	269	1.17	FENG et al. (2009)
Eupatorium adenophorum Spreng	80	65	4.86	HU et al. (2006)
Dianthus caryophllus straw	32	266	1.19	YANG et al. (2011)

TS (total solids) gas production potential multiple is the ratio of the gas production potential of tobacco residues into the gas production potential of other fermentation materials.

Transgenic *V. zizanioides* fermentation lasted for 80 days. Gas production rate by different processing reached 85% respectively on the 42nd day and 49th day, hence when designing biogas project of transgenic *V. zizanioides* the HRT is suggested to design for 45 days.

The biogas potential of anaerobic digestion of transgenic *V. zizanioides* can achieve the gas potential of excrement kind material, and much better than the straw materials. In addition to purifying water quality, water and soil conservation, improvement derelict land and desert land, transgenic *V. zizanioides* is a very good methane fermentation raw materials and a good energy plant.

Conflict of Interests

The author(s) have not declared any conflict of interests.

ACKNOWLEDGEMENT

This work was supported in part by Science and Technology Condition Platform Construction Projects of Yunnan Province (2010DH012).

REFERENCES

Feng F, Qin L, Wang X, Min Z (2009). Biogas potential and characteristics in medium temperature anaerobic fermentation of sunflower plate, wheat straw and bean straw. *Acta* Agriculturae Boreali-Occidentalis Sinica. 18(3):361-364.

Hu J, Zhang W, Yin F, Liu S, Guan H (2006). Experimental study of continuous methane fermentation by using *Eupatorium adenophorum* Spreng. Agric. Technol. 26(4):33-36.

Hu X, Zhang J, Zhang W, Yin F, Xu R (2008). Experimental study on mesophilic biogas fermentation with *Vetiveria zizanioides*. Sci. Technol. Inf. 27:8-9.

Jiang D, Zhang X, Qi G, Liao J, Wang D (2008).*Vetiver* introduction and application. Guangxi Hortic. 19(1):30 -31.

Mao P, Yang H, Ma X (2008). Progress in Research and Utilization of *Vetiveria zizanioides*. J. Agric. Sci. Technol. 13(1):88-93.

Xu Z (1999). Beijing: Chinese Agricultural Science and Technology Press. J. World Genus Grasses.

Yang H, Ma Y, Zhang W, Yin F, Li J, Xu R, Li J, Chen Y, Liu S (2011). Experimental study on potential of biogas fermentation with *Dianthus caryophyllus* Straw. J. Yunnan Normal University. 31:81-84.

Zhang W, Song H, Yin F, Li J (2004). Biogas Fermentation and Comprehensive Utilization. Kunming: Yunnan Science Press.

academicJournals

Vol. 9(9), pp. 297-302, 15 May, 2014
DOI: 10.5897/SRE2014.5906
Article Number: FEE28A444492
ISSN 1992-2248 © 2014
Copyright©2014
Author(s) retain the copyright of this article
http://www.academicjournals.org/SRE

Scientific Research and Essays

Full Length Research Paper

Sustainable development of landscape environment of traditional Changzhen

Jia Yuanyuan[1], Lu Junfu[2]* and Qing Ling[3]

[1]College of Architecture and Civil Engineering, Xihua University, Chengdu 610039, China.
[2]State Key Laboratory of Geohazard Prevention and Geoenvironment Protection, Chengdu University of Technology, Chengdu, 610059, China.
[3]Shapingba Teachers' Advanced Studies College, Chongqing 400030, China.

Received 3 January, 2013; Accepted 2 March, 2013

Old town is like living fossil which has accumulated rich historical connotations; the one carrying the history of a region's political, economic, cultural and ecological changes as well as the formative art created by collective labors and wisdoms of generations. The preservation of ancient Chinese dwellings and old towns began late; many historical architectures and traditional country fairs are forcibly removed during the transformation of old cities and towns, thus ancient towns with their original historical looks are becoming less and less. In comparison, the preservation and development of old western towns started earlier than China; with rich experience, they offer good examples for China, especially the successful developing way: eco-tourism. By comparing the preservation and development of traditional Chinese towns' landscape features to that of western ones, this paper points out that the future development of old towns rely on proper handling of the relation between preserving and the feasibility of renewing, so as to maintain the landscape features of old towns in the course of sustainable development.

Key words: Traditional Changzhen, landscape environment, sustainable development, preservation.

INTRODUCTION

Traditional Changzhen as carrier of a particular region's history and culture embodies a specific nature, geography and ecology, as well as a society, history and culture; their forms and features are made up by thousands years history, the precious heritage left by our ancestors. To research landscape features of old town, to protect them and make good use of them is significant and practical for the maintenance of historical context and local traits.

It is hard to trace when and where the names of old Chinese towns began. Looking up Encyclopedia of Cihai or Etymology, we can know "Chang" means fair or place where people gather together (Ci, 1979a), "Zheng" means town or fair (Ci, 1979b), an industrial and commercial resident area smaller than city. Changzhen in China is where country fair locates, the population and commercial center of countryside level in terms of geography and politics.

The function of traditional Chinese Changzhen as fair is weakened after long history, instead, they represent more

---

*Corresponding author. Email: junfulu05@hotmail.com cultural deposit through their architectural styles, layouts of streets and lanes, monuments and former dwellings, national and folk features; the cultural transmission interweaving tangible heritage with intangible, static heritage with dynamic (Liu, 2008), the living fossil of Chinese historical and cultural context (Shen, 2007).

The traditional Changzhen mentioned in this paper refers to those small towns which enjoy some history and traditional culture characters. The phenomena of old town developing, traveling or applying for world heritage site, etc. are the reflection of its value.

RESEARCH SIGNIFICANCE OF TRADITIONAL CHANGZHEN'S LANDSCAPE FEATURES

The landscape features of a small town are the comprehensive product of local nature, history and humanities; they can be fast changed by factors of natural disasters like earthquake, flood, tsunamis, mud-rock flow, volcanic eruption, etc., and political evolution, cultural exchange, vandalism, etc. The 5.12 Wenchuan earthquake which happened in Sichuan province and the secondary geological disasters after earthquake like large-scale landslides, ground collapse, surface dislocation, mud-rock flow and barrier-lakes, etc. ruined the only autonomous county of Qiang minority in China. The loss was serious such that lots of material carriers of Qiang culture disappeared or were heavily damaged; some of the inheritors (performers) of intangible heritage are even dead (Wu, 2009). From late 20th century till date, with the fast development of urbanizing plus foreign culture, technology, living mode flooding into China, traditional styles of small towns are replaced by the stereotyped look under globalizing context, gradually driving the local traits of rural landscapes out of the historical stage.

Therefore, the research of traditional Changzhen's landscape features, protecting and exploiting them is important and pragmatic for sustaining history and culture as well as conserving local traits.

PROTECTION STATE OF TRADITIONAL WESTERN TOWNS

The historical and cultural protection in the West first started from Europe; in terms of preserving and developing old towns, comparatively speaking, it is well done in Europe, especially in France.

The protection has been through stages. During the socially and economically underdeveloped period, natural damage was the main way to destroy cultural relics and monuments; during the initial stage of economic development, that is, the period of industrial revolution, artificial damage instead of natural damage became the primary way because people were eager to better their material condition, neglecting the spiritual need; after the economy reached a certain level; their focus was correspondingly switched to chase after colorful spiritual life, relics and monuments which were re-cherished and seemed more valuable. In between those periods, damages to cultural relics and monuments caused by construction were much more than those caused by the nature and wars.

After the Second World War, more and more people paid attention to the relation between the nature and human beings, forming the modern thinking of getting along with the nature and coordinate developing. The following practices were that western countries increased the input in environment, improving the construction of urban citizens' living condition. They would rather respect the nature than ruin their environmental quality for faster economic construction.

Western countries have made the relevant laws and measures in preserving old town. The classic ones are "three charters and one convention" in 20th century, that is, Athens Charter, Venice Charter, Washington Charter, and Convention Concerning the Protection of the World Cultural and Natural Heritage by UNESCO in November, 1972. Athens Charter in 1933 is the first international document in conserving historic architectures. The Venice Charter for the Conservation and Restoration of Monuments and Sites in 1964 (abbreviated as Venice Charter) extended the idea of conservation of historic architectures to "a unique civilization, a meaningful development, a town or country setting which has witnessed historical events. Recommendation concerning the safeguarding and contemporary role of historical areas drawn up by UNESCO in 1976 (abbreviated as Nairobi Recommendation) clearly proposed the concept of historical areas, thus the safeguarding of historical architectures are not limited in their surrounding areas, historical streets, villages, towns and ancient towns are also included. Charter for the Conservation of Historic Towns and Urban Areas in 1987 (abbreviated as Washington Charter) puts the conservation of historic cities and towns to the first place, which is identified in the form of international laws and regulations (Xiong et al., 2002); the classical European flavors are thus largely inherited.

CONSERVATION STATE OF TRADITIONAL CHINESE CHANGZHEN (OLD TOWNS)

The safeguarding of old towns and ancient dwellings in China is referred to the "Charter for the Conservation of Historic Towns and Urban Areas" adopted by ICOMOS on the 8th general assembly held in Washington, DC, October, 1987. From Figure 1a and b, we can see the first local regulation regarding ancient dwellings in China, conservation regulation concerning ancient dwellings in Southern Anhui Province, was passed on the 33th

Figure 1. Ancient Villages in Southern Anhui – Xidi and Hongcun. **(a)** The outside landscape of the village. **(b)** The inside landscape of the village.

Session of the 8th People's Congress Standing Committee of Anwei province on 21st September, 1997, which has been carried out since 1st January, 1998.

The first step among the measures to protect ancient Chinese towns is to identify those famous historic towns and classify them into the scope of legal protection. According to the statistics, in China, the number of safeguarded historical and cultural towns, reserves, monuments above county level is less than 100 000 sites; the amount and scope are far less than those countries that have smaller area, shorter history and less population. Take England as example, its area is 130 000 km^2, only 1/73 of China, whereas it has 500 000 listed architectures and over 8000 reserves. The implementation of safeguarding ancient towns/villages in China will facilitate the preservation of historical and cultural heritage in larger scale, catching up the amount to match the status of china that has thousands years civilization. Historical and cultural villages and towns constitute the important parts among conservation system of Chinese heritage (Yin, 2008).

Managers in small towns are familiar with the local conditions and closely related with the masses, while they have awareness limitation and peasant consciousness due to the cultural and educational shortage. They emphasize industrialization but depreciate urbanization; emphasize economic profit but ignore environmental and social interest; focus on their political "achievements" and "image projects" but neglect the improvement of individual quality and awareness; as well as pay little attention to developing and conserving ancient towns in long-term.

DEVELOPED STATE OF TRADITIONAL OLD TOWNS IN WESTERN COUNTRIES

The development of old towns concerns the relation between tourism, preservation and ecology. Europe proposed the thought of ecotourism after continuous exploring and comparing successes to failures. Ecotourism is travelling modes which cultivates tourists, experience and appreciate them. There are three criteria of ecotourism: nature based factors, education ingredients and continuity.

Old towns and architectures abroad are preserved mainly through the ways of developing ecotourism and transferring the ownership of properties, etc. In West Europe, governments often transfer the ownership of castles with very favorable, even zero price, to private owners, on the condition of that the buyers must strictly abide by the standards of restoration and maintenance stipulated by governments, and violation of those standards will be punished. The Russian government could not afford the preservation of old architectures, trading more than 3000 units of old castles to international market in March, 2004.

Developing and exploiting old towns as tourism are the ways to conserve them or to timely rescue the few survived ones. Tourism in France can be rated first class and it occupies a very important position in France's economy. France is one of those countries that have successfully preserved and developed old towns. Their methods and experiences are worth our borrowing.

First of all, they strictly comply with the regulations and specify the preservation of tourism resources into laws. According to the statistics, about 14 000 architectures and monuments are classified into historical sites, and 26 000 units are on the list of reserves. Among 4000 museums, about 1000 are governed by the nation. For the conservation of the tourism resources, the French government has laid down strict laws and policies on the ownership as well as safeguarding and exploiting them. All historical and cultural monuments in France have been well preserved and restored under the principle of repairing the antiques as their original looks.

Secondly, they take full advantage of tourism resources to development the tourism industry. At the time of

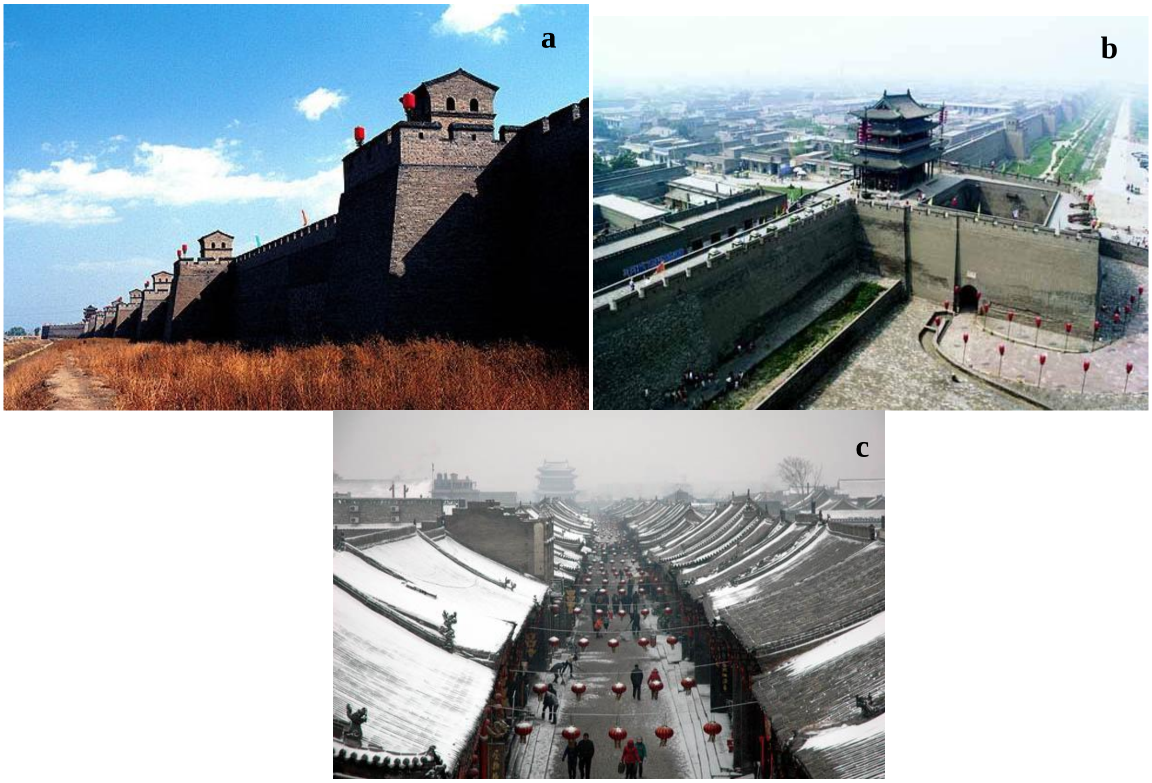

Figure 2. Ancient city of Pingyao in Shanxi province. **(a)** Wall outside the city. (b) Small town outside the city gate-Wengcheng. (c) Inner street inside the city

preserving the resources in accordance with the laws, the government has fully developed and exploited the artificial sceneries and natural landscapes. Historical and cultural heritages like the Louvre, Versailles, Notre Dame, etc. are intriguing; people fill in south France, west coast, Alps and the skiing resorts of Pyrenees.

Thirdly, the government gives weight to capital investment and policy support. They spend over 20 billion franc each year on the preservation and development of tourism resources, among which, 2 billion franc is used for cultural heritage; 1.8 billion for Museums, and the rest for developing.

Fourthly, there are highly developed transportation and service facilities. The developed transportation, fine road condition, majority of scenic spots accessing to highways, smooth traffic, service stations along roads, public convenience, catering, accommodations, etc. have brought convenience to tourists.

Fifthly, they offer high quality service and efficiency. Many French hotels are chain star hotels with the outstanding characteristics of integration, modernization and computerized management mode. Practitioners in tourism always offer good service, the management and service people in hotels are dedicated to their duties and very professional (Zhou, 2007).

The points mentioned above can be implemented in China for exploiting tourism resources of old towns, further constructing and developing them. They are practical measures worth referring to.

DEVELOPED STATE OF TRADITIONAL CHINESE CHANGZHEN (OLD TOWNS)

The development of traditional Chinese Changzhen (old towns) takes the form of tourism. From Figure 2, we can see the well-known ancient city of Pingyao in Shanxi province. Figure 3 shows the old town of Lijiang in Yunnan province, Ancient Villages in Southern Anhui – Xidi and Hongcun are on the list of world cultural heritage. Zhouzhuang and Tongli, the ancient towns in southern Yangtze, with the landscape features of small bridges and streams, have boomed the tourism industry in these regions. Behind smooth developing, the pressure ancient towns faced gradually came out. Tourism development brought problems for the preservation of old towns, example, over saturation of tourist capacity, fast increasing of tourists exceeding the capacity ancient towns could hold and tendency of over commercialized. Under the drive of economic profit, commercial networks were increased, featureless souvenirs flooded everywhere, and strong commercial air of all people being merchants gradually eroded the natural environment and humanistic atmosphere of ancient

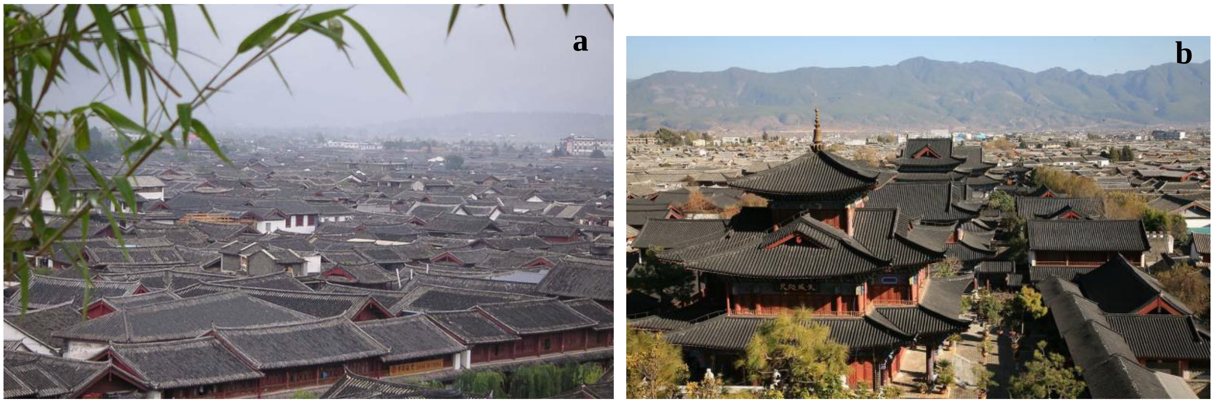

Figure 3. Old town of Lijiang in Yunnan province. **(a)** The Panoramic landscape of the ancient town. **(b)** MuFu - the inside landscape of the ancient town.

Figure 4. Ancient town Zhouzhuang.

towns. The development of tourism was not coordinate with the residents' life. The gained economic profit did not better the residents' living. Problems of aging building, incomplete infrastructure, flood and fire hazards, etc. affected harmoniously developing ancient towns that sustain the traditional styles, the unity of tourism development and monuments preservation. Developing tourism is the way to promote the value of monuments and offer the financial support for the preservation; exploiting the monuments is an important channel to develop tourism. Therefore, preserving and developing should not work against each other, but mutually promote and complement. Monuments as tourism can produce huge economic profit, but solely chasing after profit and ignoring the preservation, once the tourist recourse on monuments are ruined, it will threaten the development of tourism industry. Based on long-term interest, placing the preservation of monuments to the first position and developing them scientifically, tourist industry can be sustainable. Our pressing task is to assess the tourist resource on monuments and ascertain the reasonable capacity, seek for the balance between preserving and tourism developing of historic sites (Zhang, 2008).

From Figure 4, we can see Zhouzhuang as the leading role in terms of preserving and developing tourism industry among the ancient towns in Southern Yangtzethe has made some achievement, with the features of well preserved integrity and representativeness, since the cultivated awareness of preservation has penetrated into the minds of local residents. Zhouzhuang, as the pioneer in China, has sustained its development, and by constantly borrowing the mature thoughts and methods of planning and developing historical towns from western countries, it also offers a prototype which represents a typical Chinese style and is a set of scientific theories of preserving and planning ancient Chinese town.

CONCLUSIONS

Different from a single antique or monument, ancient towns are valuable assets for mankind representing the living condition in certain period and the simple dwelling environment created by people, thus reflecting the material and cultural level at that time. The main developing form for ancient Chinese towns is tourism with the purpose of making profit, but the capital used for later development is not much. The local governments and residents in ancient towns have not realized the direct relation between sustainable development and their lives, causing little awareness of and paying little addition into preservation of ancient towns and later development. The preserving and developing of ancient towns are always difficult to balance. In that aspect, old western towns started earlier than china. Their rich experience, especially the successful developing form - ecotourism, gave China inspiration. The future developing focus should be placed on the relation between well preserving them and developing them. Taking preservation as the priority, make clear of developing orientation and the measures of exploiting them.

Conflict of Interests

The author(s) have not declared any conflict of interests.

REFERENCES

CI HAI editor Committee (1979a). “CI HAI”, Shanghai Lexicographical Publishing House, China, P. 1203.

CI HAI editor Committee (1979b). “CI HAI”, Shanghai Lexicographical Publishing House, China, P. 3946.

Liu W (2008). Habitat environmental study of domestic ancient town of Protection, Modern Enterprise Education, Vol.11, 2008, pp. 143-150.

Shen WB (2007). Protect the town is to protect the historical context. Exploration and Free Views, 10:6-15.

Wu R (2009). The formation and development of domestic and international heritage protection theory, Lantai World, 1:80-81.

Xiong XX, Zhang S, Zhou J (2002). The Problem and Strategies of the Canal Towns' Tourism in Jiangnan: The research of the tourism in Zhouzhuang, Tongli, Luzhi, Architectural landscape along the Lake, Urban Planning Forum, 6:62-66.

Yin Z (2008). Disaster planning should focus on fieldwork Follow the scientific, City Planning Review, 7:31-40.

Zhou ZQ (2007). The old town protection should pay attention to the heritage context of the field-effect. Exploration and Free Views, 10:7-17.

Zhang Q (2008). Habitat environmental study of foreign ancient town development. J. Tourism Dev. 12:117-118.

academicJournals

Vol. 9(9), pp. 303-310, 15 May, 2014
DOI: 10.5897/SRE2014.5907
Article Number: 8E4D96844494
ISSN 1992-2248 © 2014

http://www.academicjournals.org/SRE

Scientific Research and Essays

Full Length Research Paper

Research on the transient radial force of the centrifugal pump

Wei Li[1,2*], Weidong Shi[1,2], Zhongyong Pan[1,2], Xiaoping Jiang[1,2] and Ling Zhou[1,2]

[1]Research Center of Fluid Machinery Engineering and Technology, Jiangsu University, Zhenjiang 212013, China.
[2]National Engineering Research Center of Pumps and Pumping System, Jiangsu University, Zhenjiang 212013, China.

Received 3 January, 2013; Accepted 2 March, 2013

The three-dimensional unsteady flow field in centrifugal pump under different flows was numerically simulated based on the commercial fluent software, using standard k-ε turbulence model, SIMPLE algorithm and sliding mesh technique. The characteristics of the time domain and frequency domain of the pressure pulsations, as well as fluctuation strength were analyzed. The varying locus of transient radial force vector of the centrifugal pump with time and the varying pattern of transient radial force with time were investigated. The results show that the frequencies of the pressure pulsations are mainly the blade passing frequency at the monitoring points, and the most intense pulsation appears at the volute tongue under the same frequency; the variation cycle of the transient radial force is the same with the passing cycle of the blades, and the direction of the radial force deflects anticlockwise as flow rate increases. At the designed flow rate, the distribution region of the radial force vector is the closest to the origin point and the area of the region is the smallest, with the gentlest fluctuation.

Key words: Centrifugal pump, transient radial force, pressure pulsation, numerical simulation.

INTRODUCTION

With the extensive application of large-scale centrifugal pumps in agricultural production, urban water supply and other fields, the requirements for the performance and stability of centrifugal pumps are increasing. The radial force greatly affects the efficiency and reliability of the pump, causing vibration and noise to the unit, and also fatigue failure to the shaft. Recently, with the development of the Computational Fluid Dynamics (CFD) and the computer technology, the unsteady numerical simulation is more and more widely applied in the studies of the characteristics of flow field (Meneveau and Katz, 2000; Kitano, 2005; Barrio et al., 2010; Spence and Amaral-Teixeira, 2009; González et al., 2002; Liu et al., 2013), and the numerical calculation of the unsteady force generated in centrifugal pumps has become an effective means (Ling et al., 2013). Kitano (2005) performed numerical simulation to the internal flow field of centrifugal pumps and pointed out that the unsteady characteristics of the internal flow vary in a periodic manner, and the flow causes intense pressure pulsation at the impeller outlet and inside the volute (Kelder et al., 2001; Longatte and Kueny, 2009; Wei et al., 2013). Jose et al. (2006) used unsteady numerical simulation to study the pattern that the transient radial force on the impeller

---

*Corresponding author. E-mail: lwjiangda@ujs.edu.cn

Figure 1. Model calculation domain.

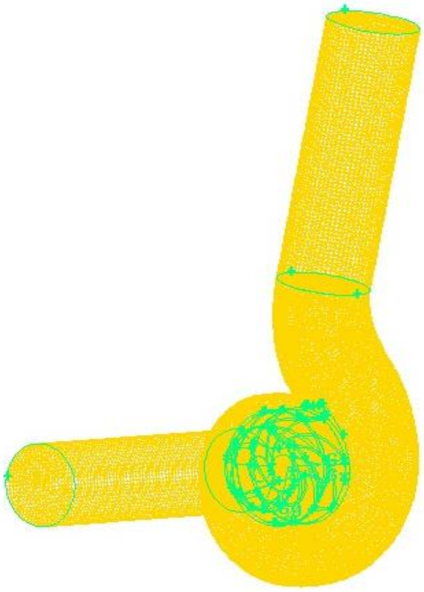

Figure 2. Mesh generation.

varies with time under different running conditions and volute tongue clearances (Adkins and Brennen, 1998; Brennen and Acosta, 2006; Guo and Okamoto, 2003). In this study, unsteady numerical calculation method is used to simulate the pressure pulsations of internal flow field in the centrifugal pump under three different running conditions; the characteristics of the time domain and frequency domain of the pressure pulsations, as well as their fluctuation strength are analyzed, and the locus of the variation of the centrifugal pump's transient radial force vector with time and the varying pattern of transient radial force with time are investigated.

The basic parameters of centrifugal pump are: designed rate of flow Q_d=1200 m^3/h, rated rotation speed

NUMERICAL CALCULATION MODEL AND METHODS

Simulation model

n=980 r/min, specific speed n_s=220, impeller outer diameter D_2=420 mm, outlet width b_2=85 mm, blade number z=7. Considering the complexity of the centrifugal pump structure, partitioning modeling is used for the convenience of mesh generation. The model calculation regions include the inlet pipe (1 m), the impeller, collector, and the outlet pipe (1 m), as shown in Figure 1. Gambit software is used for the mesh generation of the three-dimensional model, where for the impeller region and the collector region, unstructured tetrahedral mesh which is more adaptable to complex boundaries is adopted, and for the regions of the inlet pipe and the outlet pipe, structured hexahedral mesh is adopted; the total number of the meshes is about 500,000. The mesh generation of the pump model is shown in Figure 2.

Numerical calculation method

Based on fluent commercial software, the 3D incompressible N-S equation is used to describe the pump's interior flow, and the standard k-ε turbulence model close equations are adopted. The velocity inlet boundary condition is used for the inlet, the free outflow condition is used for the outlet, standard wall functions are used for regions close to the solid wall, and the non-slip boundary condition is for solid wall. Results from steady constant calculations are used for the initial flow field of the non-steady constant calculations, and 0.6Q_d, Q_d and 1.4Q_d are selected as the three working conditions. The non-steady constant calculation uses the sliding mesh model to simulate dynamic and static interfere flow field, forming two mesh slip planes at the inlet and outlet of the impeller. The impeller meshes rotate relatively to those in other fluid regions, without the superposition of grid nodes on both sides of the interface. The calculations of all the fluid regions are executed at the same time. Discrete equations' solutions at each time step are worked out using SIMPLE algorithm. Time steps will be pushed forwards after calculation convergence, at the mean time, impeller meshes turn to a new position for new time step length calculation. The time step used in this paper is 1/360 of the impeller turning cycle (0.000170068 sec), that is, the time for the impeller to turn 1°. Iterative computation would stop after the data becomes relatively strict periodic on the monitor, and then the time-dependent curve of the centrifugal pump's transient radial forces is obtained.

NUMERICAL PREDICTION OF HYDRAULIC PERFORMANCE AND EXPERIMENTAL VERIFICATION

To verify the accuracy of the numerical simulation, the value of the experimental and numerical simulation of hydraulic performance in centrifugal pump were compared. The external characteristic curve is shown in Figure 3. The analysis on diagram shows that the external characteristics curve calculated by the numerical calculation agrees well with test results. The relative error

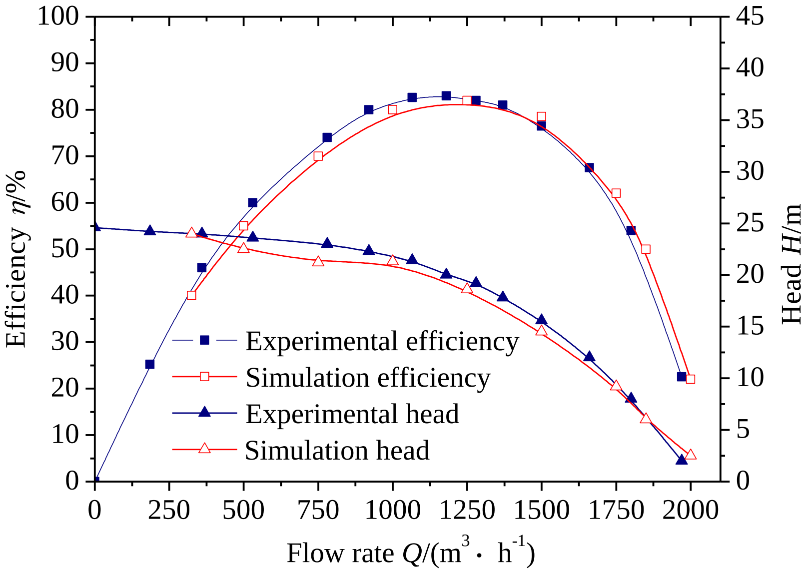

Figure 3. Comparison of external characteristics predicted curve and test curve.

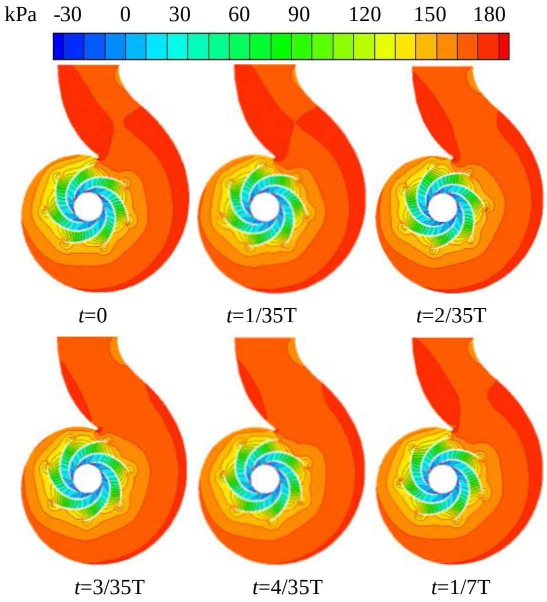

Figure 4. Static pressure distribution.

of the head and the efficiency were 2.6 and 2.0%, respectively, at maximum efficiency points of numerical calculation results and test results. The head and efficiency curves predicted by unsteady numerical calculation tend to below the test value. The main reason may be due to ignoring influence of the pump chamber and wall roughness on the performance of the pump. According to the analysis of test results and unsteady numerical calculation results, using the grid type, the turbulence model, etc. can more accurately predict the external characteristics of centrifugal pump.

STATIC PRESSURE DISTRIBUTION

The internal pressure distribution of the centrifugal pump changes with the impeller rotation. Let T be the time cost by one rotation of the impeller, since the impeller of the model has 7 blades, the passing cycle for each blade is 1/7T. Figure 4 presents the static pressure distribution of the impeller and volute areas under designed flow rate at the different time points in one blade passing cycle (1/7T).

It can be seen that in one blade passing cycle, the pressure of the area around the volute tongue varies significantly. When the blade passes by the volute tongue, the pressure of the area around the volute tongue reaches the lowest point; and when the blade goes away from the volute tongue, the pressure of the area increases gradually. At the inlet of the volute, an apparent low pressure area appears in the area that the tip of the blade passes by. Because of the dynamic-static interference between the impeller and the volute, as the relative location of the blade with the volute tongue changes, the static pressure distribution inside the volute shows a periodic change. The discrepancy of the internal pressure distributions inside the flow channel at different times is exactly the result of the dynamic-static interference between the impeller and the volute.

ANALYSIS OF PRESSURE PULSATION

Eight pressure monitoring points are set along the spiral direction of the centrifugal pump volute at the near-wall

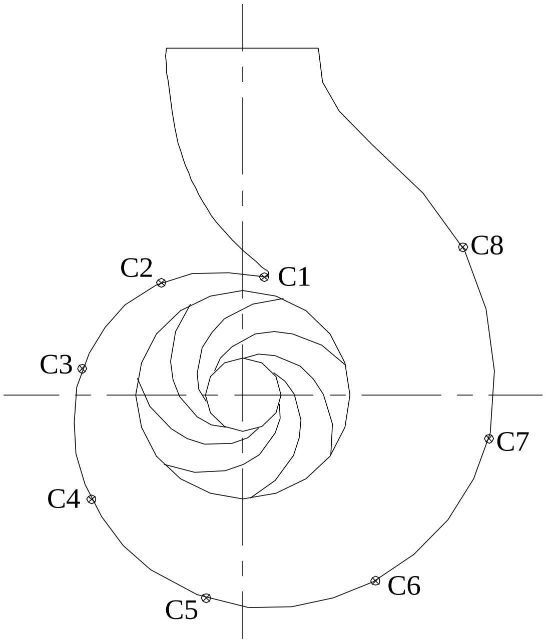

Figure 5. Pressure monitoring points.

side of eight sections of the volute. The monitoring points are named as C1~C8, while C1 is located at the volute tongue. The distribution of the monitoring points is as shown in Figure 5.

Analysis on the time domain of the pressure pulsation

Figure 6 presents the time domain charts of the pressure variations at different monitoring points of the model pump under the three running conditions of $0.6Q_d$, Q_d and $1.4Q_d$. The T in the figures indicates the time it takes for one rotation of the impeller. It can be seen from the charts that the pressure fluctuations of each point have basically consistent forms; they all have seven peaks and seven troughs, but with different amplitudes. The pressures gradually decrease with the increase of the flow rate, the amplitudes of the pulsations increase as the flow rate increases, and the difference of the pressure pulsation amplitudes in different region gradually decreases with the increase of the flow rate. Under the running condition with low flow rate, the amplitudes of the pressure pulsations from the volute tongue to Section III decrease significantly, and at Section III the flow basically stabilizes, as shown in Figure 6(a). Under the designed running condition, except for the C1 point at the volute tongue, the pressures of the other monitoring points are close, with slight increase along the spiral direction of the volute; in particular, for C5-C8, since they are far away from the volute tongue, the pressure pulsations are almost identical for these points; at the volute tongue, due to the complex fluid condition and the large pressure change gradient, the pressure of this point is quite different with other monitoring points, however, the pulsations are in pattern, the pressure change is shown in Figure 6(b). Under the running condition with large flow rate, the

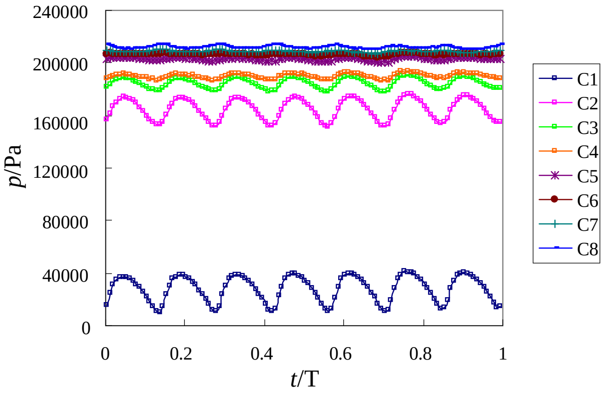

(a) $Q=0.6Q_d$

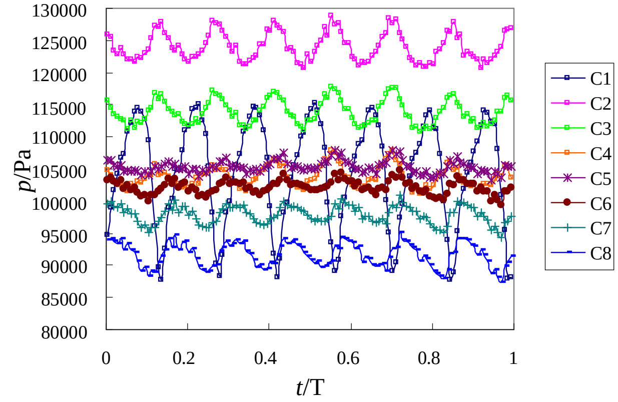

(b) $Q=Q_d$

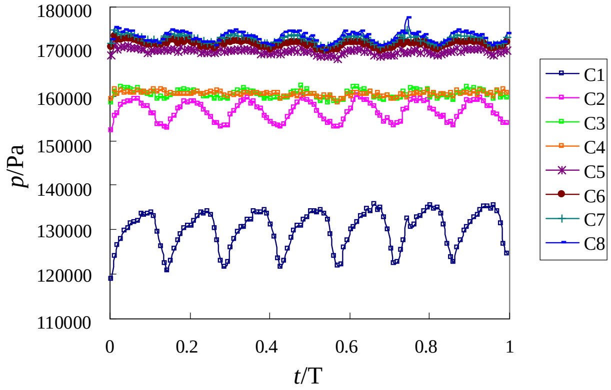

(c) $Q=1.4Q_d$

Figure 6. Pressure pulsation time domain charts.

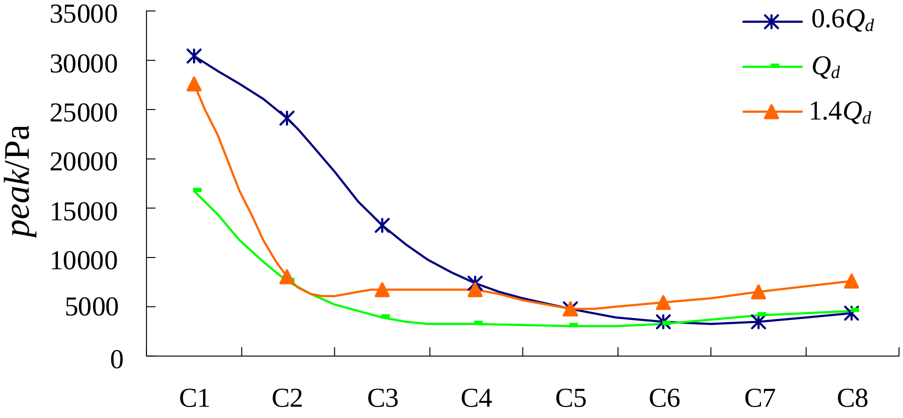

Figure 7. Peak curve of the pressure pulsation.

pressure pulsation amplitudes of the monitoring points are all large, with more disordered flow; the pulsation amplitude of the C1 point at the volute tongue is more than three times of the amplitudes of other points; the pressure of C2-C8 gradually decrease along the spiral direction of the volute, as shown in Figure 6(c).

Contrast on the peaks of the pressure pulsations

The pressure pulsation peak situation at each monitoring points along the spiral direction of the volute is shown in Figure 7. As can be seen from Figure 7, the maximum peak of the pressure pulsation is located in volute tongue position, the peaks of the pressure pulsations from the volute tongue to Section III sharp decline, and the peaks of the pressure pulsations from Section III to the volute outlet direction change more gentle, which accord with the analyzing results of the pressure pulsation time domain. Contrast can be seen, the peaks of pressure pulsations at each monitoring points under the non-design conditions always have a higher level, significantly greater than the designed running condition, and towards the outlet of the volute, the peaks pressure pulsations under the running condition with large flow rate are maximum, the peaks of the pressure pulsations under the design conditions and the running condition with low flow rate are basically consistent.

Analysis on the frequency domain of the pressure pulsation

The rotation speed of the impeller is 980 r/min, then the rotation frequency of the principle shaft is 16.333 Hz. For the number of blades is z=7, the blade passing frequency is 114.333 Hz. Convert the pressure pulsation data of the monitoring points through Fast Fourier Transform (FFT), and then the pressure pulsation frequency domain charts of the monitoring points could be obtained. Investigation shows that at each monitoring point, the frequency of the pressure pulsation is mainly blade passing frequency, followed by the doubled blade frequency, and under the same frequency the most intense pulsation appears at the volute tongue. The intensity of the pressure pulsations at each monitoring points under the blade passing frequency is shown in Figure 8, where the vertical coordinate is index coordinate. It can be seen that the pressure pulsation of the C1 point at the volute tongue is the most intense under different flow rates. With the increase of the flow rate, the intensity of the pressure pulsations of all the monitoring points increase, which accord with the analyzing result of the pressure pulsation time domain.

ANALYSIS OF THE TRANSIENT RADIAL FORCE

Variation of the transient radial join force in one rotation cycle of the impeller

Due to the coupling effect between the blades and the collector, the strength and direction of the radial force on the impeller always change in an approximate periodic manner within a certain range as the impeller rotates, where the cycle is related to the number of the blades. At the flow rates of 0.6Q_d, Q_d, and 1.4Q_d, the vector locus of the transient radial force on the model impeller in one rotation cycle T is shown in Figure 9.

It could be seen from Figure 9 that the vector locus of the pump model's transient radial forces under the three different flow rates are significantly different. When the flow rate is 0.6 Q_d or Q_d, the locus of the transient radial force are in the second quadrant, and the distributed regions have respectively 40° and 75° angles with the y axis; and when the flow rate is 1.4Q_d, the trail is in the fourth quadrant, with a 135° angle with the y axis. Meanwhile, at the flow rate of 0.6Q_d, the distributed

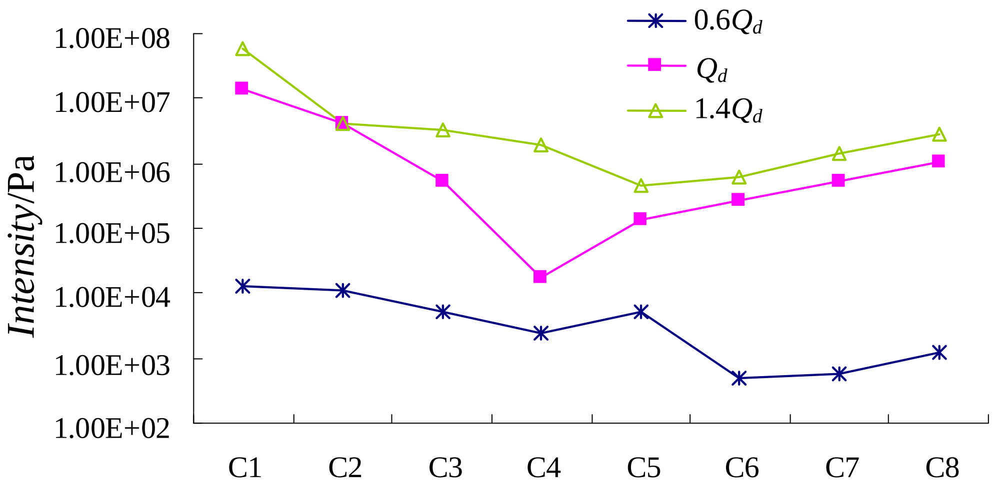

Figure 8. Intensity comparison of the pressure pulsations.

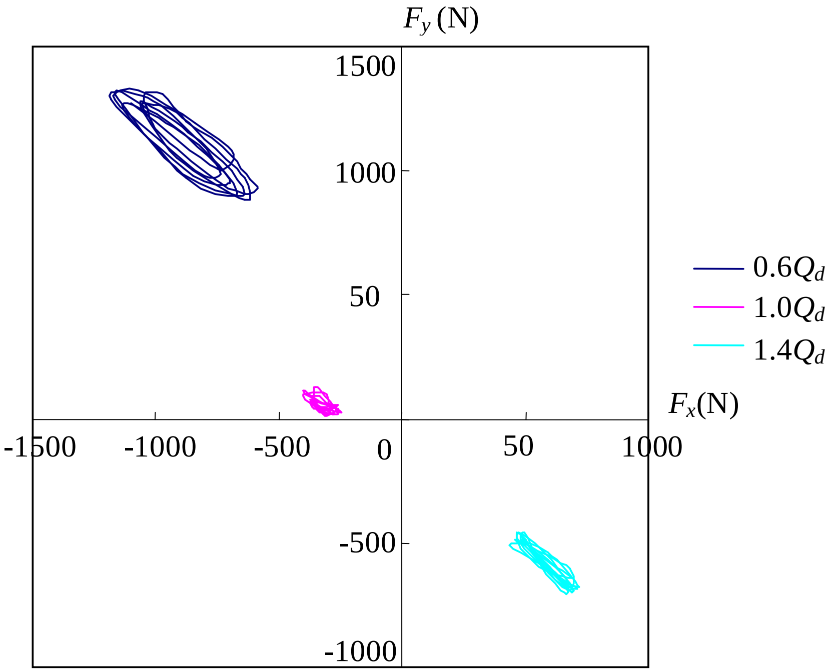

Figure 9. Vector locus of the transient radial force.

region of the transient radial force locus is the farthest from the origin of the coordinate system, and the area of the region is the largest; at the designed flow rate, the distributed region of the transient radial force locus is the closest to the origin, with the smallest area. It is indicated that the radial force on the impeller is the smallest under the designed running condition. From the distributed locations of the vector locus of the transient radial forces under different flow rates, it can be seen that the direction of the radial force on the impeller changes anticlockwise with the increase of the flow rates.

Variation of the transient radial join force in one rotation cycle of the impeller

The time domain charts of the variation of the transient radial join force during one rotation cycle T of the impeller under the three running conditions of 0.6Q_d, Q_d and 1.4Q_d is shown in Figure 10. It can be seen from Figure 10 that

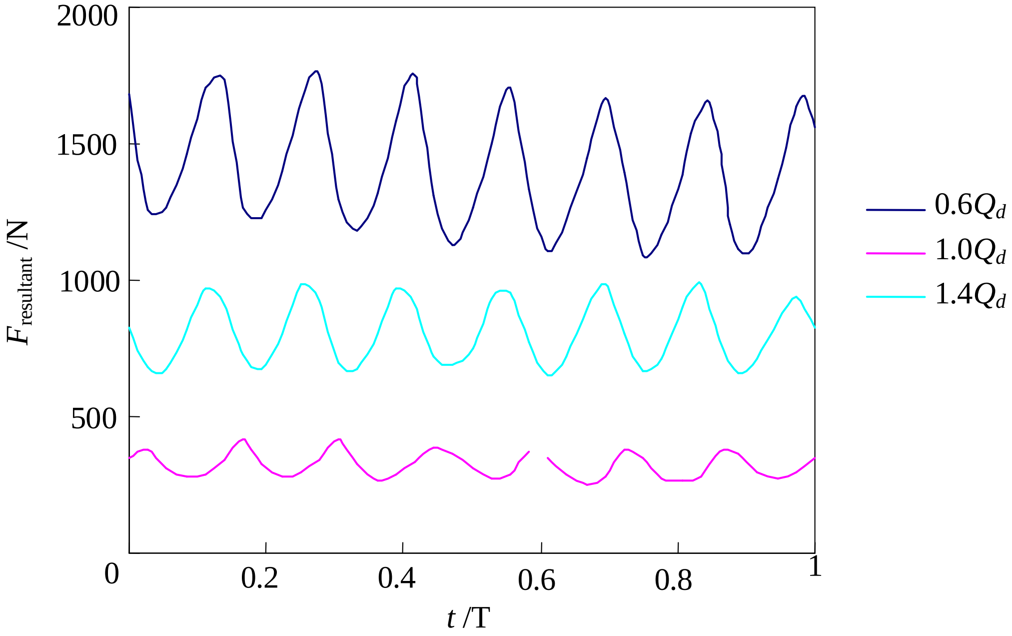

Figure 10. Time domain diagram of the transient radial force on the impeller.

the transient radial forces on the impeller under different flow rates show periodic fluctuations, with seven major peaks and troughs, where the number is the same with the number of the impeller blades and the fluctuation of each cycle is similar, indicating that the transient radial force on the impeller changes periodically with the rotation of the blades. The order of the three running conditions with small to large transient radial join forces is Q_d, 1.4Q_d, 0.6Q_d, so is the order of the three running conditions with small to large amplitudes of the periodic fluctuations of the transient radial join force. Thus, the running condition with small flow rate is the most unstable with the largest transient radial force, and the designed running condition is the most stable with the smallest transient radial force.

Conclusions

The pressure in the centrifugal pump shows periodic pulsations as the impeller rotates, where the amplitude of the pressure pulsation is the largest at the volute tongue. The main frequency of the pressure pulsations is the blade passing frequency, which is 114.333 Hz, indicating that the dynamic-static interference between the blades of the impeller and the collector is the major factor causing the pressure pulsation.

The radial force on the impeller of the centrifugal pump varies periodically during the rotation of the impeller, with the blade passing cycle as its varying cycle. Under non-designed flow rates, the radial force on the impeller is large, and the amplitude of the fluctuation is the largest under the running condition with small flow rate; under designed flow rate, the transient radial force on the impeller is small, with gentle fluctuations.

Conflict of Interests

The author(s) have not declared any conflict of interests.

ACKNOWLEDGMENTS

This work was sponsored by the Natural Science Foundation Project of Jiangsu Province (No.BK2011505), PAPD, National Science and Technology Support Program of China (No. 2011BAF14B01), Agricultural Science and Technology Support Program of Zhenjiang City (No. NY2013031), Postdoctoral Science Foundation of China (No.2013M541614), Postdoctoral Science Foundation of Jiangsu Province (No.1301062C).

REFERENCES

Adkins DR, Brennen CE (1998). Analysis of hydrodynamic radial forces on centrifugal pump impellers. J. Fluids Eng. 110(3):20-28.

Barrio R, Parrondo J, Blanco E (2010). Numerical analysis of the unsteady flow in the near-tongue region in a volute-type centrifugal pump for different operating points. Comput. Fluids (39):859-870. http://dx.doi.org/10.1016/j.compfluid.2010.01.001

Brennen CE, Acosta AJ (2006). Fluid-induced rotordynamic forces and instabilities. Struct. Control Health Monit. 13(1):10-26. http://dx.doi.org/10.1002/stc.145

Guo S, Okamoto H (2003). An experimental study on the fluid force induced by rotor-stator interaction in a centrifugal pump". Int. J.

Rotating Machinery 9(2):135-144. http://dx.doi.org/10.1155/S1023621X03000125

Jose G, Jorge P, Carlos S, Eduardo B (2006). Steady and unsteady radial forces for a centrifugal pump with impeller to tongue gap variation. J. Fluids Eng. (128):454-462.

Kelder JDH, Dijkers RJH, Van Esch BPM (2001). Experimental and theoretical study of the flow in the volute of a low specific-speed pump. Fluid Dynamics Res. (28):267-280. http://dx.doi.org/10.1016/S0169-5983(00)00032-0

Kitano Majidi (2005). Numerical study of unsteady flow in a centrifugal pump. J. Turbomachinery.127(2):363-371. http://dx.doi.org/10.1115/1.1776587

Ling Zhou, Weidong Shi, Wei Li (2013). Ramesh Agarwal. Numerical and experimental study of axial force and hydraulic performance in a deep-well centrifugal pump with different impeller rear shroud radius. J. Fluids Eng. 135:104501-8. http://dx.doi.org/10.1115/1.4024894

Liu H, Wang K, Kim H, Tan M (2013). Experimental investigation of the unsteady flow in a double-blade centrifugal pump impeller. China Technol. Sci. 56(4):812-817. http://dx.doi.org/10.1007/s11431-013-5154-0

Longatte F, Kueny JL (2009). Analysis of rotor-stator-circuit interactions in a centrifugal pump. Proceedings of the 3rd ASME/JSME Joint Fluids Engineering Conference. pp.1039-1045.

Meneveau C, Katz J (2000). Scale-invariance and turbulence models for large-eddy-simulation. Annu. Rev. Fluid Mech. (32):1-32. http://dx.doi.org/10.1146/annurev.fluid.32.1.1

Spence R, Amaral-Teixeira J (2009). A CFD parametric study of geometrical variations on the pressure pulsations and performance characteristics of a centrifugal pump. Comput. Fluids. (38):1243-1257. http://dx.doi.org/10.1016/j.compfluid.2008.11.013

Wei L, Weidong S, Yandong X, Ling Z, Pingping Z (2013). Effects of guide vane thickness on pressure pulsation of mixed-flow pump in pumped-storage power station. J. Vibroeng15(3):1077-1085.

academicJournals

Vol. 9(9), pp. 311-314, 15 May, 2014
DOI: 10.5897/SRE2014.5908
Article Number: 06AD24744496
ISSN 1992-2248 © 2014

http://www.academicjournals.org/SRE

Scientific Research and Essays

Full Length Research Paper

Development of a method to detect infectious rotavirus and astrovirus by reverse transcriptase polymerase chain reaction (RT-PCR) with propidium monoazide (PMA)

Wei Yumei [1,2], Liu Tingting[1], Wang Jingqi[1], He Xiaoqing[1]* and Wang Zijian[2]

[1]College of Biological Sciences and Technology, P. O. Box 162, Beijing Forestry University, Beijing 100083, China.
[2]State Key Laboratory of Environmental Aquatic Chemistry, Research Center for Eco-Environmental Sciences, Chinese Academy of Sciences, P. O. Box 2871, Beijing 100085, China.

Received 3 January, 2013; Accepted 2 March, 2013

Rotavirus and astrovirus are two kinds of water-borne pathogens that can cause severe diarrhea in children, infants and immunocompromised humans. Both can be present in untreated and inadequately treated water. Molecular methods, such as the reverse transcriptase polymerase chain reaction (RT-PCR), have been used to detect two viral genomes in a few hours, but they cannot distinguish between infectious and noninfectious rotavirus and astrovirus. In our study, we developed a propidium monoazide-reverse transcriptase polymerase-chain reaction (PMA-RT-PCR) assay to determine the infectivity of these two RNA viruses. Rotavirus and astrovirus stool samples were detected by RT-PCR in conjunction with PMA, respectively. Stool samples inactivated with heat treatment (95°C) were processed at the meantime as controls. The result showed that infectious virus samples gave positive results, while noninfectious virus samples presented negative results. To determine the viability of rotavirus and astrovirus in source water, a total of five source water samples were also collected from different reservoirs in July, 2012. One sample showed a positive result, which meant that PMA-RT-PCR method can be successfully applied to the viral detection in water samples. Data obtained in this study suggest that pretreatment of viruses with PMA prior to RT-PCR is a reliable method for distinguishing between infectious and noninfectious rotavirus and astrovirus. To our knowledge, this is the first report of application of this technique to rotavirus and astrovirus.

Key words: Rotavirus, astrovirus, propidium monoazide (PMA), source water.

INTRODUCTION

Rotavirus and astrovirus are the main pathogens that can cause severe infection in the immunocompromised humans (eg. children, old, patient). Infection always occurs following ingestion of contaminated food, drinking

---

*Corresponding author. E-mail: lenahe@bjfu.edu.cn water, or recreational water. Traditionally, PCR method was designed to detect rotavirus and astrovirus for drinking water. Recent research showed that only viable pathogens are likely to pose a threat to humans (Nocker and Camper, 2009; Nocker et al., 2006). However, polymerase chain reaction (PCR) method could not distinguish the infectious from noninfectious virus. This drawback has greatly limit the application of PCR.

In recent times, propidium monoazide-polymerase-chain reaction PMA-PCR was reported to be an easy-to-use alternative to PCR distinction between viable and nonviable cells (Nocker et al., 2006; Pan and Breidt, 2007). Propidium monoazide, a DNA-intercalating dye, will enter only dead cells with compromised cell capsid and then covalently bind to DNA, or attach to extracellular DNA upon exposure to bright light (Nocker et al., 2006) and PMA-PCR have successfully discriminated between viable (or intact) and dead Bacteroidales cells (Bae and Wuertz, 2009), enteric virus (Parshionikar et al., 2010). While as far as we know, there is no report on rotavirus and astrovirus with PMA-PCR detection (Belliot et al., 1997; Dubios et al., 1997).

In this study, we developed a PMA-reverse transcriptase PCR (RT-PCR) assay in respect to enteric RNA viruses. This method was also used to determine the viability of rotavirus and astrovirus in source water. The results suggested that pretreatment of viruses with PMA prior to RT-PCR was a reliable method for distinguishing between infectious and noninfectious viruses that were inactivated by treatment at 95°C. To our knowledge, this is the first report of application of this technique to rotavirus and astrovirus.

MATERIALS AND METHODS

Virus strain

Rotavirus and astrovirus stool sample were kindly provided by Professor Duan Zhaojun, Chinese Center for Disease Control and Prevention, which were detected as positive samples.

Thermal inactivation of viruses

1.5 ml PBS buffer (pH 7.2~7.4) was added into 100 µl stool specimen. Subsequently, vortex the mixture and leave it for 10 min followed by centrifuging at 8000 rpm for 5 min. Remove 200 µl supernatant to a clear and dry EP tube for dead treatment. The suspension was incubated at 95°C for 20 min.

Sampling and pretreatment

The pilot distribution system used in this study comprised of five source water reservoirs. 500 ml water was sampled by a sterile bottle and store at 4°C for less than 2 h before virus concentration. Enrichment for rotavirus and astrovirus are given in the following report (Haramoto et al., 2005).

PMA preparation

PMA {Phenanthridium, 3-amino-8-azido-5-[3-(diethylmethylammonio) propyl]-6-phenyl dichloride; Biotium, Inc.,Hayward, California} was reconstituted with 20% dimethyl sulfoxide to create a stock concentration of 1 mg/ml and stored at − 20°C in the dark.

PMA processing

Samples were treated as described by Parshionikar et al. (2010) with slight modifications. In the dark room, 50 µl PMA was added into 200 µl heat-treated and non-treated aliquot to a final concentration of 250 µg/ml. All the tubes were then placed on to a rocker for 5 min. After mixing, the tubes was placed to ice to prevent overheat and exposed to a 500 W halogen light at a distance of 20 cm for 5 min.

Viral RNA extraction

Once the exposure was completed, the viral RNA was extracted using a viral DNA/RNA extract kit (TIANGEN, Beijing) according to the manufacturer's instruction. After the RNA was eluted into a 1.5 ml EP tube, it was stored at -20°C, and subsequently thawed and analyzed by RT-PCR.

RT-PCR

Conventional RT-PCR was performed as the follows conditions. Primer used in this study are shown in Table 1. Briefly a single-step RT-PCR reaction for viruses was performed with the following reaction condition: 10 mM Tris–HCl (pH 8.3), 50 mM KCl, 1.5 mM $MgCl_2$, 0.2 mM dNTPs (Promega, Beijing, China), 200U M-MLV RT (Promega, Beijing, China), 2.5 U Ex-Taq DNA polymerase (TaKaRa, Dalian, China), 20U RNasin (Promega, Beijing, China), and 1 M each of primers. The cycling condition of rotavirus were as follows: an initial denaturation at 94°C for 3 min followed by 35 cycles of 1 min at 94°C, 1 min at 53°C and 1 min at 72°C and final extension 5 min at 72°C. And the cycling condition of Astrovirus were as follows: an initial denaturation at 94°C for 3 min followed by 30 cycles of 40 s at 94°C, 1 min at 55°C and 40 s at 72°C and final extension 10 min at 72°C. Negative and positive control samples were included. The PCR product was analyzed by gel electrophoresis with Goldview nucleic acid stain.

RESULTS

Rotavirus and astrovirus stool samples were inactivated thermally at 95°C for 20 min. The viable and inactivated viruses were then treated with PMA. RNA was extracted, and RT-PCR was performed. Figure 1 shows the results of rotavirus after PMA treatment. Inactivated rotavirus with PMA in line 3 showed no objective stripe in electrophoretogram, which suggested that PMA had successfully inhibited PCR reaction by cross linking with cDNA. However, viable rotavirus with PMA in line 5 revealed that PMA had no effect on PCR reaction, as PMA could not penetrate into the intact capsid. Meanwhile, the contrast group in line 4 and line 5 indicated that inactivated and viable rotavirus without

Table 1. Gene targets and primers used for relative of genomic RNA from the virus strains.

Strain	Gene target	Primer name and sequence (5′–3′)	Product length	References
Rotavirus	VP7	Beg9 GGCTTTAAAAGAGA GAATTTCCGTCTGG VP7-1 GATCCTGTTGGCCATCC	392 bp	Dubios et al., 1997
Astrovirus	ORF 1a	Mon340 CGTCATTGTTTGTTGTCATACT Mon348 ACATGTGCTGCTGTTACTATG	289 bp	Belliot et al., 1997

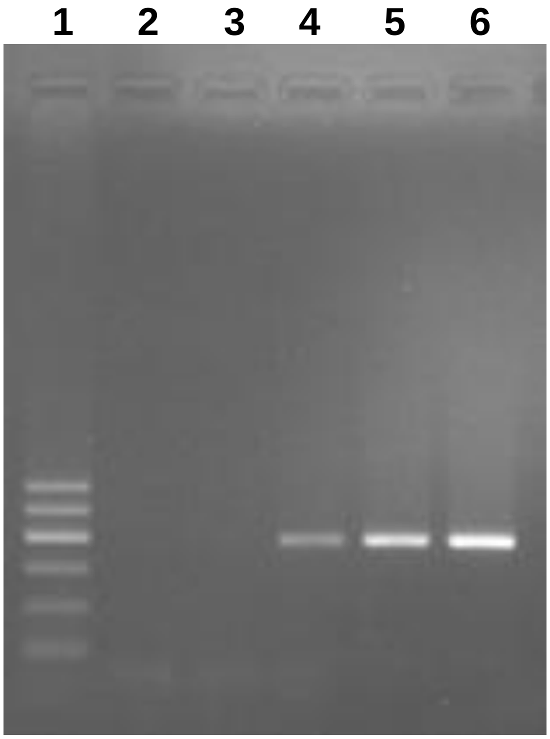

Figure 1. PMA-PCR Detection for rotavirus. (1. Marker; 2. Negative control; 3. Noninfectious rotavirus with PMA treatment; 4. Noninfectious rotavirus without PMA treatment; 5. Infectious rotavirus with PMA treatment; 6. Infectious rotavirus without PMA treatment).

PMA work as positive result as usual. The contrast demonstrated that only PMA could distinguish the viable rotavirus from inactivated one. Figure 2 shows the results of astrovirus after PMA treatment. Line 3, which represented for the inactivated astrovirus with PMA, displayed no objective stripe in electrophoretogram. It was probably because thermal treatment at 95°C for 20 min could inactivate whole astrovirus in the tube. None astrovirus survived from the heating condition. Thus this part of astrovirus could not impede PMA permeating into the capsid. Nevertheless, lines 4 to 6, which revealed positive results, indicated that viable astrovirus could get a positive result in PMA-PCR detection. PMA-RT-PCR method was used to detect the enteric virus of water reservoirs in our study. Table 2 shows that reservoir No. 2 suggested a positive results, which meant that PMA-PCR method successfully applied to the viral detection in water samples.

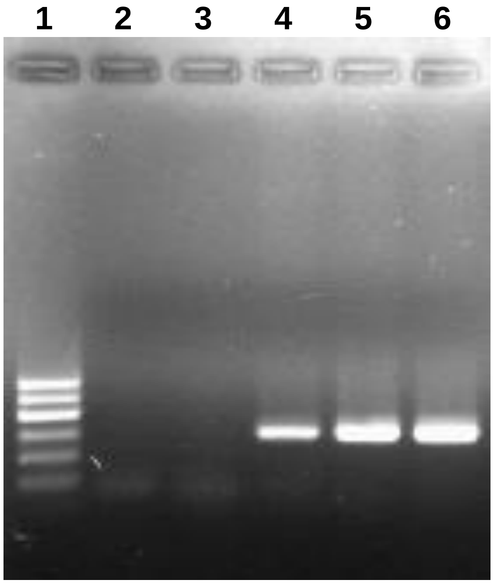

Figure 2. PMA-PCR detection for astrovirus, (1. Marker; 2. Negative control; 3. Noninfectious astrovirus virus with PMA treatment; Noninfectious astrovirus without PMA treatment; 5. Infectious astrovirus with PMA treatment; 6. Infectious astrovirus without PMA treatment).

Table 2. The results of five water reservoirs enteric viral detection by PMA-PCR method.

Water reservoir No.	Rotavirus/Astrovirus
1	-/-
2	+/-
3	-/-
4	-/-
5	-/-

"+"positive, "-"negative.

DISCUSSION

Rotavirus and astrovirus are typical waterborne virus that can cause acute diarrhea in children or infants (Prüsset al., 2002). There had been reported that enteric viruses caused a large waterborne outbreak of acute gastroenteritis in Finland (Maunula et al., 2008). The aim of this study was to validate the applicability of a PMA-PCR live-dead distinction method to determine the viability of rotavirus and astrovirus. PMA is a high affinity photoreaction DNA binding dye, which is cell membrane-impermeable, and thus can be selectively used to modify only exposed DNA from dead cells while leaving DNA from viable cells intact. Propidium monoazide has been successfully used to differentiate viable and non-viable bacteria in conjunction with qPCR (Nocker et al., 2006). This report provided more evident support on this aspect.

In our study, PMA was added as an identifying agent which distinguished viable virus from nonviable virus. Rotavirus and astrovirus got an ideal result by PMA-PCR detection. The negative results of inactivated samples with PMA treatment demonstrated that PMA penetrated into the capsid and bounded to RNA which inhibited the following reaction, and the viable aliquot suggested PMA was unavailable to the intact capsid.

Five different reservoirs are the main ones for domestic water. The viral contamination which is easily transported by water will affect the public health. Thus it is necessary to detect viral level in source water. However, traditional PCR method is not able to distinguish the survival status of viruses. In our research we used PMA-RT-PCR method to deal with this problem. The results suggested that PMA-PCR method could detect viable rotavirus at reservoir No. 2, which also revealed the contamination situation of this reservoir.

Conclusion

In conclusion, we developed a PMA-RT-PCR assay to determine the infectivity of these two RNA viruses. One sample showed a positive result, which meant that PMA-RT-PCR method could be successfully applied to the viral detection in water samples. Data obtained in this study suggested that pretreatment of viruses with PMA prior to RT-PCR was a reliable method for distinguishing between infectious and noninfectious rotavirus and astrovirus. It could provide more information to relevant administrator, and this technology will attribute to more fields in near future.

Conflict of Interests

The author(s) have not declared any conflict of interests.

ACKNOWLEDGEMENT

This work was supported by the Fundamental Research Funds for the Central University (TD2012-03), Natural Science Foundation of China (51108029) and Non-profit Industry Financial Program of MWR (201201032).

REFERENCES

Bae S, Wuertz S (2009). Rapid decay of host-specific fecal Bacteroidales cells in seawater as measured by quantitative PCR with propidium monoazide. Water Res. 43(19):4850-4859. http://dx.doi.org/10.1016/j.watres.2009.06.053

Belliot G, Laveran H, Monroe S (1997). Detection and genetic differentiation of human astrovirues:phylogenetic grouping varies by coding region. Arch. Virol. 142:1323-1334. http://dx.doi.org/10.1007/s007050050163

Dubios E, Le Guyader F, Haugarreau LK, Cormier H, Pommepuy M (1997). Molecular Epidemiological Survey of Rotaviruses in Sewage by Reverse Transcriptase Seminested PCR and Restriction Fragment Length Polymorphism Assay. Appl. Environ. Microbiol. 63(5):1794-1800.

Haramoto E, Katayama H, Oguma K, Ohgaki S (2005). Application of cation-coated filter method to detection of noroviruses, enteroviruses, adenoviruses, and torque teno viruses in the Tamagawa River in Japan. Appl. Environ. Microbiol. 71(5):2403-2411. http://dx.doi.org/10.1128/AEM.71.5.2403-2411.2005

Maunula L, Klemola P, Kauppinen A, Söderberg K, Nguyen T, Pitkänen T, Kaijalainen S, Simonen ML, Miettinen IT, Lappalainen M, Laine J, Vuento R, Kuusi M, Roivainen M (2008). Enteric Viruses in a Large Waterborne Outbreak of Acute Gastroenteritis in Finland, Food Environ. Virol. 1(1):31-36. http://dx.doi.org/10.1007/s12560-008-9004-3

Nocker A, Camper AK (2009). Novel approaches toward preferential detection of viable cells using nucleic acid amplification techniques. FEMS Microbiol. Lett. 291(2):137-142. http://dx.doi.org/10.1111/j.1574-6968.2008.01429.x

Nocker A, Cheung CY, Camper AK (2006). Comparison of propidium monoazide with ethidium monoazide for differentiation of live vs dead bacteria by selective removal of DNA from dead cells", J. Microbiol. Methods. 67(2):310-320. http://dx.doi.org/10.1016/j.mimet.2006.04.015

Pan Y, Breidt F Jr (2007). Enumeration of viable Listeria monocytogenes cells by real-time PCR with propidium monoazide and ethidium monoazide in the presence of dead cells. Appl. Environ. Microbiol. 73(24):8028-8031. http://dx.doi.org/10.1128/AEM.01198-07

Parshionikar S, Laseke I, Fout GS (20101). Use of propidium monoazide in reverse transcriptase PCR to distinguish between infectious and noninfectious enteric viruses in water samples. Appl. Environ. Microbiol. 76(13):4318-4326. http://dx.doi.org/10.1128/AEM.02800-09

Prüss A, Kay, D, Fewtrell L, Bartram J (2002). Estimating the burden of disease from water, sanitation, and hygiene at a global level. Environ. Health Perspectives. 110(5):537-542. http://dx.doi.org/10.1289/ehp.02110537

academicJournals

Vol. 9(9), pp. 315-320, 15 May, 2014
DOI: 10.5897/SRE2014.5909
Article Number: E19158C44498
ISSN 1992-2248 © 2014
Copyright©2014
Author(s) retain the copyright of this article
http://www.academicjournals.org/SRE

Scientific Research and Essays

Full Length Research Paper

Effect of Ozone fumigation on morpho-physiology and yield of field-grown rice in Pearl River Delta, China

Qiong Wang[1,2,3], Bilige Sude[2,3]*, Ming Dong[2,3,4], Yuan Shi[2,3], Chunmei Geng[2] and Xiaoke Wang[5]

[1]College of Water Sciences, Beijing Normal University, Beijing 100875, China.
[2]Chinese Research Academy of Environmental Sciences, Beijing 100012, China.
[3]State Environment Protection key Laboratory of Regional Eco-process and Function Assessment, Beijing 100012, China.
[4]College of Geographical Science, Inner Mongolia Normal University, Hohhot 010022, China.
[5]State Key Laboratory of Urban and Regional Ecology, Research Center for Eco-Environmental Sciences, Chinese Academy of Sciences, Beijing 100085, China.

Received 3 January, 2013; Accepted 2 March, 2013

Ozone pollution may cause a reduction in grain crops production. The response relationship between plants and Ozone is an important factor to assess the effect of Ozone pollution. In order to learn the effect of Ozone pollution on major grain crops in Pearl River Delta, this study used Open-top chamber (OTC) to fumigate the rice in the field, and researched the effects on the physical manifestations, physiological form and yield of rice which was fumigated by different Ozone concentrations. According to the experimental results, with increase in Ozone fumigation gradient, the rice was damaged gradually. And the height, biomass and yield of rice were reduced. By fitting concentration response model and dose response model, it can be estimated that the Ozone concentration and Ozone AOT40 value for 10% rice yield loss of single cluster were 61.7 nL/L and 13.08 h nL/L respectively in this experimental area.

Key words: Modeling, Open-top chamber (OTC), Ozone, rice, production loss, AOT40.

INTRODUCTION

With development of urbanization and living condition of the Chinese people, urban air pollution become more and more serious, especially near ground-level Ozone pollution problems (Zhang et al., 1998). As a strong oxidant (Yang, 2001), Ozone has serious harmful effects on plants (Calatayud et al., 2003; Liang et al., 2010; Zheng et al., 2007, 2009; Fuhrer and Booker, 2003; Reich et al., 1986) and is threatening the yield of grain crops (Chameides et al., 1999; Wang et al., 2007; Chen et al., 2007) in China.

Both foreign and domestic scholars have conducted experiments on the effect of Ozone exposure on grain

*Corresponding author. Email: sude@craes.org.cn

Table 1. Records of phenophase and time of different project.

Time	Phenophase	Determination of project
April 10	Reviving stage	Morphologic measurement
April 17	Tillering stage (1)	Morphologic measurement
April 29	Tillering stage (2)	Morphologic and biomass measurements
May 12	Jointing stage	Morphologic and biomass measurements
May 30	Booting stage	Morphologic measurement
June 11	Booting and heading stage	Biomass measurement
June 16	Heading stage	Morphologic measurement
June 24	Filling stage	Morphologic and biomass measurement
July 15	Mature stage	Morphologic, biomass and yield measurements

crops by means of laboratory control, field experiment, and open-top chamber (Felzer et al., 2007; Wang et al., 1993). The effect of Ozone on grain crops are mainly damaging physical characteristics (Yao et al., 2007) and physiological adjustment system (Zheng et al., 2007) of grain corps, reducing plant photosynthesis efficiency (Zheng et al., 2009, 2007), and affecting grain crop biomass and yield (Zheng et al., 2009, 2007; Xie et al., 2007). It is of significant importance to correctly assess the effect of Ozone pollution on grain crops. Wang and Guan (1995) improved the model of correlation between the Ozone concentration and crop loss rate, and assessed the effect of Ozone pollution on yield of major grain crops in China (Aunan et al., 2000). Scholars in America and Europe discovered that the effect of Ozone on grain crops was an accumulated result and put forward dose response model. United Nations Economic Commission for Europe (UNECE) determined that the critical Ozone concentration to harm grain crops is 40 nL/L and has established an AOT40 index. The method to calculate AOT40 (Fuhrer et al., 1997) is as follows (Equation 1):

$$\mathrm{AOT40} = \sum (C_{O_3} - 40) \qquad C_{O_3} \geq 40\,\mathrm{nL/L} \tag{1}$$

In the formula, AOT40 is the accumulated Ozone concentration exposure value when hour average Ozone concentration is greater than 40 nL/L,(h·μL /L). C_0 is the hour average Ozone concentration value when solar radiation is greater than 50 W·m^{-2}, (nL/L).

MATERIALS AND METHODS

Experimental region

Dongguan city is selected as experimental region in Guangdong Province. Experimental region is located in the east of Pearl River Delta, the average annual temperature of Dongguan is 23.1°C with rich sunlight and rainfall 20 (Chen, 2005). The experimental material is the Yuejingsi Seed No. 2 Rice that has been widely planted in Pearl River Delta. These were sowed on March 7 and transplanted to field on March 28, 2009. The area of experimental field is about 2 MU. Rice seedlings were transplanted manually to ensure they were evenly planted.

Gradient design

The fumigation device which manufactured by our team included octahedral cylinder OTC, ventilation, Ozone production, concentration control and automatic monitoring systems. The volume of OTC is 10 m^3, air exchange frequency is greater than twice per minute. There are four gradients for fumigation.

i) Non-filter gradient (NF): Directly connected to non-filter air.
ii) 40 gradient (NF+40): Based on connecting to the air, add some Ozone through Ozone generator to make the Ozone concentration equal to atmospheric Ozone +40 nL/L.
iii) 80 gradient (NF+80): Based on connecting to the air, add some Ozone to make the concentration equal to atmospheric Ozone +80 nL/L.
iv) 120 gradient (NF+80): Based on connecting to the air, add some Ozone to make the concentration equal to atmospheric Ozone +120 nL/L.

Every gradient has three parallel OTC, and there are altogether 12 OTC fumigation chambers. The concentrations of the four gradients for setting the highest value are no restriction, 80, 120 and 160 nL/L, respectively. Fumigation was conducted from 9:00 to 17:00 every day beginning from April 21, 2009. There are 44 days for fumigation.

Measuring method and time

Morphologic measurement: 10 clusters of rice were selected from every chamber and marked. Their heights in different phenophases were measured and their leaf colors observed.

Biomass measurement: Three clusters of rice growing in the same condition were selected from each chamber to measure their number and weight; they were separated according to organs (stem, healthy leaf, withering leaf and ear) and their dry weight after drying at 65°C for 48 h obtained.

Yield measurement: Rice of 1 m^2 at every chamber in mature stage were selected and their number of clusters recorded. From their ears, we obtained their dry weight after drying at 65°C for 48 h. The data was analysed by SPSS13.0 statistical software. The measured phenophase and time of various indexes are shown at Table 1.

Table 2. Records of visible damage on rice under Ozone fumigation.

Phenophase	NF	NF+40	NF+80	NF+120
Reviving stage and tillering stage (1)	Healthy leaves			
Tillering stage (2)	Healthy leaves	Healthy leaves	Speckles appear on few leaves	Speckles appear on some leaves
Jointing stage	Healthy leaves	Speckles appears on few leaves	Speckles appears on some leaves	Speckles appears on 10% of the leaves
Booting stage	Speckles appears on few leaves	Speckles appears on some leaves	Speckles appears on 10% of the leaves	Speckles appears on 15% of the leaves
Heading stage	Few leaves wither	10% of the leaves wither	15% of the leaves wither	20% of the leaves wither
Filling stage	10% of the leaves wither	15% of the leaves wither	20% of the leaves wither	30% of the leaves wither
Mature stage	30% of the leaves wither	50% of the leaves wither	80% of the leaves wither	90% of the leaves wither

Table 3. Height of rice under Ozone fumigation(cm).

Phenophase	NF	NF+40	NF+80	NF+120
Reviving stage	15.1±2.8b*	15.0±2.6b	16.8±3.1a	15.7±3.3ab
Tillering stage (1)	27.7±3.3b	30.6±4.0a	30.2±3.7a	30.6±3.7a
Tillering stage (2)	52.2±5.4b	56.7±5.7a	54.1±4.8ab	55.2±7.3a
Jointing stage	77.3±4.2a	76.4±5.2a	76.5±5.1a	75.1±3.1a
Booting stage	109.3±6.3a	105.6±5.0ab	102.5±6.0bc	99.0±8.2c
Heading stage	117.8±5.6a	118.7±6.1a	112.4±5.3b	105.4±5.5c
Filling stage	121.8±4.8a	120.3±5.2a	112.9±4.9b	107.0±6.0c
Mature stage	115.4±6.6a	113.3±6.3ab	106.3±13.9bc	101.1±7.6c

*The letters in the figure mean the comparing results at 5% level. Different letters indicate distinctive difference and the same letters indicate indistinctive difference.

RESULTS AND ANALYSIS

Effect of Ozone on morphologic physiology of rice

Leaves are important photosynthesis organs for plants and are playing an important role in the growth of plant. Constant Ozone fumigation makes obvious visible signs of damage on leaves. According to Table 2, in the period of reviving and tillering stages (1), the leaves of the rice at all the four gradients are peak green. In tillering stage 2 (fumigating for 9 days), there are different signs of damage on leaves at different gradients. Leaves are healthy at NF and NF+40. There are some speckle in leaves at NF+80. The speckles are very obvious on rice leaves at NF+120. With continuity of Ozone fumigation and increase of concentration gradient, the morphological damages of the rice are becoming more and more serious. At NF+120 of the mature stage, most of the rice withered. 30% of the rice at NF withered. In the whole growth period, there are distinctive differences in morphologic damages of rice leaves at different Ozone fumigation gradients.

Ozone affects rice height to certain extent. It can be concluded that the heights at NF+80 and NF+120 are distinctively greater than those at NF and NF+40 in reviving stage and tillering stage(1) (Table 3). In tillering stage(2), the heights of rice at high fumigation gradients is still greater than those at NF. The heights among gradients are no significant different in jointing stage. The rule begins to change in rice booting stage. The heights of rice at high fumigation gradients is still less than those at low gradients. After heading stage, rice at NF+120 is much less than that at other gradients; In filling stage and mature stage, the trend of height in different fumigation gradients is that: NF > NF+40> NF+ 80> NF+ 120. The above show that high-concentration Ozone fumigation has dwarfing effect on rice. The followings have the same rule.

Effect of Ozone fumigation on rice biomass

According to Table 4, rice biomass does not have

Table 4. Dry weight of one rice under Ozone fumigation(g).

Phenophase	NF	NF+40	NF+80	NF+120
Tillering stage (2)	0.44±0.17a	0.36±0.05a	0.31±0.06a	0.37±0.04a
Jointing stage	0.58±0.15a	0.60±0.06a	0.52±0.08a	0.59±0.11a
Booting stage	1.94±0.28a	1.90±0.37a	1.60±0.48a	1.69±0.27a
Filling stage	3.09±0.43a	2.56±0.45b	1.86±0.35c	2.37±0.57b
Mature stage	4.40±0.72a	3.70±1.02ab	3.46±0.49bc	2.82±0.93c

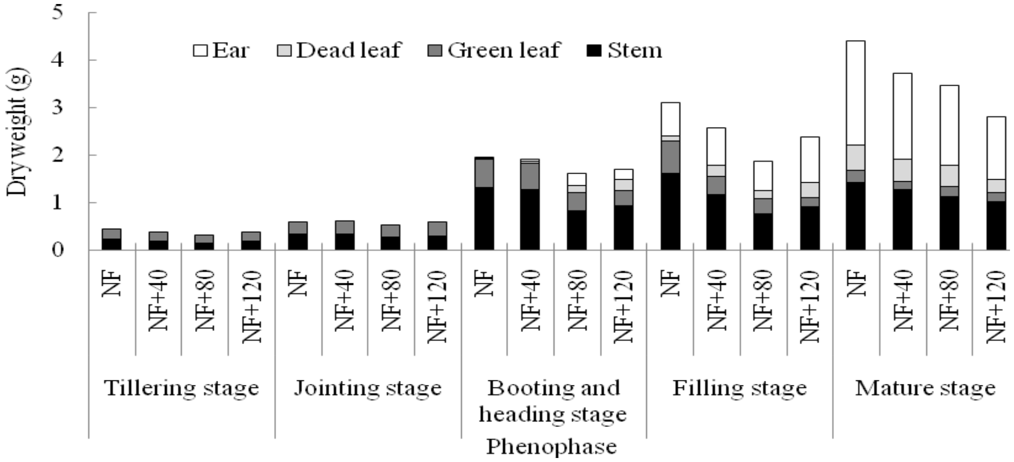

Figure 1. Allocation of biomass in various organs of rice.

distinctive differences at different gradients in tillering stage (2), jointing stage, and booting and heading stage. However, rice biomass declines with the increase of Ozone gradients after being fumigated for a certain time. In filling stage, rice biomass at NF is obviously higher than that at other gradients. The trend of rice biomass in different gradients is: NF > NF+40> NF+ 80> NF+ 120.

Ozone fumigation can affect allocation of biomass in various organs (Figure 1). The allocation percentage of biomass in different organs has no significant difference in tillering stage (2) and jointing stage. In booting and heading stage, the dry weight of ear at NF+80 and NF+120 is higher than that at NF and NF+40. On the contrary, the dry weight of stem and leaf at NF+80 and NF+120 is lower than that at NF and NF+40. In filling stage, the dry weight of stem and green leaf at NF and NF+40 is higher than that at NF+80 and NF+120. The trend of weight in ear, stem and green leaf in different gradients is that: NF > NF+40> NF+ 80> NF+ 120. The high-concentration Ozone fumigation reduced the weight of each organ.

Effect of Ozone fumigation on rice yield

High-concentration Ozone fumigation can obviously decrease the single rice yield and unit area yield of grain crops and vegetables (Zheng et al., 2007). In experiment, with the increase of Ozone fumigation gradients, the yield of single cluster rice declines greatly. In particular, the effect of high Ozone fumigation gradients on rice yield is more obviously (Figure 2).

Rice yield loss model assessment

There are three type of models for assessing the relationship between Ozone pollution and yield loss, statistic model, mechanism model, and photochemical model (Zheng and Wang, 2004; Yao et al., 2007). Statistic model mainly includes concentration response model and dose response model. In reference to the research result (Heck et al., 1982) improved by Wang and Guan (1995), we establish the relation model between yield loss of a single cluster rice and Ozone pollution, the model is that:

$$Y=aX+b$$

In this formula, Y is yield loss percentage of single cluster of rice; X is the hour average concentration of Ozone in growth season of grain crop; a and b are regression

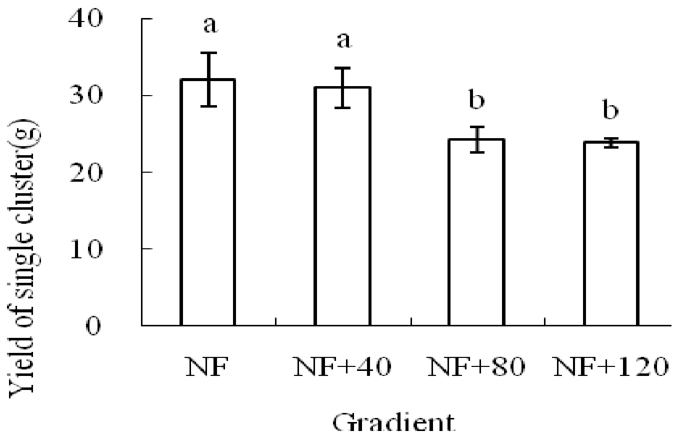

Figure 2. Yield of single cluster of rice under Ozone fumigation.

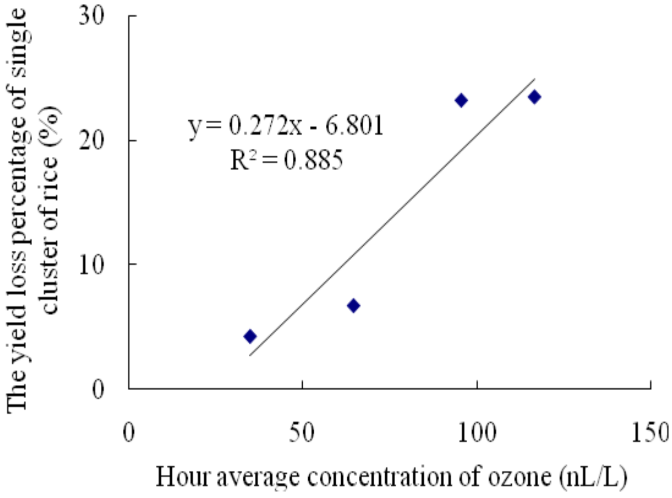

Figure 3. Concentration response model of yield loss of single cluster of rice under Ozone fumigation.

coefficients.

By fitting, the concentration response model can be obtained as shown in Figure 3. From the model, it can be learnt that the Ozone concentration which caused 10% yield loss of single cluster of rice is 61.7 nL/L.

The impact of Ozone on crops is largely due to constant Ozone accumulation by crops. Some institutions of American and European put forward the concept of dose. When AOT40 is zero, a yield data of single cluster of rice can be obtained. Take this yield data as the reference value, we can calculate the yield loss percentages. The dose response model can be obtained as shown in Figure 4 after correcting the data by 0.2; that is, correction factor represented the difference between air chamber and field (Wang and Guan, 1995). It can be concluded from the figure that the AOT40 of Ozone which caused 10% yield loss of single cluster of rice is 13.08 h·μL/L.

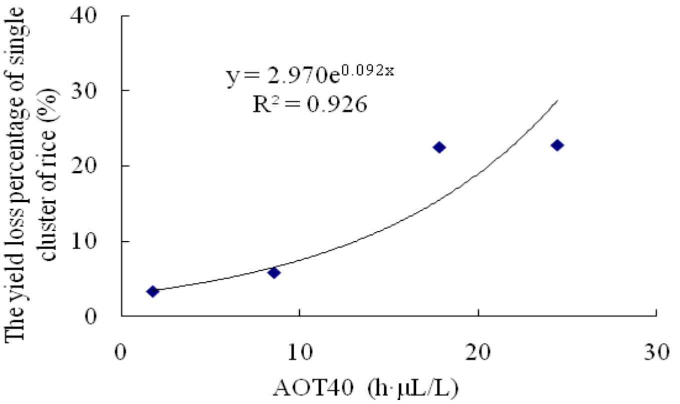

Figure 4. Dose response model of yield loss of single cluster of rice under Ozone fumigation.

Conclusions

In the experiment, high-concentration Ozone fumigation has harmful morphologic effect on rice leaves such as making them wither and bringing speckles to them. As a result, rice height decreases with increase in fumigation gradient. The oxidabillity of Ozone destroys the normal physical structure of rice leaves directly, and decreases activity of relevant enzymes and chloroplast pigments in leaves. Ozone also can affect photosynthetic efficiency of plants and reduce the yield of crops finally.

Physical damage on leaves appeared firstly. It can be observed from tillering stage (2) to mature stage. The effect of Ozone fumigation on height appears later than physical damage. High-gradient have distinctive effect on crop height in booting stage. The dwarfing effect by high-concentration Ozone has not been observed until booting stage. The influence of organ biomass allocation start from booting and heading stage.

Effect of Ozone fumigation on rice biomass postpones to filling stage and eventually affects the rice yield. It can be concluded that the high-concentration Ozone fumigation on grain crops is caused by accumulation effect and it will have better effect using dose response model to predict yield loss of crops (Massman, 2004).

Average values of atmospheric Ozone concentration and Ozone AOT40 surveyed in experimental area in rice growth season are 50 nL/L and 3.19 h·μL/L, which do not exceed model fitted values (61.7 nL/L and 13.08 h·μL/L). Also, Rice production is not seriously threatened by Ozone pollution in Dongguan city.

The maximum of Ozone concentration of atmospheric in experimental area is 99.7 nL/L. This situation suggests that extremum of Ozone concentration still exceed the critical concentration that can cause rice yield decreasing by 10%. Therefore, Ozone pollution in this area affect rice yield to certain extent and will become more and more serious with the development of social economy.

In the summer of 2006, the large field comprehensive air quality survey experiment was conducted by Lu et al. (2010) in Pearl River Delta. In this survey, the average Ozone concentration value is 40.53 nL/L at 17 surveying stations that covered the whole Pearl River Delta. The maximum average value they surveyed is 132.18 nL/L. It suggests that the Ozone pollution condition is very severe in Pearl River Delta. The economic loss incurred by regional grain crop yield decline shall not be neglected. Therefore, studies on the effect mechanism of Ozone on rice should be conducted further and various research methods should be enriched in order to accurately and scientifically estimate the effect of increase of Ozone concentration on rice yield loss.

Conflict of Interests

The author(s) have not declared any conflict of interests.

ACKNOWLEDGEMENT

The authors would like to acknowledge the support of the Special Fund for Public Service Sector of National Environmental Protection of China (No. 200809152; No. 200809077).

REFERENCES

Aunan K, Berntsen TK, Seip HM (2000). Surface Ozone in China and its possible impact on agricultural crop yields. Ambio. 29:294-301.

Calatayud A, Iglesias DJ, Talón M, Barreno E (2003). Effects of 2-month Ozone exposure in spinach leaves on photosynthesis, antioxidant systems and lipid peroxidation. Plant Physiol. Biochem. 41:839-845. http://dx.doi.org/10.1016/S0981-9428(03)00123-2

Chameides WL, Li X, Tang XY, Zhou XJ, Chao L, Kiang CS, John JS, Saylor RD, Liu SC, Lam KS, Wang T, Giorgi F (1999). Is Ozone pollution affecting crop yields in China? Geophys. Res. Lett. 26:867-870. http://dx.doi.org/10.1029/1999GL900068

Chen HL (2005). The cultivation technology for canary date palm in central square of Dongguan city. Suppl. J. Sun Yatsen Univ. 25:189-191.

Chen Z, Wang XK, Xie JQ, Zheng QW, Feng ZZ, Ouyang ZY, Feng ZW (2007). Effects of Ozone on production of rice (Oryza sativa L.) during grain filling stage. Asian J. Ecotoxicol. 2:208-213.

Felzer BS, Cronin T, Reilly JM, Melillo JM, Wang XD (2007). Impacts of Ozone on trees and crops. Comptes Rendus Geosci. 339:784-798. http://dx.doi.org/10.1016/j.crte.2007.08.008

Fuhrer J, Booker F (2003). Ecological issues related to Ozone: Agricultural issues. Environ. Int. 29:141-154. http://dx.doi.org/10.1016/S0160-4120(02)00157-5

Fuhrer J, Skarby L, Ashmore MR (1997). Critical levels for Ozone effects on vegetation in Europe. Environ. Pollut. 97: 91-106. http://dx.doi.org/10.1016/S0269-7491(97)00067-5

Heck WW, Taylor OC, Adams R, Bingham G, Miller J, Preston E, Weinstein L (1982). Assessment of crop loss from Ozone. J. Air Pollut. Cont. Assoc. 32:353-361. http://dx.doi.org/10.1080/00022470.1982.10465408

Liang J, Zeng Q, Zhu JG, Xie ZB, Liu G, Tang HZ (2010). Review of indexes for evaluating plant response to elevated near-surface Ozone concentration. Chin. J. Eco-Agric. 18:440-445.

Lu KD, Zhang YH, Su H, Shao M, Zeng LM, Zhong LJ, Xiang YR, Zhang ZZ, Zhou CG, Wahner A (2010). Regional Ozone pollution and key controlling factors of photochemical Ozone production in Pearl River Delta during summer time. Scientia Sinica (Chimica). 40:407-420.

Massman WJ (2004). Toward an Ozone standard to protect vegetation based on effective dose: A review of deposition resistance and a possible metric. Atmos. Environ. 38:2323-2337. http://dx.doi.org/10.1016/j.atmosenv.2003.09.079

Reich PB, Schlettle AW, Amundson RG (1986). Effects of O3 and acidic rain on photosynthesis and growth in sugar maple and northern red oak seedlings. Environ. Pollut. Ser. A, Ecol. Biol. 40:1-15. http://dx.doi.org/10.1016/0143-1471(86)90054-1

Wang CY, Gao SH, Pan YR, Bai YM, Wen M, Liu JG (1993). The experiment of the influences of CO2 on soybean in open top chamber OTC-1. Meteorol. 19:23-26.

Wang CY, Guan FL (1995). The potential effects of O3 concentration change on yield of main crops in China. Quart. J. Appl. Meteorol. 6:69-74.

Wang XK, Manning WJ, Feng ZW, Zhu YG (2007). Ground-level Ozone in China:Distribution and effects on crop yields. Environ. Pollut. 147:394-400. http://dx.doi.org/10.1016/j.envpol.2006.05.006; PMid:16973249

Xie JQ, Zheng QW, Wang XK, Zhang BJ (2007). Effect of Ozone on photosynthesis of rice leaves, ear character and yield component in situe. Acta Agriculturae Boreali-Occidentalis Sinica. 15:27-30.

Yang Y (2001). Ozone review. J. Panzhihua Univ. 19:84-86.

Yao FF, Wang XK, Feng ZW (2007). Research advances in simulation models of Ozone impact on crops. Chin. J. Ecol. 26:571-576.

Yao FF, Wang XK, Feng ZZ, Zheng FX, Feng ZW, Ouyang ZY (2007). Influence of Ozone and ethylenediurea (EDU) on physiological characters and foliar symptom of spinach (Spinacia oleracea L.) in open-top chambers. Ecol. Environ. 16: 1399-1405.

Zhang YH, Shao KS, Tang XY (1998). The study of urban photochemical smog pollution in China. Acta Scientiarum Naturalium Universitatis Pekinensis 34:392-400.

Zheng CL, Wang CY (2004). Review of models of Ozone impact on crops. Meteorol. Sci. Technol. 32:143-148.

Zheng FX, Wang XK, Zhang WW, Duan XN, Hou PQ (2009). Influences of elevated Ozone on rice photosynthesis and yield. J. Agro-Environ. Sci. 28:2217-2223.

Zheng QW, Wang XK, Feng ZZ, Feng ZW, Ouyang ZY (2007). Combined impact of Ozone and simulated acid rain on gas exchange, growth and yield of field-grown winter wheat. Acta Scientiae Circumstantiae 27:1542-1547.

Zheng QW, Wang XK, Feng ZZ, Song WZ, Feng ZW, Ouyang ZY (2007). Effects of elevated Ozone on biomass and yield of rice planted in open-top chamber with revolving Ozone distribution. Environ. Sci. 28:170-175.

academicJournals

Vol. 9(9), pp. 321-324, 15 May, 2014
DOI: 10.5897/SRE2014.5910
Article Number: A4D907644500
ISSN 1992-2248 © 2014
Copyright©2014
Author(s) retain the copyright of this article
http://www.academicjournals.org/SRE

Scientific Research and Essays

Full Length Research Paper

Design of indoor dust concentration monitor based on light scattering detection method

Li Tianhua and Wu Ying*

Physics and Electrical and Mechanical College, Zunyi Normal College, Zunyi, Guizhou 563002, China.

Received 3 January, 2013; Accepted 2 March, 2013

Inhalable particles and fine particulates in dust will pollute the indoor environment and endanger people's health. It is an important task to take effective measures to control indoor dust pollution. The key is to keep abreast of the dust concentration, and to monitor, control and evaluate the sources of indoor dust pollution. This paper analyzes the main sources and characteristics of indoor dust and uses dust sensor to collect dust and transform photoelectric signals. It applies micro control unit (MCU) to control the system and process data, and designs the dust concentration monitor. The monitor can be used as an independent equipment and also a combination of a variety of sensors through the serial port to monitor indoor environmental parameters and control environmental control facilities, thereby purifying indoor air.

Key words: Light scattering, dust, dust sensors, micro control unit (MCU).

INTRODUCTION

Dust, known as "airborne particles", refers to the solid particles that can be suspended in the air (diameter ≤ 100 um). Among them, dust with diameter <100 um is called "total suspended particles", named as TSP for short, while dust with diameter between 2.5 and 10 um is called “particulate matter", shortened as PM10. Dust with diameter <2.5 um, known as "fine particulate matter", is referred to as PM2.5. The harm of dust to human beings is related to their size and composition. Dust with diameter > 10 um will be blocked out from the human nasal cavity, while PM10 can enter the upper respiratory tract of the body. Particularly, after being inhaled by the human body, PM2.5 can directly enter the blood through the bronchi and alveoli, which will be phagocytized by macrophage. Their long-term stay in the alveoli will exert negative impact on the human cardiovascular, nervous system and other organs, posing threat to people’s health (Si et al., 2012). According to a survey, modern people spend up to 60 to 80% of time indoors, especially for infants, young children and the elderly as well as sick and disabled people, who stay even longer indoors. Dust in indoor air can be suspended in the air for a long time, PM10 and PM2.5 particles of small diameter permanently stay floating in the air. It is difficult for them to settle on the ground, but easy to be inhaled (Liu et al., 2009). Consequently, air quality of the indoor environment has caused great concern. Indoor dust mainly comes from outdoor air containing dust, body dust, air-conditioning

---

*Corresponding author. Email: zluwg08@163.com

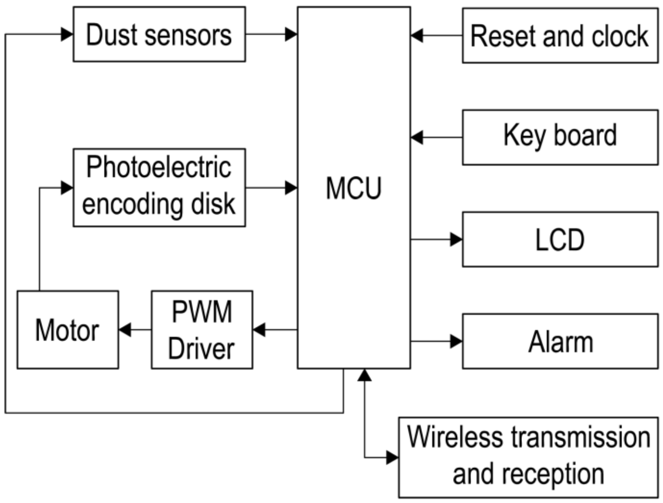

Figure 1. Structural diagram of the dust-concentration monitor.

equipment, smoking, cooking and other human activities as well as furniture, decoration materials, printers, etc., which aggravates indoor environmental pollution and even causes PM2.5 concentration higher than outdoor (Liu and Lian, 2007).

Therefore, it is an important job to take effective measures to control indoor dust pollution. The detection of indoor air dust concentration and dust diameter distribution directly reflect air quality. Therefore, the key is to keep abreast of the dust concentration, and to monitor, control and evaluate the sources of indoor dust pollution, which will encourage people to take effective measures to improve indoor air quality. The primary means to control indoor dust pollution is to develop a portable, low-cost and rapid and effective monitoring instrument with real-time online detection. This paper analyzes the main sources and characteristics of indoor dust and uses dust sensor to collect dust and transform photoelectric signals. It applies micro control unit (MCU) to control the system, process data and designs the dust concentration monitor.

DESIGN PRINCIPLE AND STRUCTURE

Design principle

Light scattering occurs to dust particles in the air when the light catches them. It is because the light will scatter to the surrounding due to the dust particle when certain wavelengths of light enter the dust area. Light scattering parameters are directly related to the dust concentration and the diameter of the dust particles, and the intensity of scattered light is directly proportional to the dust concentration. Through the measurement of the strength of scatter light perpendicular to the direction of the incident light, the concentration of dust particles in the dust region can be inferred (Zhao, 2012). Depending on the angle of scattered light of the dust particles, they are divided into two categories, forward scattered light and backward scattering light. For particles with large diameter, the energy distribution of the scattered light is more concentrated, mainly focusing on the forward direction. However, for particles with small diameter, the energy distribution of the scattered light is relatively wide. The smaller the particle diameter, the more uniform the distribution of forward scattered light and the backward scattered light. If the particle diameter is increased, the components of the forward scattered light will grow, while those of the backward scattered light will decrease.

Overall design

Dust concentration monitor mainly consists of a dust sensor, A / D conversion circuit, a wireless transmitting and receiving circuit, an alarm circuit, MCU (Micro Control Unit), reset and clock circuit, a liquid crystal display, a keyboard, a motor, a PWM (pulse Width Modulation) driver circuit and power supply circuit, etc., as shown in Figure 1. First, the dust particle information is converted into an electrical signal by the dust sensor, and after passing the pre-amplifier circuit of the sensor, it is converted to digital electrical signals by A / D conversion circuit, which is fed to MCU for processing and analysis. MCU will display processed and analyzed data through the LCD display, and when MCU determines dust concentration exceeds preset indicators, sound and light alarm will be given out through the sound and light alarm circuit. Dust concentration monitor can save the data, adjust and view the parameters, and adjust alarm intensity through the keyboard. The wireless transmitting and receiving circuit is used to achieve the sharing and real-time transmission of data and information. Leaves installed to the motor make it become a fan for the intake of air and traffic control.

DESIGN OF KEY COMPONENTS

Photoelectric detection

This paper uses a dust sensor (Model GP2Y1010AU0F, smallest particle detection capability > 0.8 um and sensitivity 0.5 V/0.1 mg/m^3) to design dust concentration monitor to get the dust concentration. The sensor is able to detect pollen, tobacco smoke and other house dust, mainly composed of LED (Light Emitting Diode), lens 1, PD (Photoelectric Diode), lens 2, the flow channel, the measuring chamber and electrical fan, as shown in Figure 2. When the electrical fans maintain a stable

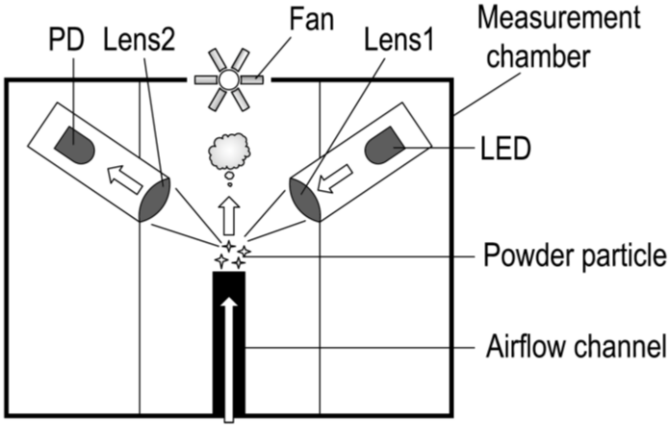

Figure 2. Structural diagram of dust sensor.

rotating speed after being powered by 30 s, external air is inhaled through the airflow channel to measurement points. LED emits strong light into the lens; when lens 1 will change the light emitted from LED into parallel light launched into the flow of measurement points to form a beam. When every dust particle in the air stream passes through the measurement point, it would be scattered by the incident ray, producing the reflected light pulse signal. The reflected light pulse signal is sent through the lens 2 to converge into stronger light pulse signal to PD, and PD will transform the light pulse signal into to an electric signal. As the photocurrent generated by PD is very weak, the dust sensor will pre-amplify it, outputting a 0 V ~ 5 V voltage signal. The voltage is inputted into MCU (Model ATmega2560) after being filtered, and MCU will do the calculation to transform the received data into the dust concentration information of corresponding units.

Air traffic control

With the volume of air divided by the number of dust particles, the monitor could be used to obtain the dust concentration. When the diameter of the air flow path (9 mm) is fixed, the change of the flow rate of air per unit determines the systematic error of the monitor. In the process of air collection, set the acquisition flow and time and calculate the deviation between the actual air flow and theoretical air flow as well as its rate of change according to the reference input and feedback signal. Then it is regarded as a reference after the fuzzy treatment to control the fan motor by calculating the controlling quantity, and regulate the gas flow of fan by adjusting the PWM width. The DC-Micro motor with photoelectric encoder is selected as the fan motor (voltage of 5 V, no load current of 35 mA, locked-rotor current of 320 mA, speed of 2600 rev / min, 334 coded discs and output rectangular pulses). Output 334 pulse voltage with motor running around. This pulse inputs the A / D conversion circuit which will then be used to convert the pressure signal to the digital signal and input it to MCU. Then MCU will generate a PWM control signal according to the number of feedback pulse, aiming to accurately control the motor speed by the motor driver chip (model ULN2003, input voltage 5 V, output voltage <50 V, output current <500 mA) as well as the air flow entering the dust sensor module, and achieve a constant flow of air collection.

Other circuits

Arduino open-source electronic platform, including hardware and software, originates from the open source code simple I / O interface version. The sensor can be easily connected with a variety of electronic components to sense the environment and feedback and affect the environment by controlling various devices. Arduino Mega control panel is adopted to control dust concentration monitor, and MUC on the control board could program by Arduino programming language, which is then compiled into a binary file and burned into the MCU.

HCI is the basic function of the intelligent instrument, which is composed by the keyboard (4 × 4 matrix) and a liquid crystal display. LCD display module (Model MK-D12864E, 2.9 inches with a resolution of 128 × 64) is connected to the system through the serial port and it could receive commands issued by it. The measurement data and system commands menu are displayed, which could achieve the real-time dust concentration and realize HCI.

In order to realize the sharing and real-time transmission of data and information, there are a variety of communication-methods used by dust concentration monitor, mainly including wired serial communications and wireless data communications. The former one adopts the USB interface for charging and computer-connection in order to ensure reliable data transmission. While the latter one adopts the wireless LAN technology and Bluetooth wireless technology to install WIFI wireless communication transceiver module (Model the CC1101, data transmission chip of 433 MHz, 868 MHz, 918 MHz, communication distance <500 m) and achieve wireless data transmission. In addition, to be connected to a smart phone, the reference node could also be set and the location information of each reference node is stored on the computer of the monitoring center to achieve the node positioning functions.

CALIBRATION TESTS

When measuring the dust concentration using dust concentration monitor, it is necessary to take into consideration the monitor system error, so the parallel calibration method is required to improve accuracy. According to the height of people's breathing, the height of the sample point is 1.3 ~ 1.6 m without using any air-conditioning system, so the calibration test is carried out under the condition of natural ventilation. Install a Laser Dust Monitor next to the monitor (Model LD-5L, configuring the 40 mm filter sampler, cutter TSP with replaceable particles, PM10, PM5, PM2.5, detection sensitivity of 0.01 mg/m^3, measuring range of 0.01 ~ 100 mg/m^3, repetitive error ± 2%, measurement accuracy ±10%, directly-readable dust mass concentration mg/m^3) when measuring the dust concentration. Record 10 sets of data measured by the detection system and take their average value as the measured value of the detection system. Record 10 sets of data measured by the laser dust monitor and take their average value as its measured value. Compare them to verify the accuracy and error of the monitor system, and extract its functional data. Input the data in the software as a relevant basis, and adjust the motor speed of the fan of dust concentration monitor via software until it is close to the measured value of the laser dust monitor.

Conclusion

The application shows that this dust concentration monitor are superior in many ways, including simple circuit structure, high integration level, easy-to-use, simplified detection process and operation, and low cost, etc. Therefore, it could be used to grasp the indoor dust concentration distribution and reduce the harm to us caused by the dust. This monitor not only can be used as stand-alone equipment, but also can be combined with a variety of sensors by the serial port integration, thus detecting indoor environmental parameters and controlling the environmental facilities to purify indoor air.

Conflict of Interests

The author(s) have not declared any conflict of interests.

ACKNOWLEDGEMENTS

This paper is Funded by Natural Science Research of Science and Technology Department of Guizhou Province Qiankehe J word No LKZS [2012] 04.

REFERENCES

Liu HL, Zhang W, Li CX (2009). Research on the indoor respirable particle concentration and the detection method of particle size distribution. Chin. J. Sci. Instrum. 2:340-344.
Liu HM, Lian ZW (2007). Research on the indoor and outdoor respirable particulate matters in Shanghai Minhang. J. Refrig. Air Cond Electr. Power Machinery (2):18-21.
Si PF, Rong XY, Fan YS (2012). The health effects of indoor particulates and its control standards. J. Refrig. Air Cond. (5):8-12.
Zhao LP (2012). Design of infrared absorbing dust sensor [D]. Qinhuangdao: Yanshan University, pp. 1-63.

academicJournals

Vol. 9(9), pp. 325-330, 15 May, 2014
DOI: 10.5897/SRE2014.5911
Article Number: 12A3E5E44502
ISSN 1992-2248 © 2014

http://www.academicjournals.org/SRE

Scientific Research and Essays

Full Length Research Paper

Analysis of the shape of bearing push-extend reamed affecting the bearing capability of the pile of push-extend multi-under-reamed pile through the finite element method

Yongmei Qian*, Xihui Wang and Guanghan Xu

College of Civil Engineering, Jilin Jianzhu University, Jilin 130118, China.

Received 3 January, 2013; Accepted 2 March, 2013

In the paper, through use of ANSYS software of the finite element method to establish the simulation analysis model about the stress of soil around the pile, we obtained the normal and shear stress curve when the bearing push-extend reamed have different shapes under the same loads. It qualitatively analyzed the influence of bearing capacity on the push-extend Multi-under-reamed pile raised by the different shapes of the bearing push-extend reamed, and puts forward the theoretical basis that further promotes application of the push-extend Multi-under-reamed Pile.

Key words: Push-extend multi-under-reamed pile, shape of bearing push-extend reamed, dimension of diameter, bearing capacity of pile, influence.

INTRODUCTION

Based on the theoretical and experimental study of the effects on the pile and soil of the Push-extended Multi-under-reamed Pile, it is further confirmed that many factors affect the bearing capacity of the Push-extend Multi-under-reamed Pile, and the situation is also more complex (Yongmei et al., 2013a). The main influence factors include: the diameter, location, height, form, distance and quantity of the bearing push-extend reamed, etc. It is difficult to provide quantitative conclusion for all these factors; however, we can give a qualitative conclusion. While researching on influence factors of the bearing capacity of the pile of Push-extend Multi-under-reamed Pile based on the theory of slip line, it was discovered that the shape of the bearing push-extend reamed has larger influence, which is one of the main influence factors of the bearing capacity of the pile (Yongmei et al., 2013a). In this paper, through theoretical analysis of the shape of the bearing push-extend reamed affecting the bearing capacity of the pile by establishing the finite element analysis model of the Push-extend Multi-under-reamed Pile, and in practical application, it is qualitatively put forward that the

---

*Corresponding author. Email: 654675316@qq.com

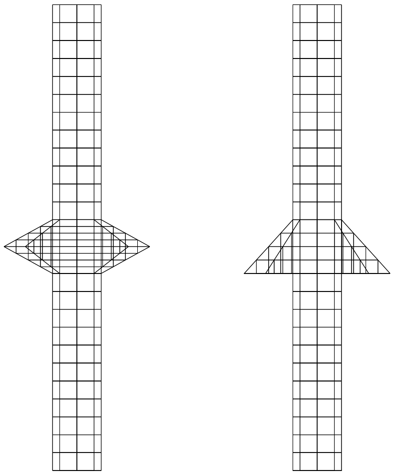

Figure 1. The perspective of unit division.

determining principle of the shape of the bearing push-extend reamed can be considered in the design and calculation of the Push-extend Multi-under-Pile.

ANALYSIS OF THE SHAPE OF THE BEARING PUSH-EXTEND REAMED AFFECTING THE BEARING CAPABILITY OF THE PILE BY USING FINITE ELEMENT METHOD

The bearing capacity of the pile of Push-extend Multi-under-reamed pile is composed of the side frictional resistance and the end-bearing force of pile. Due to existence of the bearing push-extend reamed, the soil under the bearing push-extend reamed produced large compressive stress; meanwhile, the soil on the bearing push-extend reamed produced tensile stress at a certain range; within the scope of the side frictional resistance of pile that does not exist simultaneously, the soil under the bearing push-extend reamed created slippage which led to a reduction in effective length of side frictional resistance of pile. Also the shape of the bearing push-extend reamed makes effect on it. In order to make full use of the role of the side frictional resistance of pile and the bearing push-extend reamed, further research needs to be made on the shape of the bearing push-extend reamed affecting the bearing capability of pile. The following is an analysis of the shape of the bearing push-extend reamed affecting the soil, an analysis of failure mechanism around pile and the bearing capacity of the pile through the finite element method.

ESTABLISHMENT OF THE FINITE ELEMENT MODEL

Finite element model can be set up using the 8-node space units (Yongmei et al., 2013b). The model is divided into double and single slopes of the Push-extend Multi-under-reamed Pile, as shown in Figure 1. Pile and soil around pile unit division, as well as a combination of pile and soil surface were elaborately distributed in the unit according to the stress distribution. In order to benefit from analysis and comparison of the calculation model, the establishment of the model identifies the following principles:

The concrete pile C20 (density 2.5×10^{-5} N/mm^3, elasticity modulus E=3×10^4 N/mm^2, Poisson's ratio u=0.167) takes the soil around the pile as the foundation of cohesive soil (density 2.0×10^{-5} N/mm^3, elasticity modulus E=$6\times10^{4-2}$ N/mm^2, Poisson's ratio u=0.3) (Yongmei et al., 2013b).

This research focus primarily on influence of the bearing push-extend reamed on the soil failure mechanism and the bearing capacity of pile; when the distance of the push-extend reamed is suitable, soil failure above and below the push-extend reamed does not affect each other. Thus, when one push-extend reamed is set in the calculation model tentatively, the push-extend reamed will be located in the middle along the pile length.

In order to avoid the boundary condition's influence on the soil in the calculation model, the scope of soil around pile is not too small- the dimension of diameter is 7 m and the depth of pile is 12 m.

Based on the principles above, six calculation models are established. Main pile diameter D=500 mm, pile length L=5000 mm and pile top load F=300 KN, the diameter of push-extend reamed D=1500 mm, 2000 mm, 2500 mm, the form of the bearing push-extend reamed are usually two kinds - double slope and single slope. The push-extend reamed is located in the middle along the length (as shown in Figure 1). Concrete model statistics are shown in Table 1.

ANALYSIS OF CONTENT AND CALCULATION RESULTS OF FINITE ELEMENT

Through computer simulation of the model, the contour map of the principal stress σ_x, σ_z and shear stress $\boldsymbol{\tau}_x$ was obtained from different models and the calculation results sorted. The related numerical value of representative model was extracted to form the normal stress curve of soil around the pile in different shapes of the bearing push-extend reamed, taking the pile of the dimension of diameter 2000 mm as an example (as shown in Figure 2, the horizontal axis for the pile length, the vertical axis for normal stress); shear stress curve (as shown in Figure 3, the horizontal axis for the pile length, the vertical axis for shear stress); the shear stress contour map of soil around pile (as shown in Figures 4 and 5); the vertical stress curve of soil under the pile (Figure 6) and the vertical stress curve of soil under the bearing push-extend reamed (as shown in Figure 7).

Table 1. Statistics of the basic parameters calculation model (F=300 KN).

Serial number	Model name	Diameter of push-extend reamed D (mm)	Form of push-extend reamed
1	H153	1500	The double slope form
2	H203	2000	
3	H253	2500	
4	P153	1500	The single slope form
5	P203	2000	
6	P253	2500	

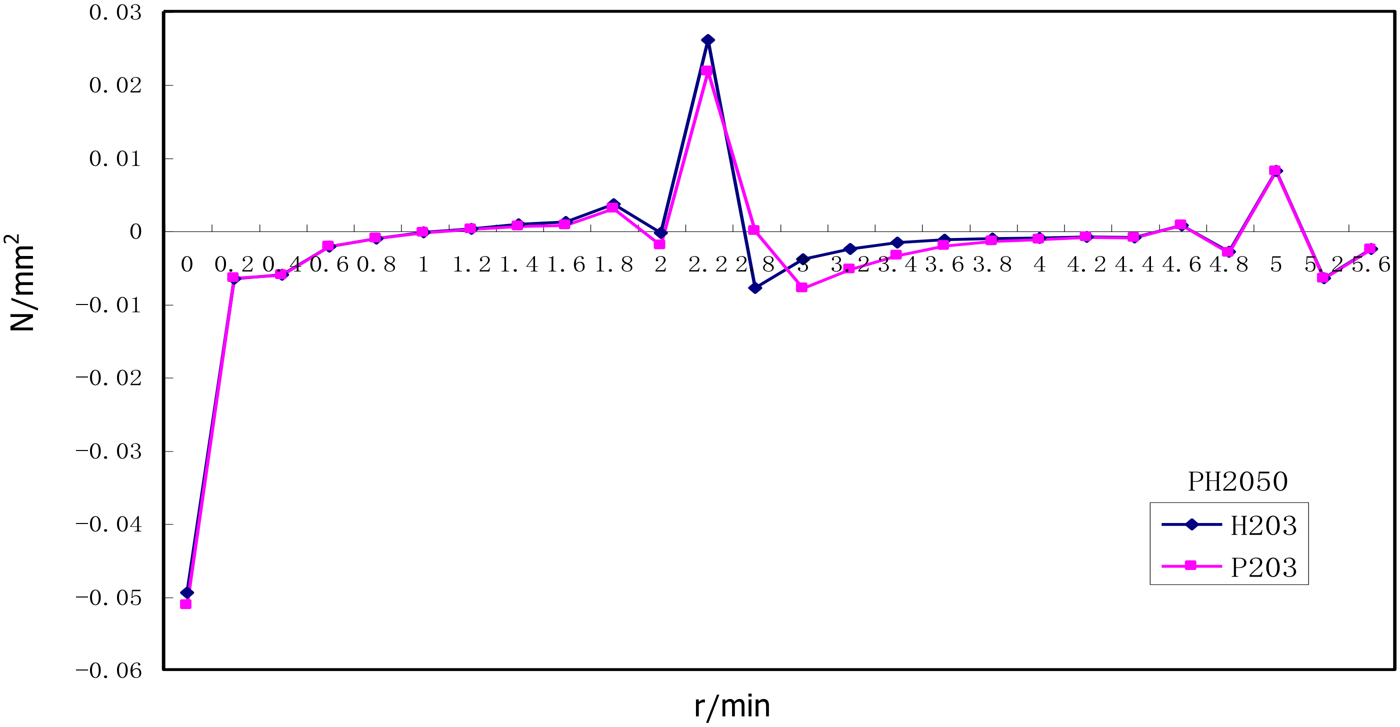

Figure 2. Normal stress curve of soil around pile (D=2000 mm).

Deductions

(1) About σ_x: It can be seen that a comparison of the double slope of the push-extend pile with the single slope of the bearing push-extend reamed pile as shown in Figure 2 revealed that for, near the bearing push-extend reamed, up the bearing push-extend reamed and under the push-extend reamed, the stress influence region are basically the same. The compressive stress under the bearing push-extend reamed is different within a certain region, but with increase in diameter of the bearing push-extend reamed, the compressive stress value approaches the same gradually.

(2) About τ_{xz}: It can be seen from the Figure 3 that the shear stress of the single slope push-extend reamed pile has a high reduction. Up the bearing push-extend reamed, the τ_{xz} of the single slope push-extend reamed pile is bigger than double slope bearing push-extend reamed pile; but σ_x is tensile stress in this region, so the τ_{xz} does not work; under the bearing push-extend reamed, τ_{xz} of single slope bearing push-extend reamed pile has more reduction than the double slope bearing push-extend reamed pile.

(3) About σ_z: It can be seen from the Figures 4 and 5 that when the vertical stress under push-extend reamed under the same diameter are compared, the double slope bearing push-extend reamed has larger influence region of soil under the push-extend reamed than the single

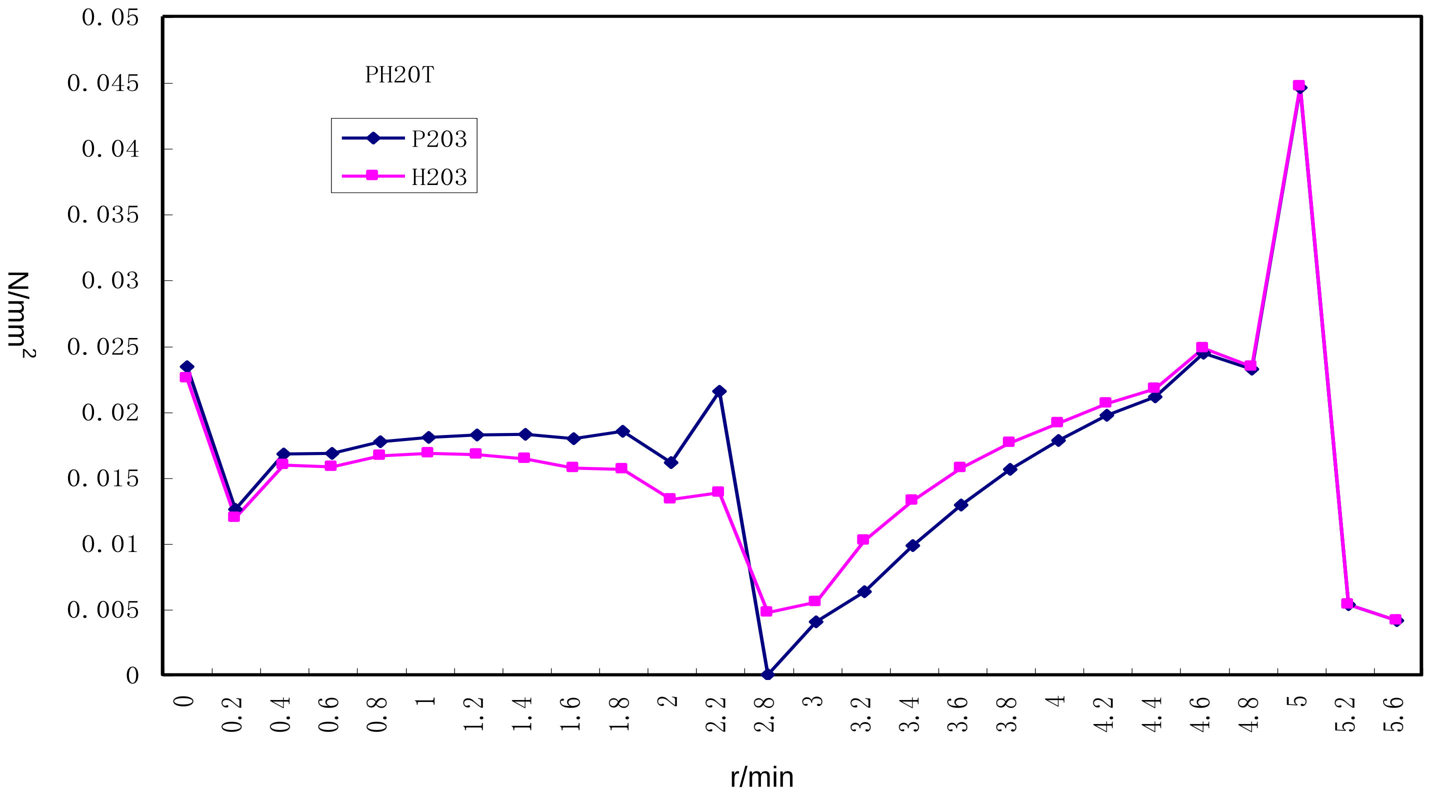

Figure 3. Shear stress curve of soil around pile (D=2000 mm).

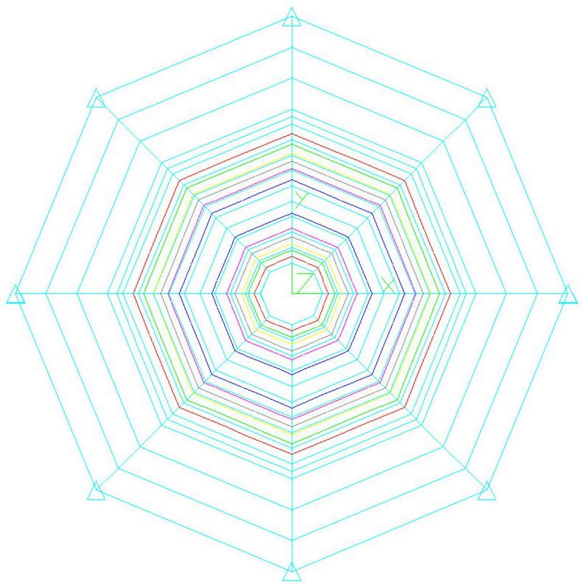

Figure 4. The contour map of vertical stress of soil under the double slope push-extend reamed (D=2000 mm).

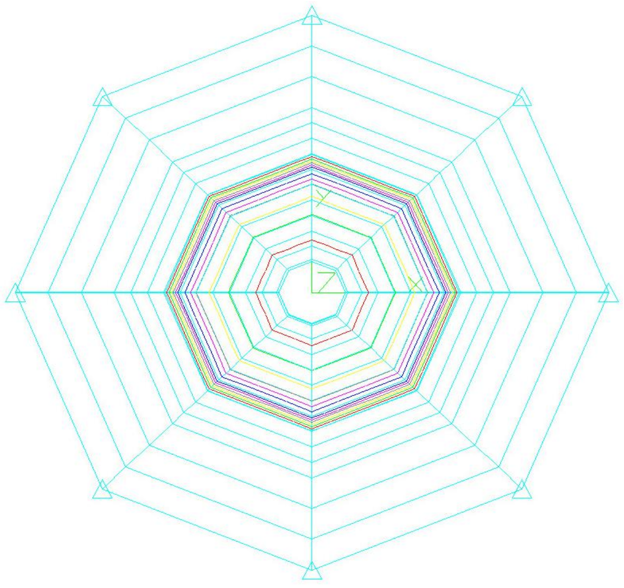

Figure 5. The contour map of vertical stress of soil under the single slope push-extend reamed (D=2000 mm).

slope bearing push-extend reamed. From Figures 6 and 7, it can be seen that the σ_z of pile tip is basically the same, but under the bearing push-extend reamed, the σ_z value of double slope bearing push-extend reamed is much larger than the single slope bearing push-extend reamed.

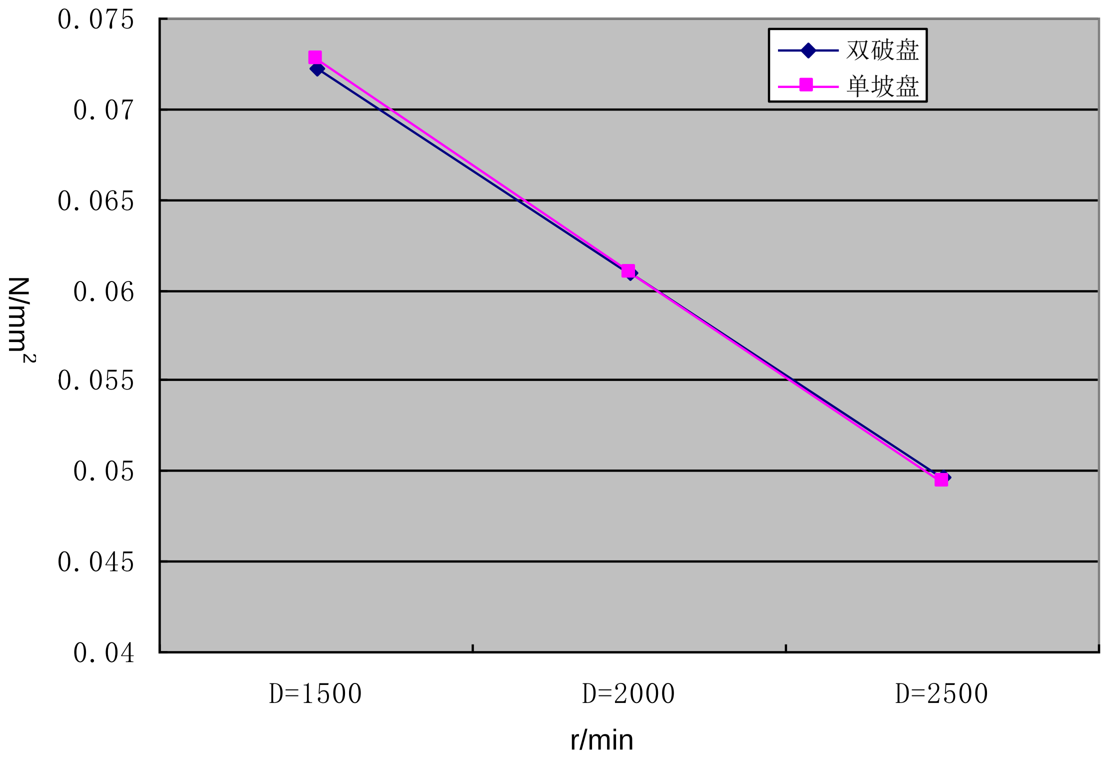

Figure 6. The vertical stress curve of pile tip soil.

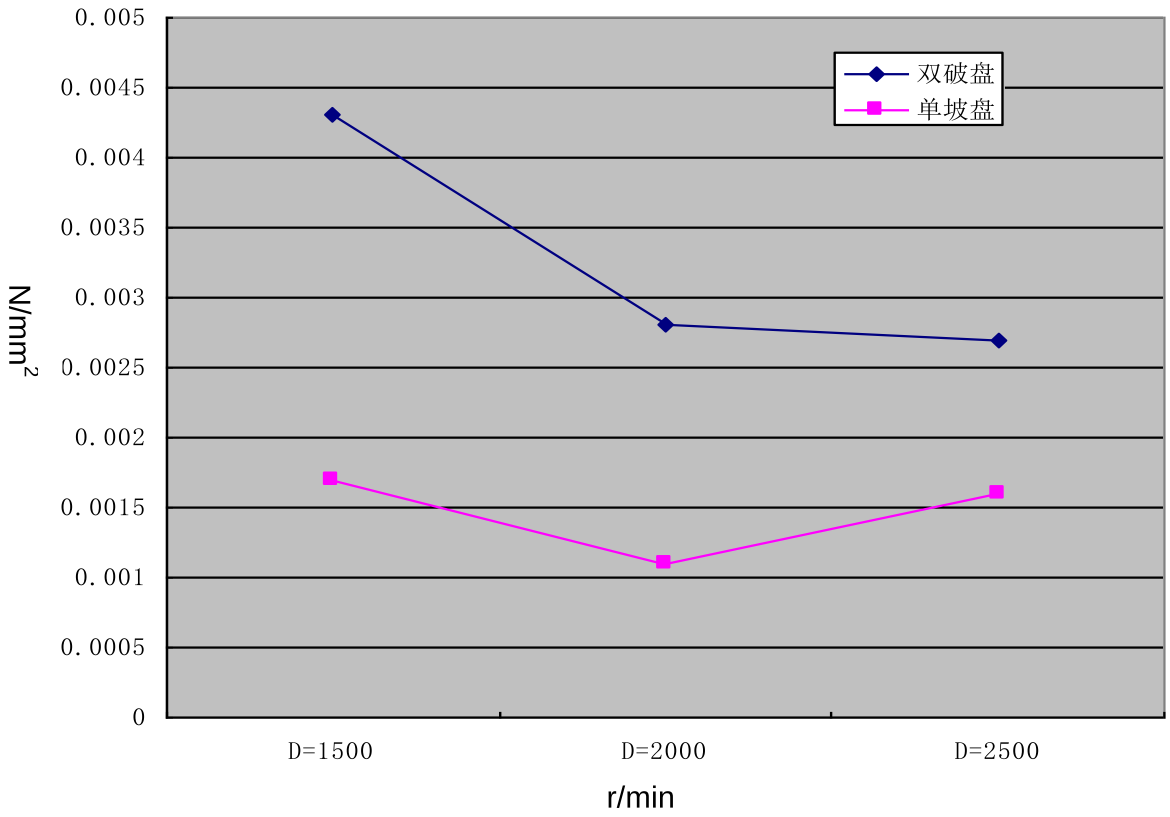

Figure 7. The vertical stress curve of soil around pile.

Conclusions

As regards selection of diameter of the bearing push-extend reamed, some qualitative conclusions can be drawn as follows:

(1) The bearing push-extend reamed can improve the end-bearing force of pile, due to the existence of the bearing push-extend reamed; and also make the failure mechanism of soil up and down the push-extend reamed change. Therefore, the influence on soil around pile, bearing capacity of pile and the shape of the bearing push-extend reamed is different. However, with increase in diameter, the difference of effect between the double slope bearing push-extend and single slope bearing push-extend reamed tends to be slight.
(2) From the deductions, it can be seen that the double slope bearing push-extend reamed pile is lesser than single slope bearing push-extend reamed pile about the bearing capacity of pile under some diameter; however the influence region is larger. Therefore, based on variation of stress for different shape of bearing push-extend reamed, when considering selecting shape of bearing push-extend reamed, if the distance between the bearing push-extend reamed is smaller, the single slope bearing push-extend reamed may be adopted; otherwise, when the distance is larger, the soil can play a significant role; using double slope bearing push-extend reamed will have better effect.
(3) Meanwhile, considering that the forms of bearing push-extend reamed can be further improved, the development will be to change the current situation of the same diameter of bearing push-extend reamed as the diameter of gradual variation. The diameter at the top of pile was largest; from pile top to pile end, the diameter is gradually diminished.

The results of the study are used in the actual design, helpful for the selection of the shape of the bearing push-extend reamed, and can better determine the bearing capacity of single pile through use of the theory of slip line. It is put forward that the theoretical foundation of the design of the Push-extend Multi-under-reamed Pile, contribute to the extensive application of this technology, so as to create greater economical and social benefits.

Conflict of Interests

The author(s) have not declared any conflict of interests.

ACKNOWLEDGEMENT

This work is sponsored by National Natural Science Foundation of China (51278224).

REFERENCES

Yongmei Q, Yi Y, Wang R (2013a). Research on Influence Factors of the Ultimate Bearing Capacity of the Soil of Push-extend Multi-under-reamed Pile under Compression. Adv. Mater. Res. 671-674:538-541. http://dx.doi.org/10.4028/www.scientific.net/AMR.671-674.538
Yongmei Q, Mu N, Wang R (2013b). The Research about the Method of Establishing the Model of Limited Unit about the Push-extend Multi-under-reamed Pile. Adv. Mater. Res. 671-674:602-605.http://dx.doi.org/10.4028/www.scientific.net/AMR.671-674.602

academicJournals

Vol. 9(9), pp. 331-335, 15 May, 2014
DOI: 10.5897/SRE2014.5912
Article Number: 2BD9F7544549
ISSN 1992-2248 © 2014
Copyright©2014
Author(s) retain the copyright of this article
http://www.academicjournals.org/SRE

Scientific Research and Essays

Full Length Research Paper

Two-phase closed-loop system identification method based on the auxiliary model

Jie Jia[1], Jiao Cao[1], Yong Yang[2]*, Zhiteng Liu[1] and Shuying Huang[3]

[1] College of Information Engineering, Nanchang Hangkong University, Nanchang 330063, China.
[2]School of Information Technology, Jiangxi University of Finance and Economics, Nanchang 330032, China.
[3]School of Software and Communication Engineering, Jiangxi University of Finance and Economics, Nanchang 330032, China.

Received 3 January, 2013; Accepted 31 July, 2013

The two-stage recursive extended least squares parameter estimation algorithm based on the auxiliary model of a class of closed-loop identification system model is presented in this paper. The basic idea of the algorithm is a combination of the auxiliary model identification ideas and the decomposition technique in which the closed-loop system is converted to a two-step process and each step identified model is an open-loop system. The more mature open-loop identification method is dealt with, the closed-loop system parameter identification problem is known in this way. The proposed algorithm has been proven to have high computational efficiency and effectiveness by the simulation examples.

Key words: Auxiliary model, least squares method, closed-loop system.

INTRODUCTION

System identification in closed-loop conditions has always been of particular concern in the field of industrial applications. The main problems of using the closed-loop data identification system is that unpredictable noise of the system output signal is related to the system control input signal through the feedback link. It is because of the existence of this correlation, resulting in many classic identification algorithms (Landau, 2001; Ding and Chen, 2005; de Klerk and Craig, 2002; Besterfield-Sacre et al., 2000) (such as: the method of least squares, instrumental variables, correlation analysis, spectrum analysis, etc.) used in the identification of the closed-loop system, that we have a greater estimation error. In recent years, many closed-loop identification algorithms have been proposed around the closed-loop data acquisition system parameters consistent unbiased estimate of the subject. Zhang and Feng (1995) and Ljung (1999) obtained the uniform convergence of the closed-loop parameters, by selecting the pre-data filter and compensating the noise covariance term.

Van Den Hof and Schrama (1993) and Laudau and Karimi (1996) made full use of process control input, the relationship between the process output and the setting, a closed-loop identification algorithm-two-stage closed-loop identification algorithm based on open-loop conversion was proposed. The algorithm will convert the closed-loop identification problem for the two open loop identification problem. By constructing the no noise

*Corresponding author. E-mail: yangyong5080@126.com

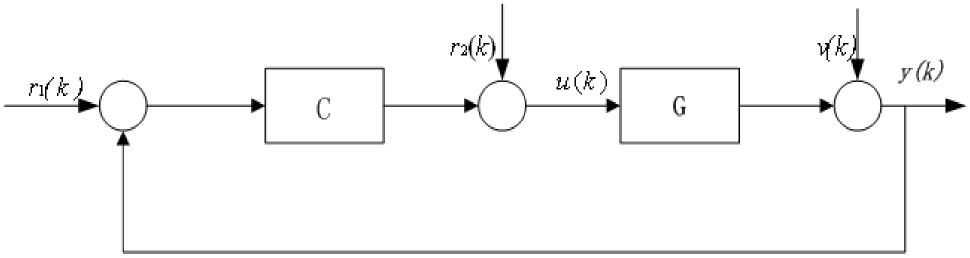

Figure 1. Closed-loop control system structure. $r_1(k)$ is the system settings, $r_2(k)$ for the applied test signal, $u(k)$ is the control input signal of the controlled object, $v(k)$ is a random white noise, $y(k)$ is the system output signal,

pollution intermediate signal instead of the actual control inputs, the correlation between the noise and the control input was removed. Then using the existing classic open-loop, identification algorithm can help to obtain system parameters consistent unbiased estimates. The algorithm idea is simple, convenient and does not require controller prior knowledge. But the original is not the final recognition result of the structure of the intermediate identification model parameters and model.

Accordingly, two stages of the closed-loop identification algorithm are given in this paper. Combined with the auxiliary model identification ideas and decomposition technique, the intermediate model is decomposed into two subsystems, each subsystem contains a parameter vector. With the auxiliary model-based recursive extended least squares theory, using the output of the auxiliary model instead of unknown intermediate variable vector, and using the estimated residuals instead of the information vector unpredictable noise term, which can use the idea of recursive identification to estimate the parameters of the intermediate model.

CLOSED-LOOP CONTROL SYSTEM MODEL DESCRIPTION AND IDENTIFICATION MODEL

First, define the symbol, "A: = X" or "X: = A" means that A is equal to X.

The symbol $I(I_n)$ indicate the unit matrix of dimension $n \times n$, I_n indicate n-dimensional unit column vector, superscript T represents the transpose of the matrix or vector.

Wherein $y(k)$ is the system output signal, $u(k)$ is the control input signal of the controlled object, $v(k)$ is a random white noise, $r_1(k)$ is the system settings, $r_2(k)$ for the applied test signal, $G(z)$ is a mathematical model of the controlled object, $C(z)$ is the controller.

The closed-loop identification task is that using the observational data sequence $[r_1(k), r_2(k), u(k), y(k)]$ estimate the parameters of the controlled object $G(z)$, and hope to get them consistent unbiased estimator. Known from Figure 1, the control system output equation can be written as:

$$y(k) = G(z)u(k) + v(k) \tag{1}$$

Due to the presence of a unit feedback loops, control of the system equation can be written as:

$$u(k) = r_2(k) + C(z)[r_1(k) - y(k)] \tag{2}$$

(1) Substituting into (2), elimination system output $y(k)$ can be obtained:

$$u(k) = \frac{C(z)r_1(k) + r_2(z)}{1 + C(z)G(z)} - \frac{C(z)}{1 + C(z)G(z)}v(k) \tag{3}$$

From Equation 3, it can be seen that random white noise $v(k)$ directly related to the control input $u(k)$ of feedback loops, which is the key that recognition results are biased when many identification algorithm about closed-loop system. Two-phase closed-loop identification algorithm by constructing intermediate signal no-noises pollution, overcome this correlation parameter identification which can be consistent unbiased estimate of the parameters.

Two-phase closed-loop identification algorithm

For convenience of description and without loss of generality, let $r(k) = r_2(k) + C(z)r_1(k)$, Equations 2 and 3 can be rewritten as:

$$u(k) = r(k) - C(z)y(k) \tag{4}$$

$$u(k)=\frac{1}{1+C(z)G(z)}r(k)-\frac{C(z)}{1+C(z)G(z)}v(k) \tag{5}$$

Equation (5) into (1), elimination of the control input $u(k)$, simplification was:

$$y(k)=\frac{G(z)}{1+C(z)G(z)}r(k)-\frac{C(z)}{1+C(z)G(z)}v(k) \tag{6}$$

Consider the system, Equations 5 and 6 make the following assumptions: (1) $r(k)$ is persistently exciting, and can be measured; (2) $r(k)$ and $v(k)$ are independent and not related in any moment. The closed-loop identification is done in two steps, that $1+C(z)G(z)=A(z),-C(z)=B(z)$ at the same time. Shift operator polynomial $A(z)$, $B(z)$ and $G(z)$ are the units $[z^{-1}z(k)=z(k-1)]$, and

$$A(z):=1+a_1z^{-1}+a_2z^{-2}+\Lambda+a_{n_a}z^{-n_a}$$
$$B(z):=b_1z^{-1}+b_2z^{-2}+\Lambda+b_{n_b}z^{-n_b}$$
$$G(z):=1+g_1z^{-1}+g_2z^{-2}+\Lambda+g_{n_g}z^{-n_g}$$

Suppose when $k\le 0$, the $u(k)=0$, $y(k)=0$, the $V(k)=0$, and the order of n_a, n_b, n_g are known:

Step 1: In formula (5), by assuming that the conditions, independent of $r(k)$ and $v(k)$ irrelevant, and $u(k)$ and $r(k)$ are measured, it can be that Equation (5) as an open-loop system, using the least squares identification unanimously unbiased estimate. The least squares parameter identification expression:

$$u(k)=\frac{1}{A(z)}r(k)+\frac{B(z)}{A(z)}v(k) \tag{7}$$

Step 2: According to the recognition result of Formula (7), to construct a no noise pollution control input *u (k)*, that is:

$$u(k)=\frac{1}{A(z)}r(k) \tag{8}$$

Equation 8 into 6, $u(k)$, $v(k)$ is not relevant, so Formula 13 can be seen as open-loop system processing, least squares identification can be consistent and unbiased estimates. Parameter identification expression:

$$y(k)=\frac{G(z)}{A(z)}r(k)-\frac{1}{A(z)}v(k) \tag{9}$$

At this point, the entire closed-loop identification task is complete, the controlled object parameters consistent unbiased estimator.

Simulation examples

Consider the following closed-loop system model,

$$A(z):=1+a_1z^{-1}+a_2z^{-2}=1+1.06z^{-1}+0.8z^{-2}$$
$$B(z):=1-b_1z^{-1}=1-0.64z^{-1}$$
$$G(z):=1+g_1z^{-1}+g_2z^{-2}=1+0.412z^{-1}-0.309z^{-2}$$

The model parameters are

$$\theta^T=[1.60,0.8,-0.64,0.412,-0.309]$$

Simulation for the first step, $\{r(k)\}$ is selected white noise of zero mean and unit, the input $\{u(k)\}$ is a zero mean and unit variance irrelevant the measurable random signal sequence, and $\{v(k)\}$ is a zero mean and variance white noise sequence. When the noise variance parameters $\sigma^2=0.4^2$, recursive least squares (RLS) estimated error vs. time curve is shown in Figure 2. In particular, using the recursive extended least squares (RELS) (Duan et al., 2012; Yue et al., 2009; Yao and Ding, 2012) algorithm simulate the first step of identification model for comparing the effectiveness of the proposed algorithm in this paper. The RELS estimated error with the time curve is shown in Figure 3:

i. With the increase in the length of data, the parameter estimation errors of RLS algorithm based on the auxiliary model tended to be stable, but parameter estimation error of the RELS algorithm is very unstable. Therefore, the second step in terms of follow-up closed-loop identification is bound to generate a lot of bad influence.
According to the recognition result of the first step, construction of a noise pollution control entry is $u(k)$ in the second step.

Simulation $\{r(k)\}$ is chose zero mean and unit white noise $\{v(k)\}$ is a white noise sequence of zero mean and variance. In the type of noise variance parameters of σ^2, RLS estimate error vs. time curve is shown in Figure 4 .

ii. With the increase in the length of the data, parameter estimation error is getting smaller and smaller, and gradually stabilized, reflecting the algorithm efficiency and stability.

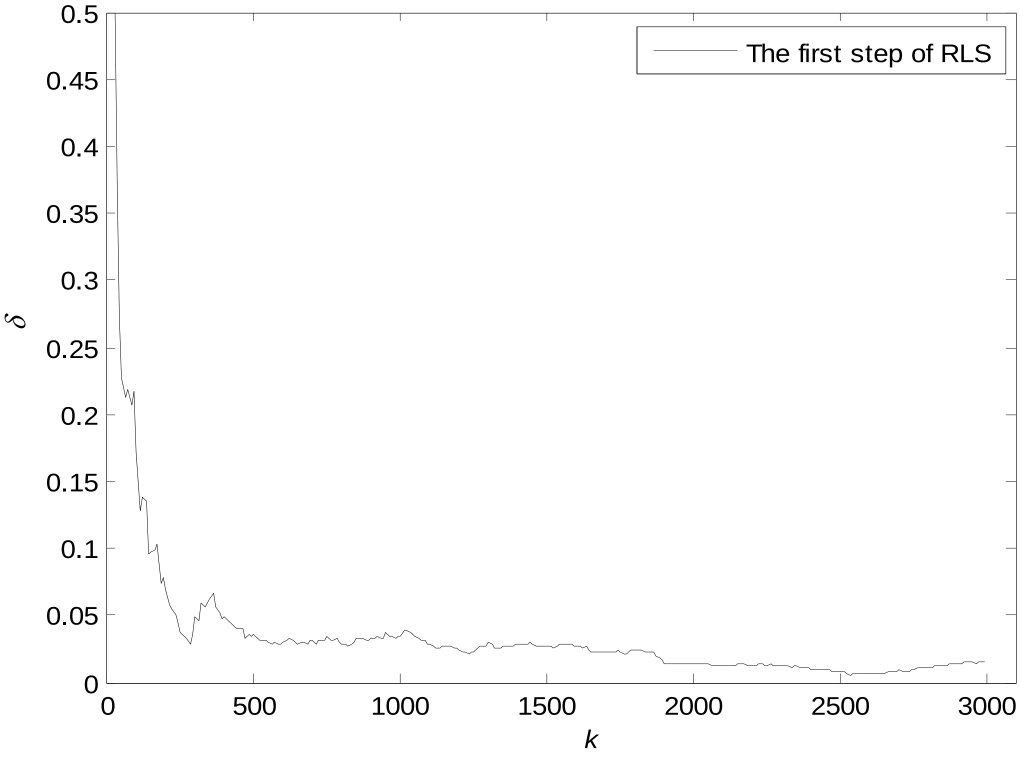

Figure 2. Recursive least squares (RLS) method of parameter estimation error change over time k.

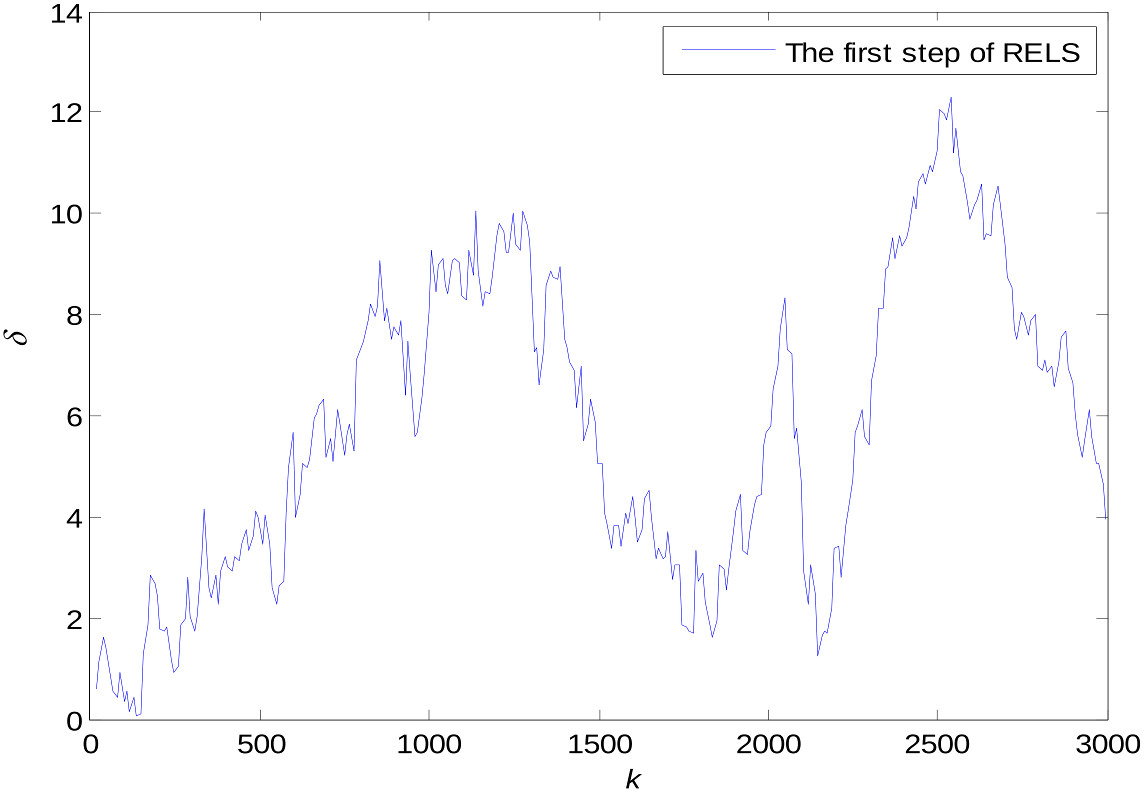

Figure 3. The recursive extended least squares (RELS) method parameter estimation error changes over time.

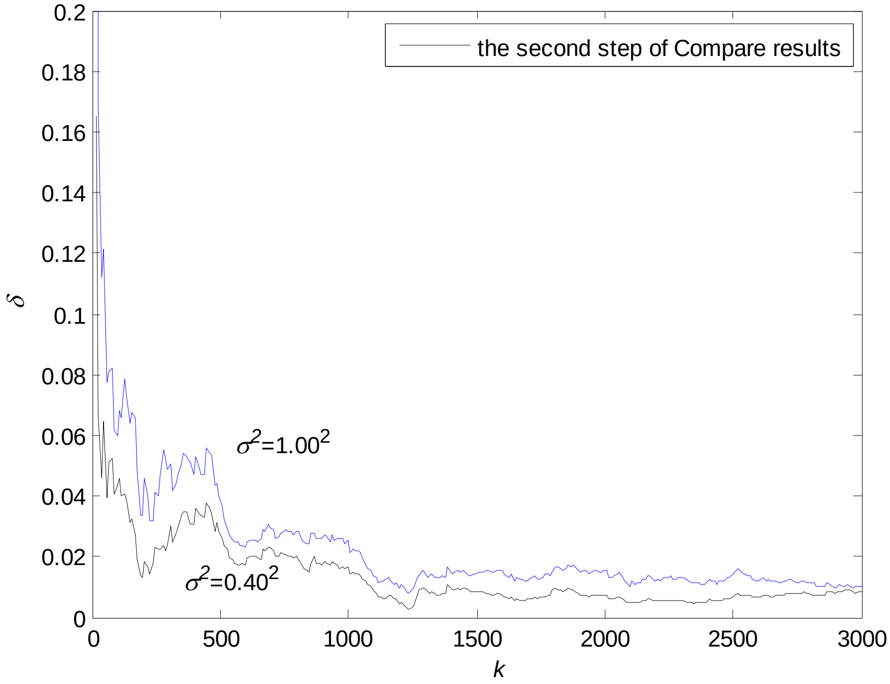

Figure 4. Parameter estimation error in the second step under different noise variance.

Conclusion

In this paper, for the converted first step in open-loop subsystem with the help of the auxiliary model and recursive extended least squares theory, the unknown intermediate variable vector was used instead of the output of the auxiliary model identification model, vector unpredictable noise term was used instead of estimated residuals; so using the recursive identification thought, estimated all the parameters of the system. In the second step, using recognition result of the first step constructed, the no noise input model, and then using the recursive extended least squares theory derived system model parameters.

Conflict of Interests

The author(s) have not declared any conflict of interests.

ACKNOWLEDGMENTS

This work was supported by the National Natural Science Foundation of China (61263012, 61263040, 61262034), Postdoctoral Foundation of China (2012M510593), Aerospace Science Foundation (20120156001), Natural Science Foundation of Jiangxi Province (20114BAB211020, 20132BAB201025), and Science and Technology Research Project of the Education Department of Jiangxi Province (No. GJJ13302).

REFRENCES

Besterfield-Sacre M, Schuman LJ, Wolfe H, Atman CI, McGourty J, Miller RL, Olds BM, Rogers GM (2000). Defining the outcome: A framework for EC-2000, IEEE Trans. 43(2):00-110.

de Klerk E, Craig IK (2002). An assignment to teach closed-loop system identification, 15th Triennial World Congress, pp. 273-278.

Ding F, Chen TW (2005). Hierarchical gradient-based identification of multivariable discrete-time system. Automatica 41(2):315-325. http://dx.doi.org/10.1016/j.automatica.2004.10.010

Duan HH, Jia J, Ding RF (2012). Two-stage recursive least squares parameter estimation algorithm for output error models." Math. Comput. Modell. 55(3-4):1151-1159. http://dx.doi.org/10.1016/j.mcm.2011.09.039

Landau ID (2001). Identification in closed loop: A powerful design tool. Cont. Eng. Pract. 9(1):51-65. http://dx.doi.org/10.1016/S0967-0661(00)00082-4

Laudau ID, Karimi A (1996). Recursive algorithms for identification in closed loop a unified approach and evaluation. Proc. 35th IEEE Conf. 2:1391-1396.

Ljung L (1999). System Identification Theory for the User, Prentice-Hall.

Van Den Hof PMJ, Schrama R JP (1993). An indirect method for transfer function estimation from closed-loop data. Automatica, 29(6):1523-1527. http://dx.doi.org/10.1016/0005-1098(93)90015-L

Yao GY, Ding RF (2012). Two-stage least squares based iterative identification algorithm for Controlled autoregressive moving average (CARMA) systems. Comput. Math. Appl. 63(5):975-984. http://dx.doi.org/10.1016/j.camwa.2011.12.002

Yue N, Zhu FZ, Zhou Y, Ding F (2009). The autoregressive moving average model two-stage identification method based on RLS. Sci. Technol. Eng. 9(7):1918-1920.

Zhang WX, Feng CB (1995). A bias-crrection method for indirect identification of closed-loop systems. Automatica 31(7):1019-1024. http://dx.doi.org/10.1016/0005-1098(95)00006-I

academicJournals

Vol. 9(9), pp. 336-342, 15 May, 2014
DOI: 10.5897/SRE2014.5913
Article Number: C6B102A44551
ISSN 1992-2248 © 2014

http://www.academicjournals.org/SRE

Scientific Research and Essays

Full Length Research Paper

Research on the topology control algorithm to maximize the Ad Hoc life cycle

Wenbo Zhang*, Yongxin Feng, Xiaobo Tan and Lidong Fu

School of Information Science and Engineering, Shenyang Ligong University, Shenyang 110159, China.

Received 3 January, 2013; Accepted 24 Mar, 2014

For Ad Hoc network, nodes move randomly with limited energy and self-organization; there is multi-hop of complex network, however, in order to extend the life cycle of Ad Hoc network effectively. This research was aimed at improving LEACH algorithm clustering on Ad Hoc network, constructing Ad Hoc network topology based on small world, making nodes that can still continue to maintain communication under the circumstances of communication link failure, appearance, disappearance and move. Namely, the work aims to improve the stability of the network topology and overall network anti-destroying. The simulation experiment verifies the correctness and effectiveness of algorithm.

Key words: Ad Hoc network, complex network, small world network, life cycle, survivability.

INTRODUCTION

In this paper, an approach for topology control to extend the lifetime of Ad Hoc network was studied, in order to synthesize various factors as far as possible to maximize network survival time, and to make node maintain communications under the circumstances such as appearance, disappearance, movement and communication link failure. There are some ways about survivability study as follows. Firstly, the network topology structure is designed in the beginning, and during the design, various factors that prolong the survival time of the network, maintain network stability and improve the overall performance of the network are all considered. Secondly, Ad Hoc network is self-organizing and multi-hop. It has some characteristics of complex network. So the complex network theory could be used in Ad Hoc network to enhance its survivability. Finally, in order to maintain the stability of the network, the node or link failure and other factors such as redundancy, reconstruction and other measures should be considered (Liu et al., 2011, 2012; Mistra and Thomasinous, 2010; Ok et al., 2009; Ren et al., 2011; Uster and Lin, 2011).

The Ad hoc network topology is flat. So in order to enhance its survivability, it should have high connectivity between each node, that is to say, there are many paths between two nodes, if one path fails, start the other one. To make node strong connected, it is essential to increase the transmission power of the node, enlarge transmission range of nodes and cover more nodes. But increasing the transmission power of the node consumes its energy and shorts the network lifetime, so the energy consumption and network survivability is contradictory. This paper constructs a hierarchical network, which has different clustering algorithms by means of cluster head election, and synthesizes the residual energy of node, mobility, deviation of node degree (cluster size) and other factors to cluster (Wendi et al., 2002; Xiaohua et al., 2005;

---

*Corresponding author. E-Mail: zhangwenbo@yahoo.com

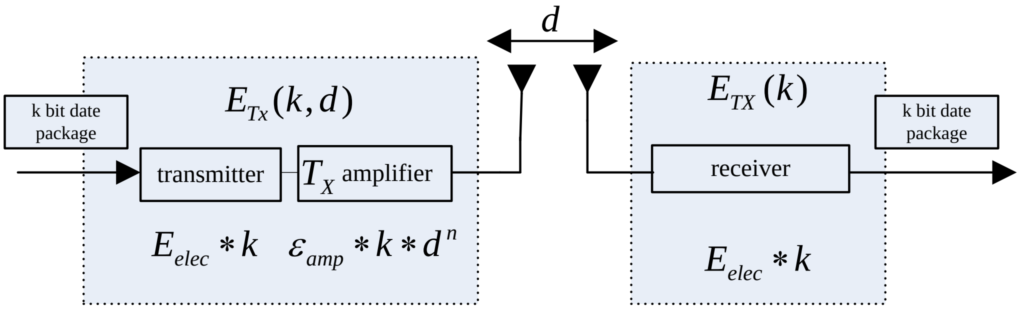

Figure 1. Radio energy model.

Xu and Liang, 2011).

LOW-ENERGY ADAPTIVE CLUSTERING HIERARCHY (LEACH), MODIFIED WEIGHTED CLUSTERING ALGORITHM (MWCA) CLUSTERING ALGORITHM ANALYSIS

The process of the cluster head election

At this stage, cluster head election algorithm combines low energy adaptive clustering hierarchical (LEACH) improvement algorithm in wireless sensor networks with an on-demand weighted clustering algorithm (WCA). That is, the clustering algorithm $\begin{cases} LEACH(T = 0) \\ WCA(T > 0) \end{cases}$

The threshold for LEACH algorithm:

$$T_n = \frac{P}{1 - P[r \bmod (1/P)]} \qquad n \in G \tag{1}$$

The calculation method of on-demand weighted clustering algorithm:

$$weight = aEv_{resident} + b/M_v + c/D_v \tag{2}$$

$Ev_{resident}$ is the remaining energy of nodes, which was obtained from node energy model (Yao-Chung et al., 2006) .

Figure 1 shows the diagram of energy model of nodes. Assuming a simple model for the energy consumption of wireless hardware, in this model, the sending end energy consumption includes sending radio electronics and amplifier energy consumption, the receiving end energy consumption includes receiving radio electronic energy consumption as shown in Figure 1. For this description, there are two kinds of channel model, free space model (energy loss and transmission distance is proportional to the square) and multi-path fading model (the energy loss is proportional to transmission distance to the fourth power), conversion between the two models is based on the distance between the sending and the receiving end, and power control can be set by the appropriate power amplifier and change the distance between the sending and receiving end. If the distance is less than the threshold value d_0 , we use the free space model, otherwise, we use multi-path attenuation model. Therefore, when the distance between sending and receiving end is d with a $l - bit$ message, the radio energy consumption is:

$$E_{Tx}(l,d) = E_{Tx-elec(l)} + E_{Tx-amp}(l,d) = \begin{cases} lE_{elec} + l\varepsilon_{fs}d^2, d < d_0 \\ lE_{elec} + l\varepsilon_{amp}d^4, d \geq d_0 \end{cases} \tag{3}$$

To receive this message, the radio energy consumption:

$$E_{Rx}(l) = E_{Rx-elec}(l) = lE_{elec} \tag{4}$$

The energy consumption of sending and receiving end is the sum of the total energy consumption of the node, the difference of the initial energy and total energy consumption is the residual energy of the node.

The M_v presents the local mobility of the node, it can be calculated by a set of relative mobility metric values from all the neighboring nodes.

For the relative mobility metric value of node u to node v :

$$M_v^{rel}(u) = 10\lg\frac{R_xP_{r^{new}_{u\to v}}}{R_xP_{r^{old}_{u\to v}}}$$, if $R_xP_{r^{new}_{u\to v}} < R_xP_{r^{old}_{u\to v}}$,

then $M_v^{rel}(u) < 0$, it means that the two node are far away from each other, contrary, if $R_xP_{r^{new}_{u\to v}} > R_xP_{r^{old}_{u\to v}}$, it shows that the two nodes are close to each other. If a node v has m neighbor nodes, there are m value M_v^{rel} , the local mobility value is the difference between the relative mobility value of all neighbors and 0, that is:

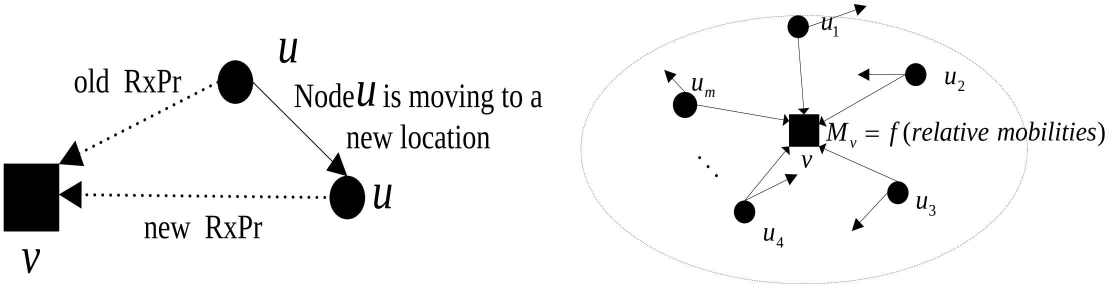

Figure 2. Local movement and relative movement.

$M_v = \mathrm{var}_0\{M_v^{rel}(u_i)\}_{i=1}^{m} = E[(M_v^{rel})^2]$, M_v is calculated. If $M_v < 0$, it indicates that the node is away from neighbors, if $M_v > 0$, it shows the node is close to neighbor nodes (Figure 2).

D_v means the difference between node degree (number of neighbor nodes) and the ideal degree, as the $D_v = |d_v - M|$, where d_v denotes the number of neighbor nodes. The calculation formula of d_v is as follow:

$$d_v = |N(v)| = \sum_{v',v\in V,v'\neq v} \{dist(v,v')\} < tx_{range} \quad (5)$$

here tx_{range} represents the transmission range of the nodes.

A $weight$ implies the combination weight of node, namely to the ability to act as cluster head node. For the weight factor a, b and c, we set $a > b > c$ in this thesis, and they satisfy $a + b + c = 1$. Based on the calculation formula of combination weight, we are mainly considering three factors: the energy of node, the mobility of node (cluster stability) and the size of cluster (node degree). Among them, if the local mobility and the difference between the node degree and the ideal degree are small, the possibility of a node becoming cluster head node is big, and the stability of clusters is strong. If the remaining energy is large, the probability of the node becoming cluster head is high. Therefore, by calculating, it shows that we should choose the larger weight as the cluster head node.

The initial stage of establishing a cluster

During the initial process of creating a cluster in mobile Ad Hoc networks, a mobile node first starts and then enters into networking; and at last forms a relatively stable cluster structure within the scope of the entire network. When we initially create a cluster or a new node join in, through the initialization process, deciding what role of the node should play in.

When a system boots, a globally unique node ID is given, all nodes are randomly well-distributed in a region with the same initial energy, the energy consumption of mobile nodes are not the same each round. In the first round, we use the LEACH algorithm, namely t = 0, during a short time of executing the clustering algorithm, the mobile node in Ad Hoc network nodes do not move. Each node is randomly assigned a random number, comparing the random number with threshold, when the random number is less than the T_n, the node is selected as the cluster head node. Then, the node which was selected as the cluster head broadcast Hello message packet, which includes the serial number of the cluster head node. The non-cluster head nodes which received the broadcast message packet, choose to add to the strong signal clusters, according to the distance between them and the cluster head nodes, notify the cluster head, when cluster head node receives all the information added to the cluster, it will create a time division multiple access (TDMA) timing information and inform all the nodes within the cluster. In order to avoid the interference of signal from nearby cluster, the cluster head node can decide code division multiple access (CDMA) code of all nodes in the cluster, CDMA code along with the TDMA are sent at scheduled times, when a node within the cluster receives the message, it begins to enter the data communication phase. In this phase, each node has the trend to move in the cluster. We should consider this dynamic problem time discretization.

Assuming that each node has different energy consumptions in each round, namely the node's residual energy is different. In order to balance the energy consumption of all nodes, we should select each node to become a cluster head periodically so that each node has to the opportunity to act as the cluster head. In the second round of the cycle, we use the on-demand weighted clustering algorithm to initialize the node information along with the weight of the node. The weight of the node includes the current residual energy, local mobility and the degrees (one-hop neighbor node of the nodes), the number of cluster head and the ID information of the cluster heads. In addition, we also initialize neighbor list information of the node and the cluster head table information.

The node should put its own ID, transmit and receive signal power into broadcast message, and broadcast to one-hop neighbors. When neighbor nodes receive broadcast message of that node, it checks its own neighbor list. If the node has already existed in the neighbor list, update is made to the information in neighbor list of the node with mobile information and update time. Node should be added, if it does not exist in the neighbor list. After a node transmits broadcast message a period of time, when assuming that it has received the message from all neighbors, that is to say, there is no new neighbor node to be added to the neighbor list of the node in a period of time, it begins to calculate its own weights.

First through the energy model of the node, when we calculate weights, the residual energy $E_{resident}$ is obtained. The node goes through its own neighbor list. Through the neighbor list stored in, the node receives the same at different times of signal power; we can figure out $M_v^{rel}(u)$, along with M_v.

The total number of neighbors is extracted from the neighbor list, d_v is calculated and then we obtain the $D_v = \left|d_v - M\right|$. According to the calculated $E_{resident}$, M_v, D_v and the importance of the three factors that are previously set as a、b、c to calculate the combination weight of each node, each node puts combination weight and node ID in the node weight broadcast message, and broadcasts to one-hop neighbors.

After each node receives the neighbor node weight message, they update their neighbor list information. Within a period of time, if the node does not receive the node weight message in the original neighbor list, the node should be deleted from original neighbor list; if a node receives weights message in original neighbor list, it is necessary to update the neighbor node weight; if a node receives weight message instead of the original neighbor list, we have to discard it.

After the node sends weight message a period of time, if all weights in the neighbor node list are updated, the node determines whether its weight are larger than all the neighbors' nodes or not; if the weights are equal, the node compares whether node ID is smaller than the neighbor's. If it satisfies this condition, node sends a message that it acts as the cluster head, otherwise waits for news of neighbor nodes becoming cluster heads.

For ordinary nodes which have not be elected as cluster head, if they receive the message of neighbors becoming cluster head, its state turn into cluster members, next to update their cluster head table and retreat from cluster head election. Otherwise, the node sets itself to the cluster head, and sends a message that it becomes the cluster head. If there are still nodes in the initial state, following the round cycle to execute cluster head election process until the status of all nodes turn into cluster head or cluster members is necessary. This facilitates selecting cluster head periodically so that each node has opportunity to become a cluster head, and thus the energy consumptions of nodes are more balanced.

INTER-CLUSTER COMMUNICATION

The inter-cluster communications connect cluster heads to form a ring network, for each node can become a cluster head, the nodes in ring network also periodically change. We construct the small world network based on this topology according to two properties of the small world network: the big clustering coefficient and the small shortest path. Firstly, long links were constructed; where N represents the number of vertex ring, the P represents the random connection probability, and the K is the number of adjacent nodes, according to the formula, the average path length: $L = \frac{N}{K} f(NKP)$, and the clustering coefficient $C = \frac{3(k-1)}{2(2k-1)}(1-p)^3$, according to the parameters of N, P, K (both determine the number of long links). The purpose is to construct the topology with the shortest path, while the clustering coefficient is used to describe the node graph or network integration group coefficient. The network is divided into clusters on the whole, and its clustering coefficient is very high. Thus on the whole, we construct the topology of Ad Hoc network based on small world network, each cluster can communicates with each other. The topology diagram of Ad Hoc networks is based on small world network (Figure 3).

After the cluster is created, it is essential for the reasonable maintenance mechanism of clusters to try to maintain the stability of the cluster structure, due to the limited energy and the natural failure or link failure and the mobility of the node. At the moment of the node failure or link failure, node can still maintain the ability of communication, namely to prolong the network life cycle. Therefore, in this paper, the maintenance of clusters are mainly a node joins, disappears and moves. Node joining makes use of network reconfiguration, in order to quickly start backup node to backup link if node disappears and the link fails.

LOW-ENERGY ADAPTIVE CLUSTERING HIERARCHY (LEACH) AND MODIFIED WEIGHTED CLUSTERING ALGORITHM (MWCA) SIMULATIION AND ANALYSIS

The simulation model comprised 50 nodes, randomly distributed in the range of 100 m * 100 m; the network is divided into 10 clusters, namely 10 cluster heads. The

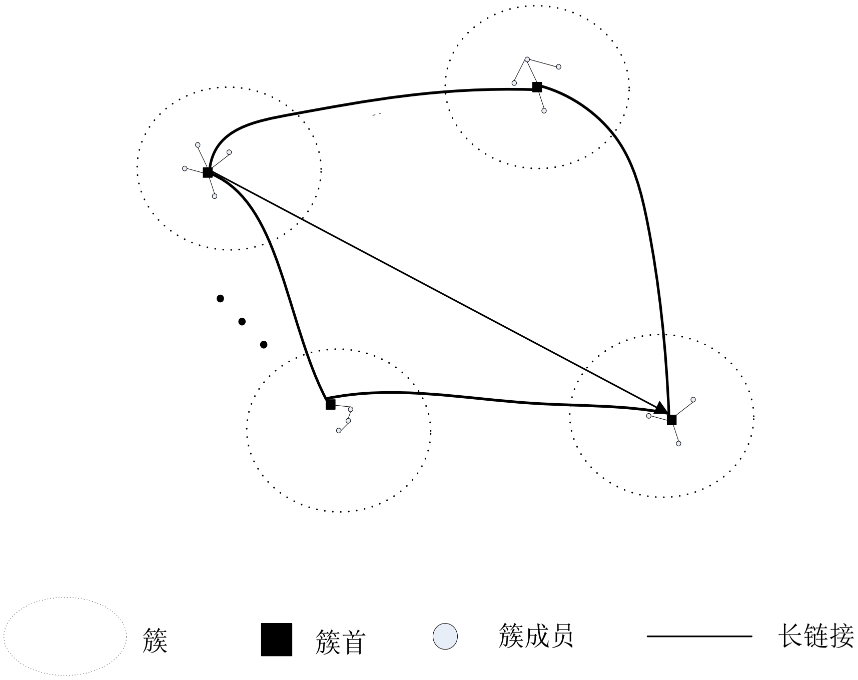

Figure 3. Topology diagram of Ad Hoc networks based on small world network.

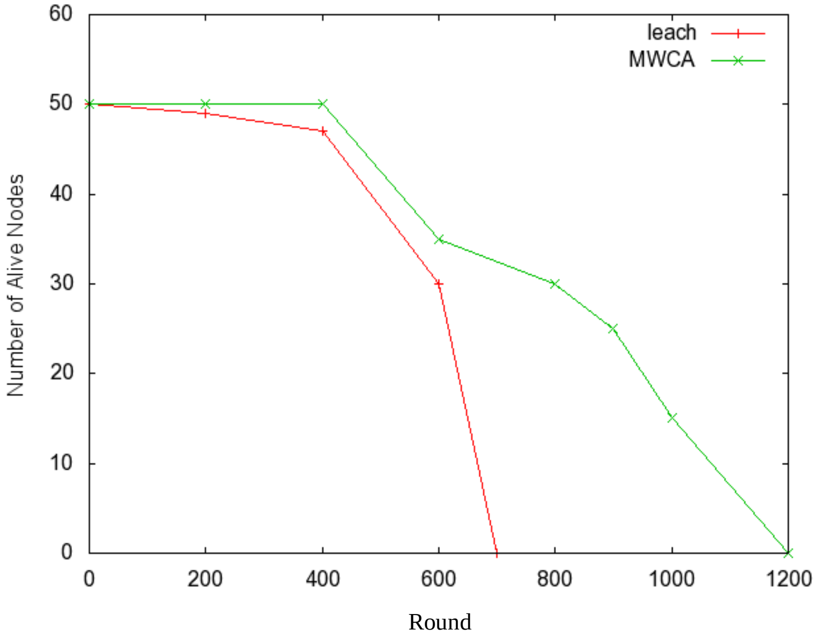

Figure 4. The diagram of election times and survival node numbers.

initial energy of the nodes is 1J, the actual connection degree is M = 4, the total simulation time is 800 min. The related parameters of the small world network is set to N = 10, P = 0.2, K = 4 (adjacent nodes), each round of cycle interval is 50 s, a total of 960 rounds.

Figure 4 shows the relationship between curve of cluster heads election rounds and the remaining nodes in Ad Hoc network based on the small world. From Figure 4 using the simulation of LEACH algorithm, all nodes are dead after 700 rounds of the cluster head election, but applying the LEACH and MWCA clustering algorithm we put forward, the life cycle of the node is 1200 rounds, not

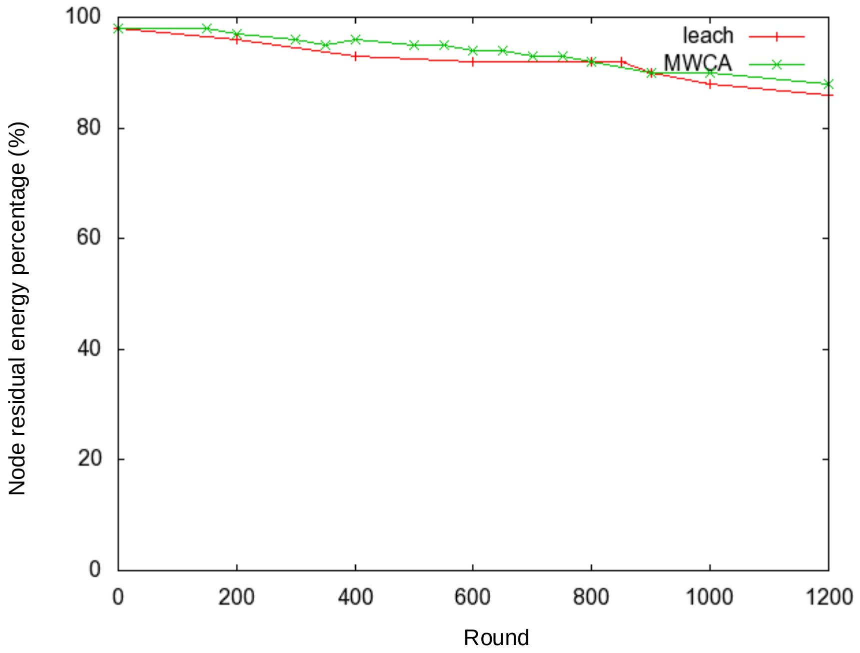

Figure 5. The diagram of election times and network node residual energy percentage.

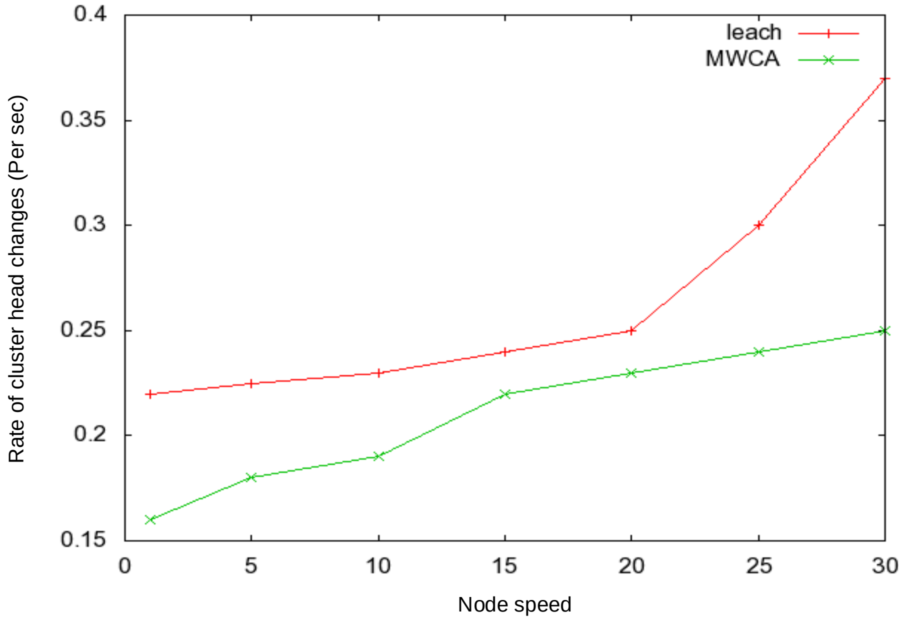

Figure 6. The diagram of node speed and rate of cluster head changes.

because of the hasten death of nodes due to the excessive energy consumption of the cluster head node, to improve the stability of the network topology and the survivability of overall network, but because of the cluster heads election algorithm proposed in this paper considers the residual energy and mobility of the node and the maximum number of nodes for cluster head nodes handling, to make the energy consumption of nodes in the network more homogeneous and stable.

From Figures 5 and 6 shown, the LEACH algorithm does not consider the residual energy and mobility of nodes, although each node has the probability of acting as cluster head, individual cluster head nodes accelerate the death due to excessive energy consumption. As the node speed increases, the cluster head change rate is larger; if the entire cluster is not stable, maintaining the stability of the cluster and network topology will consume more energy, while the algorithm proposed in this paper considers the residual energy and mobility of nodes, the nodes which have much residual energy and low moving rate act as cluster head, the cluster head is more stable, the lifetime of all nodes in the whole network is longer, according to the passage above, we know that the LEACH and MWCA clustering algorithm in the Ad Hoc network based on the small world is more stable, the anti-destroying ability of the whole Ad Hoc network is stronger.

CONCLUSIONS

In this research, the approach to hierarchical topology control in maximizing network lifetime of Ad Hoc network based on small world was put forward. In the process of the cluster head election, we do not only comprehensively consider the residual energy of the node, mobility of the node and the maximum number for cluster head node to handle, but also make use of small-world model to maintain the stability of the node and to enhance the anti-destroying ability of the network. The simulation results show that compared with other clustering algorithms, the proposed clustering algorithm in this paper can prolong the network lifetime effectively.

Conflict of Interests

The author(s) have not declared any conflict of interests.

ACKNOWLEDGEMENTS

This paper is sponsored by New Century Program for Excellent Talents of Ministry of Education of China and Shenyang Ligong University Computer Science and Technology Key Discipline Open Foundation.

REFERENCES

Liu A, Ren J, Li X, Chen Z, Shen X (2012). Design principles and improvement of cost function based energy ware routing algorithms for wireless sensor networks. Comput. Netw. 56:1951-1967. http://dx.doi.org/10.1016/j.comnet.2012.01.023

Luo D, Zhu X, Wu X, Chen G (2011). Maximizing lifetime for the shortest path aggregation tree in wireless sensor networks. In: Proc. of IEEE INFOCOM '1 1, 2011, April 10-15, pp. 1566-1574. PMid:21714026 PMCid:PMC3190151

Mistra S, Thomasinous PD (2010). A simple, least-time and energy efficient routing protocol with one level data aggregation for wireless sensor networks. Syst. Softw. 83:852-860. http://dx.doi.org/10.1016/j.jss.2009.12.021

Ok CS, Lee S, Mitra P, Kumara S (2009). Distributed energy balanced routing for wireless sensor networks." Comput. Ind. Eng. 57:125-135. http://dx.doi.org/10.1016/j.cie.2009.01.013

Ren F, Zhang J, He T, Lin C, Das SK (2011). Energy balanced routing protocol for data gathering in wireless sensor networks. IEEE Trans. Parallel Distrib. Syst. 22(12). http://dx.doi.org/10.1109/TPDS.2011.40

Uster H, Lin H (2011). Integrated topology control and routing in wireless sensor networks for prolonged network lifetime. Adhoc Netw. 9(5):835-851. http://dx.doi.org/10.1016/j.adhoc.2010.09.010

Wendi BH, Anantha PC, Hari B (2002). An Application-Specific Protocol Architecture for Wireless Microsensor Networks. IEEE Trans. Wireless Commun. 1(4):660-670. http://dx.doi.org/10.1109/TWC.2002.804190

Xiaohua J, Dongsoo K, Sam M, Peng-Jun W, Chih-Wei Y (2005). Power Assignment for k-Connectivity in Wireless Ad Hoc Networks. In 24th Annual Joint Conference of the IEEE Computer and Communications Societies (INFOCOM2005), Miami, Florida, USA.

Xu X, Liang W (2011). Placing optimal number of sinks in sensor networks for network lifetime maximization. In: Proc. IEEE ICC'11, 2011, June 5-9, pp. 1-6.

Yao-Chung C, Zhi-Sheng L, Jiann-Liang C (2006). Cluster Based Self-Organization Management Protocols for Wireless Sensor Networks. IEEE Trans. Consum. Electron. 52(1):75-80. http://dx.doi.org/10.1109/TCE.2006.1605028

academicJournals

Vol. 9(9), pp. 343-351, 15 May, 2014
DOI: 10.5897/SRE2014.5914
Article Number: 12AC3FC44553
ISSN 1992-2248 © 2014
Copyright©2014
Author(s) retain the copyright of this article
http://www.academicjournals.org/SRE

Scientific Research and Essays

Full Length Research Paper

Hydrochemical characteristics of groundwater in Tongchuan City, China

Zhang Yuxi, Zhang Yuanjing* and Liu Jingtao

The Institute of Hydrogeology and Environmental Geology, Chinese Academy of Geological Sciences, Shijiazhuang 050061, China.

Received 3 January, 2013; Accepted 2 March, 2013

In order to reveal the formation mechanism of hydrochemical characteristics in Tongchuan City, we collected and detected 39 samples of underground water. Correlation analytical method, hydrochemical method and ion ratio coefficient method were employed to investigate the hydrochemical characteristics, influencing factors and principles of changing. Results demonstrate that the main factors, controlling the shallow water salinization, are the SO_4^{2-}, NO_3^-, Cl^- and K^+. The contents of SO_4^{2-}, NO_3^- and Cl^- are greatly different and other indexes are relatively stable. The values of γNa/γCl demonstrate that the Na^+ is released from the soil aquifer in the runoff process. There is an exchange between the Ca^{2+} in water and Na^+ in soil, which leads to γNa＞γCl. As the exchange time in deep water is longer than that of shallow water, the exchange and adsorption of ions are more sufficient. The value of γNa/(γNa+γCl) demonstrates that with increasing of ground water depth, the level of cation exchange enhances, which leads to the dominant cation turning to Ca^{2+} from Na^+. The value of $\gamma HCO_3+\gamma SO_4/\gamma Ca+\gamma Mg$ demonstrates the shallow water is mainly from atmospheric rainfall and the influence of cation exchange is more obvious on deep water. The types of shallow water in Tongchuan City are mainly $HCO_3 \cdot SO_4$-Ca. Its classification is relatively complex. Whereas, the deep water is mainly HCO_3-Na and the category of underground water is simple. As for shallow water, the content of alkaline earth metal is larger than that of alkali metal. For the deep water, the content of weak acid group is larger than that of strong acid group. In the region of upper reaches, the features of both shallow and deep waters are mainly weak acid and alkaline earth metal. The chemical composition mainly consists of carbonate leaching. With the flowing of underground water, the shallow water turns to be strong acid and alkaline earth metal and the deep water turns to be weak acid and alkali metal.

Key words: Tongchuan City, underground water, hydrochemical characteristics, ion ratio coefficient method.

INTRODUCTION

The composition and distribution of hydrochemistry are direct proofs to study the formation and change of underground water. They are basic principles for exploitation and planning. The composition and concentration distribution of hydrochemistry are formed in the development of geological history. Some geochemical conditions play important roles in the process of formation, such as the topographical distribution, meteorological and

---

*Corresponding author. Email: kobzhang@qq.com

hydrological changes, geological structures, changes of hydrological conditions and human activities. Through hydrochemical information, we can explore the features of occurrence environment, runoff channels and material exchanges, which can help us to reveal the cycle principles of underground water (Florian, 2011; Ravikumar et al., 2010).

Tongchuan City is an industrial city with plenty of coal mines. Its coal and building-material industries are highly developed. So it is an important industrial base for energy and raw materials in northwest of China. In the process of development, there are large populations settled down. What is more, the scales of industry and agriculture, commerce and tourism have increased rapidly. These changes have propelled a high demand for underground water. However, the underground water has been seriously destroyed, which has affected the living water, industrial water and agricultural water. The study of underground water hydrochemistry is the main contents of water resources quality evaluation, which has an important meaning in water resources utilization and management together with the protection of the ecological environment.

In this paper, we collected underground water with the principle of scientific system. Then, relative hydrogeochemical parameters were studied. Descriptive statistics, correlation analysis, ion ratio coefficient method and Piper diagrammatic method were employed to study the characteristics of spatial and temporal variability together with the evolution rules. We also revealed the hydrochemical procedure of underground water quality evolution, which provides scientific proof for water resources protection and rational development.

MATERIALS AND METHODS

Overview of the research area

Tongchuan City is located in the transitional zone of Guanzhong Plain to loess plateau of Shanxi Province (E108°34′~109°29′, N34°50′~35°34′), with an area of 3882 km^2. Tongchuan City has a warm temperate continental climate, which is dry and cold in winter and with scarce rain and snow. Affected by the warm moist air mass of Pacific Ocean, it is hot and humid with relative abundant rain in the summer. There are usually droughts in spring and water-logging in autumn. The topography of Tongchuan City is north-west high and south-east low, which results in the obvious difference of climate. The average precipitation is 555.8~709.3 mm and the average temperature is 8.9~12.3°C.

Collection and analysis of samples

In August 2011, we collected 39 samples of underground water in Tongchuan City, which consists of 25 groups of shallow water (well total depth less than 30 m) and 14 groups of deep water (well total depth more than 100 m), which are shown in Figure 1. The parameters to be detected include HCO_3^-, SO_4^{2-}, NO_3^-, Cl^-, Ca^{2+}, Na^+, Mg^{2+}, K^+ and total dissolved solids (TDS). The detection of samples was carried out in underground mineral water and environmental monitoring center of the Ministry of Land and Resources. The equipments used are as follows: flame atomic absorption spectrophotometry was employed to detect the concentration of K^+ and Na^+; Ion chromatography was used to detect SO_4^{2-} and Cl^-; ethylenediaminetetraacetic acid (EDTA) titrimetry was used to study HCO_3^-; Gas phase molecular absorption spectrometry was used to detect NO_3^-; The value of TDS is the sum of ion concentration; we use SPSS18.0 and AquaChem3.7 were used to analyze the data.

RESULTS AND DISCUSSION

Descriptive statistics

The negative ions of underground water in Tongchuan City mainly consist of HCO_3^-, SO_4^{2-}, NO_3^- and Cl^- (as shown in Table 1). Especially, the concentration of HCO_3^- is the most high (in the range from 213 to 621.7 mg/L), with an average value of 353.11 mg/L. The contents of other ions are as follows: SO_4^{2-} (in the range from 13.18 to 897 mg/L) has an average value of 221.95 mg/L; NO_3^- (in the range from 6.98 to 482.5 mg/L) has an average value of 96.61 mg/L; Cl^- (in the range from 5.25 to 208.3 mg/L) has an average value of 53.06 mg/L. The positive ions of underground water mainly consist of Ca^{2+}, Na^+, Mg^{2+} and K^+. Especially, the concentration of Ca^{2+} is most high (in the range from 12.71 to 457.2 mg/L), with an average value of 129.32 mg/L. The contents of other ions are as follows: Mg^{2+} (in the range from 15.64 to 126.5 mg/L) has an average value of 42.99 mg/L; K^+ (in the range from 0.31 ~ 31.6 mg/L) has an average value of 3.21 mg/L. The value of TDS is in the range between 305.8 and 2343 mg/L, with an average value of 821.59 mg/L. For all the samples, 71.79% are fresh water and 28.21% belong to the brackish water. From the variation coefficients of components, we can conclude that NO_3^- has the highest variation coefficients in negative ions, which suggests that there is a large distribution in the contents of NO_3^-. There are also a large variation in the contents of SO_4^{2-} and Cl^-. However, the variation coefficient of HCO_3^- is the smallest, which suggests that its content is relative stable. In the four positive ions, K^+ has the highest variation coefficient, which suggests it has a wider distribution difference than others. The changing degree of negative ions is larger than that of positive ions.

There are some differences between the hydrochemical characteristics of shallow water and deep water. As for the negative ions, the concentration of HCO_3^- and NO_3^- show no obvious difference between the shallow water and deep water; the concentrations of SO_4^{2-} and Cl^- are 3 and 2 times higher than that of deep water respectively. Compared with deep water; the proportions of HCO_3^- and NO_3^- in negative ions are lower and the proportions of SO_4^{2-} and Cl^- are higher. As for positive ions, the average contents of Ca^{2+}, Mg^{2+} and K^+ are all higher than that of deep water. However, the concentration of Na^+ is lower than deep water. Ca^{2+} possess the maximum percentage

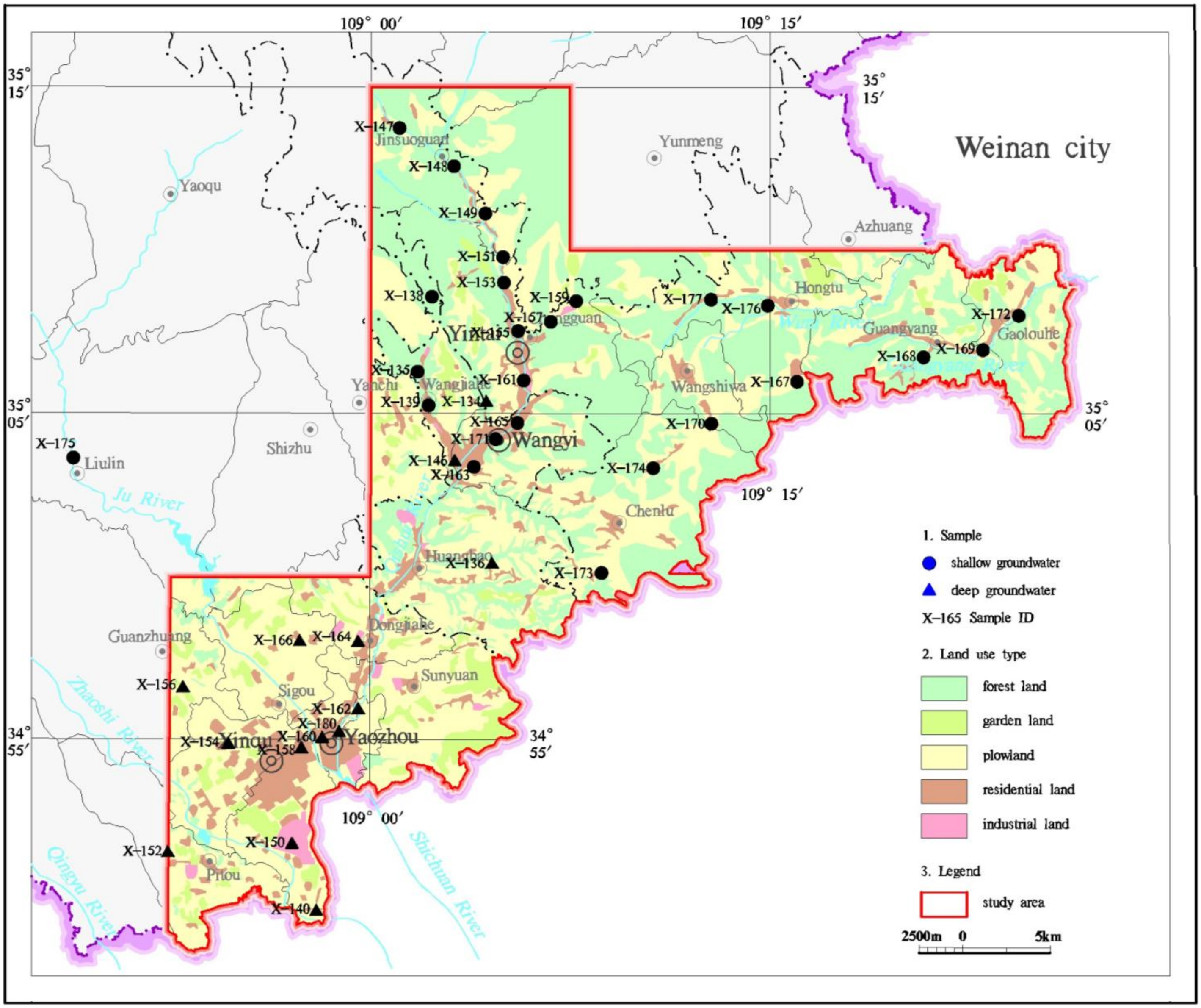

Figure 1. Location and detailed land use regionalization of the study area [groundwater sampling sites are shown as triangles (deep groundwater) and circles (shallow groundwater)].

in shallow water, which is 54.86% and Na^+ is the maximum one in deep water, which is 55.47%. What is more, the average value of TDS in shallow water is 1 times more than that of deep water, which suggests that there is a high ion content in the shallow water.

Generally, the ion variation coefficient of shallow water is higher than that of deep water. Among them, K^+ has the biggest change, which suggests that there is a more obvious variation in shallow water than that in deep water. This is caused by the aquifer medium, topography, hydrology-weather conditions and human activities. There shallow water, which demonstrates that they have relatively stable features. Among them, HCO_3^- has a is a smaller variation for HCO_3^-, Ca^{2+}, Na^+ and Mg^{2+} in maximum average value, with a minimum variation coefficient, which suggests that it has a higher relative contents and it is the main negative ions. There are higher variation coefficients in SO_4^{2-}, NO_3^-, Cl^- and K^+, which suggests they are sensitive to the change of environment, with bigger change in shallow water. In deep water, there are bigger variation coefficient in SO_4^{2-}, NO_3^- and Cl^-. We can conclude that they have a bigger contents change and a smaller variation in shallow water.

Correlation statistics

Correlation statistics can be used to reveal the similarity,

Table 1. Summary statistics of the analytical data and groundwater samples of the study area.

Groundwater samples	Statistical evaluation	Unit	HCO_3^-	SO_4^{2-}	NO_3^-	Cl^-	Ca^{2+}	Na^+	Mg^{2+}	K^+	TDS
All samples	Min	mg/L	213	13.18	6.98	5.25	12.71	19.02	15.64	0.31	305.8
	Max	mg/L	621.7	897	482.5	208.3	457.2	205.7	126.5	31.6	2343
	Mean	mg/L	353.11	221.95	96.61	53.06	129.32	79.24	42.99	3.21	821.59
	S.D	mg/L	76.8	226.45	116.77	51.73	96.8	43.04	27.16	5.87	448.24
	C.V	%	21.75	102.03	120.86	97.5	74.85	54.31	63.17	183.02	59.43
Shallow groundwater	Min	mg/L	224.5	21.19	9.8	5.25	24.31	19.02	20.12	0.31	305.8
	Max	mg/L	488.1	854.7	482.5	208.3	331.6	155.8	126.5	31.6	1944
	Mean	mg/L	355.2	266.02	92.69	63.31	153.94	72.07	50.38	4.21	924.92
	S.D	mg/L	67.68	223.04	119.4	55.51	81.86	41.24	30.07	7.27	458.72
	C.V	%	19.05	83.84	128.81	87.68	53.18	57.22	59.69	172.85	49.6
Deep groundwater	Min	mg/L	279.2	13.18	9.3	5.25	12.71	50.24	15.64	0.77	354.4
	Max	mg/L	621.7	185.5	364	64.77	90.26	205.7	41.56	1.71	695.7
	Mean	mg/L	369.56	63.48	106.47	23.14	48.5	95.29	26.78	1.22	491.3
	S.D	mg/L	96.46	49.13	128.54	18.36	24.04	46.11	9.74	0.29	119.74
	C.V	%	26.1	77.39	120.73	79.33	49.56	48.38	36.38	23.6	24.37

S.D: Standard deviation; C.V: coefficient of variation.

Table 2. Correlation matrices of hydrochemical parameters of groundwater in the study area.

Parameters		HCO_3^-	SO_4^{2-}	NO_3^-	Cl^-	Ca^{2+}	Na^+	Mg^{2+}	K^+	TDS
Shallow groundwater	**HCO_3^-**	1								
	SO_4^{2-}	-0.07	1							
	NO_3^-	-0.06	0.22	1						
	Cl^-	0.05	0.57[b]	0.16	1					
	Ca^{2+}	-0.09	0.92[b]	0.2	0.67[b]	1				
	Na^+	0.46[a]	0.25	0.19	0.63[b]	0.16	1			
	Mg^{2+}	0.13	0.84[b]	0.09	0.82[b]	0.78[b]	0.53[b]	1		
	K^+	-0.07	0.11	0.57[b]	0.27	0.18	0.17	0.08	1	
	TDS	0.07	0.89[b]	0.22	0.86[b]	0.91[b]	0.53[b]	0.93[b]	0.23	1
Deep groundwater	**HCO_3^-**	1								
	SO_4^{2-}	-0.19	1							
	NO_3^-	0.03	-0.15	1						
	Cl^-	-0.35	0.97[b]	-0.12	1					
	Ca^{2+}	-0.44	0.72[a]	0.21	0.75[b]	1				
	Na^+	0.86[b]	-0.11	-0.29	-0.25	-0.65[a]	1			
	Mg^{2+}	0.28	0.71[a]	0.15	0.67[a]	0.46	0.2	1		
	K^+	0.15	0.47	0.07	0.38	0.55	-0.06	0.48	1	
	TDS	0.56	0.68[a]	-0.11	0.56	0.23	0.56	0.87[b]	0.48	1

a $p<0.05$; b $p<0.01$.

dissimilarity, consistency and difference of underground water hydrochemical characteristics (Kshetrimayum and Bajpai, 2012). The Pearson correlation coefficients of shallow and deep waters in Tongchuan City are calculated as shown in Table 2. In shallow water, there is strong positive correlation between TDS and SO_4^{2-}, Cl^-, Ca^{2+}, Na^+ and Mg^{2+}. However, HCO_3^-, NO_3^- and K^+ have no effects on TDS. Above results demonstrate that TDS is

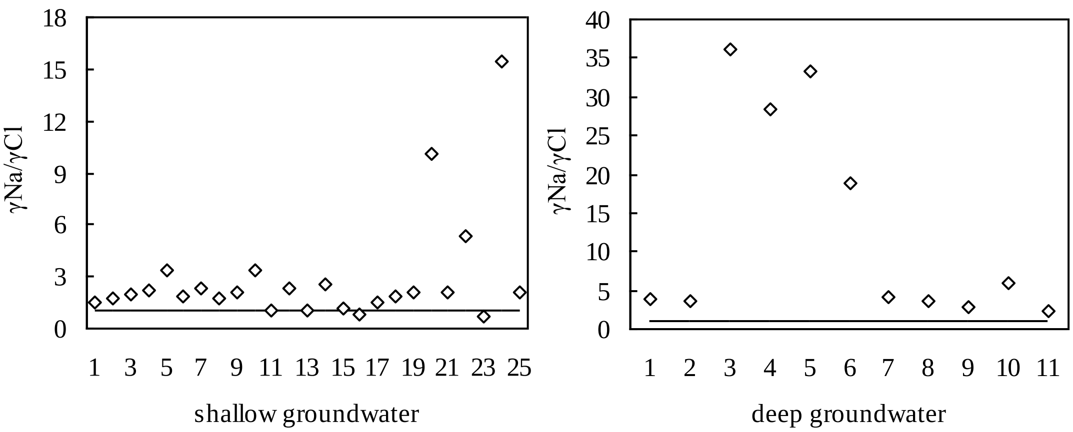

Figure 2. Scattergram of γNa/γCl values of groundwater.

mainly controlled by SO_4^{2-}, Cl^-, Ca^{2+}, Na^+ and Mg^{2+}. There are perfect positive correlations between Ca^{2+}, Mg^{2+} and SO_4^{2-}, Cl^-, which suggests that Ca^{2+} and Mg^{2+} are mainly from sulfate and chlorate. There is a strong positive correlation between Na^+ and Cl^-, which suggests that Na^+ and Cl^- are mainly from chlorate. There is also positive correlation between K^+ and NO_3^-, which demonstrates that they are from the same source (Dudeja et al., 2011). There is a strong positive correlation between TDS and Mg^{2+} and it also has some relationships with SO_4^{2-}. The effects of other indexes are relatively slight. All of the above results demonstrate that in the deep water TDS is mainly controlled by Mg^{2+} and SO_4^{2-}. Consistent with shallow water, there are perfect positive correlations between Ca^{2+}, Mg^{2+} and SO_4^{2-}, Cl^- in deep water. Different from shallow water, there is no positive correlation between Na^+ and Cl^-. There is also no relationship between K^+ and other ions in deep water.

Analysis of ion ratio coefficient

In the flow field of underground water, there is an organic relationship among the chemical compositions. The coefficients of proportionality between compositions are often used to study some chemical problems in hydrological earth (Anita and Gita, 2011). The MEq concentration ratio (γ_{Na}/γ_{Cl}) is called the genetic factor of underground water. It is a hydrogeochemical parameter to characterize the enriching of Na^+ (Chen et al., 2012). The average value of γ_{Na}/γ_{Cl} for seawater is 0.85. There is a higher value for low salinity water ($\gamma_{Na}/\gamma_{Cl}>0.85$) and a lower value for concentrated water ($\gamma_{Na}/\gamma_{Cl}<0.85$) (Aghazadeh and Mogaddam, 2011). In the shallow water of Tongchuan City, the γ_{Na}/γ_{Cl} value of γ_{Na}/γ_{Cl} is in the range from 0.75 to 15.41, with an average value of 2.90. Among them, most of the samples have a γ_{Na}/γ_{Cl} value of less than 1 (as shown in Figure 2) and only two samples are larger than 1. In deep water, the value of γ_{Na}/γ_{Cl} is in the range from 2.3 to 36.25, with an average value of 13.01. The values of all samples are larger than 1. Above results demonstrate that in the runoff process, the water is hydrolyzed and acidized, which releases Na^+ from soil and aquifers (Ahmad Dar et al., 2011). There is also ion exchange between Ca^{2+} from water and Na^+ from the soil, which results in $\gamma_{Na}>\gamma_{Cl}$. The value of γ_{Na}/γ_{Cl} is higher in deep water than that of shallow water, which may be caused by the long time lixiviation and replacing (Figure 3).

Research has demonstrated that the value of $\gamma_{Na}/(\gamma_{Na}+\gamma_{Cl})$ could reflect the exchange of positive ions. When the value is larger than 0.5, it means the exchange of positive ions happens. After the Na of soil and aquifers are replaced by Ca and Mg in water, it flows into underground water. The value of $\gamma_{Na}/(\gamma_{Na}+\gamma_{Cl})$ is in the range from 0.429 to 0.939, with an average value of 0.665. Among them, there are only two samples, whose value of $\gamma_{Na}/(\gamma_{Na}+\gamma_{Cl})$ is less than 0.5. In the deep water, the value of $\gamma_{Na}/(\gamma_{Na}+\gamma_{Cl})$ is in the range from 0.697 to 0.973, with an average value of 0.848. The values of all samples are larger than 0.5 and higher than that in shallow water. Above results demonstrate that there is different degree of cations exchange adsorption and the deep water has a relatively strong adsorption. This leads to the fact that with the increasing of depth the advantage ion turns to be Na^+ from Ca^{2+}.

As seen in Figure 4, the ratio of $\gamma_{HCO3}+\gamma_{SO4}$ and $\gamma_{Ca}+\gamma_{Mg}$ is close to 1. Above results demonstrate that the underground water is mainly from rainfall and the ions of Ca^{2+}, Mg^{2+} and HCO_3^- are mainly from the weathering dissolution of carbonate rock. The ratio of $\gamma_{HCO3}+\gamma_{SO4}$ and $\gamma_{Ca}+\gamma_{Mg}$ is larger than 1:1, which demonstrates that the contents of Ca^{2+} and Mg^{2+} have dramatically decreased.

Classification of underground water

According to the classification method of Shug Kalev, the

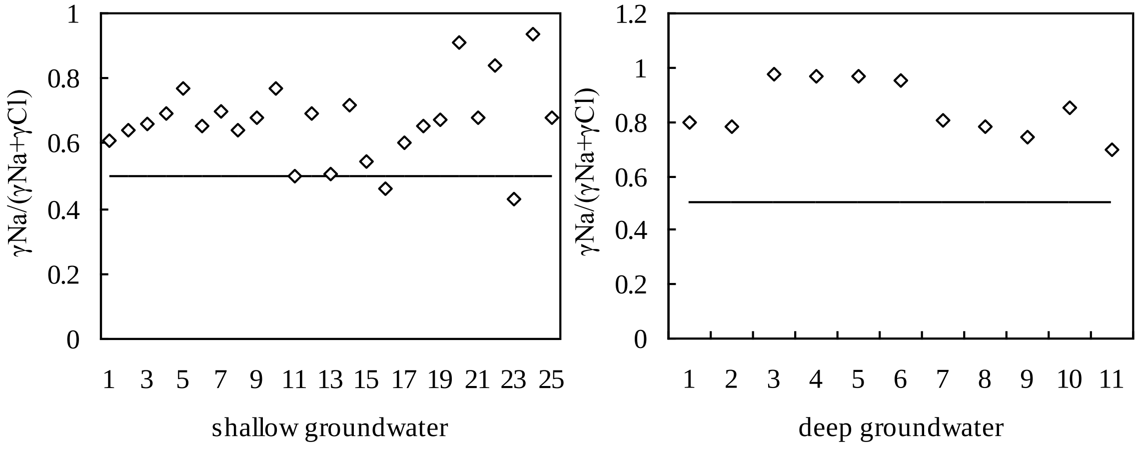

Figure 3. Scattergram of γNa/(γNa+γCl) values of groundwater.

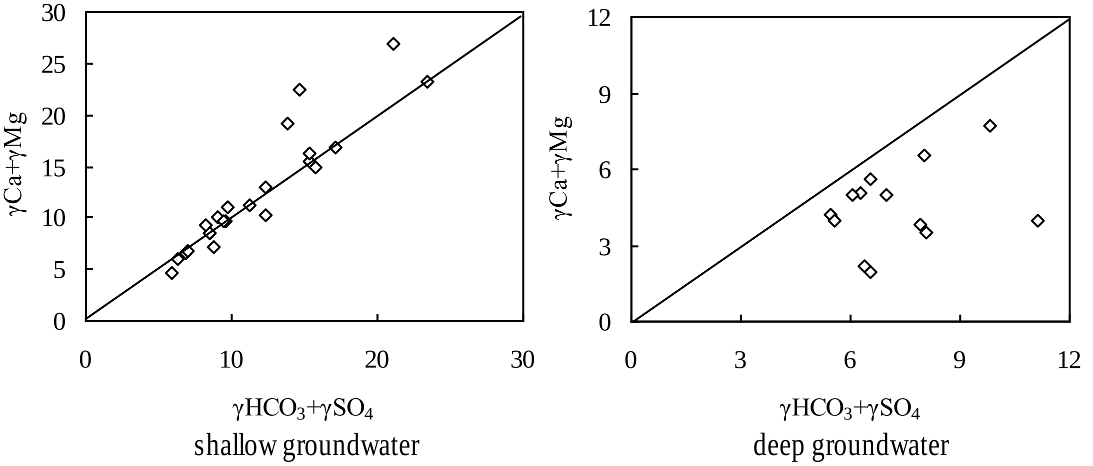

Figure 4. Scattergram of ($\gamma HCO_3+\gamma SO_4/\gamma Ca+\gamma Mg$) values of groundwater.

samples of underground water in Tongchuan City can be divided into 22 types as shown in Table 3. There are various categories of hydrochemical types. Among them, the type $HCO_3 \cdot SO_4$-Ca accounts for the largest proportion, which is 10.26% of the samples (4 samples). For other samples, HCO_3-Ca·Na·Mg, HCO_3-N and $HCO_3 \cdot SO_4$-Ca·Na·Mg accounts for 7.69% proportion (3 samples). There are 15 kinds of water samples in shallow water. The type of $HCO_3 \cdot SO_4$-Ca accounts for the largest proportion, followed by HCO_3-Ca, HCO_3-Ca·Mg, $HCO_3 \cdot SO_4$-Ca·Na, $HCO_3 \cdot SO_4$-Ca·Na·Mg, SO_4-Ca, SO_4-Ca·Mg and $SO_4 \cdot HCO_3$-Ca water types. There are 10 kinds of water types in deep water, with type HCO_3-Na as the largest. Then, they are HCO_3-Ca·Na·Mg and HCO_3-Ca·Na type water as shown in Table 3. We can conclude that the types of water chemistry of shallow groundwater are complex and the deep water is relatively simple. Generally, the hydrochemical types of shallow water are simpler than that of deep water. This is caused by the longer time of leaching and replacing, which makes the composition of water more complex. The adverse consequences are caused by the contamination of shallow water.

Features of the hydrochemical evolution

We obtained the Piper trilinear chart using software of ‘information system of groundwater pollution investigation’ as seen in Figure 5. It can be concluded that there are obvious differences in the chart of shallow and deep waters. In the shallow water, the positive ions mainly consist of Ca^{2+} and the concentration of Na^+ and K^+ are relative low. In deep water, the positive ions mainly consist of Na^+ and K^+. The concentration of Mg^{2+} and Ca^{2+} are relative low. The negative ions of shallow water

Table 3. Hydrochemical type of groundwater.

Hydrochemical type		Sample number	Ratio (%)
Shallow groundwater	$HCO_3\cdot SO_4$-Ca	4	16
	HCO_3-Ca	2	8
	HCO_3-Ca·Mg	2	8
	$HCO_3\cdot SO_4$-Ca·Na	2	8
	$HCO_3\cdot SO_4$-Ca·Na·Mg	2	8
	SO_4-Ca	2	8
	SO_4-Ca·Mg	2	8
	$SO_4\cdot HCO_3$-Ca	2	8
	HCO_3-Ca·Na·Mg	1	4
	$HCO_3\cdot SO_4$-Ca·Mg	1	4
	$HCO_3\cdot SO_4$-Na·Mg	1	4
	$SO_4\cdot$Cl-Ca	1	4
	$SO_4\cdot Cl\cdot HCO_3$-Mg·Ca	1	4
	$SO_4\cdot HCO_3$-Ca·Mg	1	4
	$SO_4\cdot HCO_3$-Ca·Na	1	4
Deep groundwater	HCO_3-Na	3	21.43
	HCO_3-Ca·Na·Mg	2	14.29
	HCO_3-Ca·Na	2	14.29
	HCO_3- Mg·Na·Ca	1	7.14
	HCO_3- Mg·Ca·Na	1	7.14
	HCO_3-Na·Mg	1	7.14
	HCO_3-Na·Ca	1	7.14
	$HCO_3\cdot SO_4$-Na·Ca·Mg	1	7.14
	$HCO_3\cdot SO_4$-Na·Mg	1	7.14
	$HCO_3\cdot SO_4$-Ca·Na·Mg	1	7.14

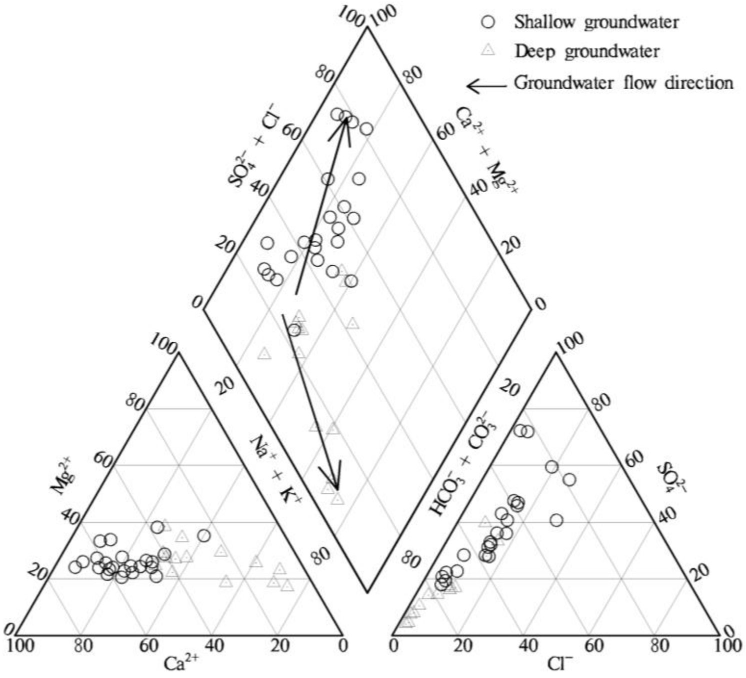

Figure 5. The piper diagram for the groundwater samples.

mainly consist of HCO_3^- and SO_4^{2-}. The concentration of Cl^- is relatively low. In deep water, the negative ions mainly consist of HCO_3^- and the concentration of Cl^- and SO_4^{2-} are relatively low. Along the direction of flow, the change of negative ions in deep water is not obvious. The ratio of positive ions increases and the concentration of Ca^{2+} and Mg^{2+} decrease. With the increase of runoff channels, the Na^+ in water-bearing media has exchanged with Ca^{2+} and Mg^{2+} in water. The type of underground water turns to be HCO_3-Na from HCO_3-Mg·Ca·Na and HCO_3-Ca·Na. Along the direction of flow, there is no obvious exchange in the positive ions of shallow water and the change of negative ions are obvious. With the increasing of SO_4^{2-}, the concentration of HCO_3^- decreases and the concentration of Cl^- is almost the same. The increasing of SO_4^{2-} means the contamination is more serious along the flow, which has a relationship with the city and industrial zone in the downstream region. The types of water turn to SO_4-Ca·Mg, SO_4·HCO_3-Ca·Na from HCO_3-Ca, HCO_3-Ca·Mg.

Generally, as for underground water, the containment of alkaline earth metal is larger than that of alkali metal. For the deep water, the containment of weak acid is larger than that of strong acid. In the upstream area, both the carbonate hardness of shallow and deep waters are higher than 50%. The feature of water is mainly weak acid and alkaline earth metal, which suggests that the formation of water is mainly from carbonate leaching. With the flowing of water, carbonate hardness of deep water becomes higher than 50% and the content of alkali metal is larger than alkaline earth metal. The underground water changes into weak acid and alkali metal.

Distribution characteristics of hydrochemical type

The underground water of North Ziwuling mountain area is mainly bedrock fissure water. The most common type of water is HCO_3·SO_4-Ca. In this area, the water is mainly provided by atmospheric precipitation. The runoff is beyond compare and the stay time is relatively short in aquifer. The water is easy to exchange with the environment and the soluble components, such as Cl^-, Na^+ and K^+. Most of the ions are Ca^{2+}, HCO_3^- and SO_4^{2-}, which can form the water type of HCO_3·SO_4-Ca. The underground water of Qishui River Valley Area, from south Zhifang to stream outlet, is alluvium pore water. From upstream to downstream, the water type changes into HCO_3·SO_4-Ca·Na from HCO_3·SO_4-Ca. Especially, the composition of some areas are complex and the water type is HCO_3·SO_4-Ca·Na·Mg. The contents of negative ions are relatively stable and the concentration of Na^+ gradually increases. The value of TDS is also increased. The underground water of Wang River Valley, from south Aipu village to stream outlet, is shallow fissure water. From upstream to downstream, the water type changes into SO_4·HCO_3-Ca·Mg from HCO_3·SO_4-Ca. There is an increase in the concentration of SO_4^{2-} and Mg^{2+}. The TDS rises from 621.1 to 1318 mg/L. The underground water of Guangyang River Valley, west of Guangyang town, is alluvium pore water. From upstream to downstream, the water type changes into SO_4·HCO_3-Ca·Mg from HCO_3-Ca. There is a gradual increase in the concentration of SO_4^{2-} and Mg^{2+}. The TDS rises from 458.4 to 1586 mg/L. The underground water of southern Sichuan area is mainly alluvial pore water. Most of the water is deeply confined water and the water type is mainly HCO_3-Na. The underground water of valley area is mainly HCO_3-Ca·Na·Mg. The type of underground water is simplex. The TDS is in the range from 400 to 600 mg/L. The concentration of Na^+ is high, which is mainly affected by loess components. The water yield for gully region of Loess Plateau is small. The sample is relatively shortage. After reading papers, we know that the water type is mainly HCO_3-Ca·Mg. There are other types, such as HCO_3·SO_4-Na·Mg, HCO_3-Mg·Ca·Na, HCO_3-Mg·Na·Ca and SO_4·HCO_3-Ca. The negative ions are mainly HCO_3^-. The sample of karst water is in relative shortage. After reading papers, we conclude that the water types are mainly HCO_3·SO_4-Na·Ca·Mg and HCO_3·SO_4-Ca·Na·Mg. The water type of Ju and Qishui Rivers are both HCO_3·SO_4-Ca. There are close connections between the water and shallow water, which is an important reason for the high concentration of SO_4^{2-}. It is also the source of SO_4^{2-} in karst water. Recently, with the exacerbating of contamination, the name of some area stems from its region. When considering hydrogen nitrate using the method of Shug Kalev, there are six groups of samples that belongs to hydrogen nitrate types. Telling from the distribution, it is mainly focused on the area of southern Chuanyuan and the area along the QI River. The area of southern Chuanyuan is the main farmland area. Compared with loess tableland, it has more water and the land has more fertilizer. The pollution is more serious than that of loess tableland. Above factors may act as the reasons for the forming of hydrogen nitrate type.

Conclusion

The salinization of shallow underground water in Tongchuan City is determined by the SO_4^{2-}, NO_3^-, Cl^- and K^+. In deep water, the contents of SO_4^{2-}, NO_3^-, Cl^- are largely different and other indexes are relatively stable. The values of γ_{Na}/γ_{Cl} demonstrate that the process of runoff makes the Na^+ release from soil and aquifer and there is exchange between the Ca^{2+} in water and Na^+ in soil, which leads to $\gamma_{Na}>\gamma_{Cl}$. Due to long time leaching and replacing, the cation exchange adsorption is very sufficient in deep water. This leads to a higher γ_{Na}/γ_{Cl} value than that of shallow water. The value of $\gamma_{Na}/(\gamma_{Na}+\gamma_{Cl})$ demonstrates that with the increasing of underwater depth, the cation exchange adsorption increases, which leads to the advantage ion change into Na^+ from Ca^{2+}. The ratio of $\gamma_{HCO3}+\gamma_{SO4}$ and $\gamma_{Ca}+\gamma_{Mg}$ demonstrates that the shallow water mainly stems from rainfall and the effects of cation exchange are more obvious in deep water.

The type of underground water in Tongchuan City is mainly $HCO_3 \cdot SO_4$-Ca. Its hydrochemical types are relatively complex. It is mainly HCO_3-Na in deep water. As for the shallow water, the content of weak acid is larger than that of strong acid. In the upstream area, the shallow water mainly consists of weak acid and alkaline earth metal. Its components are mainly carbonated leaching. With the flowing of water, the shallow water changes into strong acid and alkaline earth metal and the deep water change into weak acid and alkali metal.

Conflict of Interests

The author(s) have not declared any conflict of interests.

ACKNOWLEDGEMENT

The study was financially supported by project of Investigation and Evaluation of Groundwater Pollution in Major Cities of Northwest China (No.1212011220982).

REFERENCES

Ahmad Dar M, Sankar K, Imran AD (2011). Major ion chemistry and hydrochemical studies of groundwater of parts of Palar River basin, Tamil Nadu, India. J. Environ. Monit. Assess. 176(1-4):621-636. http://dx.doi.org/10.1007/s10661-010-1608-z; PMid:20886289

Anita J, Gita S (2011). Hydrochemical profile for assessing the groundwater quality of Sambhar Lake City and its Adjoining area J. Environ. Monit. Assess. 174(1-4):547-554. http://dx.doi.org/10.1007/s10661-010-1477-5; PMid:20559718

Chen JS, Sun XX, Gu WZ (2012). Isotopic and hydrochemical data to restrict the origin of the groundwater in the Badain Jaran Desert, Northern China. J. Geochem. Int. 50(5):455-465. http://dx.doi.org/10.1134/S0016702912030044

Dudeja D, Sukesh KB, Biyani AK (2011). Hydrochemical and water quality assessment of groundwater in Doon Valley of Outer Himalaya, Uttarakhand, India. J. Environ. Monit. Assess. 181(1-4):183-204. http://dx.doi.org/10.1007/s10661-010-1823-7; PMid:21229306

Florian L (2011). Ingrid Stober, Kurt Bucher. Hydrochemical Groundwater Evolution in the Bunter Sandstone Sequence of the Odenwald Mountain Range, Germany: A Laboratory and Field Study. J. Aquat. Geochem. 17(2):165-193.

Kshetrimayum KS, Bajpai VN (2012). Assessment of groundwater quality for irrigation use and evolution of hydrochemical facies in the Markanda River basin, northwestern India. J. Geol. Soc. India 79(2):189-198. http://dx.doi.org/10.1007/s12594-012-0024-0

Nosrat A, Mogaddam AA (2011). Investigation of hydrochemical characteristics of groundwater in the Harzandat aquifer, Northwest of Iran. J. Environ. Monit. Assess. 176(1-4):183-195. http://dx.doi.org/10.1007/s10661-010-1575-4; PMid:20625825

Ravikumar P, Venkatesharaju K, Somashekar RK (2010). Major ion chemistry and hydrochemical studies of groundwater of Bangalore South Taluk, India J. Environ. Monit. Assess. 163(1-4):643-653. http://dx.doi.org/10.1007/s10661-009-0865-1; PMid:19415520

academicJournals

Vol. 9(9), pp. 352-356, 15 May, 2014
DOI: 10.5897/SRE2014.5915
Article Number: B8A1C8344555
ISSN 1992-2248 © 2014
Copyright©2014
Author(s) retain the copyright of this article
http://www.academicjournals.org/SRE

Scientific Research and Essays

Full Length Research Paper

Calculating cyan-magenta-yellow-black (CMYK) printer' gray component data based on polynomial modeling

Sun Bangyong[1,2]*, Liu Han[2] and Zhou Shisheng[2]

[1]School of Printing and Packaging Engineering, Xi'An University of Technology, Xi'an 710048, China.
[2]School of Automation and Information Engineering, Xi'An University of Technology, Xi'an 710048, China.

Received: 3 January, 2013 ; Accepted 2 March, 2013

As gray color data is very important for printing quality, a method based on polynomial modeling is proposed to calculate the gray color data of different lightness. Firstly, the IT8.7/3 color target which defines input cyan-magenta-yellow-black (CMYK) signals is printed, and the corresponding CIELAB (Commission Internationale de l'Eclairage L*, a* and b*) values are obtained by a spectrophotometer with color sensors. Secondly, the polynomial regression method is used to determine the relationship between these two color spaces, in which the given CIELAB color's CMY value is calculated. At last, as the obtained cyan-magenta-yellow (CMY) gray color may contain Chroma information due to the computational error, a new color target is developed to find the real gray colors based on the relationship above, and the final relationship between CIE-L* and CMY are obtained. In the experiment, the average color error is 2.65ΔE, which is below the printing error threshold, hence the proposed algorithm for calculating gray color data can be used in printing process.

Key words: Gray balance, polynomial modeling, CIELAB (Commission Internationale de l'Eclairage L*, a* and b*) color, color sensors.

INTRODUCTION

The primary colors within subtractive imaging are cyan (C), magenta (M), yellow (Y). When combination of certain percentage of C, M, Y are printed, they produce color black (K). In printing or textile industry, cyan-magenta-yellow-black (CMYK) is often the primary color where K is used to replace a quantity of C, M and Y. There are many advantages with color K, such as the high color density, good color contrast, big gamut volume, low cost and so on.

When K color is used to replace certain amount of CMY, a black replacement algorithm is commonly used, which determines the correspondence between K and combination of C, M, and Y. Now there are mainly two kinds of black replacement algorithms, GCR (gray component replacement) and UCR (under color removal) (Guo et al., 2011). It is very important to determine the relationship between the CMY and K, because the black ink has no Chroma, the issues turns into finding the same lightness between the K color and the combination of C, M and Y. In color science, the CIELAB space is independent of the color device, thus it is often used to connect the device color space. For CMYK printers,

---

*Corresponding author. E-mail: sunbangyong@xaut.edu.cn

during the process of calculating gray color data, the CIE-L* can be selected to link the CMY and K, where the combination of C, M, Y colors and the K color correspond to CIE-L* value.

During the conversion between CIELAB and CMY colors, the color targets has to be used which includes many color patches (Fashandi et al., 2010). For example the IT8.7/3 target has 928 color patches, and ECI2002 has 1485 patches. In this paper, the former target is employed for gathering sample data; and then six gray colors with different CIELAB values are used for calculating CMY values; at last, taking into account the conversion errors, the calculated CMY values may present some Chroma after printing; a new gray color target is developed to modify the CMY values.

In general, the process of converting colors from CMY to CIELAB can be defined as characterization (Lee and Lee, 2013), while the contrary process is often called calibration (Yang et al., 2012); obviously the paper mainly interests the latter process. Now the commonly used calibration algorithms are 3D interpolation (Pekkucuksen and Altunbasak, 2013; Liu et al., 2013; Srivastava et al., 2010), polynomial regression (Hong et al., 2001; Nussbaum et al., 2011), neural network (Kang and Anderson, 1992; Hwang et al., 2013), Neugebauer equations (Morovic et al., 2012; Hebert and Hersch Roger, 2011), and so on. Taking into account the quantity of color patches, the precision and computing efficiency of the algorithms, polynomial regression modes is selected in this paper.

POLYNOMIAL REGRESSION MODEL

During the printer calibration process, the standard color target IT8.7/3 is firstly printed out. Among the 928 color patches most of them are not gray colors, hence it is hard to find the CMY patches which contain none Chroma information. Within the IT8.7/3 target, there are 216 CMY patches and each of their area coverage ranges within 0, 10, 20, 40, 70 and 100%; their CIELAB values can be measured by the spectrophotometer X-Rite 530 with color sensors. In experiment, the 216 color patches' CMY and CIELAB values form the training sample data. Then the relationship between CIELAB and CMY can be obtained by polynomial regression model.

In the process of calculating gray color data, the training sample data is generally less than regular color device calibration process. Because the polynomial regression model can obtain acceptable accuracy with less sample data, and it take less simulation time than neural network, it is used to calculate the gray color data.

Within the polynomial regression method, the relationship between independent variable x and dependent variable f(x) can be modeled as an nth degree polynomial as below.

$$f(x)=\alpha_0+\alpha_1 x+\alpha_2 x^2+\alpha_3 x^3+...+\alpha_n x^n \tag{1}$$

where the coefficients α and the degree of x are selected reasonably, the complicated relationship between x and f(x) can be described accurately. As the CMY and CIELAB color have three variables respectively, the three-variable polynomials of different degrees are used.

$$f(x,y,z)=\sum_{i=1}^{n}\sum_{j=1}^{n}\sum_{k=1}^{n}a_{ijk}x^i y^j z^k \tag{2}$$

where i+j+k≤n, αijk are the coefficients, x, y, z are the independent variables. For example, when the 2nd degree polynomial are selected, the given CIELAB color's corresponding CMY values can be expressed as:

$$\begin{aligned}
&C(L^*,a^*,b^*)=\alpha_0+\alpha_1 L^*+\alpha_2 a^*+\alpha_3 b^*+\alpha_4 L^* a^*\\
&+\alpha_5 a^* b^*+\alpha_6 L^* b^*\\
&M(L^*,a^*,b^*)=\beta_0+\beta_1 L^*+\beta_2 a^*+\beta_3 b^*+\beta_4 L^* a^*\\
&+\beta_5 a^* b^*+\beta_6 L^* b^*\\
&Y(L^*,a^*,b^*)=\gamma_0+\gamma_1 L^*+\gamma_2 a^*+\gamma_3 b^*+\gamma_4 L^* a^*\\
&+\gamma_5 a^* b^*+\gamma_6 L^* b^*
\end{aligned} \tag{3}$$

Therefore, when the coefficient α, β, and γ are determined, the CMY values can be calculated. The calculation of polynomial regression coefficients are usually based on the least squares method, which minimizes the variance of the unbiased estimators of the coefficients, under the conditions of the Gauss–Markov theorem. When enough samples are supplied, the coefficients of Equation 2 can be calculated as below:

$$U=(VV^T)^{-1}(VP) \tag{4}$$

where U is the coefficient matrix, P is the CMY sample data matrix, V is the CIELAB sample data matrix. If the sample matrix V's size is m×n, where m is the number of polynomial items, n is the number of sample points, to ensure U can be resolved, the requirement of n>m must be satisfied.

EXPERIMENTAL RESULTS

In the experiment, the color target IT8.7/3 is printed out on a 120 g copper paper by the HP Indigo5500 printer, and the spectrometer X-Rite 530 is used to measure CIELAB values. Within the measured results for the sample data of 216 CMY colors, the maximal and minimal CIE-L* values are 94 and 21 respectively. Between these two lightness, another six CIELAB colors are selected to calculate the CMY values which form gray colors. By using the relationship between CMY and CIELAB calculated with polynomial modeling, the six gray colors' CMY and CIELAB values are obtained below.

As there are solving errors within the polynomial modeling, the directly calculated gray color data may be inconsistent with the actual gray data. For example, within the second gray color in Table 1, the calculated CMY is (70, 60, 59) for the CIELAB value (40, 0, 0), but when the CMY color is sent to the printer, the printed color' CIELAB value is (39, -1, 0). Therefore a new testing target similar to GrayFinder19 is developed according the color data in Table 1. As shown in Figure 1, six groups of low-Chroma patches are arranged, and the center patch's

Table 1. The preliminary calculated gray colors by polynomial modeling.

No.	CIELAB	CMY
1	(21,0,0)	(100, 100,100)
2	(40,0,0)	(70,60,59)
3	(50,0,0)	(60,50,48)
4	(60,0,0)	(50,40,38)
5	(65,0,0)	(42,32,31)
6	(75,0,0)	(30,22,20)
7	(85,0,0)	(20,12,11)
8	(94,0,0)	(0,0,0)

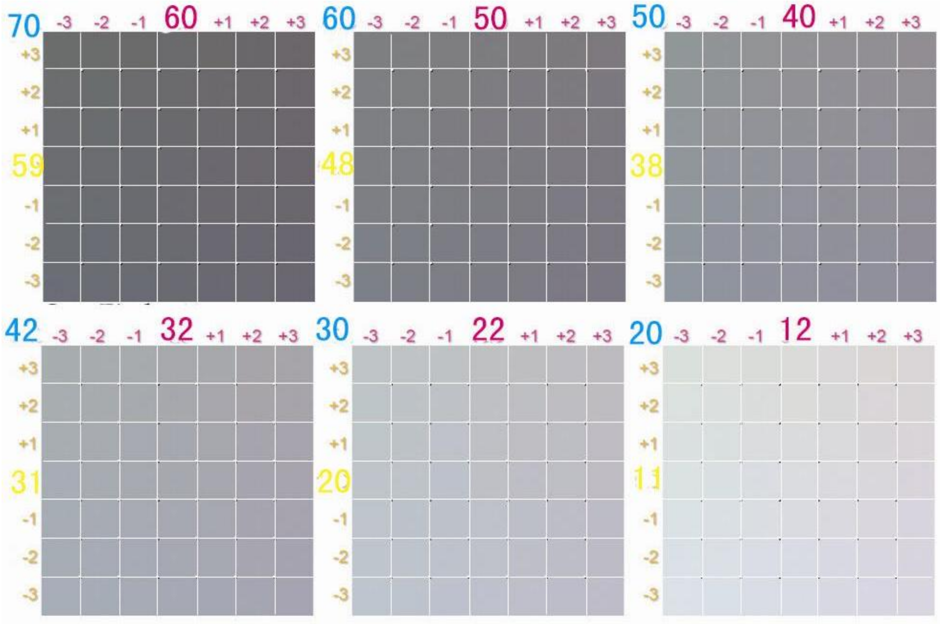

Figure 1. The gray target used for finding real gray colors.

Table 2. Gray colors by reprinting and measuring.

No.	CIELAB	CMY
1	(21, 0, 0)	(100, 100, 100)
2	(39, 0, 0)	(70, 61, 59)
3	(49, 0, 0)	(60, 52, 49)
4	(61, 0, 0)	(50, 39, 37)
5	(65, 0, 0)	(42, 31, 31)
6	(74, 0, 0)	(30, 21, 20)
7	(86, 0, 0)	(20, 11, 10)
8	(94, 0, 0)	(0, 0, 0)

CMY value is from the data of Table 1. Taking the first group for example, the center patch's CMY is (70, 60, 59), and all the patches' C values remains unchanged, while the left patches' M values are 60-1, 60-2, 60-3 respectively, the right patches' M values are 60+1, 60+2, 60+3; similarly the upper patches' Y value are 59+1, 59+2, 59+3, and the underneath patches' Y are 59-1, 59-2, 59-3.

When the gray target is printed out and measured, the real gray colors can be found with CIE-a* =0 and CIE-b*=0. Finally, the real gray colors' CIE-L* and CMY are obtained in Table 2.

With this gray color data above, the relationship between CIE-L* and CMY are determined, and any given lightness gray color' CMY can be simulated. The fourth-degree polynomial is used to calculate the CMY values (Figure 2).

$$\begin{aligned} C(L^*) &= \alpha_0 + \alpha_1 L^* + \alpha_2 L^{*2} + \alpha_3 L^{*3} + \alpha_4 L^{*4} \\ M(L^*) &= \beta_0 + \beta_1 L^* + \beta_2 L^{*2} + \beta_3 L^{*3} + \beta_4 L^{*4} \\ Y(L^*) &= \gamma_0 + \gamma_1 L^* + \gamma_2 L^{*2} + \gamma_3 L^{*3} + \gamma_4 L^{*4} \end{aligned} \tag{5}$$

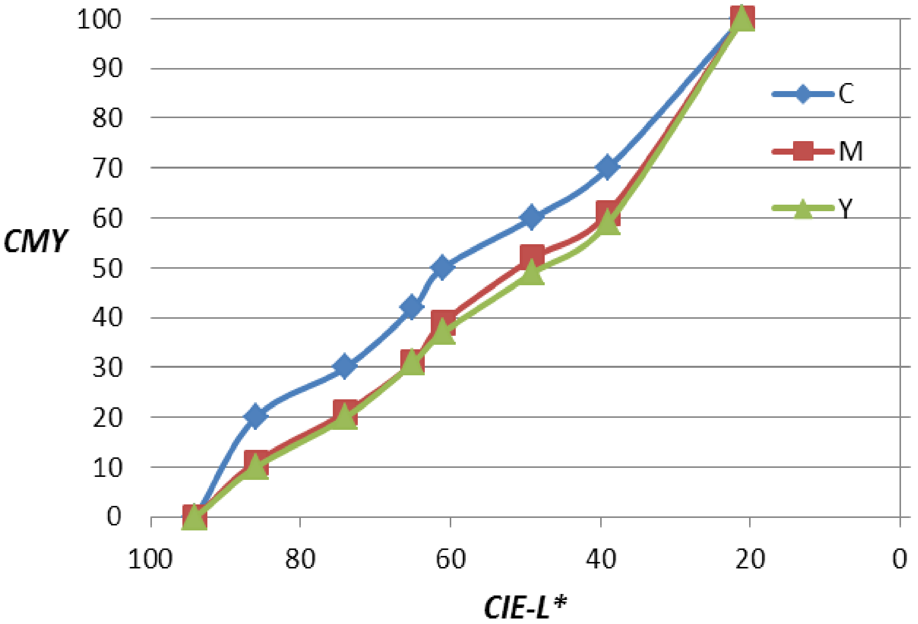

Figure 2. The gray color data curves.

From Equation 5, the gray data curve for lightness L* from 21 to 94 are described from the scattered data below.

For the purpose of testing the accuracy of the obtained gray color data, twenty testing patches were created to calculate the color errors. Firstly, twenty CIELAB gray colors were randomly selected between the maximal and minimal lightness (CIE-a*=0 and CIE-b*=0); secondly, for the given CIE-L* values, the corresponding CMYs are calculated according to the Equation 5; finally, these CMYs are printed out and measured with the new CIELAB values obtained. To test the errors, the two groups of CIELAB values are compared using the CIEDE76 color difference formula. For all testing colors, the average error is 2.65ΔE with the maximal error 5.2ΔE. Because for most of the printing process, the average error threshold is 5ΔE, the experiment result in the paper is acceptable, which indicates polynomial regression modeling is suitable for gray color calculations.

Conclusions

The calculation of CMY gray color data is essential for color reproduction including scanning, proofing, and printing process. If the CMY gray color data is not accurate, the gray images will show some Chroma information in the highlights, mid-tones, or shadows. In this paper, a method of finding gray color data based on polynomial modeling is proposed, which can be used in UCR/GCR algorithms. In this experiment, 20 testing gray colors were used to calculate CMY values, and the result shows the accuracy is acceptable.

Conflict of Interests

The author(s) have not declared any conflict of interests.

ACKNOWLEDGEMENTS

This work is supported by: The Natural Science Foundation of Education Department in Shan'Xi Province (No. 11JK0541), Doctor Foundation of Xi'an University of Technology (104-211302), "13115" Creative Foundation of Science and Technology, Shaanxi Province of China.

REFERENCES

Fashandi H, Amirshahi SH, Tehran MA (2010). Evaluation of Scanner Capability for Measuring the Color of Fabrics with Different Textures in Different Setups. Fibers Polym. 11(5):767-774. http://dx.doi.org/10.1007/s12221-010-0767-4

Guo J, Xu H, Luo MR (2011). Spectral characterisation of colour printer based on a novel grey component replacement method. Chin. Optics Lett. 9(7):073301. http://dx.doi.org/10.3788/COL201109.073301

Hebert M, Hersch RD (2011). Yule-Nielsen based recto-verso color halftone transmittance prediction model. Appl. Optics. 50(4):519-525. http://dx.doi.org/10.1364/AO.50.000519; PMid:21283243

Hong GW, Luo MR, Rhodes PA (2001). A study of digital camera colorimetric characterization based on polynomial modeling. Color Res. Appl. 26(1):76-84. http://dx.doi.org/10.1002/1520-6378(200102)26:1<76::AID-COL8>3.0.CO;2-3

Hwang C-L, Lu K-D, Pan Y-T (2013). Segmentation of Different Skin Colors with Different Lighting Conditions by Combining Graph Cuts Algorithm with Probability Neural Network Classification, and its

Application. Neural Process. Lett. 37(1):89-109. http://dx.doi.org/10.1007/s11063-012-9275-4

Kang HR, Anderson G (1992). Neural network application to color scanner and printer calibrations. J. Electron. Imag. 1(2):125-135. http://dx.doi.org/10.1117/12.57526

Lee K-J, Lee B-W (2013). Estimation of rice growth and nitrogen nutrition status using color digital camera image analysis. Eur. J. Agron. 48:57-65. http://dx.doi.org/10.1016/j.eja.2013.02.011

Liu Q, Wan X-X, Xu H-P (2013). Study on Ink Restriction of Ink-Jet Printing Based on Spectral Gamut Maximization. Spectrosc. Spectral Analys. 33(6):1636-1641.

Morovic J, Morovic P, Arnabat J (2012). HANS: Controlling Ink-Jet Print Attributes Via Neugebauer Primary Area Coverages. IEEE Trans. Image Process. 21(2):688-696. http://dx.doi.org/10.1109/TIP.2011.2164418; PMid:21846605

Nussbaum P, Hardeberg JY, Albregtsen F (2011). Regression based characterization of color measurement instruments in printing applications. Conference on Color Imaging XVI - Displaying, Processing, Hardcopy, and Applications, Proceedings of SPIE. San Francisco, CA. 7866:78661R.

Pekkucuksen I, Altunbasak Y (2013). Multiscale Gradients-Based Color Filter Array Interpolation. IEEE Trans. Image Process. 22(1):157-165. http://dx.doi.org/10.1109/TIP.2012.2210726; PMid:22868571

Srivastava S, Delp EJ, Ha TH, Allebach J (2010). Color Management Using Optimal Three-Dimensional Look-Up Tables. J. Imag. Sci. Technol. 54(3):030402. http://dx.doi.org/10.2352/J.ImagingSci.Technol.2010.54.3.030402

Yang F, Murakami Y, Yamaguchi M (2012). Digital color management in full-color holographic three-dimensional printer. Appl. Optics. 51(19):4343-4352. http://dx.doi.org/10.1364/AO.51.004343; PMid:22772106

academicJournals

Vol. 9(9), pp. 357-361, 15 May, 2014
DOI: 10.5897/SRE2014.5916
Article Number: 63ADC3044558
ISSN 1992-2248 © 2014
Copyright©2014
Author(s) retain the copyright of this article
http://www.academicjournals.org/SRE

Scientific Research and Essays

Full Length Research Paper

The reliability test assessment of three-parameter Weibull distribution of material life by Bayesian method

Xintao Xia, Yuanyuan Qin*, Yinping Jin and Ming Qiu

School of Mechatronical Engineering, Henan University of Science and Technology, Luoyang 471003, China.

Received: 3 January, 2013; Accepted 2 March, 2013

This paper is mainly according to Bayesian formula and using Bayesian method to estimate parameter truth-values of three-parameter Weibull distribution to achieve material reliability evaluation. The parameter values estimated by maximum likelihood method as the prior information of Bayesian estimation, assume that the parameter obeys a certain distribution and let the certain distribution as the prior distribution of parameter, and the three-parameter Weibull distribution is known, so the posterior distribution function of the parameter can be obtained. According to Bayesian estimation, the maximum posteriori estimation is chosen as the truth-value of the estimated parameter, the lifetime data are substituted into the truth-value estimated function of reliability and the theoretical values of the reliability can be got. Case study shows that the Bayesian method has general applicability to the material reliability evaluation.

Key words: Material lifetime, test assessment, three-parameter Weibull distribution, Bayesian method.

INTRODUCTION

Material is the foundation and the forerunner of modern high-new technology and industry. For example, as the aerospace and trains material research and innovation, the space industry and transportation industry etc have rapid development, to ensure that the components are reliable, high demands are put forward about material properties and the use efficiency. The material reliability research has become one of the hot issues in recent years.

There are many results about the material reliability research at home and abroad. For examples, Kasprzyk (2005) mainly discussed to improve the reliability and performance of the non-metallic materials, enhance the utilization of non-metallic materials; Johnsen and Nyhus (2007) adopted the method of reliability test to ensure eligibility and safety use of stainless steel materials; Wang et al. (2008) through research show that coating materials affect the reliability of the sample; Xu et al. (2012) by raising the casting material performance, optimized the casting process, to ensure the reliability of the casting use, which is now in the CRH2, CRH380A type trains of application. The material reliability method was used to research the above, thereby effectively enhancing the applicability and reliability of materials.

Material life is the main factor that influences the reliability of the components used, and according to the material life data, to study the material use reliability is also very necessary. In this paper with three-parameter

---

*Corresponding author. E-mail: aiyuan275685336@163.com

Weibull distribution as the reliability model of the material life, Bayesian method is used to estimate the parameters of three-parameter Weibull model, and then the reliability evaluation of material was carried out. So far, the effective parameter estimation methods mainly have the bootstrap weighted-norm method (Xia et al., 2013), maximum likelihood method (Yan et al., 2005), random number method (El-Adll, 2011), moments and probability weighted moment method Paul-Dario and Thomas, 2011; Deng et al., 2004; Zhao et al., 2010), dual-linear regression method (Zhuang, 1999), correlation coefficient optimization method (Richard and Stepnens, 1993) etc. Because Bayesian method (Mao, 1999) has obvious superiority on the basis of the theory, Sinha and Sloan (1988) and Qin et al. (1988) have introduced application of Bayesian method to the Weibull model. This paper mainly discussed the application of Bayesian method in material reliability evaluation.

THREE-PARAMETER WEIBULL DISTRIBUTION

The three-parameter Weibull distribution is defined as:

$$f(t;\eta,\beta,\tau)=\frac{\beta}{\eta}\left(\frac{t-\tau}{\eta}\right)^{\beta-1}\exp\left(-\left(\frac{t-\tau}{\eta}\right)^{\beta}\right),\qquad (1)$$
$$t\ge\tau>0,\quad \beta>0,\quad \eta>0$$

where, $f(t;\eta,\beta,\tau)$ is the three-parameter Weibull distribution, t is a stochastic variable of the lifetime, (η,β,τ) are the Weibull parameters, η is the scale parameter, β is the shape parameter, and τ is the location parameter.

The reliability function with the three-parameter Weibull distribution can be expressed as:

$$R(t;\eta,\beta,\tau)=1-\int_{\tau}^{\infty}f(t;\eta,\beta,\tau)dt=\exp\left(-\left(\frac{t-\tau}{\eta}\right)^{\beta}\right)\qquad (2)$$

where, $R(t;\eta,\beta,\tau)$ is the reliability function with the three-parameter Weibull distribution.

For many products in engineering practice, the value of the Weibull parameter is unknown and needs to be found with the help of test evaluation. To this end, a lifetime experiment must be conducted. Assume that the lifetime data of a product are obtained by life tests as follows:

$$\mathbf{T}=\{t_i\},\quad t_1\le t_2\le\ldots\le t_i\le\ldots\le t_n,\quad i=1,2,\ldots,n\qquad (3)$$

where, $\mathbf{T}$ is the lifetime data vector, t_i is the ith lifetime datum in $\mathbf{T}$, i is the sequence number of t_i, and n is the number of the data in $\mathbf{T}$.

The lifetime data in $\mathbf{T}$ are substituted into Equation (2), and the theoretical value of the reliability can be calculated by

$$\mathbf{R}=\{R(t_i;\eta,\beta,\tau)\}\qquad (4)$$

where, $R(t_i;\eta,\beta,\tau)$ is the theoretical value of the reliability.

BAYESIAN METHOD

Maximum likelihood method is a widely used analytical method in parameter estimation. In this paper, let the values of the parameters solved by maximum likelihood method as a priori information of Bayesian estimation, be assumed to obey a certain distribution and let the certain distribution be the prior distribution; meanwhile, the three-parameter Weibull distribution is known, the posterior distribution function of the parameter finally can be obtained (Mao, 1999).

In parameter estimation, using the maximum likelihood method to estimate the truth-values of parameters not only can solve the likelihood equations but also can directly use optimization method to obtain the model parameter values when the logarithmic likelihood function achieve the maximum.

For complete data, the likelihood function of three-parameter Weibull distribution can be written as:

$$L(t_i;\eta,\beta,\tau)=\left(\frac{\beta}{\eta}\right)^{n}\left(\prod_{i=1}^{n}\left(\frac{t_i-\tau}{\eta}\right)\right)^{(\beta-1)}\exp\left[-\sum_{i=1}^{n}\left(\frac{t_i-\tau}{\eta}\right)^{\beta}\right]\qquad (5)$$

The logarithm likelihood function can be expressed as:

$$\ln\left[L(t_i;\eta,\beta,\tau)\right]=\ln\left(\frac{\beta}{\eta}\right)^{n}+(\beta-1)\sum_{i=1}^{n}\ln\left(\frac{t_i-\tau}{\eta}\right)-\sum_{i=1}^{n}\left(\frac{t_i-\tau}{\eta}\right)^{\beta}\qquad (6)$$

Calculate the partial differential of Equation (6) and let the partial differential equal to zero, so the equations can be written as follows:

$$\frac{\partial\ln\left[L(t_i;\eta,\beta,\tau)\right]}{\partial\eta}=-\frac{n\beta}{\eta}+\sum_{i=1}^{n}\left(\frac{\beta}{\eta}\left(\frac{t_i-\tau}{\eta}\right)^{\beta}\right)=0\qquad (7)$$

$$\frac{\partial\ln\left[L(t_i;\eta,\beta,\tau)\right]}{\partial\beta}=\frac{n}{\beta}+\sum_{i=1}^{n}\ln\left(\frac{t_i-\tau}{\eta}\right)-\sum_{i=1}^{n}\left(\left(\frac{t_i-\tau}{\eta}\right)^{\beta}\ln\left(\frac{t_i-\tau}{\eta}\right)\right)=0\qquad (8)$$

$$\frac{\partial\ln\left[L(t_i;\eta,\beta,\tau)\right]}{\partial\tau}=(\beta-1)\sum_{i=1}^{n}\left(-\frac{1}{t_i-\tau}\right)+\sum_{i=1}^{n}\left(\frac{\beta}{\eta}\left(\frac{t_i-\tau}{\eta}\right)^{(\beta-1)}\right)=0\qquad (9)$$

Use the iteration method to solve the Equations (7) to (9), and the estimated truth-values of the three parameters by maximum likelihood estimation can be obtained. The values of the three parameters are also written as (η_1,β_1,τ_1) .

Assumed that $\pi(\theta)$ is the prior distribution and $\theta=(\theta_1,\ldots,\theta_k)$ are the parameters of the model, $t=(t_1,\ldots,t_n)$ are the observations of a sample, and use $\pi(\theta;t)$ as the posterior distribution, $f(t;\theta)$ is the density function of sample, so according to Bayesian rule, the density function of Bayesian formula can be expressed as:

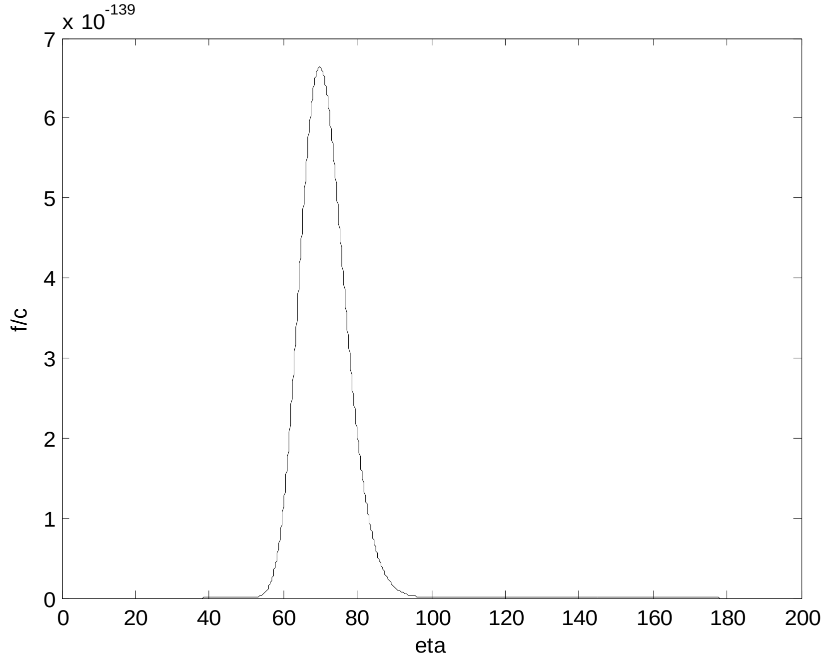

Figure 1. The Distribution of parameter η of the posterior distribution in ceramic material case.

$$\pi(\theta;t)=\frac{f(t;\theta)\pi(\theta)}{m(t)} \quad (10)$$

where, $m(t)=\int_{-\infty}^{+\infty} f(t;\theta)\pi(\theta)d\theta$.

The value θ_{MD} which makes the posterior density function $\pi(\theta;t)$ reach the maximum value called maximum posteriori estimation, is also called Bayesian estimation. In this paper, the maximum posteriori estimation θ_{MD} is the estimated truth-value of the parameter θ . The values of the three parameters by Bayesian method can be written as $\theta=(\eta_2,\beta_2,\tau_2)$.

CERAMIC MATERIAL CASE STUDY AND DISCUSSION

In life tests, Duffy et al. (1993) obtained the lifetime data (h) of aluminum oxide ceramics, as follows (*n*=35):

T= (307 308 322 328 328 329 331 332 335 337 343 345 347 350 352 353 355 356 357 364 371 373 374 375 376 376 381 385 388 395 402 411 413 415 456)

The three parameters truth-values of Weibull distribution estimated by maximum likelihood method are（69.8392,1.9708,300.0086）.

In Bayesian estimation, assume that the value of shape parameter β is 1.9708. It is know that τ is the location parameter. In this case, τ is the minimum lifetime and the scope of τ is $[0,307]$. A suitable value of τ chosed in the scope is 300. Only think that the scale parameter η is a random variable, assume the prior distribution of η is:

$$\pi(\eta)=C'\eta^3 e^{-0.043\eta}$$

where, C' is a constant. When the prior distribution gets maximum value, the value of scale parameter η is 69.8392.

For complete data:

$$f(t|\eta)=\left(\frac{\beta}{\eta}\right)^n\left(\prod_{i=1}^{n}\left(\frac{t_i-\tau}{\eta}\right)\right)^{(\beta-1)}\exp\left[-\sum_{i=1}^{n}\left(\frac{t_i-\tau}{\eta}\right)^{\beta}\right]$$

meanwhile, $m(t)=\int_{-\infty}^{+\infty} f(t;\eta)\pi(\eta)d\eta$. Let

$C=C'\frac{1}{m(t)}\beta^n\left(\prod_{i=1}^{n}(t_i-\tau)\right)^{(\beta-1)}$, the posterior distribution function of parameter to be estimated is formulated as:

$$\pi(\eta|t)=C\eta^{-65.978}\exp\left[-0.043\eta-\sum_{i=1}^{35}\left(\frac{t_i-300}{\eta}\right)^{1.9708}\right]$$

Where, C is a constant that it has no relation with η .

The maximum posteriori estimation of this distribution is $\hat{\eta}=69.8$. The distribution of η is a unimodal shape, as shown in Figure 1.

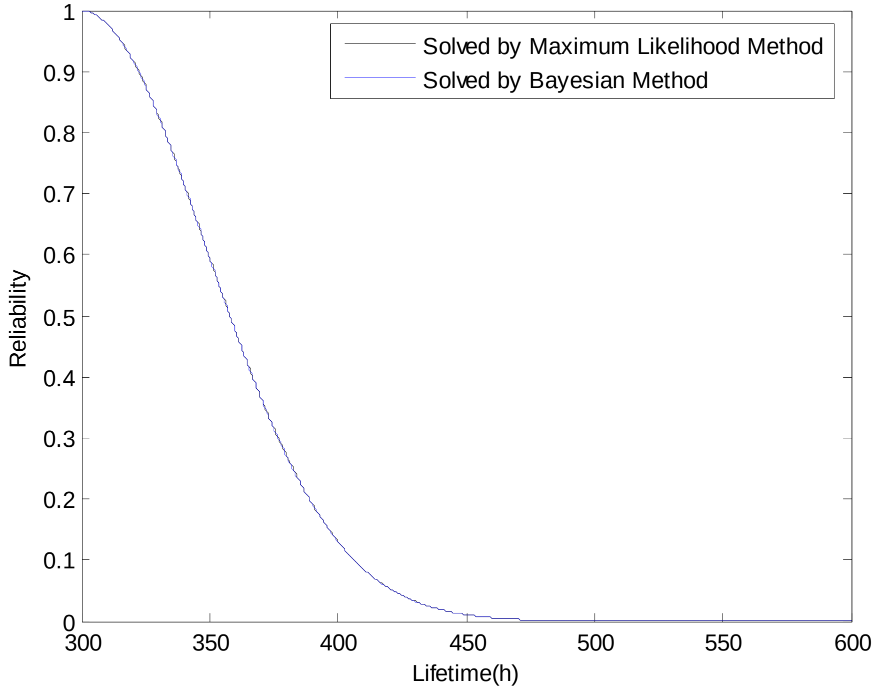

Figure 2. The theoretical value vectors of reliability in ceramic material case.

The three parameters truth-values of Weibull distribution estimated by Bayesian method is（$69.8,1.9708,300$）. Let the values of $(\eta_1, \beta_1, \tau_1)$ and $(\eta_2, \beta_2, \tau_2)$ are substituted into the three-parameter Weibull reliability function respectively, then the reliability truth-value functions can be gotten. The theoretical value vectors of reliability solved by the two methods are shown in Figure 2.

The $K-S$ test values of the reliability fitting models respectively gotten by maximum likelihood method and Bayesian method are 0.0547 and 0.0542. For a given confidence level $\alpha = 0.01$, look-up table can get the critical value $D_c = 0.26896$. The test values of the two methods are less than the critical value D_c that the three-parameter Weibull distribution models fitted by the two methods are appropriate. From Figure 2, we can see that the theoretical values vectors of the reliability $R(t_i; \eta, \beta, \tau)$ are obtained by the two methods are consistent in the overall.

Conclusions

The results of $K-S$ test in the case studied show that three-parameter Weibull distrubution model fitted by Bayesian method is better than the model fitted by maximum likelihood method. And a proper fitting model is more beneficial to assess and improve the reliability of the materials. The two methods to evaluate the reliability of the material are applicable. Although Bayesian method based on the theory has superiority, however, both are specific to a proper prior distribution and the numerical calculation which multiple parameter models will be involved are of considerable complexity.

Conflict of Interests

The author(s) have not declared any conflict of interests.

ACKNOWLEDGEMENTS

This project was funded by the National Natural Science Foundation of China (Grant No. 51075123) and the Foundation of Innovation and Research Team of Science and Technology in Universities in Henan Province (Grant No. 13IRTSTHN025).

REFERENCES

Deng J, Gu DS, Li XB (2004). Parameters and quantile estimation for fatigue life distribution using probability weighted moments. Chin. J. Comput. Mech. 21(5):609-613.

Duffy SF, Palko JL, Gyekenyesi JP (1993). Structural reliability analysis of laminated CMC components. J. Eng. Gas Turb. Power 115(1):103-108. http://dx.doi.org/10.1115/1.2906663

El-Adll ME (2011). Predicting future lifetime based on random number of three parameters Weibull distribution. Math. Comput. Simul. 81(9):1842-1854. http://dx.doi.org/10.1016/j.matcom.2011.02.003

Johnsen R, Nyhus B (2007). New improved method for hisc testing of stainless steels under cathodic protection. NACE - International Corrosion Conference Series, pp. 074961-0749620.

Kasprzyk MC (2005). The use of non-metallic materials in heat treating. Heat Treating Progress 5(5):40-42.

Qin M, SJ Wu, Peng X (1988). A reliability evaluation method for equipment with a Weibull failure Weibull Distribution. IEEE Trans. Reliab. 37(4):364-368.

Mao SS (1999). Bayesian statistics. Beijing: China Statistics Press.

Paul DTC, Thomas U (2011). General probability weighted moments for the three-parameter Weibull distribution and their application in S-N curves modeling. Int. J. Fatigue 33(12):1533-1538. http://dx.doi.org/10.1016/j.ijfatigue.2011.06.009

Richard AL, Stephens MA (1993). Estimation and test-of-fit for the three parameter Weibull distribution[R]. Technichal Report No.476. Stanford, Califomia.

Sinha SK, Sloan JAB (1988). Estimation of the Parameter Weibull Distribution. IEEE Trans. Reliab. 37(4):364-368. http://dx.doi.org/10.1109/24.9840

Wang M, Wu F, Su YF (2008). Electrochemical characteristics of Y2O3-coated LiCo1/3Ni1/3Mn1/3O2. Acta Physico-Chimica Sinica. 24(7):1175-1179.

Xia XT, Xu YZ, Jin YP, Shang YT, Chen L (2013). Assessment of optimum confidence interval of reliability with three-parameter Weibull distribution using bootstrap weighted-norm method. J. Aerospace Power 28(3);481-488.

Xu GB, Zhu ZF, Cao JF (2012). The research of material technology of the key casting steel of high-speed trains [C]. The Proceedings of China Railway Institute and Vehicle Commission Trains and Coach Academic Communication, pp. 177-181.

Yan XD, Ma X, Zheng RY (2005). Comparison of the Parameters Estimation Methods for 3-Parameter Weibull Distribution [J]. J. Ningbo Univ. (Natl. Sci. Eng. Edition), 18(3):301-305.

Zhao XP, Lv ZZ, Wang WH (2010). A Practical and Effective Method for Estimating Confidence Limits of Population Percentile and Reliability of Three-Parameter Weibull Distribution on Probability Weighted Moment. J. Northwestern Polytech. Univ. 38(3):470-475.

Zhuang WF (1999). The Least Square Assessment of Bilinear Regression for Weibull Parameters Realized by Microcomputer [J]. Electron. Product Reliab. Environ. Test. 5:2-7.

academicJournals

Vol. 9(9), pp. 362-366, 15 May, 2014
DOI: 10.5897/SRE2014.5917
Article Number: 2EEA9D344560
ISSN 1992-2248 © 2014

http://www.academicjournals.org/SRE

Scientific Research and Essays

Full Length Research Paper

Assessment for the quality of rolling bearing parts based on fuzzy theory

Xintao Xia, Yanyan Meng*, Yantao Shang and Ming Qiu

College of Mechatronical Engineering, Henan University of Science and Technology, Luoyang 471003, China.

Received 3 January, 2013; Accepted 2 March, 2013

There are many factors leading to rolling bearing failure, and the issue of parts quality like roller error and inner ring error is one of the main influence factors causing premature failure of the bearing. Assessment for bearing parts quality can obviously eliminate or minimize the chance of potential failure, and can improve the service life of bearing, wear-resisting property and reliability. For the sake of the assessment for the rolling bearing parts quality, a new fuzzy comprehensive evaluation method of parts quality was brought forward to account for it. Based on fuzzy theory and mathematical statistics, bearing parts quality evaluation model was established. Fuzzy comprehensive evaluation can objectively and truly reflect the quality of the bearing parts. That we synthetically evaluate the parts quality by the aid of the fuzzy comprehensive evaluation model has great value in theory and practice, and lays a new foundation for the quality evaluation of bearing parts. Then, with the condition of poor information, we take type 30204 tapered roller bearing roller quality evaluation for example to illustrate the application of the model, and the results show that using this model to assess the quality of parts is feasible.

Key words: Rolling bearing, parts, fuzzy theory, quality evaluation, wear-resisting property.

INTRODUCTION

Rolling bearing is an important support for shafts and other rotating components, and it plays an important role in the normal operation of the equipment (Bana et al., 2007; Rho et al., 2005; Ju et al., 2013). It is hoped that information on the roller bearing performance analysis will be useful for the early detection of hidden danger of degradation and the failure of the whole product performance. Thus, greater attention has been paid to evaluate the performance of rolling bearings, with the help of many new findings. For example, gray chaos evaluation model constructed by Xia et al. (2010) for prediction of rolling bearing friction torque; Kovarskii et al. (2010) assessed effectiveness of using rolling bearings in a low-noise electrical engineering; using fuzzy set theory and chaos theory, Sun et al. (2012) evaluate the rolling bearing vibration; Sochting et al. (2006) gave an evaluation of the effect of simulated launch vibration on the friction performance and lubrication of ball bearings; Zaretsky and Branzai (2005) analyzed the effect of rolling bearing refurbishment and restoration on bearing life and reliability. Yu and Yang (2011) made the fatigue failure analysis for a grease-lubricated roller bearing from an

*Corresponding author. Email: myy895@163.com

electric motor; and a fuzzy chaos method is proposed by Xia and Chen (2013) to evaluate the nonlinearly evolutionary process of rolling bearing performance.

It can be seen that the primary concern in roller bearing analysis is mainly focused on friction torque, vibration and noise, life and reliability, fatigue failure, nonlinear dynamic characteristics, etc. (Xia et al., 2010; Kovarskii, et al., 2010; Sun et al., 2012; Sochting et al., 2006; Zaretsky and Branzai, 2005; Yu and Yang, 2011; Xia and Chen, 2013).

However, so far comprehensive evaluation of the bearing parts quality still in a puzzle, for the fact that the fuzziness and uncertain relation between the quality and its influence factors. For this reason, a new method, viz., fuzzy comprehensive evaluation is proposed to evaluate the bearing parts quality and to lay a new foundation for the quality evaluation of bearing parts. Assessment for bearing parts quality can obviously eliminate or minimize the chance of potential failure, and can hence improve the service life of bearing, wear-resisting property etc. Usually, for quality evaluation of bearing parts, a certain factors index, viz., surface quality, dimensional accuracy or shape and position errors is detected. This single factor evaluation method cannot truly reflect the quality of the bearing parts. The quality of a part should be the comprehensive reflection of three output precision, viz., surface quality, dimensional accuracy or shape and position errors. Based on fuzzy theory (Liu et al., 2004; Lu and Sun (2007), this paper analyzes the parts quality influence factors and creates a comprehensive assessment model of rolling bearing parts quality. An experimental investigation on the roller quality of roller bearing is conducted to illustrate the application of the proposed model.

FUZZY EVALUATION MODEL

Fuzzy comprehensive evaluation (Liu et al., 2004) is an effective multifactor decision-making evaluation method for comprehensive evaluation of the product quality affected by many factors, which has been widely used in the product evaluation. Here, we develop the characteristics of influence factors and the establishment of the model.

Factors set

Factors set are the collection of all the factors affecting the quality of products. Fuzzy evaluation for the quality of rolling bearing parts needs to determine the evaluation factors of quality, and all of the quality evaluation factors constitute the set. The factors set of bearing parts quality can be defined as

$$U = \{u_1, u_2, \ldots, u_i, \ldots u_m\} \tag{1}$$

where u_i is the ith influence of product quality, $i = 1, 2, \ldots, m$; Usually, they are roundness, convexity, roughness, base surface roughness, etc.

Judgment set

Fuzzy evaluation for rolling bearing parts quality needs evaluation level, which are parts quality processing requirements by national standards, mechanical standards or industry standards, and the parts quality evaluation set can be constituted by all of quality evaluation rating. The ith evaluation set of the bearing parts quality can be defined as

$$V = \{v_{i1}, v_{i2}, \ldots, v_{ij}, \ldots, v_{iJ}\} \tag{2}$$

where v_{ij} is the judgment standard of the ith quality influence factors in level j, $i = 1, 2, \ldots, m$, $j = 1, 2, \ldots, J$.

Single factor evaluation

Suppose that there are m factors in the quality factor set, through the performance test, a part's quality data sequence of the ith influence factors u_i can be described as

$$u_i = (u_i(1), u_i(2), \cdots, u_i(k), \cdots, u_i(n)) \tag{3}$$

where i is the serial number of quality influence factors, $i = 1, 2, \ldots, m$; k is the data serial number, $k = 1, 2, \cdots, n$; $u_i(k)$ is the kth test status value of the quality influence factors. The composite matrix U of the quality affecting factors test data sequence made up of parts quality affecting factors sequence u_i can be obtained as:

$$U = \begin{bmatrix} u_1 \\ u_2 \\ \vdots \\ u_i \\ \vdots \\ u_m \end{bmatrix} = \begin{bmatrix} u_1(1) & u_1(2) & \cdots & u_1(k) & \cdots & u_1(n) \\ u_2(1) & u_2(2) & \cdots & u_2(k) & \cdots & u_2(n) \\ \vdots & \vdots & \vdots & \vdots & \vdots & \vdots \\ u_i(1) & u_i(2) & \cdots & u_i(k) & \cdots & u_i(n) \\ \vdots & \vdots & \vdots & \vdots & \vdots & \vdots \\ u_m(1) & u_m(2) & \cdots & u_m(k) & \cdots & u_m(n) \end{bmatrix}; i = 1, 2, ..., m \tag{4}$$

From Equation (2), judgment standard matrix V made up of the evaluation standard value of the parts quality influence factors can be expressed as:

$$V = \begin{bmatrix} v_{1j} \\ v_{2j} \\ \vdots \\ v_{ij} \\ \vdots \\ v_{mj} \end{bmatrix} = \begin{bmatrix} v_{11} & v_{12} & \cdots & v_{1j} & \cdots & v_{1J} \\ v_{21} & v_{22} & \cdots & v_{2j} & \cdots & v_{2J} \\ \vdots & \vdots & \vdots & \vdots & \vdots & \vdots \\ v_{i1} & v_{i2} & \cdots & v_{ij} & \cdots & v_{iJ} \\ \vdots & \vdots & \vdots & \vdots & \vdots & \vdots \\ v_{m1} & v_{m2} & \cdots & v_{mj} & \cdots & v_{mJ} \end{bmatrix}; i = 1, 2, ..., m, j = 1, 2, \ldots, J \tag{5}$$

Let v_{ij} be level evaluation standard value of the *i*th bearing parts quality influence factor in grade *j* (serial number *j* = 1, 2,...,*J*), u_i (*k*) is the test status value. If a status value of rolling bearing quality influence factors meets the following condition (6)

$$v_{i(j-1)} < u_i(k) \le v_{ij};\quad i=1,,2,\cdots,m; k=1,2,\cdots,n; j=1,2,\cdots,J \tag{6}$$

then the status value $u_i(k)$ corresponding to quality grade is level *j*. According to the above description, fuzzy transformation can be made for each influence factors of parts quality, and the fuzzy mapping relation can be defined as:

$$f: U \to F(V) \tag{7}$$

$$u_i \mapsto f(u_i) = \{r_{i1}, r_{i2}, \ldots, r_{im}\} \in F(V) \tag{8}$$

Fuzzy relations can be induced by the fuzzy mapping *f* as:

$$R_f(u_i, v_j) = f(u_i)(v_j) = r_{ij} \tag{9}$$

$$r_{ij} = f_{ij} / n \tag{10}$$

where f_{ij} is number of a test value of *i*th quality influence factors in the scope of level *j*.

Fuzzy matrix R composed of R_f can be expressed as:

$$R = \begin{pmatrix} r_{11} & r_{12} & \cdots & r_{1J} \\ r_{21} & r_{22} & \cdots & r_{2J} \\ \vdots & \vdots & & \vdots \\ r_{m1} & r_{m2} & \cdots & r_{mJ} \end{pmatrix} \tag{11}$$

R can be said to be a single factor evaluation matrix.

Weighting set

The selection of the affecting factors weighting set A is more complex. We can consider the mathematical expectation (average) and dispersion scope (standard deviation or range) of each output factors in the test results, and also can consider technical requirements of the parts machining process. The *i*th influence factor weight can be defined as:

$$a_i = \frac{u_{Ri}}{u_{mi}} \bullet \frac{1}{\sum_{i=1}^{m} \frac{u_{Ri}}{u_{mi}}} \tag{12}$$

where u_{Ri} is the *i*th range or standard deviation of the quality influence factors in the *n* test data; u_{mi} is the average of the *i*th quality influence factors u_i.

From Equation (11), the weight set of components quality affecting factors can be attained as:

$$A = (a_1, a_2, \ldots, a_m) \tag{13}$$

Fuzzy comprehensive evaluation model

Bearing parts quality comprehensive evaluation model can be defined as

$$B = A \circ R = (b_1, b_2, \ldots b_j, \ldots, b_J) \tag{14}$$

where "$\circ$" is the fuzzy operator, with

$$b_j = \overset{m}{\underset{i=1}{\vee}} (a_i \wedge r_{ij}),\ j = 1,2,\ldots,J \tag{15}$$

EXPERIMENTAL INVESTIGATION

Taking the roller (type 30204) as an example to illustrate the application of the model, and the number of the bearing samples is 30, viz., *n*=30. There are many factors affecting the quality of roller, in this paper mainly considering the processing quality parameters of angle error, crown diameter error parameters, namely, *m* = 8, and related symbols and their meaning are shown in Table 1.

In the scene of the production, we randomly selected 30 sets of tapered roller bearing, and measured influence factors status values after numbered and disassembled. Main technical parameters and measuring instrument are shown in Table 2. Then we respectively measured the influence factors value of roller after disassembled, and recorded the various influence factors measured value. According to bearing parts processing requirements of the national standard, each evaluation standard of influence factor, evaluation standard score 6, influence factors judgment set V composed of the evaluation standard value can be attained as

$$V = \{v_{i1}, v_{i2}, \ldots, v_{i6}\}$$

with the judgment matrix V

$$V = \begin{pmatrix} 0.0070 & 0.0090 & 0.0120 & 0.0140 & 0.0160 & 0.0180 \\ 0.0004 & 0.0010 & 0.0017 & 0.0023 & 0.0030 & 0.0040 \\ 3.3000 & 3.6000 & 3.9000 & 4.2000 & 4.8000 & 5.5000 \\ 0.2500 & 0.5000 & 0.8000 & 1.2000 & 2.0000 & 3.0000 \\ 0.1000 & 0.2000 & 0.3200 & 0.5000 & 0.8000 & 1.0000 \\ 0.0120 & 0.0250 & 0.0400 & 0.0800 & 0.1250 & 0.1600 \\ 0.0800 & 0.1000 & 0.1250 & 0.1600 & 0.3200 & 0.4000 \\ 0.0025 & 0.0030 & 0.0035 & 0.0040 & 0.0050 & 0.0070 \end{pmatrix}$$

Table 1. symbols and meanings.

Sequence number, *i*	Symbol	Meaning	Unit
1	u_1	Diameter error	μm
2	u_2	Angle error	μm
3	u_3	Convexity	μm
4	u_4	Roundness	μm
5	u_5	Waviness	μm
6	u_6	Roughness	μm
7	u_7	Base surface roughness	μm
8	u_8	Run-out error of base surface	μm

Table 2. Measuring instrument of parameter.

Sequence number	Symbol of parameter	Measuring instrument	Precision (μm)
1	u_1	Roller tester D744	1
2	u_2	Roller tester D744	1
3	u_3	Convexity tester ZT-1	0.1
4	u_4	Roundness tester Y9025C	0.01
5	u_5	Roundness tester Y9025C	0.01
6	u_6	Roughometer CX-1	0.001
7	u_7	Roughometer CX-1	0.001
8	u_8	Roller run-out error tester C742	1

From Equations (6) to (10), fuzzy transform for the record test data, obtaining fuzzy matrix R

$$R = \begin{pmatrix} 0.0333 & 0.0000 & 0.7333 & 0.2333 & 0.0000 & 0.0000 \\ 0.1000 & 0.0667 & 0.3667 & 0.2333 & 0.1000 & 0.1333 \\ 0.0333 & 0.0000 & 0.1333 & 0.3667 & 0.4667 & 0.0000 \\ 0.0333 & 0.2333 & 0.4333 & 0.2333 & 0.0667 & 0.0000 \\ 0.2000 & 0.1667 & 0.3000 & 0.2000 & 0.1000 & 0.0333 \\ 0.0000 & 0.0000 & 0.6333 & 0.3667 & 0.0000 & 0.0000 \\ 0.0000 & 0.0000 & 0.0000 & 0.0667 & 0.9000 & 0.0333 \\ 0.0000 & 0.0333 & 0.1000 & 0.2000 & 0.4667 & 0.2000 \end{pmatrix}$$

The weight of all the factors can be calculated by Equation (11), thus getting weighting set A

A= (0.0585, 0.1749, 0.0307, 0.1712, 0.3071, 0.0880, 0.1057, 0.0638)

From Equation (14), the comprehensive evaluation for roller quality can be expressed as

B= (0.2000, 0.1712, 0.3000, 0.2000, 0.1057, 0.1333)

According to the principle of maximum membership, under the given conditions, the bearing roller belongs to grade 3 for the consideration factors. The experimental investigation on the roller shows that the evaluation value is in very good accordance with the practice value, and the roller can meet the accuracy and quality requirement of the roller bearing.

CONCLUSIONS

Based on fuzzy theory, the paper puts forward a new method of rolling bearing parts quality evaluation, and establishes a fuzzy evaluation model; with the condition of poor information, the experimental investigation on bearing roller quality evaluation shows that the model can be used to evaluate bearing roller quality only with small samples and without any prior information of probability distributions.

Conflict of Interests

The author(s) have not declared any conflict of interests.

ACKNOWLEDGEMENTS

This project was funded by the National Natural Science Foundation of China (Grant No. 51075123) and the Foundation of Innovation and Research Team of Science and Technology in Universities in Henan Province (Grant No. 13IRTSTHN025).

REFERENCES

Bana JE, Rhob BH, Kim KW (2007). A study on the sound of roller bearings operating under radial load. Tribol. Int. 40(1):21-28. http://dx.doi.org/10.1016/j.triboint.2006.01.026

Ju SN, Kim HE, Kyeong UK (2013). A new accelerated zero-failure test model for rolling bearings under elevated temperature conditions. J. Mech. Sci. Technol. 27(6):1801-1807. http://dx.doi.org/10.1007/s12206-013-0431-1

Kovarskii ME, Volovik AP, Zaitsev VA (2010). On the effectiveness of using rolling bearings in low-noise electrical engineering. Russ. Elect. Eng. 81(9):476-479. http://dx.doi.org/10.3103/S106837121009004X

Liu HZ, Zhang WF, Yuan XP (2004). Fuzzy method in judging the capability grade of gun barrels. Acta Armamentarii 25(5):517-519. (In Chinese)

Lu Z, Sun YC (2007). Research on maintainability evaluation model based on fuzzy theory. Chin. J. Aeronaut. 20(5):402-407. http://dx.doi.org/10.1016/S1000-9361(07)60061-2

Rho BH, Kim DG, Kim KW (2005). A noise analysis of cylindrical roller bearings operating under zero external load. Tribol. Trans. 48:238-244. http://dx.doi.org/10.1080/05698190590929080

Sochting S, Sherrington I, Lewis SD (2006). An evaluation of the effect of simulated launch vibration on the friction performance and lubrication of ball bearings for space applications. Wear 260(11-12):1190-1202. http://dx.doi.org/10.1016/j.wear.2005.07.012

Sun XC, Xia XT, Liu YB, Gao LL (2012). Evaluation of rolling bearing vibration using fuzzy set theory and chaos theory. Adv. Res. Eng. Mater. Energy Manage. Cont. 424-425:338-341.

Xia XT, Chen L (2013). Fuzzy chaos method for evaluation of nonlinearly evolutionary process of rolling bearing performance. Measurement 46(3):1349-1354. http://dx.doi.org/10.1016/j.measurement.2012.11.003

Xia XT, Lv TM, Meng FN (2010). Gray chaos evaluation model for prediction of rolling bearing friction torque. J. Test. Eval. 38(3):291-300.

Yu ZQ, Yang ZG (2011). Fatigue failure analysis of a grease-lubricated roller bearing from an electric motor. J. Failure Anal. Prev. 11(2):158-166. http://dx.doi.org/10.1007/s11668-010-9422-z

Zaretsky VE, Branzai VE (2005). Effect of rolling bearing refurbishment and restoration on bearing life and reliability. Tribol. Trans. 48(1):32-44. http://dx.doi.org/10.1080/05698190590893143

academicJournals

Vol. 9(9), pp. 367-373, 15 May, 2014
DOI: 10.5897/SRE2014.5918
Article Number: 2EEA9D344560
ISSN 1992-2248 © 2014
Copyright©2014
Author(s) retain the copyright of this article
http://www.academicjournals.org/SRE

Scientific Research and Essays

Full Length Research Paper

Air gap field-oriented vector control strategy for high-power electrically excited synchronous motor based on full-order flux linkage observer

Jing Shang*, Xiaohong Nian and Kean Liu

Central South University, Changsha 412100, China.

Received 3 January, 2013; Accepted 2 March, 2013

This paper raises a full-order flux linkage observer for the high-power electrically excited synchronous motor and proposes a design for its feedback matrix based on modern control theories which ensure excellent dynamic and static performances of this full-order flux linkage observer. On the basis of the said full-order flux linkage observer, an air gap field-oriented vector control strategy for the electrically excited synchronous motor based on the full-order flux linkage observer has been established and it is possible for the electrically excited synchronous motor to operate with the unity power factor. Through simulation and experiments, the effectiveness of the full-order flux linkage observer as well as the control strategy has been further verified.

Key words: Electrically excited synchronous motor, full-order flux linkage observer, air gap field-oriented vector control.

INTRODUCTION

As a typical AC drive motor, the electrically excited synchronous motor beats the asynchronous motor in power factor, efficiency, overload magnification and rotational inertia (Beliaev and Weinger, 2005). Therefore, the application mode of electrically excited synchronous motor based on IGCT three-level neutral point clamped inverter become the mainstream in the field of high-power high-performance industrial drive and thus is widely applied to industries such as mine hoisting, metallurgy and steel rolling, and marine propulsion. There are mainly two kinds of control of the electrically excited synchronous motor, that is, vector control (Szabo, 2006) and direct torque control (Pyrbonen, 1998; Pyrhonen et al., 1997). In order to achieve high-performance control, flux linkage is required for both of them. As control performance is largely depend on the accuracy of flux linkage, an accurate flux linkage model is crucial to control performance. In the literature (Szabo et al., 2010), an open-loop model is used to observe excitation, which is greatly influenced by the motor parameters; in the literature (Wu and Tan, 2010), a voltage-current model is adopted, with a filter for switchover to observe the flux linkage, but it is essentially a reduced-order model with limited properties. This paper raises a full-order flux linkage observer for the electrically excited synchronous motor based on the dynamic mathematical model of the electrically excited synchronous motor, thus making it possible to obtain accurate flux linkage value.

---

*Corresponding author. E-mail: shangjing@teg.cn

FULL-ORDER FLUX LINKAGE OBSERVER OF ELECTRICALLY EXCITED SYNCHRONOUS MOTOR MATHEMATICAL MODEL OF ELECTRICALLY EXCITED SYNCHRONOUS MOTOR

Flux-linkage and Voltage equations:

$$\begin{bmatrix}\psi_{sd}\\ \psi_{sq}\\ \psi_f\\ \psi_D\\ \psi_Q\end{bmatrix}=\begin{bmatrix}L_{sd} & 0 & L_{ad} & L_{ad} & 0\\ 0 & L_{sd} & 0 & 0 & L_{ad}\\ L_{ad} & 0 & L_f & L_{ad} & 0\\ L_{ad} & 0 & L_{ad} & L_D & 0\\ 0 & L_{ad} & 0 & 0 & L_Q\end{bmatrix}\begin{bmatrix}i_{sd}\\ i_{sq}\\ i_f\\ i_D\\ i_Q\end{bmatrix}\qquad \begin{bmatrix}u_{sd}\\ u_{sq}\\ u_f\\ u_D\\ u_Q\end{bmatrix}=\begin{bmatrix}R_s & 0 & 0 & 0 & 0\\ 0 & R_s & 0 & 0 & 0\\ 0 & 0 & R_f & 0 & 0\\ 0 & 0 & 0 & R_D & 0\\ 0 & 0 & 0 & 0 & R_Q\end{bmatrix}\begin{bmatrix}i_{sd}\\ i_{sq}\\ i_f\\ i_D\\ i_Q\end{bmatrix}+\frac{d}{dt}\begin{bmatrix}\psi_{sd}\\ \psi_{sq}\\ \psi_f\\ \psi_D\\ \psi_Q\end{bmatrix}+\begin{bmatrix}-\omega_r\psi_{sq}\\ \omega_r\psi_{sd}\\ 0\\ 0\\ 0\end{bmatrix}$$

Torque equation:

$$T_e=\psi_{sd}i_{sq}-\psi_{sq}i_{sd}$$

Full-order flux linkage observer of electrically excited synchronous motor

Based on the mathematical model, a state equation of the electrically excited synchronous motor is established with stator, rotor and damped flux linkages as state variables:

$$\dot{x}=Ax+Bu \qquad x=\begin{bmatrix}\psi_{sd} & \psi_{sq} & \psi_f & \psi_D & \psi_Q\end{bmatrix}^T$$

$$y=Cx \qquad u=\begin{bmatrix}u_d & u_q & u_f & 0 & 0\end{bmatrix}^T$$

$$y=\begin{bmatrix}i_d & i_q & i_f\end{bmatrix}^T$$

Where x is a state variable, u is an input variable and y is an output variable. Where coefficient matrixes of A, B and C are respectively as follows:

A full-order state observer for the electrically excited synchronous motor can be established with modern control theories and on the basis of the state equation, as shown below:

$$\dot{\hat{x}}=A\hat{x}+Bu+G(y-\hat{y})$$

$$\hat{y}=C\hat{x}$$

Where ^ refers to the observed quantity of state and G is a feedback matrix.

$$A=\begin{bmatrix}-\frac{R_s m}{1+mL_{s\sigma}} & \omega_r & \frac{R_s}{(1+mL_{sl})L_{f\sigma}} & \frac{R_s}{(1+mL_{sl})L_{D\sigma}} & 0\\ -\omega_r & -\frac{R_s n}{1+nL_{sl}} & 0 & 0 & \frac{R_s}{(1+nL_{sl})L_{Q\sigma}}\\ \frac{R_f}{(1+mL_{s\sigma})L_{f\sigma}} & 0 & -R_f\frac{(1+mL_{sl})L_{f\sigma}-L_{sl}}{(1+mL_{sl})L_{f\sigma}{}^2} & \frac{R_f L_{sl}}{(1+mL_{sl})L_{f\sigma}L_{D\sigma}} & 0\\ \frac{R_D}{(1+mL_{s\sigma})L_{D\sigma}} & 0 & \frac{R_D L_{sl}}{(1+mL_{sl})L_{f\sigma}L_{D\sigma}} & -R_D\frac{(1+mL_{sl})L_{D\sigma}-L_{sl}}{(1+mL_{sl})L_{D\sigma}{}^2} & 0\\ 0 & \frac{R_Q}{(1+nL_{sl})L_{Q\sigma}} & 0 & 0 & -R_Q\frac{(1+nL_{sl})L_{Q\sigma}-L_{sl}}{(1+nL_{sl})L_{Q\sigma}{}^2}\end{bmatrix}$$

$$B=\begin{bmatrix}1 & 0 & 0 & 0 & 0\\ 0 & 1 & 0 & 0 & 0\\ 0 & 0 & 1 & 0 & 0\\ 0 & 0 & 0 & 0 & 0\\ 0 & 0 & 0 & 0 & 0\end{bmatrix}\quad \mathrm{C}=\begin{bmatrix}\frac{m}{1+mL_{sl}} & 0 & -\frac{1}{(1+mL_{sl})L_{f\sigma}} & -\frac{1}{(1+mL_{sl})L_{D\sigma}} & 0\\ 0 & \frac{n}{1+nL_{sl}} & 0 & 0 & -\frac{1}{(1+nL_{sl})L_{Q\sigma}}\\ -\frac{1}{(1+mL_{sl})L_{f\sigma}} & 0 & \frac{(1+mL_{sl})L_{f\sigma}-L_{sl}}{(1+mL_{sl})L_{f\sigma}{}^2} & -\frac{L_{sl}}{(1+mL_{sl})L_{f\sigma}L_{D\sigma}} & 0\end{bmatrix}$$

$$m=\frac{1}{L_{md}}+\frac{1}{L_{D\sigma}}+\frac{1}{L_{f\sigma}} \qquad n=(\frac{1}{L_{mq}}+\frac{1}{L_{Q\sigma}})$$

Feedback matrix design for full-order flux linkage observer of electrically excited synchronous motor

The performance of the full-order flux linkage observer depends on the feedback matrix. In order to obtain accurate flux linkage values, the feedback matrix must be designed properly. First, the form of the feedback matrix should be determined. As there are 5 state variables and 3 output variables, the feedback matrix should be a 5 × 3 matrix; meanwhile, the system is a 5-order one, so there can be 5 degrees of freedom for the configuration of the feedback matrix. The rotor flux linkage is related to intensity of rotor current, so rotor current errors can be independently used to correct the rotor flux linkage, and as the rotor current is single-phase DC, only one degree of freedom is required; the stator flux linkage is related to intensity of stator current, so stator current errors can be independently used to correct the stator flux linkage, and as the stator current is symmetrical three-phase current, two degrees of freedom are required; the damper current is immeasurable, so there is no way to correct damped flux linkage with damper current, but as there are two degrees of freedom left for the feedback matrix, it is reasonable to correct the damped flux linkage with the stator current. To sum up, the determined form of the feedback matrix is as follows:

$$G=\begin{bmatrix}g_1 & -g_2 & 0\\ g_2 & g_1 & 0\\ 0 & 0 & g_3\\ g_4 & -g_5 & 0\\ g_5 & g_4 & 0\end{bmatrix}$$

Then, values of the feedback matrix should be determined. The feedback matrix is decisive for the pole position of the flux linkage observer, i.e. for the performance of the flux linkage observer. In order to ensure faster convergence of the flux linkage observer than that of the actual flux linkage, the pole of the flux linkage observer can be allocated K times of that of the original motor; the larger the K value is, the higher convergence rate the flux linkage observer has and the more sensitive the observer is to external disturbance. Therefore, selection of K should achieve a compromise between the rapidity and sensitivity to disturbance and noise. Since the form and the pole position of the feedback matrix has been determined, the design method based on the modern control theory for the full-order state observer can be used to calculate and obtain the feedback matrix. However, as the system is a 5-order one, analytical expressions of the feedback matrix are rather formidable, so mathematical tools such as maple and matlab can be used for calculation, thus to obtain the feedback matrix.

AIR GAP FIELD-ORIENTED VECTOR CONTROL FOR THREE-LEVEL ELECTRICALLY EXCITED SYNCHRONOUS MOTOR

Air gap field-oriented mathematical model of electrically excited synchronous motor

Voltage equation:

$$u_{sm} = R_s i_{sm} - L_{sl} i_{st} \omega_r$$
$$u_{st} = R_s i_{st} + (\psi_\sigma + L_{sl} i_{st}) \omega_r$$

Torque equation:

$$T_e = \psi_\sigma i_{st}$$

Control of unity power factor

In order to improve the system efficiency, the electrically excited synchronous motor generally operates at the unity power factor. Due to stator leakage reactance, the conventional control mode of ism = 0 cannot meet the requirement of the unity power factor.

Operation at the unity power factor is to ensure in-phase of stator voltage and stator current, that is,

$$\frac{i_{sm}}{i_{st}} = \frac{u_{sm}}{u_{st}}$$

Substitute the equation into the above equation:

$$L_{sl} i_{sm}{}^2 + \psi_\sigma i_{sm} + L_{sl} i_{st}{}^2 = 0$$

Rearrange the above equation:

$$i_{sm} = \frac{\sqrt{\psi_\sigma{}^2 - 4 L_{sl}{}^2 i_{st}{}^2} - \psi_\sigma}{2 L_{sl}}$$

As long as the magnetic component of stator current meets the equation, the electrically excited synchronous motor can operate at the unity power factor.

Air gap field-oriented vector control based on full-order flux linkage observer

To sum up, it is possible to develop an air gap field-oriented vector control strategy for the electrically excited synchronous motor based on the full-order flux linkage observer, and the control block diagram is shown in Figure 1.

SIMULATION AND EXPERIMENTAL VERIFICATION

Simulation verification

According to the full-order flux linkage model of and the air gap field-oriented control strategy for the electrically excited synchronous motor mentioned above, an air gap-oriented vector control model of the electrically excited synchronous motor is established on the matlab/simulink simulation platform, with simulation results as follows:

It can be seen from Figure 2 that no matter in the steady-state or dynamic-state process, the air gap flux linkage observed by the full-order flux linkage model stays the same as the actual flux linkage of the motor and the full-order flux linkage model presents high steady-state precision and excellent dynamic-state performance, which indicates effectiveness and accuracy of the full-order flux linkage model of the electrically excited synchronous motor.

Figure 3 shows the simulation results of the air gap field-oriented vector control for the electrically excited synchronous motor based on the full-order flux linkage observer. It can be seen that the no matter in the steady-state or dynamic-state process, the control strategy presents excellent performance, and the reactive power is zero after the control is stabilized, thus realizing unity power factor control of the electrically excited synchronous motor.

Experimental verification

To further verify the effectiveness of the control strategy, an experimental system for the high-power electrically excited synchronous motor is established. Table 1 shows the three-phase electrically excited synchronous motor parameters.

Figure 4 shows the experimental waveforms recorded by the monitoring software CSR_DRIVE. It can be seen that the speed of the electrically excited synchronous motor is kept stable, thus realizing the air gas field-oriented vector control strategy for the electrically excited synchronous motor and the motor presents excellent dynamic and static performances. Meanwhile, during this process, the voltage at the DC side is kept stable as well. Figure 5 shows the torque step response of electrically excited synchronous motor. It can be seen that the system has rapid response and small overshoot.

Figures 6 and 7 show the waveforms of voltage and current of the electrically excited synchronous motor saved by the analysis software (Xviewer) from experimental data recorded by the oscilloscope (DLM2032). It can be seen from Figure 6 that, in the diode-clamped three-level circuit, the phase voltage is three-level, so the line voltage is five-level. The three-level circuit system is well controlled and the current of the electrically excited synchronous motor is kept stable and symmetrical. It can be seen from Figure 7 that phase voltage and phase current of the electrically excited synchronous motor are in phase, so the power factor is 1, realizing the air gap field-oriented control strategy for the electrically excited synchronous motor based on the full-order flux linkage observer.

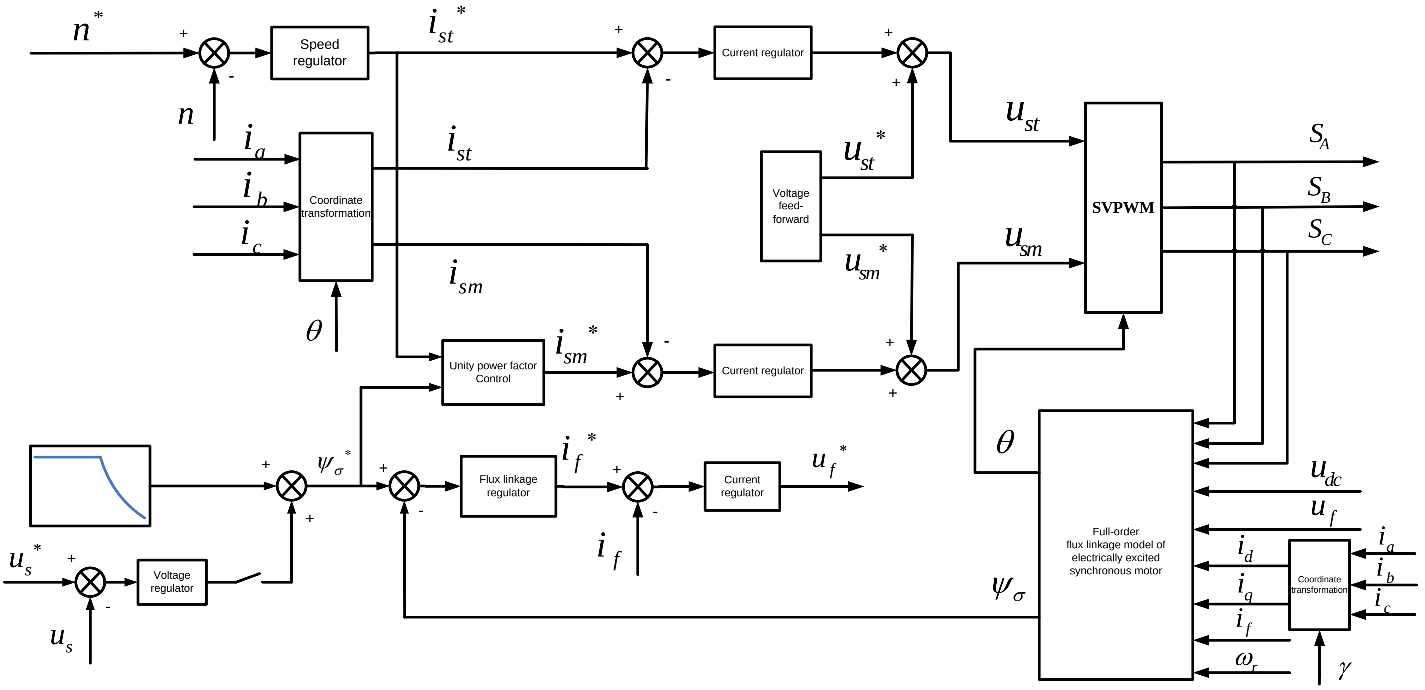

Figure 1. Diagram of air gap field-oriented vector control for electrically excited synchronous motor based on full-order stator flux observer.

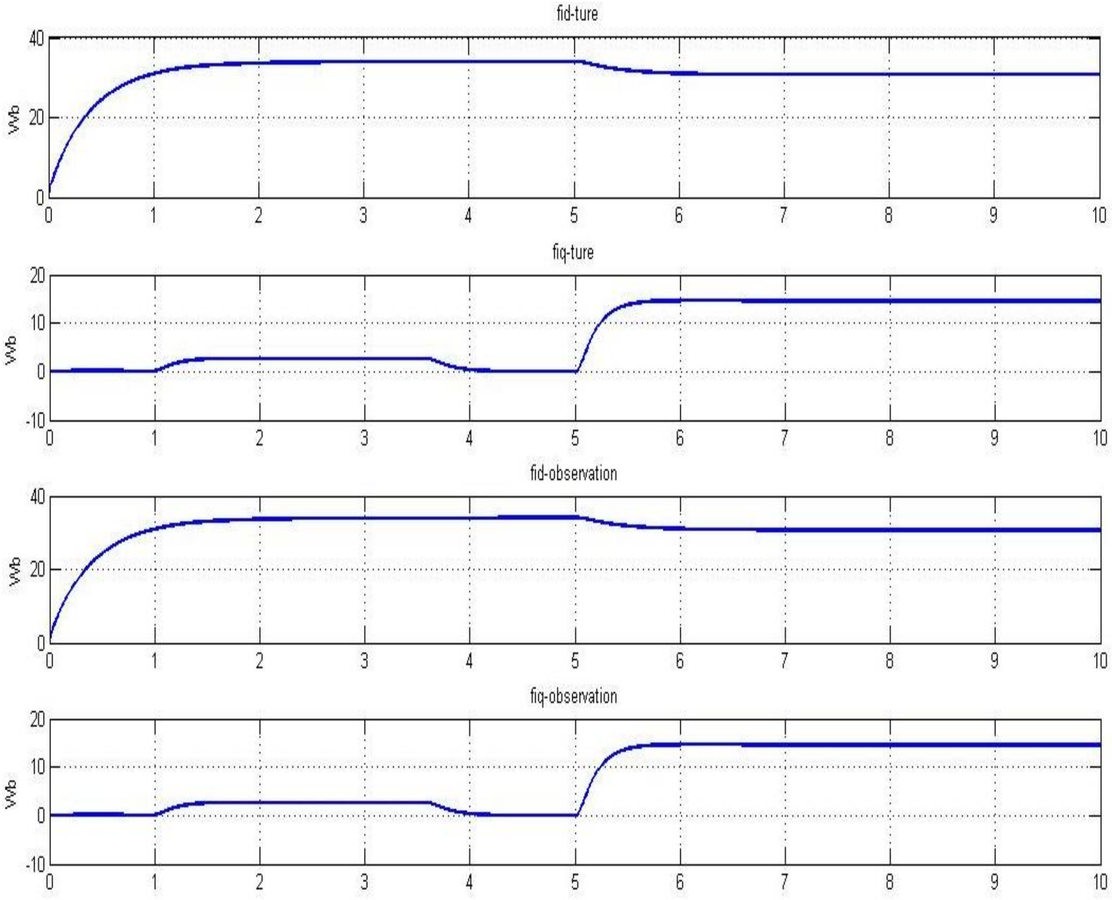

Figure 2. Actual and observed values of d-axis and q-axis components of air gap flux linkage.

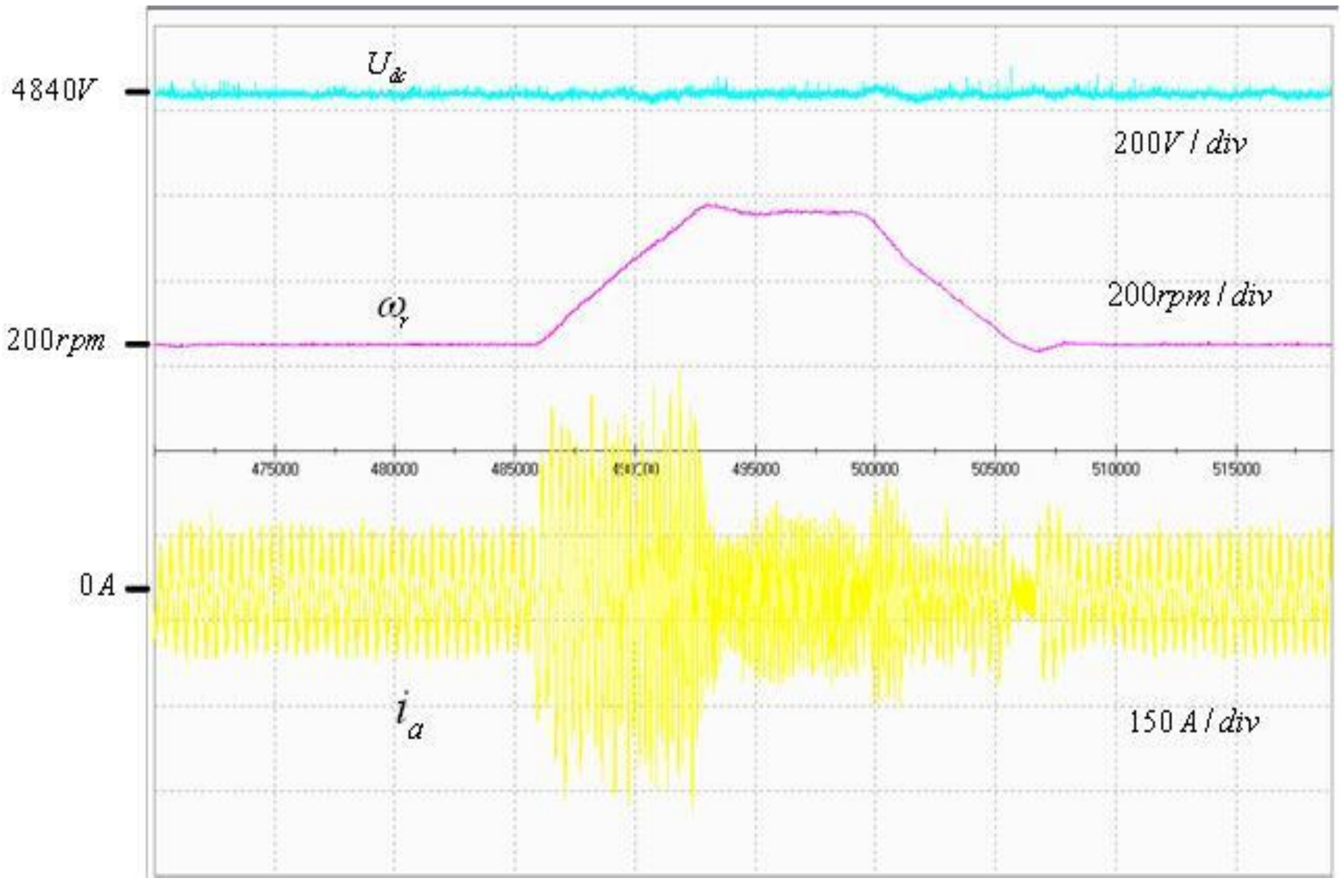

Figure 4. Waveforms of rotating speed, a-phase current and voltage at dc side of electrically excited synchronous motor.

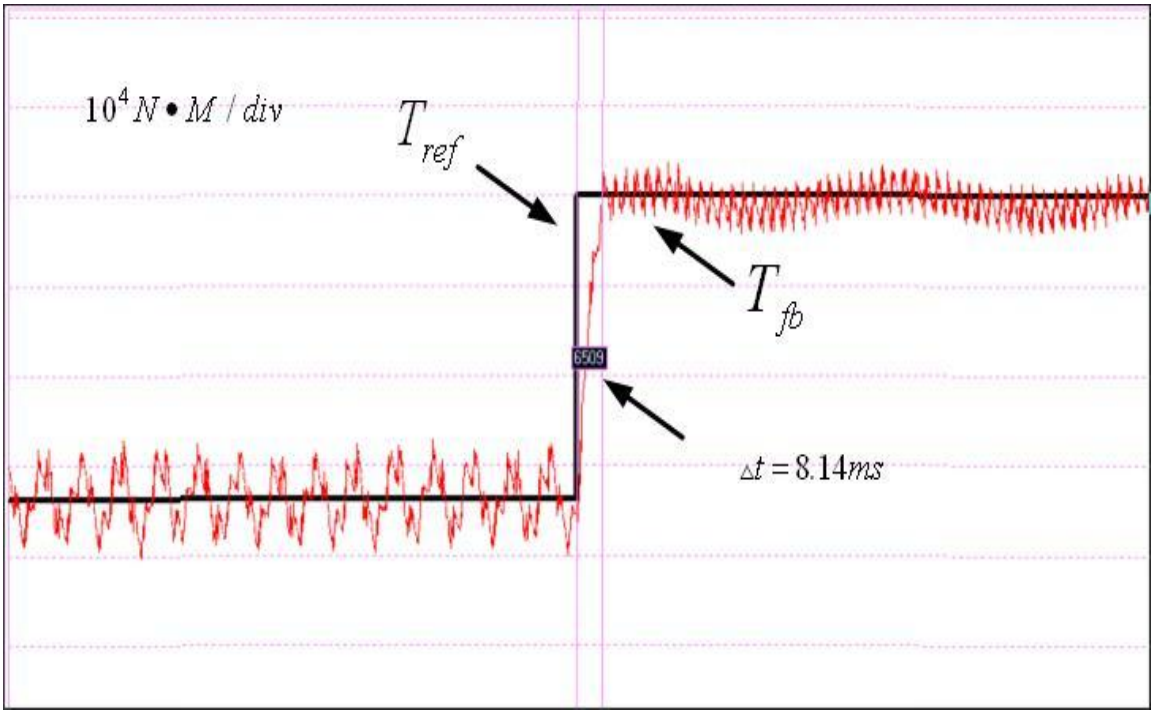

Figure 5. Waveforms of torque step response of electrically excited synchronous motor.

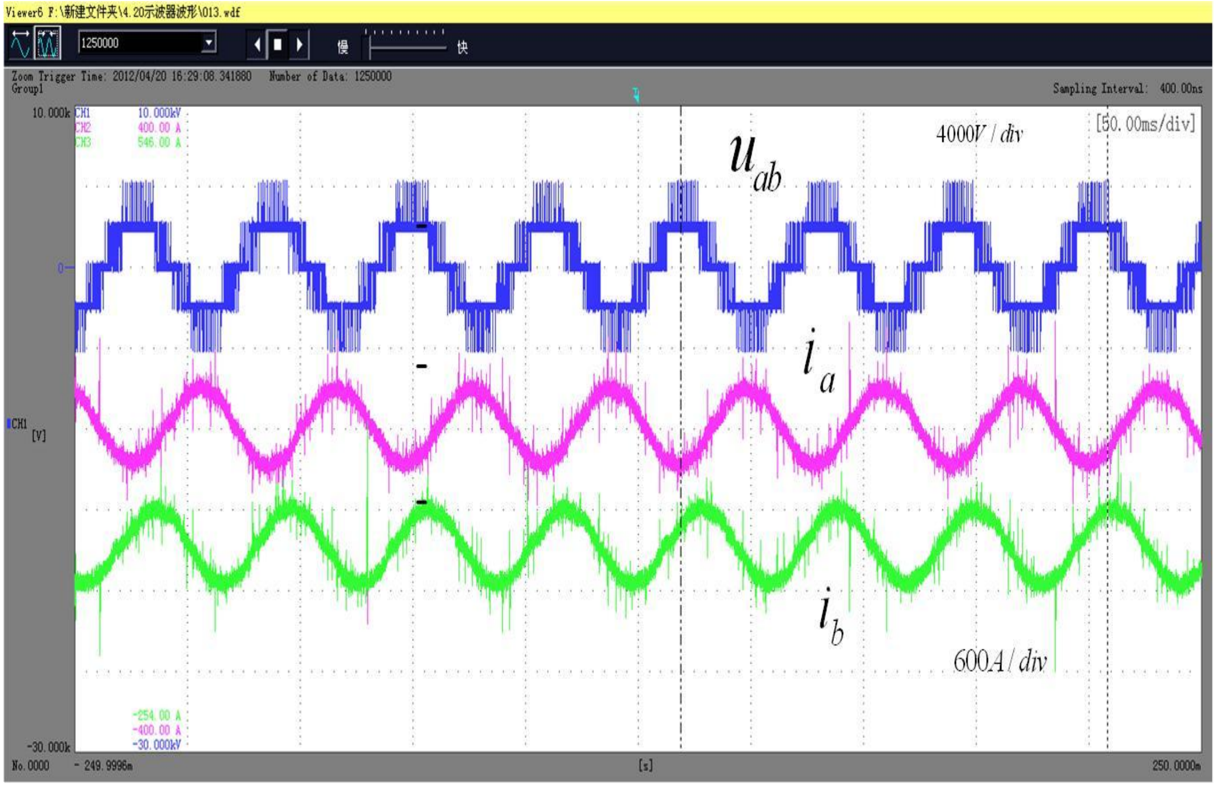

Figure 6. Waveforms of line voltage, a-phase current and b-phase current of electrically excited synchronous motor.

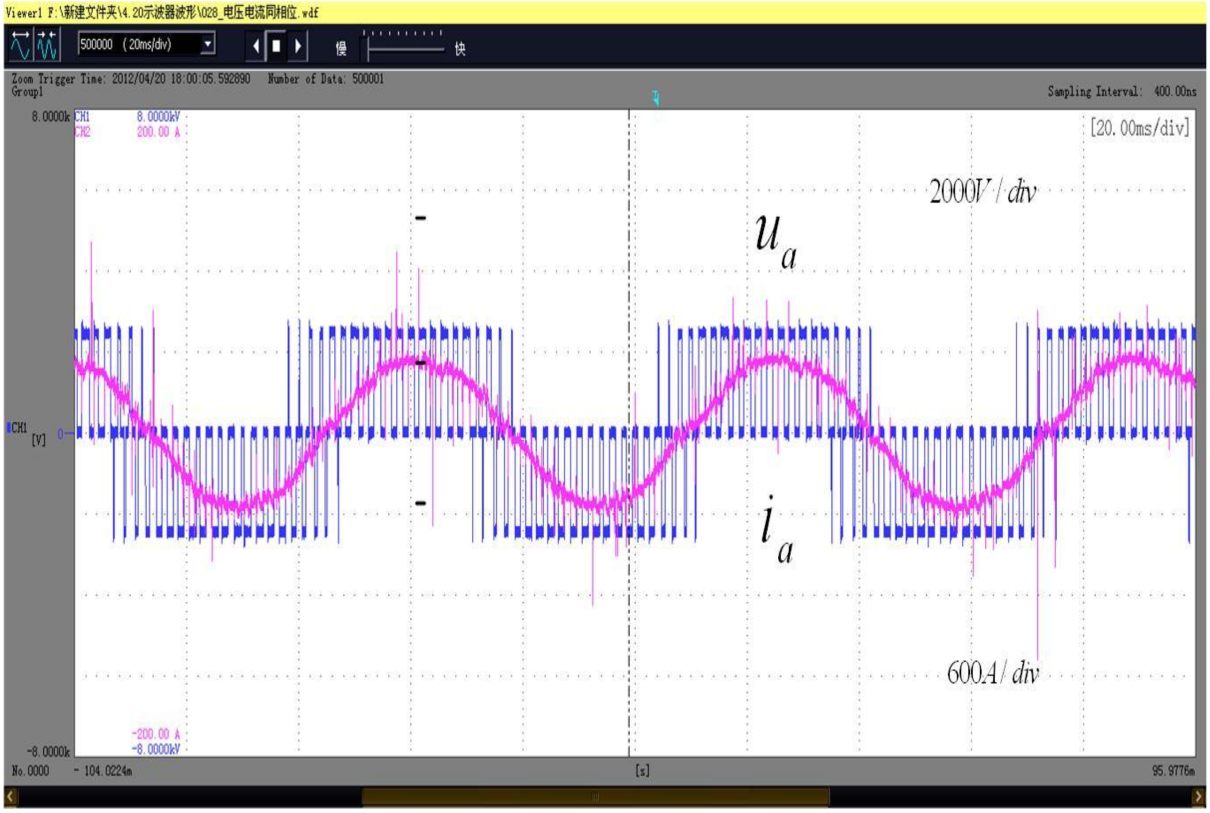

Figure 7. Waveforms of a-phase voltage and a-phase current of electrically excited synchronous motor.

Conclusions

This paper raises a full-order flux linkage observer for the electrically excited synchronous motor on the basis of the mathematical model of the electrically excited synchronous motor on the d-p axis and proposes a design method for feedback matrix of the full-order flux linkage observer. The full-order flux linkage observer proposed in this paper can not only obtain accurate flux linkage values under the steady state, but also present excellent performance under the dynamic state, thus fully meeting the requirements of the high-performance control strategy. Based on the full-order flux linkage observer proposed in this paper, an air gap field-oriented control strategy for the electrically excited synchronous motor is developed and a control method for the unity power factor is proposed.

Conflict of Interests

The author(s) have not declared any conflict of interests.

ACKNOWLEDGEMENTS

This work was supported by the China National Scientific and Technological Support Projects (2012BAF090B02).

REFERENCES

Beliaev D, Weinger A (2005). Field oriented control of a synchronous drive[C]. IEEE Int. Conf. Electric Machine Drives pp. 957-961.

Pyrbonen O (1998). Analysis and control of excitation, field weakening and stability in direct torque controlled electrically excited synchronous motor drives [D]. Finland: Lappeenranta University of Technology.

Pyrhonen J, Niemela M, Kaukonen J, Tiitinen P (1997). Synchronous motor drives based on direct flux linkage control. Proc. Eur. Power Electron. Conf., Norway: Trondheim, 1:434-430.

Szabo C (2006). Implementation of scalar and vector control structures for synchronous motors[D]. Technical University of Cluj-Napoca, Romania.

Szabo CS, Maria I, Incze II (2010). Double-Field orientation of unity power factor synchronous motor drive[C]. Intelligent Engineering Systems, 2010 14th International Conference, pp. 237-242. http://dx.doi.org/10.1109/INES.2010.5483842

Wu X, Tan G (2010). Electrically excited synchronous motor three-level DTC_SVM control based on novel flux observer [C]. Elect. Cont. Eng. pp. 3689-3692.

academicJournals

Vol. 9(9), pp. 374-379, 15 May, 2014
DOI: 10.5897/SRE2014.5919
Article Number: 626336744564
ISSN 1992-2248 © 2014
Copyright©2014
Author(s) retain the copyright of this article
http://www.academicjournals.org/SRE

Scientific Research and Essays

Full Length Research Paper

A novel fusion algorithm for infrared image and visible light image based on non-subsampled contourlet transform

Yucheng Liu[1]* and Yubin Liu[2]

[1]College of Electrical and Information Engineering, Chongqing University of Science and Technology, Chongqing, 401331, China.
[2]School of Continuing Education, Panzhihua Univerisity, Panzhihua, 617000, China.

Received 3 January, 2013; Accepted 2 March, 2013

Aiming at the different characteristics of the infrared image and visible light image, the paper proposed a kind of fusion algorithm for the infrared image and visible light image based on non-subsampled contourlet transform. Firstly, the source images are made multiscale and multi-direction decomposition by using non-subsampled contourlet transform (NSCT). Secondly, to decomposed low frequency subband, a decision-making value with regional energy and variance is constructed and used in fusing the coefficients by choosing larger decision-making value. And for the decomposed high frequency subband, different fusion rules are employed for different levels. The fusion rule of selecting large absolute value of pixel is used for the highest level, and the fusion rule of selecting large regional variance based on regional energy matching degree is used to fuse the other levels. Finally, the final fused image is reconstructed by using the non-subsampled contourlet inverse transform. The experimental results have shown that the proposed algorithm can get more detail information and can exhibit better fusion performance.

Key words: Fusion algorithm, regional energy matching degree, image fusion, non-subsampled contourlet transform, infrared image, visible light image, shift invariant.

INTRODUCTION

Image fusion refers to the information process of integrating the images or image sequence information of the particular scene which two or more than two sensors get at the same time or at the different time to generate a new interpretation about this scene (Lian et al., 2011). The fusion of the infrared image and visible light image is an image fusion method which has been widely used in military and security monitoring field. The infrared image is generally dark, low in signal-to-noise ratio and absent in the sense of hierarchy. It has no color information. But it often has obvious target information. The visible light image is abundant in the spectral information, large in the dynamic range, relatively high in the contrast ratio and abundant in the spectral information (Ye et al., 2008). It

---

*Corresponding author. E-mail: lych68782763@163.com

contains rich detailed information. But it is not easy to be observed on the dark background (Yang et al., 2012). To fuse infrared image and visible light image to improve the infrared target recognition and image clarity and to obtain more detailed and accurate information enable us to accurately determine the accuracy location of the heat source even in harsh environment, which has extensive practical value in the many fields of military operations, electronic products testing, resources exploration.

At present, the image fusion based on the multiscale decomposition is a research hotspot. Commonly used methods of multi scale decomposition of the image are mainly pyramid transform, wavelet transform, contourlet transform and the nonsubsampled contourlet transform (NSCT) and other methods. The different resolution details in the decomposition structure of the pyramid transform are related to each other, the stability of the algorithm is poor. Wavelet transform overcomes the instability of pyramid algorithm. However, although the traditional wavelet transform can efficiently handle the one-dimensional piecewise continuous signals, two dimensional wavelet base formed by the one-dimensional wavelet with tensor product can only obtain the information in the three directions of the horizontal direction, vertical direction and the diagonal direction, can not accurately describe the information of image edge direction, also can not represent two-dimensional images containing a line or surface singularity. Contourlet transform has the multi-resolution and time-frequency localization characteristic of the wavelet transform, also has a high directionality and anisotropy. It can well capture the geometric structure of two-dimensional image. But, because of requiring upsampling and downsampling operation in the transformation process, so it does not have the translation invariance. There is the spectrum aliasing phenomenon in the transformation process (Ye et al., 2012). NSCT not only has the wavelet multi-resolution and time-frequency localization characteristic of the wavelet transform, but also has a good directionality, anisotropy and translation invariance. The image information in any direction can be obtained. Therefore, this paper used the method based on NSCT to perform image fusion.

NON-SUBSAMPLED CONTOURLET TRANSFORM

Non-subsampled contourlet transform (NSCT) (Tang, 2012) is a multi-scale and multi-direction decomposition method of the discrete image. It is presented based on the theory of the contourlet transform. NSCT transform can be divided into two parts of non-subsampled pyramid filter bank (NSPFB) and nonsubsampled directional filter bank (NSDFB). It separately performs the multi-scale analysis and multi-direction analysis and cancels the direct upsampling and downsampling operation on the corresponding signal component. Firstly, NSPFB is used to perform the multi-scale decomposition of the image in the NSCT transform process. The original image produces a low pass subband image and a band-pass subband image through a level NSPFB decomposition. After that, each level of NSPFB decomposition can be performed by the iteration of the low pass subband image. Then NSDFB is used to perform the direction decomposition of the high frequency component obtained by the each level of NSPFB decomposition, thus the subband images (coefficients) with the different scales and different directions are obtained. Finally, the singular points distributed in the same direction are connected into a contour segment. Among them, NSPFB decomposition makes NSCT with the multiscale. And to use the à Trous algorithm to realize NSDFB makes NSCT with the multi-direction. The organic combination of both makes the NSCT with multi-scale and multi direction of contourlet transform, but also with translation invariance (Figure 1).

IMAGE FUSION BASED ON NSCT

The low frequency parts and high frequency parts can be obtained by the multi-scale decomposition of the image. The low frequency parts represent the approximate components of the image. They mainly reflect the average characteristics of the source image and include spectral information of the source image and most of energy information. The high frequency parts represent the detail components of the image, such as edge, line, region boundary. They descript structure information of the image (Sun et al., 2012).

FUSION STEP

The image fusion specific steps based on NSCT are as follows:

(1) To respectively perform the J level NSCT decomposition of the infrared image I and visible light image V to obtain respective NSCT coefficients for each of the decomposed image: $\left\{C_{j_0}^{I}(x,y), C_{j,l}^{I}(x,y)\right\}(j \geq j_0)$ and $\left\{C_{j_0}^{V}(x,y), C_{j,l}^{V}(x,y)\right\}(j \geq j_0)$, where $C_{j_0}(x,y)$ is the low frequency subband coefficients, $C_{j,l}(x,y)$ is the high frequency subband coefficients in the lth direction under the jth scale.

(2) To use certain fusion rules to perform fusion processing on the different frequency components of each sub-class to obtain NSCT coefficients of the fusion image F: $\left\{C_{j_0}^{F}(x,y), C_{j,l}^{F}(x,y)\right\}(j \geq j_0)$.

(3) To perform the NSCT inverse transform for the fused low frequency subband coefficients and the fused high

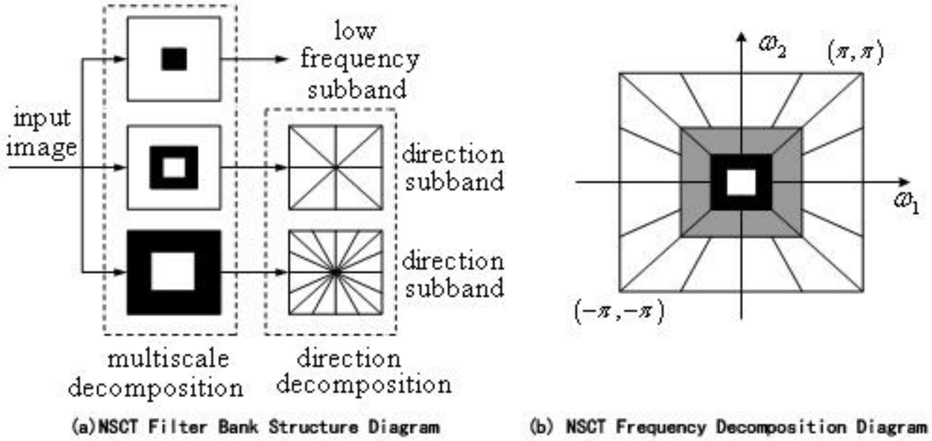

(a)NSCT Filter Bank Structure Diagram

(b) NSCT Frequency Decomposition Diagram

Figure 1. Schematic diagram of NSCT.

frequency direction subband coefficients under the each scale layer to obtain the fusion image F.

FUSION RULES

To select fusion rule is an important link in the image fusion, fusion rules will directly affect the quality of fusion results. The paper chooses the fusion rules based on the regional energy matching degree measure. And the high frequency sub-band and the low frequency sub-band are respectively fused. Regional energy is defined as shown in Equation (1).

$$E_{j_0}^{S}(x,y)=\frac{1}{MN}\sum_{m=-(M-1)/2}^{(M-1)/2}\sum_{n=-(N-1)/2}^{(N-1)/2} w(m,n)\left(C_{j_0}^{S}(x+m,y+n)\right)^2 \qquad (1)$$

In which, the size of $M \times N$ is 3×3, $5 \times 5$and so on (the paper take 3×3), $w(m,n)$ is the window mask. $w(m,n) = [1,2,1;2,4,2,1,2,1]/16$·

Regional energy matching degree is defined as shown in Equation (2).

$$M_{I,V}(x,y)=\frac{\left|\sum_{m=-(M-1)/2}^{(M-1)/2}\sum_{n=-(N-1)/2}^{(N-1)/2} w(m,n)C_{j_0}^{I}(x+m,y+n)C_{j_0}^{V}(x+m,y+n)\right|}{E_{j_0}^{I}(x,y)+E_{j_0}^{V}(x,y)} \qquad (2)$$

Set λ be the threshold value of the regional energy matching degree. Usually λ =0.5 ~ 1. The paper takes 0.7.

Fusion rule for low frequency part

The low frequency part is the approximate description of the source image, containing most information of the source image. Its energy accounted for a larger proportion of total energy of image. And the regional variance of the image reflects the richness of the image information in the local region (Xue et al., 2011). Therefore, the fusion method of the harmony of the energy variance decision selection based on regional energy matching degree and the weighted average is used to select the fusion coefficients of the low frequency subband. Regional variance is defined as shown in Equation (3).

$$V_{j_0}^{S}(x,y)=\frac{1}{(M-1)(N-1)}\sum_{m=-(M-1)/2}^{(M-1)/2}\sum_{n=-(N-1)/2}^{(N-1)/2}\left|C_{j_0}^{S}(x+m,y+n)-\bar{C}\right|^2 \qquad (3)$$

Energy variance decision value is defined as shown in Equation (4).

$$D_{j_0}^{S}(x,y)=E_{j_0}^{S}(x,y)V_{j_0}^{S}(x,y) \qquad (4)$$

If $M_{I,V}(x,y) < \alpha$, then the fusion coefficient is shown in Equation (5).

$$C_{j_0}^{F}(x,y)=\begin{cases} C_{j_0}^{I}(x,y) & if \quad D_{j_0}^{I}(x,y)\geq D_{j_0}^{V}(x,y) \\ C_{j_0}^{V}(x,y) & if \quad D_{j_0}^{I}(x,y)< D_{j_0}^{V}(x,y) \end{cases} \qquad (5)$$

If $M_{I,V}(x,y)\geq\alpha$, then the weighted average is used to perform the fusion of low frequency coefficients. The fusion coefficient is shown in Equation (6).

$$C_{j_0}^{F}(x,y)=\begin{cases} p_1C_{j_0}^{I}(x,y)+p_2C_{j_0}^{V}(x,y) & if \quad D_{j_0}^{I}(x,y)\geq D_{j_0}^{V}(x,y) \\ p_2C_{j_0}^{I}(x,y)+p_1C_{j_0}^{V}(x,y) & if \quad D_{j_0}^{I}(x,y)< D_{j_0}^{V}(x,y) \end{cases} \qquad (6)$$

In which, p_1 and p_2 are adaptive adjustment factor as

Table 1. Fusion rules used in the fusion experiment.

Fusion rule	Lowpass subband	Highpass subband
1	Simple average	Take big Absolute value
2	Simple average	Take big regional variance
3	Energy weighted average	Take big Absolute value
4	Energy weighted average	Take big regional variance
5	The proposed method	

shown in Equation (7)

$$\begin{cases} p_1 = \dfrac{1}{2} - \dfrac{M_{I,V}(x,y)}{2(1-\alpha)} \\ p_2 = \dfrac{1}{2} + \dfrac{M_{I,V}(x,y)}{2(1-\alpha)} \end{cases} \quad (7)$$

Fusion rule for high frequency part

High frequency part represents the detail components of the image, including the source image edge details. For the fusion of the high frequency part, a hybrid fusion rule is used. Because what the low layer reflects is the coarse information, so the fusion method of selecting large regional variance based on the regional energy matching degree is used to maintain the relationship between the pixel neighborhoods better so as to make the edge lines more natural. Because what the high layer reflects is the details and there are great deal of independence among various information, so the fusion method of selecting large absolute value of pixel is used (Ye et al., 2008). The specific fusion rules are as follows:

(1) The high frequency coefficient on the highest layer whose decomposition scale is J (here take J=4) of the fusion image is as shown in Equation (8).

$$C^F_{J,l}(x,y) = \begin{cases} C^I_{J,l}(x,y) & if \quad \left|C^I_{J,l}(x,y)\right| \geq \left|C^V_{J,l}(x,y)\right| \\ C^V_{J,l}(x,y) & if \quad \left|C^I_{J,l}(x,y)\right| < \left|C^V_{J,l}(x,y)\right| \end{cases} \quad (8)$$

(2) The high frequency coefficient on the (J-l) (l≥1) layer whose decomposition scale is (J-l) of the fusion image is fused by the method of selecting larger region variance based on the regional energy matching degree. The fusion rules are as follows: if $M_{I,V}(x,y) < \alpha$, then high frequency coefficient is as shown in Equation (9).

$$C^F_{j,l}(x,y) = \begin{cases} C^I_{j,l}(x,y) & if \quad V^I_{j,l}(x,y) \geq V^V_{j,l}(x,y) \\ C^V_{j,l}(x,y) & if \quad V^I_{j,l}(x,y) < V^V_{j,l}(x,y) \end{cases} \quad (9)$$

Where, $V^s_{j,l}(x,y)$ is the regional variance defined as previously in Equation (3).

If $M_{I,V}(x,y) \geq \alpha$, then the weighted average is used to fuse the low frequency coefficients. The coefficient after the fusion is $C^F_{j,l}(x,y) = q_1 C^I_{j,l}(x,y) + q_2 C^V_{j,l}(x,y)$. In which, p_1 and p_2 are adaptive adjustment factor as shown in Equation (10)

$$\begin{cases} q_1 = \dfrac{E^I_{j,l}(x,y)}{E^I_{j,l}(x,y) + E^V_{j,l}(x,y)} \\ q_2 = \dfrac{E^V_{j,l}(x,y)}{E^I_{j,l}(x,y) + E^V_{j,l}(x,y)} \end{cases} \quad (10)$$

FUSION EVALUATION INDEX AND EXPERIMENTAL RESULT ANALYSIS

To use MATLAB 7.0 to perform programming algorithm based on the above theory and rule can verify the effectiveness of the fusion algorithm for the infrared image and visible light image. The method proposed in this paper was compared with the following several fusion methods as shown in Table 1. The following are the results of the experiments: Figure 2(a) and (b) are respectively for infrared source image and visible light image; Figure 2(c) to (g) are respectively for the fusion image using fusion rule 1~ 5 in Table 1. Four layer NSCT was adopted to perform the image decomposition in the experiment (Figure 1).

To quantitatively evaluate the fusion performance of different fusion methods for infrared image and visible light image, this paper used the standard deviation, information entropy, average gradient and cross-entropy as indexes to assess the fusion method. The standard deviation of the image reflects the discrete degree of the image gray relative to the average gray value. If the standard deviation is large, the image gray level is scattered and image contrast is large. So much information can be seen. The information entropy reflects the richness of the image information. The bigger the information entropy is, the more abundant the information in the image and the better the quality of the image fusion. The average gradient reflects the clear degree of the

(a) Infrared Image (b) Visible Light Image (c) Fusion Rule 1

(d) Fusion Rule 2 (e) Fusion Rule 3 (f) Fusion Rule 4 (g) Fusion Rule 5

Figure 2. Infrared image and visible light image and their fusion images in different fusion rules.

Table 2. Performance evaluation of image fusion.

Parameter	Rule 1	Rule 2	Rule 3	Rule 4	Rule 5
Standard deviation	26.9195	24.8947	29.5481	27.7417	28.4992
Information entropy	6.5389	6.3753	6.7255	6.5935	6.6188
Average gradient	6.0417	5.3719	6.1263	5.4591	6.0444
Cross entropy	0.6181	0.8970	0.8775	1.2636	0.4644

image. And it can reflect the tiny detail contrasts and texture variation characteristics. It is a physical quantity describing the image clarity. The larger the average gradient, the clearer the image, and the more the information being retained. The cross entropy directly reflects the difference between the corresponding pixels of the two images. That cross entropy is smaller illustrates that the difference between the images is smaller and the information which is extracted from the original images by the fused image is more, therefore, the fusion effect is better. The comparison results are shown in Table 2.

As can be seen from Table 2 that no matter from the information entropy, cross entropy, or from the average gradient and standard deviation, the fused image obtained by using the NSCT transform and the fusion rule in this paper to perform fusion of the images is better than one obtained by using other fusion rules.

CONCLUSIONS

By means of the complementary information and redundant information provided by the infrared and visible light images, the noise-signal ratio of the image can effectively be improved and more reliable image information can be obtained. The experiments showed that the fused image obtained by using the method proposed in this paper has more details and better fusion effect.

Conflict of Interests

The author(s) have not declared any conflict of interests.

ACKNOWLEDGEMENT

This work was supported by Program for Innovation Team Building at Institutions of Higher Education in Chongqing (KJTD 201324).

REFRENCES

Lian W, Zhang H, Zhang T (2011). Study on Multi-focus Color Image Fusion Based on Color Space and Wavelet Transform. J. Jiamusi Univer. (Natl. Sci. Edition). 29(6):879-881.

Sun M, Zhang C, Liu J (2012). Fusion of visible and infrared images based on multi-scale image enhancement. J. Jilin Univ. Eng. Technol. Ed. 42(3):738-742.

Tang S (2012). Fusion of Visible Imaging and Infrared Imaging for Multi-mode Composite Guidance, Infrared. 33(2):22-27, 32.

Xue Q, Fan Y, LI H, Wang J, Xiong P, Tang Z (2011). Infrared and Visible Images Fusion Algorithm Based on Curvelet Transform, Comput. Eng. 37(3):224-226.

Yang S, Tian X, Wu C (2012). Multi-focus image fusion scheme based on wavelet transform. J. Xi'an Univ. Posts Telecommun. 17(3):24-29.

Ye C, Wang B, Miao Q (2008). Fusion algorithm of infrared and visible light images based on NSCT transform, Sys. Eng. Electr. 30(4):593-596.

Ye Y, Wang X, Wang Y (2012). Study on the Intelligent Lighting Control System Based on Wavelet Transform and Image Fusion. ZHAOMING C-ONGCHENG XUEBAO 23(3):97-101.

academicJournals

Vol. 9(9), pp. 380-383, 15 May, 2014
DOI: 10.5897/SRE2014.5921
Article Number: F93951144566
ISSN 1992-2248 © 2014
Copyright©2014
Author(s) retain the copyright of this article
http://www.academicjournals.org/SRE

Scientific Research and Essays

Full Length Research Paper

Rural residents' acceptance towards a telehealth system: The integrative perspective of technology acceptance model and social cognitive theory

Chung-Hung Tsai

Department of Health Administration, Tzu Chi College of Technology, Hualien, Taiwan, R.O.C.

Received 3 January, 2013; Accepted 2 March, 2013

The purpose of the study is to integrate technology acceptance model (TAM) and social cognitive theory (SCT) to explore the usage intention model of telehealth systems. A survey of valid 480 users of telehealth was conducted to validate the proposed model. The findings show that computer anxiety has negatively significant effects on computer self-efficacy. Computer self-efficacy has positively significant effects on perceived ease of use. Both computer self-efficacy and perceived ease of use have jointly significant effects on perceived usefulness. In addition, both perceived ease of use and perceived usefulness have positively significant effects on usage intention. This study also confirms that both perceived ease of use and perceived usefulness are important mediators between computer self-efficacy and usage intention. According to the statistical results, the proposed model fits very well for the samples. The integrative viewpoint of this research can provide telehealth designers and managers of the hospital with the implication that hospitals should promote both technological aspect (perceived ease of use and perceived usefulness), and psychosocial aspect (self- efficacy and computer anxiety) simultaneously to increase rural residents' intention of using telehealth.

Key words: Technology acceptance model, social cognitive theory, telehealth system.

INTRODUCTION

Recently, technical suitability, clinical feasibility, and the costs of medical care services have been improved due to the rapid development of information-related technology and biomedical technology. Currently, many countries have attempted to apply information technology to telehealth and to develop other functions, such as the emergency notification of unusual events, medication reminders, physiological recording and monitoring, remote video, and medical consultation by combining medical care and information technology. It is expected that these will reduce medical costs, lower labor costs, and become one of the important potential industries.

Technology acceptance model (TAM) is a well-accepted intention model for predicting and explaining IT (Information Technology) usage. TAM has been found more favorable in many studies (Venkatesh, 2000). Because TAM is a well-defined model, the proposed model of the study is based on this model to explore the intention to use a telehealth system in Taiwan. In addition, computer self-efficacy and computer anxiety of social

E-mail: tsairob@tccn.edu.tw

cognitive theory (SCT) (Bandura, 1977) can also provide good ability in predicting people's behaviors in using new technology. This study is therefore aimed, on the bases of TAM and SCT, to discuss the behaviors of the residents in a rural community in using telehealth and to understand the factors which affect their use of telehealth, thus popularizing the use of telehealth in a community.

LITERATURE REVIEW

Telehealth

Telehealth refers to the remote exchange of data between a patient (usually at home) and healthcare professionals (at a monitoring center) to assist in the management of an existing long-term condition (Hendy and Barlow, 2012). Telehealth has been considered a partial solution to the problems of delivering health care to remote areas as well as to areas underserved by health care professionals (Miller et al., 2003). The devices monitor vital signs of patients (or rural residents) including blood pressure, blood glucose, blood oxygen, and weight.

Technology acceptance model (TAM)

The Technology Acceptance Model (TAM) is the most widely applied model of user acceptance and usage. TAM identifies two relevant beliefs, that is, perceived ease of use and perceived usefulness. Perceived ease of use is defined as the extent to which an individual believes that using the system will be free of effort, while perceived usefulness is defined as the extent to which an individual believes that using the system will enhance the job performance. According to TAM, the behavioral intention is determined jointly by perceived ease of use and perceived usefulness. Furthermore, perceived usefulness is also influenced by perceived ease of use and external variables. TAM has been widely applied in practice, extended in academics, and empirically tested in the field of information management in the last decade (Venkatesh, 2000).

Social cognitive theory (SCT), computer self-efficacy, computer anxiety

Social Cognitive Theory (SCT) emphasizes the role of self-referent thinking in guiding human motivation and behavior. SCT is a theoretical framework for analyzing human motivation, thought, and action that embraces an interact model of causation in which behavior, cognition and other personal factors, and environment influences all operate as interacting determinants that influence each other bidirectionally (Bandura, 1977).

Computer self-efficacy is a special application of the more general construct of self-efficacy, which is a key element of SCT. Compeau and Higgins (1995) defined computer self-efficacy as "people's judgments about their abilities to use a computer system successfully". According to Venkatesh (2000), computer self-efficacy is the important determinants of perceived ease of use. Some studies have also found a positive relationship between computer self-efficacy and perceived usefulness (Mathieson, 1991).

According to SCT, anxiety is an emotional arousal that is caused partly by fear of aversive physiological reactions (Bandura, 1977). Computer anxiety refers to a feeling of apprehension or anxiety toward using computers. Computer anxiety is associated with negative perceptions about computers, problems in playing with them, and avoidance of the technology (Igbaria and Iivari, 1995). Igbaria et al. (1996) proved that computer anxiety is negatively related to computer usage, perceived usefulness, perceived enjoyment, and social pressure. Also, van Raaij and Schepers (2008) have shown that computer anxiety has negatively direct effects on perceived ease of use. In addition, previous empirical studies have repeatedly observed the relationship between computer anxiety and computer self-efficacy as negative and strong (He and Freeman, 2010). The previous arguments support the proposed research model depicted in Figure 1.

METHODOLOGY

We adopted the Likert-type questionnaire survey for data collection, and examined our hypotheses by applying the structural equation modeling (SEM) method to validate the model. The measurement instruments for variables in the questionnaire were developed from previous studies to enhance the variability and reliability.

The survey subjects of the questionnaire were those rural residents who are the end users of a telehealth system from Nantou County, Taiwan. The first generation of telehealth system was developed and installed by a community hospital in Jhushang township, namely Chu Shang Show Chwan Hospital in 2009. Recently, the new generation of telehealth system is running and these respondents all have used the system for at least one month since 2012.

RESULTS

The data analysis proceeds according to the two-step approach recommended by Anderson and Gerbing (1988). First, we assess the measurement model, which consists of the five latent factors, and includes the assessment of reliability, discriminant validity, and convergent validity of the scales. Second, we validate the structural model, which represents the series of path relationships linking the five constructs.

Sample characteristics

Of the recruited 500 subjects, there were 480 subjects

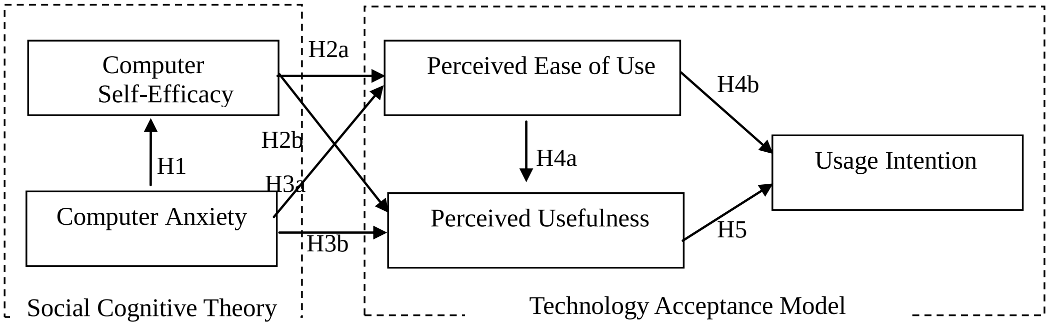

Figure 1. The proposed research model.

Table 1. Construct reliability and convergent validity.

Construct	Cronbach's α	Composite reliability	Average variance extracted
Computer Self-Efficacy	0.976	0.976	0.933
Computer Anxiety	0.975	0.975	0.929
Perceived Ease of Use	0.992	0.991	0.983
Perceived Usefulness	0.957	0.957	0.882
Usage Intention	0.970	0.970	0.942

who agreed to participate in the study. Of these respondents, 262 respondents are women (54.6%) and 218 respondents are men (45.4%). Most of the respondents were 71 to 80 years of age (48.2%). Most respondents hold elementary school degrees (54.4%). A majority of the caregivers are spouses (40.2%). The respondents mostly suffered from at least one chronic disease (69.4%).

Measurement model results

To validate the measurement model, three types of validity were assessed: content validity, convergent validity, and discriminant validity. Content validity was done by interviewing senior system users and pilot-testing the instrument. And the convergent validity was validated by examining Cronbach's α, composite reliability and average variance extracted from the measures (Hair et al., 1998). As shown in Table 1, the Cronbach's α of every subscale range from 0.957 to 0.992 was above the acceptability value 0.7. Moreover, the composite reliability values, which ranged from 0.957 to 0.991, and the average variances extracted by our measures, which ranged from 0.882 to 0.983, are all within the commonly accepted range greater than 0.5. In addition, all measures are significant on their path loadings at the level of 0.001. Therefore, the convergent validities of all five constructs are confirmed.

In addition, discriminant validity can be tested among all constructs by comparing the average variance extracted (AVE) of each construct with the squared correlation of that construct and all the other constructs. All squared correlations between two constructs are less than the average variance extracted of both constructs. Therefore, the results confirm that the discriminant validity of the constructs in the study is satisfactory.

Structural model results

To validate the measurement model, we used AMOS 8.0 to assess the analysis. As shown in the Table 2, the goodness-of-fit indices are within the accepted thresholds. Generally, these fit indexes are all greater than or equal to 0.9 for Goodness Of Fit Index (GFI), Adjusted Goodness Of Fit Index (AGFI), Normed Fit Index (NFI), Comparative Fit Index (CFI). Furthermore, χ^2/d.f. value is less than 3 and RMSEA value is less than 0.08. Accordingly, the summary of the overall goodness-of-fit indices indicate an excellent fit of the model and data.

Table 3 illustrates the results of the structural model with the estimated standardized path coefficients and path significance among constructs (non-significant paths as dotted lines). As predicted, almost all proposed hypotheses except for H_{3a} and H_{3b} are supported. However, computer anxiety has insignificant effect on perceived ease of use and perceived usefulness (H_{3a} and H_{3b}). The unexpected finding can be explained that the residents have enough resources about telehealth system from the community hospital (Chu Shang Show Chwan Hospital), such as explanation sessions, training

Table 2. Fit Indices for the structural model.

Structural model statistic	Fit indexes	Recommended threshold
χ^2 / d.f	2.988	< 3
GFI	0.949	> 0.9
RMSEA	0.064	< 0.08
AGFI	0.919	> 0.9
NFI	0.982	> 0.9
CFI	0.988	> 0.9

Table 3. Hypotheses validated results.

Path	Results	Standardized path estimate
H1 Computer Anxiety → Computer Self-Efficacy	Supported	-0.500***
H2a Computer Self-Efficacy → Perceived Ease of Use	Supported	0.634***
H2b Computer Self-Efficacy → Perceived Usefulness	Supported	0.142*
H3a Computer Anxiety → Perceived Ease of Use	Not Supported	-0.062
H3b Computer Anxiety → Perceived Usefulness	Not Supported	-0.050
H4a Perceived Ease of Use → Perceived Usefulness	Supported	0.331***
H4b Perceived Ease of Use → Usage Intention	Supported	0.205***
H5 Perceived Usefulness → Usage Intention	Supported	0.477***

*** path is significant at the 0.001 level, ** path is significant at the 0.01 level, * path is significant at the 0.05 level.

courses and community volunteers. If the residents feel themselves unable to use the system, they may request the community nurses or volunteers to show the usage processes directly. Therefore, computer anxiety of the residents may not impact significantly on perceived ease of use and perceived usefulness of telehealth system.

Conclusion

The findings of this study suggest that both perceived ease of use and perceived usefulness are two important antecedents that directly influence behavioral intention to use the telehealth system. In addition, computer self-efficacy has significantly positive effects on perceived ease of use, and perceived usefulness separately. Furthermore, both computer anxiety and computer self-efficacy have significant impacts on usage intention mediated by perceived ease of use, and perceived usefulness. The integrative viewpoint implies that hospitals should promote both technological aspect (perceived ease of use and perceived useful), and psychosocial aspect (self-efficacy and computer anxiety) simultaneously, to increase rural residents' intention of using telehealth. We believe that the integrative perspective of TAM and SCT applied in future studies should provide more valuable and informative contributions toward development of successful telehealth.

REFERENCES

Anderson JC, Gerbing DW (1988). Structural equation modeling in practice: A review and recommended two-step approach. Psychol. Bull. 103(3):411-423. http://dx.doi.org/10.1037/0033-2909.103.3.411

Bandura A (1977). Self-Efficacy: Toward a unifying theory of behavioral change. Psychol. Rev. 84(2): 191-215. http://dx.doi.org/10.1037/0033-295X.84.2.191

Compeau DR, Higgins CA (1995). Computer self-efficacy: Development of A Measure and Initial Test. MIS Quart. 19:189-211. http://dx.doi.org/10.2307/249688

Hair JF, Anderson RE, Tatham RL, Black WC (1998). Multivariate Data Analysis. NJ: Prentice Hall.

He J, Freeman LA (2010). Understanding the formation of general computer self-efficacy. Commun. Assoc. Inf. Syst. 26:225-244.

Hendy J, Barlow J (2012). The adoption of telecare in the community. Community Practitioner 85(3):41-43. PMid:22479805

Igbaria M, Iivari J (1995). The effects of self-efficacy on computer usage. Omega 23:587-605. http://dx.doi.org/10.1016/0305-0483(95)00035-6

Igbaria M, Parasuraman S, Baroudi JJ (1996). A motivation model of microcomputer usage. J. Manage. Inf. Sys. 13(1):127-143.

Mathieson K (1991). Predicting user intentions: Comparing the technology acceptance model with the theory of planned behavior. Inf. Sys. Res. 2(3):173-191. http://dx.doi.org/10.1287/isre.2.3.173

Miller TW, Miller JM, Kraus RF, Kaak O, Sprang R, Veltkamp LJ (2003). Telehealth: A clinical application model for rural consultation. Consult. Psychol. J. Pract. Res. 55:119-127. http://dx.doi.org/10.1037/1061-4087.55.2.119

van Raaij EM, Schepers JJL (2008). The Acceptance and use of a virtual learning environment in China. Comput. Edu. 50(3):838-852. http://dx.doi.org/10.1016/j.compedu.2006.09.001

Venkatesh V (2000). Determinants of perceived ease of use: Integrating control, intrinsic motivation, and emotion into the technology acceptance model. Inf. Sys. Res. 11(4):342-365. http://dx.doi.org/10.1287/isre.11.4.342.11872

academicJournals

Vol. 9(9), pp. 384-390, 15 May, 2014
DOI: 10.5897/SRE2014.5950
Article Number: E866CEE44568
ISSN 1992-2248 © 2014
Copyright©2014
Author(s) retain the copyright of this article
http://www.academicjournals.org/SRE

Scientific Research and Essays

Full Length Research Paper

Safe and efficient mining technology for full-mechanized caving face of deep mine with capacity of ten million tons

Ma Liqiang[1,2,3], Sun Hai[1,2,3], Jin Zhiyuan[1,2,3]*, Wang Fei[1,2,3] and Li Pan[1,2,3]

[1]School of Mines, China University of Mining and Technology, Xuzhou, Jiangsu 221116, China.
[2]Sate Key Laboratory of Coal Resource and Safe Mining, Xuzhou, Jiangsu 221116, China.
[3]Key Laboratory of Deep Coal Resource Mining, Ministry of Education of China, Xuzhou, Jiangsu 221116, China.

Received 3 January, 2014; Accepted 2 March, 2014

Based on a highly intensive mining mode of "one mine, one coalface, ten million tons", safe and efficient mining technology for full-mechanized caving face of deep mine with capacity of ten million tons is proposed to deal with technical problems such as high ground pressure, high ground temperature, high water pressure and easy spontaneous combustion of coal seam in Longgu coal mine. The surrounding rock control technology was researched to effectively control the high ground pressure. The treatment and utilization technology for high temperature and heat hazard was initiated to lower the average temperature in main workplaces by 8 L. The treatment and utilization technology of high-pressure massive water gushing was adopted to ensure safe mining under the condition of 8 MPa water pressure in deep mine. A precautionary and preventive technology for spontaneous combustion of coal seam of "coal body inhibition + air-leakage control + local inerting" is proposed to stop spontaneous firing of coalface in high ground temperature. The research results have effectively solved the technical difficulties and have realized safe and efficient production for deep mine with capacity of ten million tons.

Key words: Deep mine, high ground pressure, high ground temperature, high water pressure, easy spontaneous combustion.

INTRODUCTION

Among the coal reserves in China, those with the burial depth of over 1,000 m reach 2.95 trillion tons, which account for about 53% of the total. The average mining depth in China is increasing at a rate of 8~12 m/a. After the mines have been explored further deeply, mine production is generally made more difficult due to high strata pressure, growth of water gushing, and increased ground temperature (Wan et al., 2013).

Longgu coal mine covers an area of about 180 km^2 and has geological reserves of 1.68 billion ton. With 2301 coalface as its demonstration project, Longgu coal mine researches the mining technology for full-mechanized

---

*Corresponding author. E-mail: ckma@cumt.edu.cn

Figure 1. ZF15000/23/43hydraulic support.

caving face with capacity of ten million tons under the conditions of high ground pressure, high ground temperature, high water pressure, and easy spontaneous combustion, having formulated highly productive and efficient production technology for coalface with burial depth of 1,000 m to ensure coal output of ten million tons.

TECHNICAL DIFFICULTIES

Located -810 under the ground, the 2301 coalface of Longgu coal mine has an average burial depth of nearly 1,000 m, inclined length of 256 m, and strike length of 1,600 m. The main mining coal seam is No.3 coal seam, with coal thickness of 3.6~10.4 m (average: 9.2 m). The average thickness of thin bedrock on the coal seam is about 200 m, but there is extremely thick alluvium with an average thickness of 700 m on the bedrock. Long-wall method of full-mechanized caving is adopted, with mining height of 4.0 m, roof caving height of 5.2 m.

(1) High ground Pressure: The burial depth of mining roadway project is rather deep, and the roadway is overlaid with thin bedrock of extremely thick alluvium, which makes the supporting difficult.
(2) High ground temperature: The original rock temperature in the mining area is up to 46 L. The air temperature of the coalface is even above 35 L and its humidity reaches 95%.
(3) High water pressure: Aquifer is mainly the sandstone of roof and floor, and limestone of floor for No.3 coal seam, with water pressure up to 8 MPa.
(4) Easy spontaneous combustion: Because of the relatively higher ground temperature, the 34-day period of spontaneous combustion of coal seam is shortened to 29 days.

KEY TECHNOLOGY

Stability control of surrounding rocks

Structural features and movement law of overlying strata

Structural features and movement law of overlying strata of coalface were researched by using UDEC numerical simulation software (Qian et al., 1994; Itasca Consulting Group Inc., 2003). The results showed that the stress concentration factor of the largest vertical stress at the bottom of thick alluvium is about 1.15. With its weak self-carrying capacity, thick alluvium have integrated feature in the process of mining unloading, which means that the whole deposits sink to be tightly pressed with whole bearing capacity.

For thin bedrock thicker than 120 m, though impacted by thick alluvium loading, its caving zone height is about 25 m and the height of the fractured zone is about 105 m, which enable the bedrock to form a stable structure with loading capacity so that the roof face would not press in the form of “cut down by full thick”. The bedrock (fractured zone strata) can form a stable structure with loading capacity (Jin et al., 2013). The overlying thin bedrock can form a structure with loading capacity to transfer the pressure of surrounding rocks to the two sides of the mining area so as to ease the pressure of supports in the coalface.

Support selection

No.3 coal seam is medium hard but relatively soft coal seam (*f* = 1.44). If two-pillar full-mechanized rack is used, the head of the support is easy to go upward so that it is hard to control rib spalling and roof falling. The largest domestic four-pillar full-mechanized support ZF15000/23/43 for its working resistance is researched and developed since the two-pillar support is unreasonable for its improper position which results in difficulties in controlling the roof, as is shown in Figure 1.

Roof control

139 groups of sublevel top-coal carving hydraulic support ZF15000/23/43 are equipped on the coalface, with one group of transition support ZF15000/23/43 on both upper and lower sides, three groups and four groups of transition support ZFG15000/23/43F on the upper and lower sides respectively, and 148 groups of supports on the whole (Fang and Qian, 2006).

The average first weighting interval of the main roof is 36 m. During the period of initial weighting, the average circulation resistance is 13,300 kN, the support strength is 1.29 MPa, and the dynamic load coefficient is 1.40. The periodic weighting length of main roof is 19.6 m.

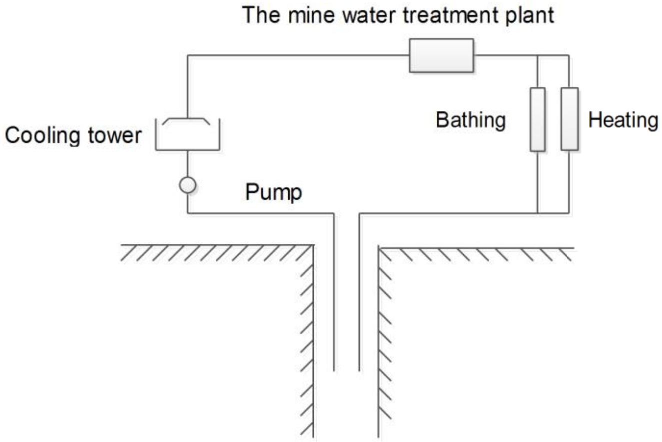

Figure 2. Centralized cooling and geothermal utilization.

During the periodic weighting, the average support resistance is 12,751 kN, the average support strength is 1.24 MPa, which is 85 % of the rated support strength.

Treatment and utilization of geothermal

Initiation of centralized cooling by pipes buried underground and geothermal utilization

The underground mine installed two refrigeration units KM3000 with refrigeration capacity of 6,600 kW. To solve the difficulty in discharging condensing heat of the intensive refrigeration model in the mine, surface borehole was initiated to establish a circulation system of the utilization of geothermal with high temperature, which are mainly responsible for bringing condensing heat in the mine back to the surface, through which condensing heat in the mine is discharged by taking the used waste heat back to the mine for recycling after it has been naturally cooled by cooling tower. The utilization system of refrigerated waste heat was established in the cold water circulation system to convert harm into benefit so as to use the waste heat in the mine, as is shown in Figure 2.

Not restricted by pipe diameter, the two refrigeration pipelines under the separate drilling holes can meet the demand of cooling in the mine; the freely selected drilling position and the cooling load center placed in the cooling chambers in the mine can greatly reduce the cold energy loss in the process of delivering chilled water; the minimum cold energy loss and the low temperature of water supply at the end of air cooler equipment enable the efficient cooling and the saving of operation cost (Du et al., 2013).

Integrated optimization of various cooling models

In light of the total cooling demand of 11,000 kW in the mine, multiple mine cooling models such as the centralized cooling by pipes buried underground, the freezing and low-temperature radiation cooling and the cooling of water-source heat pump have been established and all technologies have undergone integrated optimization. In combination with the optimized wind-blowing and cooling technology for the coalface under the mine, the integrated utilization of all cooling models has effectively solved the heat hazard in the main mining workplaces under the mine such as the coal coalface, roadway heading face, roadway, chambers and pumping rooms, etc., having realized the comprehensive cooling of the whole mine and lowered the average temperature in the main mining workplaces by 8 L so as to create a good working environment in the mine.

Treatment and utilization of high-pressure massive water

Water drainage and pressure decrease in deep mine

According to the evolution law of the water pressure of the mining-induced fissure and pore space, drilling sockets for water drainage of the limestone and sandstone were installed at intervals of 200 m in the No.1 supplementary mine and the main roadways in No.2 supplementary mine (Hu et al., 2011). There were in total 20 drainage holes for the limestone and 10 for the sandstone. Meanwhile, along the transport entry and tail entry on 2301 coalface there are 26 drainage holes, 3 of which were for the limestone. The discharge amount of each hole was designed to be 30 m^3/h, which enables an accumulative discharge amount of 900 m^3/h for the limestone.

Since its operation in November 2006, the plan of water drainage and pressure decrease has reduced the water pressure -810 m from 8 MPa to about 2.8 MPa. The superpositioning and drainage and decrease effects of group holes in the process of water drainage and pressure decrease are shown in Figure 3. The water pressure of the limestone in No.1 league roadway is 2.1 MPa, as is shown in Figure 4. The water pressure of limestone and sandstone is greatly reduced and safe mining is strengthened.

Quick grouting and sealing

On the basis of water drainage and pressure decrease, quick grouting and sealing technology was used for water-conducting channels with local advantages in the process of mining and heading. Since the water outflow after the heading, five locations are applied grouting and sealing and 68 drilling holes are constructed with a total drilling depth of over 6,228 m, over 538 tons cement grouted, over 119 tons water glass, and over 60 tons chemical serum.

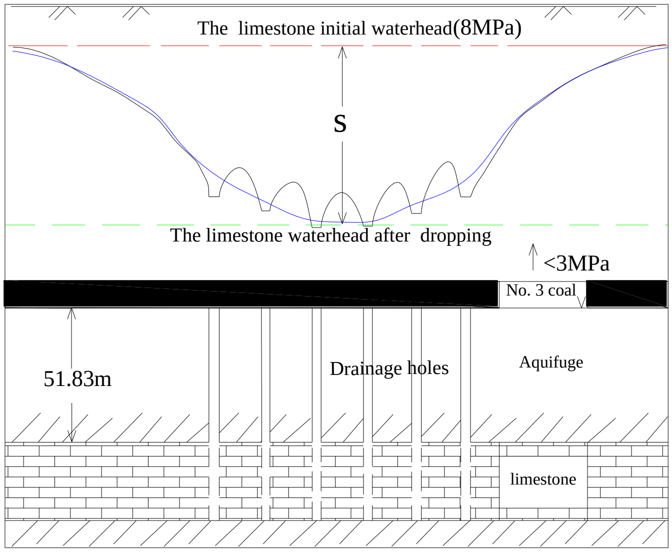

Figure 3. Design sketch of drained limestone.

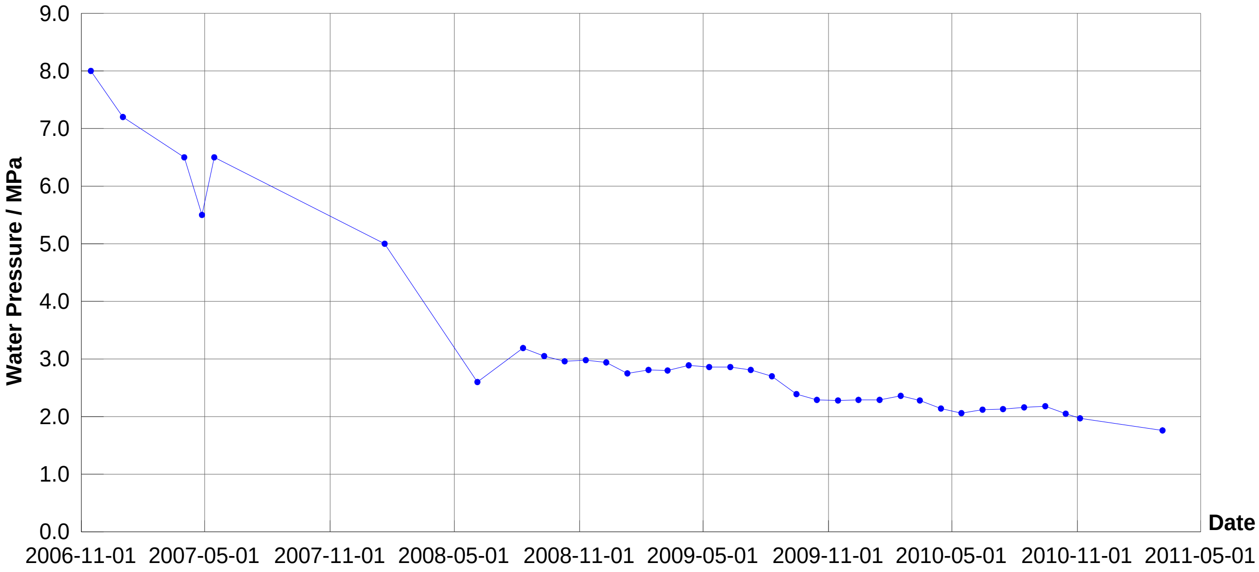

Figure 4. Water pressure of limestone corresponding to water drainage and pressure decrease.

The effectively decreased water pressure of the roof and floor of the aquifer by previous water drainage and pressure decrease creates a good condition for the quick grouting and sealing through water-conducting channels with local advantages to achieve good grouting effects and further improves the mining conditions of 1,000 m deep mine. The operation of water sealing is shown in Figure 5.

Highly efficient water drainage system

The key for large water gushing is to establish highly efficient water drainage system. Five (5) pumps of PJ200 × 10 were installed in the central pump room of the mine, while 6 pumps of PJ200 × 10 were installed in the pump room for expanded drainage. The water drainage pump can supply the largest water gushing volume of 3,150 m^3/h. The effective volume of -810 mine sump is 5,067 m^3; that of the mine sump for expanded drainage is 7,685 m^3; the volume for mine sump totals 12,752 m^3.

Recycled utilization of mine water

For integrated treatment of the mine water, water

Figure 5. Schematic diagram for operations of grouting and water sealing in the mine.

treatment plant was established to adopt the combined technology of clarification, filtration and disinfection corresponding with the quality of the mine water and the requirements on the quality of outflowing water (Vosloo et al., 2011). Water treatment capacity is 1,000 m^3/h. The quality of inflowing water with a pH value ranges from 7 to 9, SS (suspended matter) = 300~400 mg/L, $COD_{Cr} \leq$ 600 mg/L. The index for treated mine water with a pH value ranges from 6.55 to 8.5, SS ≤ 5 mg/L, $COD_{Cr} \leq 50$ mg/L, particle size of suspended matter (mm) ≤0.3. The treated mine water is used by coal preparation plants for water pumping, circulation water for water source heat pump, fire-fighting sprinkling in the mine, grouting water for fire-prevention, and systematic cleaning of ground production.

Prevention for spontaneous firing of coalface with high ground temperature

Spontaneous combustion nature of coal under conditions of high ground temperature

From the experiment on spontaneous combustion of coal fired 2 t by using the “XK-β type” laboratory table of coal spontaneous combustion at low temperatures, the conclusion that the spontaneous combustion period of tested coal sample is shortened from 34 to 29 days is drawn and regular patterns of fastening spontaneous combustion oxidation at high ground temperature are discovered.

Distribution of “three zones” in Goaf

According to the superpositioned isoline mapping of the thickness of suspended coal, oxygen concentration and air-leakage intensity distribution, a static “three zones” distribution in Goaf of the 2301 coalface (workface) was made, as is shown in Figure 6.

When the heading speed of the coalface is less than 87.8 m per month, there is a danger of spontaneous combustion in the upper gate road. The “two roads” of serious air leakage are important areas to prevent combustion (Adamus et al., 2011).

Integrated technology for preventing and extinguishing fire

i) Coal Body Inhibition: By experimental analyses on the elements and constituents of yellow mud, pulping effect is the best at an optimal serum proportion of 4:5~1:1. According to the spontaneous combustion nature of coal on the 2301 coalface, a mobile and multi-functional fire-proof grouting system integrating grouting, colloidal gel grouting, composite gel grouting and pressure infusion of high polymer gel is developed on the basis of the testing of the spontaneous combustion nature of coal and on-the-spot observations of “three zones” distribution in Goaf.

Based on the actual need on the spot, the mobile and multi-functional fire-proof grouting system can prevent and extinguish fire by grouting such fire extinguishing materials as common slurry, colloidal gel, composite gel, and high polymer gel, etc. Without excessively long transport pipelines for slurry, the mobile and multi-functional fire-proof grouting system, by which grouted slurry can reach the target areas quickly, and can achieve effects of preventing and extinguishing fire at the quickest speed when combined with measures of air-leakage control and local inerting (Boleslav and Zdeněk, 2011).

ii) Air-leakage control: For each roadway heading of 40 m, the coal sack with the carving width of about 2 m at the upper corner of intake entry is injected with nitrogen through grouting pipelines, and it takes 8 h to infuse nitrogen each day.

iii) Local Inerting: According to the “three zones” distribution, optimal grouting conditions, intervals of nitrogen injection openings, nitrogen injection time and transition period of nitrogen injection openings are confirmed.

Nitrogen exit should be at the spontaneous combustion area of oxidized risky zones of spontaneous combustion in Goaf. According to the “three zones” distribution, the shortest distance between zones of spontaneous combustion and coalface is 20 m and the longest distance

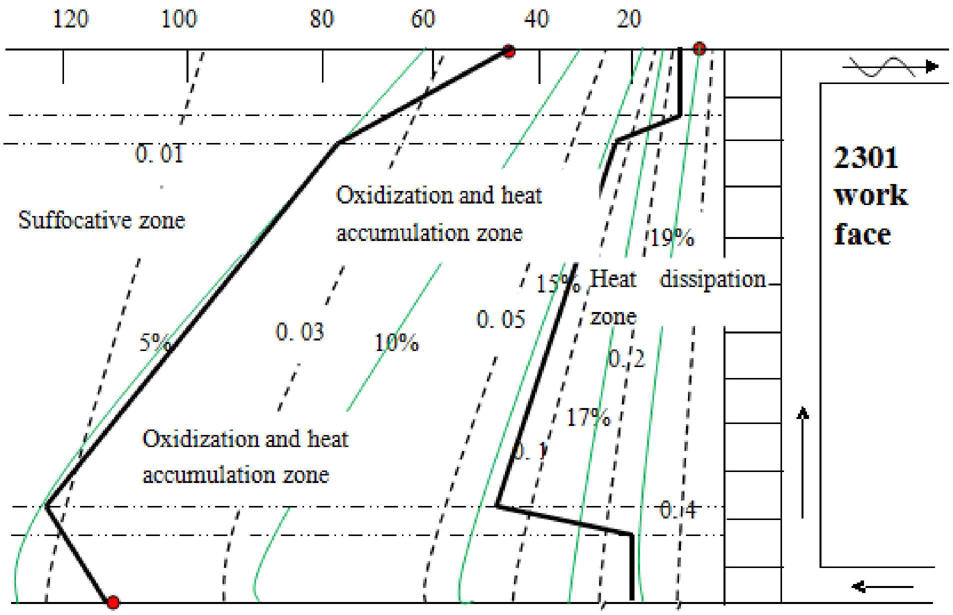

Figure 6. Schematic diagram for “three zones” distribution in Goaf.

is 120 m. The width of zones of spontaneous combustion of coalface is 100 m, within which the nitrogen exit should be placed to inject nitrogen.

IMPLEMENTATION EFFECT

The longgu coal mine was officially put into operation in November, 2009. The 2301 coalface began its operation in the morning shift on 18th, November, 2010. Its annual capacity has reached 10 Mt in 2011. The highest daily yield is 33 thousand tons, and the death rate of coal production of one million tons is zero. The work efficiency of coalface is 100.7 t per miner. The work efficiency of the staff in the mine is 9.3 t per miner.

Conclusions

(1) Features of support stress and support resistance are confirmed. Full-mechanized mining support ZF15000/23/43, face-end support ZTZ20000/25/50, and ahead support rack ZTC30000/25/50 are used to effectively control the coalface surrounding rock with high ground pressure.

(2) Centralized cooling model by high-power pipes buried underground was initiated to transfer condensing heat in the mine to the earth’s surface for recycling and further utilization. The largest integrated mine cooling system in China was established, having realized overall cooling of the mine so as to meet the demand of production.

(3) The technology of water drainage and pressure decrease in deep mine by “group-hole - large flow - long delaying - interfering mine” has achieved safe mining under the condition of 8 MPa roof and floor water pressure.

(4) The precautionary and preventive technology for spontaneous combustion of coal seam of “coal body inhibition + air-leakage control + local inerting” is proposed to fit coalface with capacity of ten million tons in high ground temperature.

Conflict of Interests

The author(s) have not declared any conflict of interests.

ACKNOWLEDGEMENTS

This work was supported by “the Fundamental Research Funds for the Central Universities (China University of Mining and Technology) with the project number 2014YC01, and Project Funded by the Priority Academic Program Development of Jiangsu Higher Education Institutions (number: SZBF2011-6-B35).

REFERENCES

Adamus AJ. Sancer PG, Zubicek V (2011). An investigation of the factors associated with interpretation of mine atmosphere for spontaneous combustion in coal mines. Fuel Process. Technol. 92(3):663-670. http://dx.doi.org/10.1016/j.fuproc.2010.11.025

Boleslav T, Zdeněk M (2011). Effect of longwall coalface advance rate on spontaneous heating process in the gob area - CFD modeling. Fuel. 90(8):2790-2797.http://dx.doi.org/10.1016/j.fuel.2011.03.033

Du PGE, Liebenberg L, Mathews EH (2013). Case study: The effects of a variable flow energy saving strategy on a deep-mine cooling system". Appl. Energy 102(SI):700-709.

Fang X-Q, Qian M-G (2006). Theory and application of monitor system about support-surrounding rocks in fully-mechanized mining with top coal caving. Progress Saf. Sci. Technol. Ser. (ISSST2006) 6:1777-1781.

Hu L-T, Chen C-X, Chen X-H (2011). Simulation of groundwater flow within observation boreholes for confined aquifers. J. Hydrol. 398(1-2):101-108. http://dx.doi.org/10.1016/j.jhydrol.2010.12.013

Itasca Consulting Group Inc. (2003). Universal Distinct Element Code User's Guide." Minneapolis, USA: Itasca Consulting Group Inc.

Jin Z-Y, Zhang D-S, Ma L-G, Xu M-T, Wang F-T (2013). Breaking mechanism of longwall mining face roof under room-and-pillar goaf of shallow-buried short distance coal seams and its control." Disaster Adv. 6(S5):208-215.

Qian M-G, Miao X-X, He F-L (1994). Analysis of key block in the structure of voussoir beam in longwall mining. J. China Coal Soc. 19(6):557-563.

Vosloo J, Liebenberg L, Velleman D (2011). Case study: Energy savings for a deep-mine water reticulation system. Appl. Energy. 92:328-335. http://dx.doi.org/10.1016/j.apenergy.2011.10.024

Wan Z-J, Zhang Y, Cheng J-Y, Zhou C-B, Gu B, Zhou P (2013). Mine geothermal and heat hazard prevention and control in China. Disaster Adv. 6(S5):85-93.

academicJournals

Vol. 9(9), pp. 391-399, 15 May, 2014
DOI: 10.5897/SRE2014.5951
Article Number: AA953F244570
ISSN 1992-2248 © 2014

http://www.academicjournals.org/SRE

Scientific Research and Essays

Full Length Research Paper

Characterization of WPI-NaCas composite films modified by transglutaminase

Lei Qiao[1,2], Pan Jiazhen[1]*, Huang Zhiying[2], Bao Jianqiang[2] and Xun Qiannan[2]

[1]School of Mechanical and Power Engineering, East China University of Science and Technology, Shanghai 200237, China.
[2]College of Food Science and Technology, Shanghai Ocean University, Shanghai 201306, China.

Received 3 January, 2013; Accepted 2 March, 2013

Synergistic effects of additive amount, reaction time and temperature of transglutaminase on properties of WPI-NaCas composite protein films were discussed by orthogonal experiments. Results indicated that transglutaminase (TGase) modification decreased D50 and D90 of film-forming solution particles, resulting in decrease in water solubility and increase in both mechanical and water barrier properties of films under most conditions. Compared with control sample, scanning electron microscope analysis indicated that cross-section of enzyme modification sample was denser and more impermeable. However, there was no significant difference in both thermogravimetric analysis and solution apparent viscosity changes for all samples. Orthogonal experiment results also showed that TGase reaction time was the most effective factor on tensile strength (TS) and water vapor permeability (WVP) properties of film, and the secondary, tertiary factors were reaction temperature, TGase additive amount respectively. Films modified by 0.1 mg/ml TGase at 50°C for 30 min exhibited the optimum mechanical and water barrier performance.

Key words: Transglutaminase (TGase), mechanical properties, water vapor permeability (WVP), scanning electron microscopy analysis.

INTRODUCTION

Edible films receive great attention in recent years because of the increasing consumer demand for high quality foods, the need of food processing for new storing technology, dealing of non-renewable food packaging materials and the use of agricultural waste products for film-forming components (Ferreira et al., 2009; Liu et al., 2006). Among various edible films, great interest is given to protein based films because of their moderate barrier properties of water, oil volatile components, selective gas permeability and unique nutritional functions. Proteins are polymers with specific amino acid sequences and molecular structure. Depending on the sequential order of the amino acids, the protein will assume different structures along the polymer chain which will determine the secondary, tertiary, and quaternary structures. The secondary, tertiary, and quaternary structures of proteins can be easily modified to optimize the protein configuration, protein interactions, and resulting film

---

*Corresponding author. E-mail: jzpan@ecust.edu.cn

properties. Films based on proteins are edible or biodegradable, depending on formulation, formation method, and modification treatments. As long as food-grade proteins and additives are used only protein changes due to heating, pH modification, salt addition, enzymatic modification, and water removal occur, the resulting film is edible (Baldwin et al., 2012).

Whey protein isolate (WPI) obtained from whey-a co-product of cheese-making and casein manufacture in the dairy industry, consists of special nutritional composition and exhibits good film forming characteristics, while WPI-based films shows excellent oxygen barrier at low or intermediate RH (Oses et al., 2009).

Sodium caseinate (NaCas) is one kind of soluble calcium phosphate compound, which contains a variety of amino acids and trace elements that the human body needs, showing good film forming properties and water solubility (Yu et al., 2009). Caseins form films from aqueous solutions without further treatment due to their random-coil nature and their ability to hydrogen bond. Extensive hydrogen and electrostatic bonds and hydrophobic interactions facilitate the formation of intermolecular interactions to form casein edible films.

WPI-NaCas based edible films show better barrier properties of gas, optical properties, water solubility, but lower mechanical properties and barrier properties of water vapor than polyethylene (PE) due to a synergistic effect (Chen and Lei, 2011).

Transglutaminase (TGase) is a kind of bio-enzyme and can catalyze the formation of covalent linkage through an acyl-transfer reaction intra- or inter- protein molecular to changing structure of protein, forming high polymer and improving properties of protein, thereby ameliorating the rheology and sensory characteristics of food (Kuraishi et al., 2001; Mahmoud and Savello, 1993; Motoki et a., 1987; Nielsen et al., 1995). Research also showed that TGase could ameliorate the properties of edible films, for example improving tensile strength, elongation at break and decreasing moisture content, water vapor permeability of soy protein isolate- wheat gluten edible film (Wang et al., 2009). TGase has been used to decrease the solubility of the films (Carvalho and Grosso, 2004; Yildirim and Hettiarachchy, 1998). However, the results (regarding the effect of cross-linking), using TGase, on the water vapor permeability (WVP) and mechanical properties were inconsistent, probably due to different protein components of the films, various conditions of enzymatic reaction and preparation of films.

Our previous experiments by uniform design method showed that the edible WPI-NaCas films were smooth, transparent and showed acceptable mechanical properties and good barrier properties to gas higher than PE. The increases of WPI concentration resulted in a decrease in water solubility and gas barriers. Sodium caseinate was efficient for improving transparency and water solubility, though decreasing the barrier properties to some extent. The addition of glycerol provoked an increase of elongation, water solubility and flexibility, while film tensile strength exhibited a reverse trend. Films prepared with 5% whey protein isolate, 2% sodium caseinate, 50% glycerol at 50°C showed moderate mechanical properties, optical properties, water solubility and maximum barrier properties of gas and water vapor, with tensile strength=5.85 MPa, elongation=101.20%, transparency=91.4%, gas permeability rate=49.92 $cm^3 \cdot m^{-2} \cdot d^{-1} \cdot 0.1\ MPa^{-1}$ and water vapor permeability were $1.252 \times 10^{-11} g \cdot m^{-1} \cdot s^{-1} \cdot pa^{-1}$, (RH:10%/70%), respectively. It is possible that they may be alternatives to some plastics, as inner packaging materials for food with low water activity (Chen and Lei, 2011). The unfavorable properties of protein films are excessive water solubility and poor WVP compared with plastic. The possibility of using TGase as a modifying agent of WPI-NaCas films was estimated to improve their resistance to solubility and water vapor.

The objective of this work was to find the influence of additive amount, reaction time and temperature of TGase on properties of WPI-NaCas films, so as to design biodegradable material with good mechanical and barrier properties, suitable for packages of many kinds of food products with different acidities and contents of moisture.

MATERIALS AND METHODS

Whey protein isolate (WPI, protein > 92.0%, Hilmar Company, California, USA) and Sodium caseinate (NaCas, with 92.9% protein, Murray Goulburn Company, Australia) were used as film-forming components. Glycerol (GLY, analytical grade, SCRC, China) was used as a plasticizer to improve the flexibility properties of the films. Transglutaminase was obtained from Dongsheng Food Technological Company in China.

Orthogonal experiment of enzymatic modifications

Orthogonal experiment in three factors and three levels was designed based on the results of single-factor experiment, with the unmodified experimental group as control group. Orthogonal test schedule was shown in Table 1.

Films preparation

WPI solution was prepared by dispersing 5 g protein powder in 100 ml distilled water, stirring continuously at room temperature for 2 h with a magnetic stirring apparatus (ZNCL-T, Qiangqiang instrument corporation, Shanghai, China). Then the solution was placed in a water bath and kept at 85°C for 30 min to denature the protein and then cooled down to room temperature until the powders completely dissolved. NaCas solution was prepared by dispersing 5 g sodium caseinate powder in 100 ml distilled water at room temperature until the powders were completely dissolved. GLY was added as 30% (w/w) of the total polymers. The blending ratio of WPI solution and NaCas solution was 1:1 (v/v). WPI, NaCas and GLY were completely mixed, to achieving the composite protein solution. TGase was added into the solution with reaction parameters shown in Table 1, and then inactivated at 75°C for 15 min. After cooling down to room temperature, the composite solution was degassed by vacuum pump and casted on organic glass plates, then heated

Table 1. Orthogonal test schedule.

Test number	TGase reaction time/min (A)	TGase additive amount/mg/ml (B)	TGase reaction temperature/°C (C)
01	22.5(1)	0.10(1)	40(1)
02	22.5(1)	0.15(2)	50(2)
03	22.5(1)	0.20(3)	60(3)
04	30.0(2)	0.10(1)	50(2)
05	30.0(2)	0.15(2)	60(3)
06	30.0(2)	0.20(3)	40(1)
07	37.5(3)	0.10(1)	60(3)
08	37.5(3)	0.15(2)	40(1)
09	37.5(3)	0.20(3)	50(2)
10	0.0	0.00	0

at 50°C in air blow drying cabinet (GX-ZGF101, Hede Co. Ltd, shanghai, china). The films obtained were peeled from the plates and conditioned in a thermostatic and humidistatic chamber (GDS-100L, Suoyate Co. Ltd., Jiangsu, China) at 50 ± 5% RH and 23 ± 2°C for no less than 48 h prior to testing.

Properties testing

Particle size distribution

Particle size distribution of film-forming solution was measured using laser particle analyzer (BT-9300HT, BaiTe Co. Ltd, Dandong, China), with optical mode, analysis mode and medium set as Mie, multimodal and water. Four measurements of each sample were taken, then calculating the average value.

The apparent viscosity of film-forming solution

The apparent viscosities of film-forming solutions were measured by Rheometer (Anton Paar, Austria) at 25°C, with shearing rate: 0 to 100 rpm/s, testing system: CC27-SN23937, equipment TU1=C-PTD200-SN80910176. Each sample was 40 ml.

Mechanical properties

Tensile strength (TS) and elongation at break (EB) were measured using a computer control tensile testing machine (DCP-KZ300, CDMC Co. Ltd., Sichuan, China). Samples were cut into 15 × 100 mm pieces. According to ASTM D882-09 (ASTM, 2009), the initial grip separation was set at 50 mm, with cross-head speed 500 mm/min. At least ten samples of each type of film were measured. Tensile strength was calculated by this formula:

$$TS = F/S \quad (1)$$

Where, F is the force when the film was broken, S is the cross section area.

Water solubility

The method modified from Rhim (2004) was used to determine water solubility (WS). Samples were cut into 30 × 30 mm pieces and firstly dried at 105°C for 24 h in an air blow drying cabinet (GX-ZGF101, Hede Co. Ltd., Shanghai, China) to obtain the initial weight w_1. After drying, the films were submerged with 50 ml water in 100 ml breakers for 24 h at room temperature. Undissolved dry matters were removed from the breakers and dried at 105°C again until they reach a constant weigh (±0.0001 g). The final dry weight was taken as w_2. Each type of film was determined in triplicate.

$$WS(\%)=(w_1- w_2) / w_1\times100 \quad (2)$$

Water vapor permeability

The water vapor permeability (WVP) of films was measured according to ASTM E398 (ASTM, 2003), standardized by a water permeability tester (PERMATRAN-W Model 1/50G, MOCON, USA). Tank pressure was set to 30 ± 2 psig (approximately 0.2 MPa). The 100%RH test cell and saturated pad were used in correction test. Test mode was set to continuous, with test temperature 37.8°C, and RH at two sides of tested films was 10%/50% respectively.

Thermogravimetric analysis (TGA)

Thermogravimetric measurement was carried out on a thermogravimetric analyzer (TG209 F1, NETZSCN, Germany) in the temperature range 35 to 500°C at heating rate of 10 K/min. Mass of each tested sample was 3 to 5 mg, while flow-rate of sweep gas and protective gas (both were nitrogen) were 30 and 20 ml/min, respectively.

Scanning electron microscopy

Cross-section morphologies of films were obtained by scanning electron microscope (S3400N, Hitachi Co. Ltd, Japan) with gold-plating time under vacuum state, accelerating potential, amplification factor were 10 min, 10 kv, 2000, respectively.

RESULTS AND DISCUSSION

Particle size distribution of film-forming solutions

No significant difference was observed in film-forming solutions of 01-09 experimental groups (Figure 1). However, reductions in both median particle (D50) and

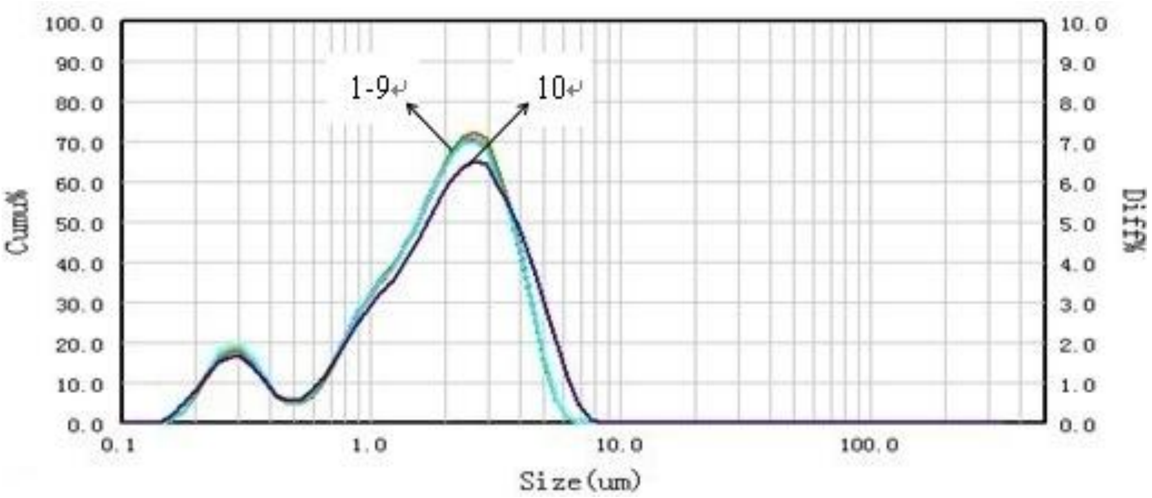

Figure 1. Particle size dispersion of film forming solutions.

Table 2. Particle size of film forming solutions.

Sample number	D10	D50	D90	D4.3 (um)	D3.2 (um)	AN (m^2/g)
01	0.426	1.971	3.783	2.079	1.125	1.719
02	0.401	1.960	3.776	2.067	1.109	1.744
03	0.415	1.950	3.762	2.060	1.114	1.737
04	0.442	1.968	3.777	2.077	1.132	1.709
05	0.385	1.948	3.774	2.057	1.091	1.772
06	0.428	1.961	3.769	2.070	1.123	1.721
07	0.435	1.971	3.777	2.079	1.131	1.710
08	0.408	1.982	3.762	2.079	1.122	1.724
09	0.383	1.943	3.768	2.052	1.088	1.777
10	0.417	2.080	4.305	2.271	1.136	1.702

volume average diameter (D4,3) were compared with control group (Table 2); the reduction resulted from the hydrolysis or cross-linking reaction of protein, causing the change of particle size value by the addition of TGase in the film preparation process.

Rheology characteristics of film-forming solutions

Intermediate concentration for film solutions will generally result in the highest cohesive strength as a compromise between optimal viscosity and polymer salvation. The functionality of the polymer is related to solvent characteristics. Maximum coating, solution salvation and polymer chain extension will produce the most efficient films. A high sol viscosity is a good indication of the adequacy of salvation and chain extension according to the formulation and method of preparation prior to film application. The apparent viscosity of WPI-NaCas composite film-forming solutions remained higher preventing deposition of solution particles at low shearing rates, while with the increase of shearing rates, molecule forces weakened and free space enlarged which directly caused a decrease of viscosity. Results indicated that experimental samples belong to non-Newtonian fluid with little lower viscosity than that of control sample due to the effects of TGase (Figure 2).

Effects of TGase on mechanical properties of films

Except for Group 1 and 8 (lower to control group for inadequate reaction time and TGase addition) and Group 9, TS of other groups significantly increased by about 25～50% after TGase modification, which associated to the cross-linking reaction of protein caused by TGase, and forming covalent bond, thereby improving TS and decreasing flexibility of films (Figure 3). On the other hand, the elongations at break of most of the enzymatic modified films were about 2～3 times higher than the

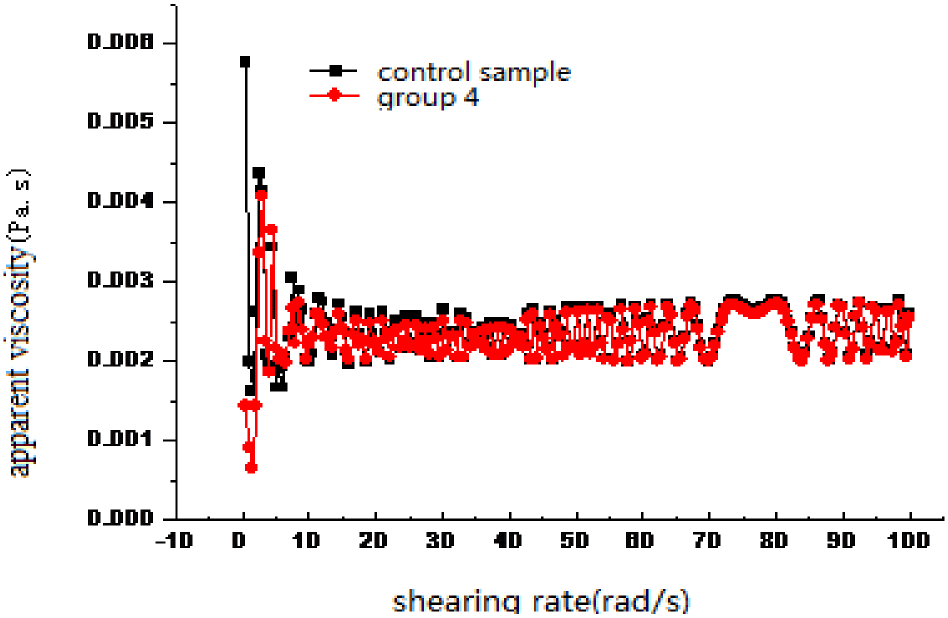

Figure 2. The apparent viscosity of film solutions.

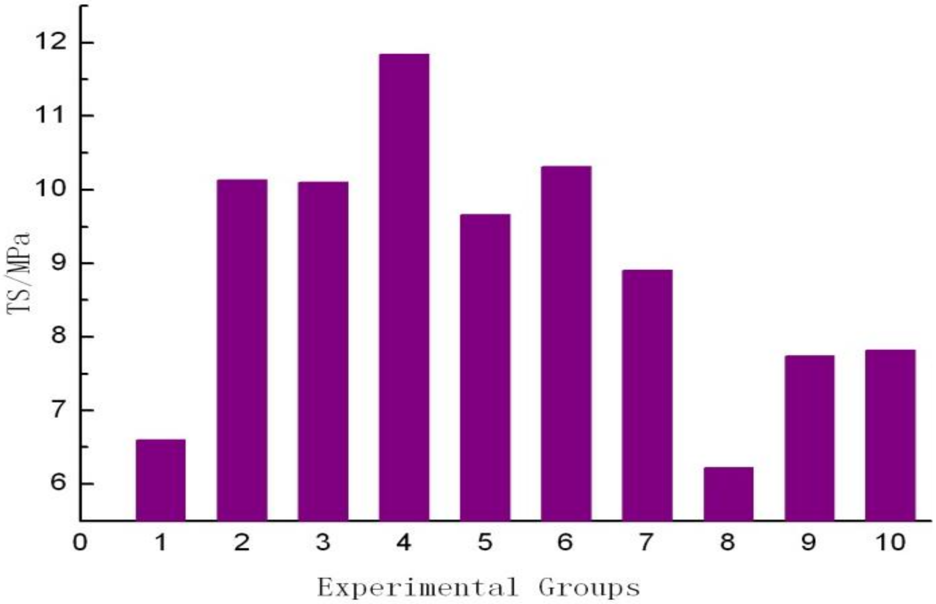

Figure 3. Tensile strength of different films.

control one except Group 2, 4 and 6, differently from TS (Figure 4). However, higher reaction temperature especially at 60°C allowed better improvements in both TS and elongation (Groups 3, 5 and 7).

Without adequate content of TGase or experimental reaction condition, the cross-linking reaction did not germinate intra- or inter-molecular, then forming heteropolymer, which resulted in a decrease in mechanical properties of films.

Effect of TGase on water solubility of films

The addition of TGase resulted in a marked decrease in WS of WPI-NaCas films (Figure 5), from 44.51% (unmodified samples) to 28.62% (Group 4), which

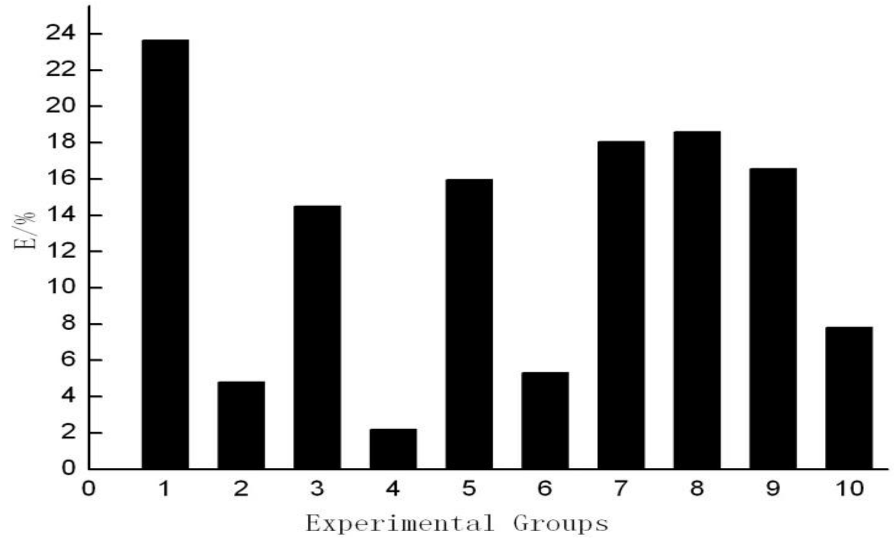

Figure 4. Elongation of different films.

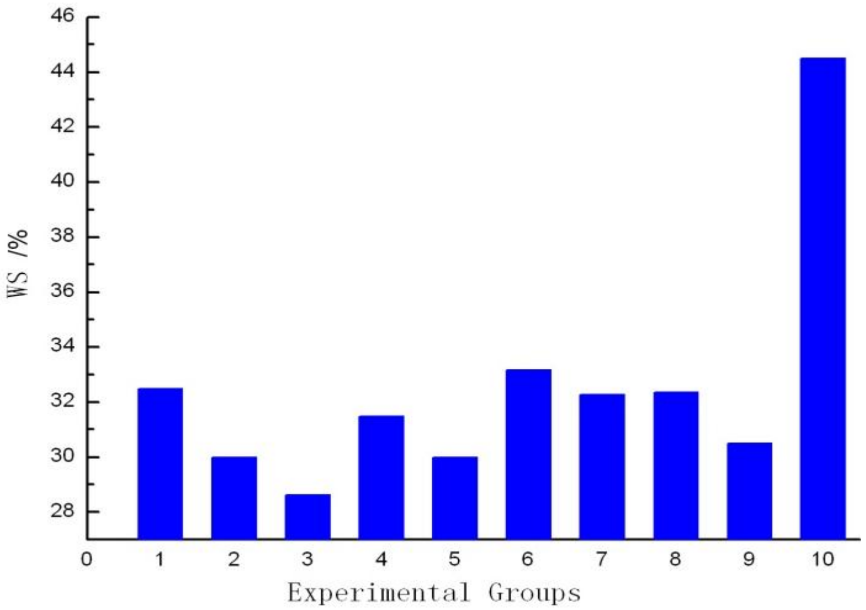

Figure 5. Water solubility of different films.

corresponded to the results of Kołodziejska' research (Kołodziejska and Piotrowska, 2007). This can be explained that cross-linking reaction of protein caused by TGase resulted in non exposition of hydrophilic groups, which decreased WS of films. And the unfolded structure of enzyme-heat-denatured proteins and the covalent S-S bonding during drying led to film insolubility in water and produced films that were stronger and could withstand higher deformations.

Water-resistance of modified films was improved, however, no statistically significant difference of WS was observed from Group 1 to 9, with the lowest value of 28.62% (Group 3) and the highest of 33.16% (Group 6). On the other hand, the higher enzyme reaction temperature and additive amount rather than enzyme reaction time caused further reduction in solubility of the films.

WVP of films modified by TGase

Protein based films generally embody poor vapor barrier

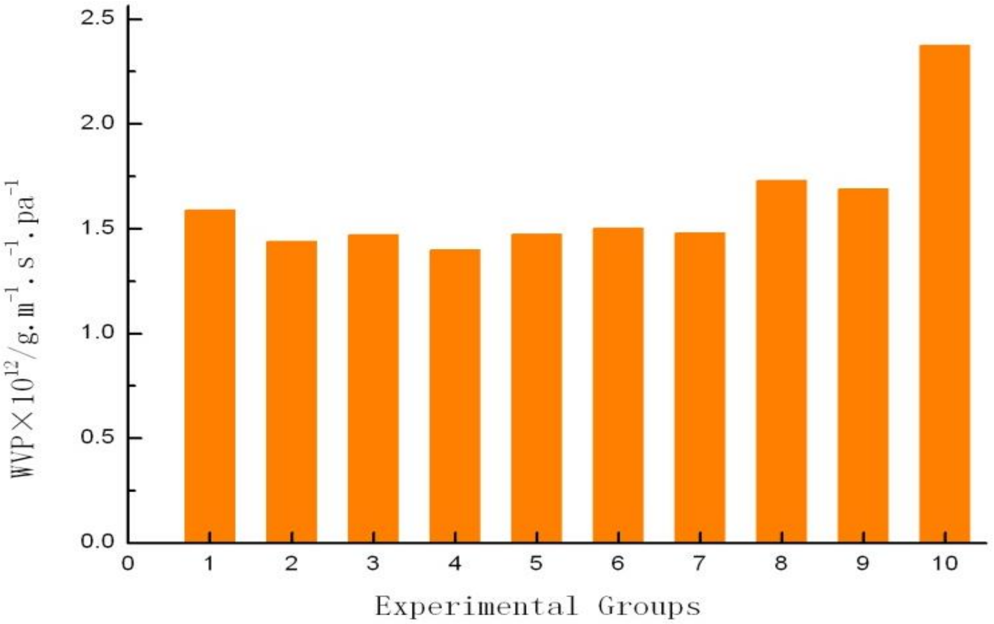

Figure 6. The WVP of different films.

Table 3. Scheme of range analysis.

Index	K	A	B	C	Major factor	Optimum group
TS	k_1	26.83	27.33	23.13	ACB	A2 C2 B3 30 min/50°C /0.20 mg/ml
	k_2	31.80	26.02	29.71		
	k_3	22.86	28.14	28.66		
	R	8.95	2.12	6.58		
WVP	k_1	4.50E-12	4.47E-12	4.82E-12	ACB	A2 C3 B1 30 min/60°C/0.10 mg/ml
	k_2	4.38E-12	4.64E-12	4.53E-12		
	k_3	4.90E-12	4.67E-12	4.43E-12		
	R	5.20E-13	1.96E-13	3.98E-13		

property, which becomes a limitation in their application. It was found that TGase addition reduced the moisture transmission coefficient of WPI-NaCas films to 1.400～1.732 × $10^{-12}g\cdot m^{-1}\cdot s^{-1}\cdot pa^{-1}$, about 42% lower than that of unmodified films (Figure 6). Cross-linking reaction of protein resulted in the reduction or diminution of free space intra- and inter-molecular, thereby impeding the penetration of water vapor molecules. So, the water barrier properties of WPI-NaCas films were improved by cross-linking of the components with TGase and increasing hydrophobicity, which widened the practical applications of modified films as packaging material.

Range analysis of orthogonal experiment

TS and WVP values of orthogonal experiments were selected as the objective parameters of range analysis for their significant differences and relative importance in properties and applications of films. Range analysis of orthogonal experiment results showed that reaction time of TGase was the most effective factor on both TS and WVP properties of film, and the secondary, tertiary factors were reaction temperature and TGase additive amount respectively (Table 3). Films modified by 0.1mg/ml TG at 50°C for 30 min (being optimized technological parameters) as a compromise showed the largest TS with 11.84 Mpa and the lowest WVP with $1.40\times10^{-12}g\cdot m^{-1}\cdot s^{-1}\cdot pa^{-1}$.

Thermogravimetric analysis

TGA thermograms revealing thermal degradation

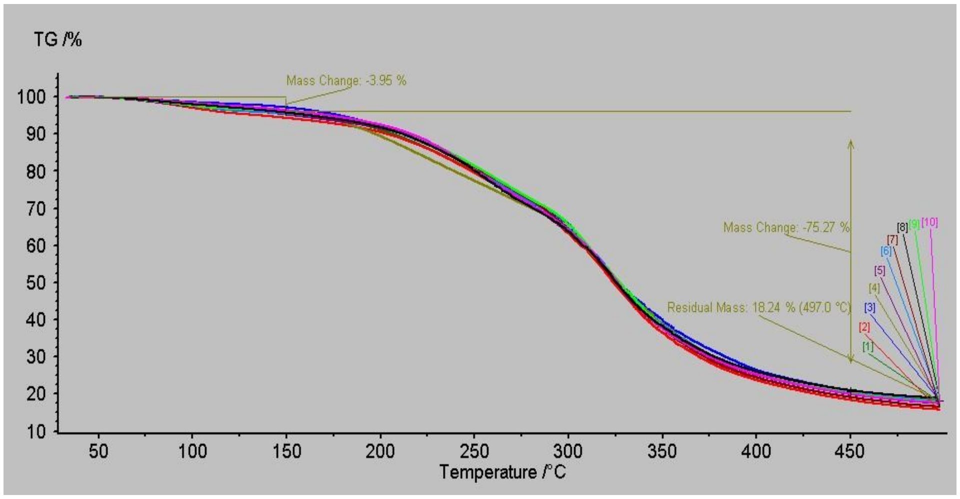

Figure 7. Weight loss profiles of control sample and films prepared by orthogonal test.

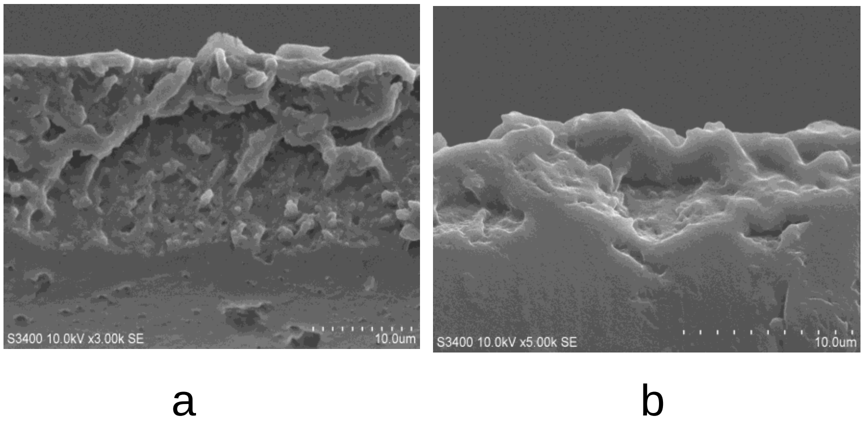

Figure 8. Cross-section morphology: (a) control sample, (b) sample in group 4.

behavior of composite protein films in the presence of transglutaminase at different levels were depicted in Figure 7. All films exhibited similar three main stages of weight loss. The first stage weight loss was observed approximately up to 3.95% at 35～150°C, possibly related to the loss of free water adsorbed in the film. The second stage weight loss gave a maximum degradation rate at 150～200°C, and was most likely associated with the loss of glycerol compound and structurally bound water. For the third stage, weight loss appeared at 200～450°C attributed to the degradation of protein chain. The high temperature step caused the decomposition of more thermally stable structures due to crosslinking reactions produced during heating (Hoque et al., 2011; Martucci and Ruseckaite, 2009; Martucci et al., 2007; Mu et al., 2012), when the non-covalent bonds (hydrogen bond, ionic bond), hydrophobic interactions and Van der Waals attraction of protein molecules were destroyed and oxidized into carbon dioxide, water, nitrogen oxide, sulfur dioxide and so on. However, no significant difference between control group and experimental groups was noticed. It was also suggested that degradation temperature of protein based films was relatively high and the temperature of 150°C could be considered as the critical temperature for use.

Scanning electron microscopy analysis

The results (Figure 8) showed that cross-section of unmodified films were relatively rough, unordered and porous, while those of the modified films became smooth and compact, which explained that enzymatic modification could be used to promote crystallinity and molecular order and caused greater changes in microstructure of WPI-NaCas composite films. This effect resulted from the decrease in the free volume between polymer chains due to increasing attractive intermolecular forces made by the polymer network denser and more impermeable

Conclusions

TGase could ameliorate the properties of edible WPI-NaCas composite films. Synergistic effects of content, reaction time and temperature of TGase on WPI-NaCas edible films by orthogonal experiments indicated that D50 and D90 of film-forming solutions decreased by the enzyme modification, which also resulted in a decrease in water solubility and an increase in both mechanical and water barrier properties under proper conditions. Compared with control sample, scanning electron microscope analysis indicated that cross-section of enzyme modification sample was more compact and smooth. However, there was no significant difference in thermogravimetric analysis and solution apparent viscosity changes for all the samples. Orthogonal experiment results also showed that reaction time was the most effective factor on TS and WVP properties of film, and the secondary, tertiary factors were reaction temperature, TGase additive amount respectively. Films modified by 0.1 mg/ml TGase at 50°C for 30 min exhibited the largest TS 11.84 Mpa and lowest WVP $1.40\times10^{-12}g\cdot m^{-1}\cdot s^{-1}\cdot pa^{-1}$.

Enzyme modified and denatured protein films were rather more water resistant, rigid and impermeable but less flexible and transparent. Orthogonal experiments showed the potential of WPI-NaCas composite films modifided by TGase as alternative biodegradable polymers for practical applications.

Conflict of Interests

The author(s) have not declared any conflict of interests.

ACKNOWLEDGEMENT

This research project was financed by the Shanghai University Knowledge Service Platform and Shanghai Ocean University Aquatic Animal Breeding Center (ZF1206).

REFRENCES

ASTM (2003). Standard Test Method for Water Vapor Transmission Rate of Sheet Materials Using Dynamic Relative Humidity Measurement. E 398, Annual book of ASTM 2009, Philadelphia, PA: American Society for Testing and Materials.

ASTM (2009). Standard Test Method for Tensile Properties of Thin Plastic Sheeting. D 882-09, Annual book of ASTM (2009). Philadelphia, PA: American Society for Testing and Materials.

Baldwin E, Hagenmaier A, Robert D, Jinhe B (2012). Edible coatings and films to improve food quality, ed. Boca Raton, FL, Chap. 2, p. 15.

Carvalho RA, Grosso CRF (2004). Characterization of gelatin based films modified with transglutaminase, glyoxal and formaldehyde. Food Hydrocoll. 18:717-726. http://dx.doi.org/10.1016/j.foodhyd.2003.10.005

Chen GY, Lei Q (2011). Research on preparation and properties of edible composite protein films. Appl. Mech. Mater. .87:213-222. http://dx.doi.org/10.4028/www.scientific.net/AMM.87.213

Ferreira CO, Nunes CA, Delgadillo I, Lopes-da-Silva JA (2009).Characterization of chitosan-whey protein films at acid pH. Res. Int. 42:807-813.

Hoque MS, Benjakul S, Prodpran T (2011). Effects of partial hydrolysis and plasticizer content on the properties of film from cuttlefish (Sepia pharaonis) skin gelatin. Food Hydrocoll. 25:82-90. http://dx.doi.org/10.1016/j.foodhyd.2010.05.008

Kołodziejska I, Piotrowska B (2007). The water vapour permeability, mechanical properties and solubility of fish gelatin–chitosan films modified with transglutaminase or1-ethyl-3-(3-dimethylaminopropyl) carbodiimide (EDC) and plasticized with glycerol. Food Chem. 103:295-300. http://dx.doi.org/10.1016/j.foodchem.2006.07.049

Kuraishi C, Yamazaki K, Susa Y (2001). Transglutaminase: Its utilization in the food industry." Food Rev. Int. 7:221-226. http://dx.doi.org/10.1081/FRI-100001258

Liu JT, Hong R, Yang Y (2006). The preparation of curdlan and its application on edible films. Mod. Food Sci. Technol. 22:57-60.

Mahmoud R, Savello PA (1993). Solubility and hydrolyzability of films produced by transglutaminase catalytic cross-linking of whey protein. J. Dairy Sci. 76:29-35. http://dx.doi.org/10.3168/jds.S0022-0302(93)77320-8

Martucci JF, Ruseckaite RA (2009). Tensile properties,barrier properties and biodegradation in soil of compression-molded gelatin-dialdehyde starch films. J. Appl. Polym. Sci. 112:2166-2178. http://dx.doi.org/10.1002/app.29695

Martucci JF, Vázquez A, Ruseckaite RA (2007). Nanocomposites based on gelatin and montmorillonite: Morphological and thermal studies. J. Therm. Anal. Calorimet. 89:117-122. http://dx.doi.org/10.1007/s10973-006-7454-0

Motoki M, Aso H, Seguro K, Nio N (1987). AsI-Casein film prepared using transglutaminase. Agric. Biol. Chem. 51:993-996. http://dx.doi.org/10.1271/bbb1961.51.993

Mu CD, Guo JM, Li XY (2012). Preparation and properties of dialdehyde carboxymethyl cellulose crosslinked gelatin edible films. Food Hydrocoll. 27:22-29. http://dx.doi.org/10.1016/j.foodhyd.2011.09.005

Nielsen GS, Petersen BR, Moller AJ (1995). Impact of salt, phosphate and temperature on the effect of a transglutaminase (F XIIIA) on the texture of restructured meat. Meat Sci. 41:293-299. http://dx.doi.org/10.1016/0309-1740(94)00002-O

Oses J, Fabregat-Vazquez M, Pedroza-Islas R, Tomas SA, Cruz-Orea A, Mate JI (2009). Development and characterization of composite edible films based on whey protein isolate and mesquite gum. J. Food Eng. 92:56-62. http://dx.doi.org/10.1016/j.jfoodeng.2008.10.029

Rhim JW (2004). Physical and mechanical properties of water-resistant sodium alginate films. Lebensmittel-Wissenschaftund-Technologie. 37:323-330.

Wang C, Zhang CH, Zhao QC (2009). Research on the composite films modified by transglutaminase. Cereal Feed Ind. 5:3-5.

Yildirim M, Hettiarachchy NS (1998). Properties of films produced by cross-linking whey proteins and 11S globulin using transglutaminase. J. Food Sci. 63:248-252. http://dx.doi.org/10.1111/j.1365-2621.1998.tb15719.x

Yu XL, Zhou GH, Li XB (2009). The application of Sodium alginate based edible films in food processing industry. Food Res. Dev. 9:181-184.

academicJournals

Vol. 9(9), pp. 400-406, 15 May, 2014
DOI: 10.5897/SRE2014.5965
Article Number: AE0983344572
ISSN 1992-2248 © 2014
Copyright©2014
Author(s) retain the copyright of this article
http://www.academicjournals.org/SRE

Scientific Research and Essays

Full Length Research Paper

Microarrays revealed general-key genes responsive to implantation of low-energy N^+ ion beam in rice

Ya Huiyuan[1,2]*, Chen Qiufang[2], Wang Weidong[2] and [2]Jiao Zhen

[1]Life Science Department, Luoyang Normal University, Luoyang 471022, Henan, China.
[2]Key Laboratory of Ion Beam Bioengineering in Henan Province, Zhengzhou University, Zhengzhou 450052, Henan, China.

Received 3 January, 2013; Accepted 2 March, 2013

Implantation with low-energy ion beam can induce various plant biological effects including stimulation, damage and mutation. But the adaptive mechanism altering gene expression in response to this stressor in plant is not fully understood. A highly thorough and comprehensive analysis to investigate the general-key genes responsive to implantation with low-energy ion beam in plant is important to understand the diverse mechanism. We used Agilent Rice Gene Expression Microarray to investigate the overlap differentially expressed genes between two independent implantation experiments underlying three ion fluences. Our microarray data showed that 26 up-regulated overlap genes and 6 down-regulated overlap genes were observed. The Gene Ontology terms analysis showed that genes with functions including kinase, transporter, acceptor, transcription regulation were involved in signaling and response biological processes in rice responding to the implantation with ion beam. Our data also implied that ABA signal transduction pathway is involved in response to ion-beam implantation in rice. The RiceNet co-expressed network analysis showed the direct and indirect co-expressed linkages among these up-regulated genes, which suggested some signal transduction pathways should be involved in this response and remained unclear. Our microarray data revealed the general and key genes responsive to the stress of implantation with low-energy ion beam during the rice germination. These data provide information on the candidate genes for further elucidation regarding the molecular mechanisms of the biological effects of ion-beam implantation and its application for improvement of corn.

Key words: Microarray; key genes responsive to implantation of low-energy N+ ion beam; Rice

INTRODUCTION

Low-energy ion beam as a new mutagen has been extensively applied to organisms for genetic transformation, breeding and creation of aneuploids (Feng et al., 2007). As a kind of environmental stress, it can induce various biological effects including growth stimulation, damage, lethality, mutation (Yu, 2007). Numerous adaptive mechanisms in cells alter gene expression in response to stressors. Many functional

---

*Corresponding author. Email: yahuiyuan@yahoo.com.cn proteins, involved in signaling pathways are responsible for response to environmental stresses including salinity, drought, submergence, temperature extremes (high and low temperatures); and heavy metals are identified and recognized (Tardif et al., 2007; Zhu, 2002). However, the key genes and their network responsive to implantation with low-energy ion beam remain not fully elucidated because few of these genes need to be identified and recognized in plant. Recently, genome expression analysis was used to identify the key functional genes involved in response to abiotic stress for its high throughput detection, especially the whole-genome microarrays (Zhou et al., 2007; Walia et al., 2007; Wang et al., 2007).

Rice's (*Oryza sativa*) compact genome size (≈430 Mb), well-established methods for genetic transformation, availability of high density genetic maps and whole-genome microarrays (Jung et al., 2008), finished genome sequence (Matsumoto et al., 2005), and close relationships with other cereals, all make rice an ideal model system that studies plant physiology including tolerance of stress, development, agronomics, and genomics of grasses (Shimamoto and Kyozuka, 2002). In previous extensive studies, many research groups have been examining the effects of a wide variety of abiotic and biotic stresses in rice (Jwa et al., 2006). So, we selected the rice seeds as the experimental materials in this study. Previously, we focused on gene expression profiles in promoted-growth rice with germination stage from the seeds implanted by low-energy N^+ beam. However, it was observed that various experiments with different-ion-fluence implantation showed the great divergent gene expression profiles, even different experimental replicates (Ya et al., 2012). So, it is difficult to identify and recognize the general-key functional genes that were ubiquitous in response to the stress of implantation with low-energy ion beam in rice.

In this study, we propose a strategy to find out the overlap differentially expressed genes (DEGs) in rice among the multiple microarrays on two independent implantation experiments with three ion fluences. These DEGs should be commonly differentially expressed and the key role in response to the stress of implantation with low-energy ion beam in rice. The results enable the identification of genes regulating response to implantation with low-energy ion beam, facilitating engineering of pathways critical to rice tolerance.

MATERIALS AND METHODS

Rice seeds and culture

Dry seeds of rice cultivar Xindao-18 (*Oryza sativa* L. ssp. japonica) were used in ion implantation experiments. After implantation with the ion beam, all seeds were planted on sterile medium with 0.8% agar (Sigma) in a climate chamber in the dark at 28°C. After the seeds for the microarrays had been incubated for 96 h, the seedlings were divided into two groups. One group was used for the RNA isolation, while the other was used for investigation of the simplified seed vigor index from the 10-day-old seedlings grown in a climate chamber during a 12-h dark/12-h light cycle at 28°C.

Implantation of low-energy N^+ ion beam and investigation of simplified seed vigor index

The low-energy ion beam implantation of seeds was performed with the Ion Beam Bioengineering Facility (UIL.0.512, TNV, Russia). In the present study, we carried out two independent implantation experiments for microarray. In the first implantation experiments, the seeds were used at 62 days after harvesting and seed moisture content is 7.0%; the ion fluences used for energetic N^+- ion-beam (40 KeV) implantation were at 3×10^{17} N^+/cm^2, 6×10^{17} N^+/cm^2 and 9×10^{17} N^+/cm^2, respectively. Controls included seeds that were in normal surroundings and a vacuum without ion implantation for 264 min that was similar to the time of implantation with fluence at 6×10^{17} N^+/cm^2. In the second implantation experiments, seeds were used at seven months after harvesting and its seed moisture content is 6.5%; the ion fluences used for implantation with low-energy (40 KeV) N^+ were at 2×10^{17} N^+/cm^2, 5×10^{17} N^+/cm^2 and 8×10^{17} N^+/cm^2. Controls included seeds that were in normal surroundings and a vacuum without ion implantation for 352 min that was similar to the time of implantation with fluence at 8×10^{17} N^+/cm^2. For each ion fluence implantation, three independent biological replicates were used. Two hundred seeds were implanted in each replicate. The germination rate (from 100 seeds) was investigated from the 7-day-old seedlings, and all the seedlings that were used to investigate the germination rate (from 100 seeds) were oven dried at 80°C for 12 h to investigate the dry weight (g).

Germination rate = Number of the seedlings/total seeds×100%

and

Simplified seed vigor index = Drought weight of the seedlings (g) × Germination rate × 100.

Data were pooled from three independent experiments.

RNA extraction

We mixed thirty uniformed rice seedlings underling each ion fluence as a sample to prepare for mixed RNAs and constructed the RNA pool from three biological replicates. A total of mixed RNAs were isolated using RNA plant reagents (Tiangen Biotech) and purified by use of the RNeasy Plant Kit (Qiagen).

Agilent microarray hybridization and data analysis

The Agilent Microarray hybridization (Agilent-015241 Rice Gene Expression Microarray) and raw data analysis were carried out by the Shanghai Bio Company Ltd., including the procedures for cDNA and cRNA synthesis, cRNA Cy3 fluorescence labeling, hybridization, washing, scanning (Agilent G2565BA Microarray Scanner System), data collection, and normalization. This experiment was performed three times, resulting in three biological replication samples for each ion fluence for the significant statistics.

We collected the expression signals, and the present/absent calls from the raw data and analyzed them using the SBC Analysis System in one-way ANOVA (SAS, a web server, http://sas.ebioserivce.com), and sorted the differentially expressed transcripts data in Excel. Based on the statistics analysis, a transcript was considered significantly up-or down regulated if it met all of the following criteria:

Table 1. Simplified vigor index of implanted seeds from the first implantation.

Samples	Germination rate*100 (Mean±STD)	Vigor index (Mean±STD)	P-value to T-test
Controls	81.85±2.31	9.55±1.69	
Vacuum	84.81±2.21	12.14±0.8	0.074
Fluence1	86.67±1.11	12.14±1.02	0.085
Fluence2	88.89±0.00	14.52±1.36	0.017
Fluence3	51±7.2	5.29±0.99	0.02

Simplified vigor index was investigated using the 10-day rice seedlings in each independent experiment replicates. Fluence1 referring to $3×10^{17}$ N+/cm^2; fluence 2 referring to $6×10^{17}$ N+/cm^2; fluence3 referring to $9×10^{17}$ N+/cm^2. STD, standard deviation.

Table 2. Simplified vigor index of implanted seeds from the second implantation.

Samples	Germination rate*100 (Mean±STD)	Vigor index (Mean±STD)	P-value to T-test
Controls	78.33±1.15	16.29±1.29	
Vacuum	78.0±1.73	16.68±3.51	0.82
Fluence1	70.67±4.16	10.42±2.35	0.021
Fluence2	72.67±3.05	11.56±2.05	0.14
Fluence3	74.67±3.21	15.16±2.0	0.15

Simplified vigor index was investigated using the 10-day rice seedlings in each independent experiment replicates. Fluence1 referring to $2×10^{17}$ N+/cm^2; fluence 2 referring to $5×10^{17}$ N+/cm^2; fluence3 referring to$8×10^{17}$ N+/cm^2. STD, standard deviation.

1) showed a statistically significant differential expression at the adjusted p value< 0.05;
2) had a cut-off value at a 2-fold change;
3) had "present" calls on all of the three replicates samples for the controls and/or the implantation.

Bioinformatics analysis

The annotation for the transcripts represented by the microarray was described according to the following databases: Agilent probe name (http://www.ebi.ac.uk/microarray-as/aer/lob? name= adss&id= 2375208716), SAS web server, and the RAP database (http://rapdb. dna.affrc.go.jp/).

Detection of the key DEGs

We collect overlapping DEGs in multi-microarrays for the samples with different ion fluence and different experimental replicates.

RESULTS AND DISCUSSION

Biological effects of the implantation with low-energy N$^+$ ion beam

In this study we investigate the biological effects of the implantation with low-energy N$^+$ ion beam according the rice simplified seed vigor index. The results showed that energetic N$^+$ (40 Kev) ion beam can produce biological effects of growth promotion (Table 1, in first implantation with ion fluence at $6×10^{17}$ N$^+$/cm^2) and growth inhibition (Table 2, in the first implantation with ion fluence at $9×10^{17}$ N$^+$/cm^2, in the second implantation with ion fluence at 2×1017 N$^+$/cm^2). Here, we selected the sample that is implanted by N$^+$ ion beam with fluence at $6×10^{17}$ N$^+$/cm^2 in the first implantation experiment and that is implanted by N$^+$ ion beam with fluence at $2×10^{17}$ N$^+$/cm^2, $8×10^{17}$ N$^+$/cm^2 (a larger-fluence ion beam implantation) in the second implantation experiment for the micaroarrays.

Profiles of the DEGs

We detected the DEGs by comparing the expression signals value of the genes between the implanted samples and the blank control. The microarray analysis showed that there are 821 DEGs underlying the ion-beam fluence at $6×10^{17}$ N$^+$/cm^2 in the first implantation experiment (Table 3); 1256 DEGs underlying the ion-beam fluence at $2×10^{17}$ N$^+$/cm^2 and 1136 DEGs underlying the ion-beam fluence at $8×10^{17}$ N$^+$/cm^2 in the second implantation experiment (Table 4).

The DEGs number has greater difference between the samples implanted by different ion fluence. It suggested that a single independent microarray can not reflect the comprehensive and general key genes responsive to the ion-beam implantation stress. So we considered the genes that were differentially expressed in all microarrays date underlying three ion fluence implantation as the comprehensive and general DEGs associated with response to the ion-beam implantation stress in rice. By

Table 3. DEGs number in the first implantation experiment.

Treatment	Up regulation		Down regulation	
	Number	Score of FC	Number	Score of FC
$6*10^{17}$ vs control	351	2~21.62	470	2.0~176.89

Table 4. DEGs number in the second implantation experiment.

Treatment	Up regulation		Down regulation	
	Number	Score of FC	Number	Score of FC
$2*10^{17}$ vs control	780	2~38.00	476	2.0~1535.14
$8*10^{17}$ vs control	794	2~51.11	342	2.0~13.65
$8*10^{17}$ vs $2*10^{17}$	833	2~2087.34	1355	2.0~26.74

Table 5. The up-regulated general-key DEGs.

Gene ID	Short Description	FC (p-value)		
		2*1017	6*1017	8*1017
Os01g0959100	Similar to abscisic stress ripening protein 1	4.02	4.51	4.68
Os01g0723000	Elongation factor 2 (EF-2)	24.26	10.34	51.10
Os01g0155000	Esterase/lipase/thioesterase	6.04	3.22	3.28
Os01g0311800	Pectin methylesterase isoform alpha	2.67	2.0	2.44
Os01g0660200	(Chitinase) (EC 3.2.1.14)	15.74	2.95	2.67
Os01g0959200	Similar to abscisic stress ripening protein 1	3.54	6.60	5.31
Os02g0787600	Ionotropic glutamate receptor	3.63	2.06	2.10
Os03g0575200	K+ potassium transporter family protein	4.86	2.42	3.0
Os03g0830500	PGPS/D12	19.74	2.77	2.23
Os04g0339400	Aldo/keto reductase family protein	6.34	3.47	9.50
Os04g0368000	Serine/threonine protein kinase	2.18	2.35	3.16
Os04g0524500	Oligopeptide transporter	2.47	2.03	2.16
Os05g0276500	Expansin Os-EXPA3	2.04	4.61	2.72
Os06g0147300	Conserved hypothetical protein	3.30	3.0	2.42
Os06g0521500	Haem peroxidase	5.02	2.40	3.0
Os07g0493800	Protein kinase domain containing protein	3.65	2.24	2.20
Os07g0638400	Peroxiredoxin (B15C)	4.31	5.63	3.53
Os07g0690900	Hytochelatin synthetase-like protein	4.54	2.71	3.56
Os08g0136700	Protein of unknown function DUF26	7.11	2.48	14.05
Os08g0190100	Germin-like protein (Germin-like 8)	10.17	4.38	2.80
Os09g0367700	GST6 protein (EC 2.5.1.18)	3.50	7.15	3.08
Os09g0483200	Ubiquitin domain containing protein	2.45	18.18	32.52
Os10g0452300	Eggshell protein family protein	4.07	6.26	3.11
Os11g0227200	NBS-LRR disease resistance protein homologue ; nucleotide binding / protein binding	6.68	2.32	3.11
Os11g0482200	Pathogenic type III effector avirulence factor	5.43	2.31	2.73
Os11g0669100	Calmodulin binding protein	5.91	2.94	2.14

Short descriptions were annotated according to RAP-DB (Rice Annotation Project Database). Fold change in each gene is not expressed as log2. The P-value threshold of 0.05 was used for significant differential expression.

comparing the microarray data between the two independent implantation experiments resulting in different biological effect, we obtained 26 up-regulated (Table 5) and 6 down-regulated overlap general-key DEGs (Table 6) related to response to ion-beam implantation in rice. The short description (Tables 5 and

Table 6. The down-regulated general-key DEGs.

Gene ID	Short description	Fold changes		
		$2*10^{17}$	$6*10^{17}$	$8*10^{17}$
Os01g0800800	Hypothetical protein	2.13	2.23	5.26
Os06g0654600	Protein kinase	2.10	2.0	2.60
Os07g0543300	Glycoside hydrolase, family 14B	2.83	3.35	10.0
Os12g0140700	Zn-finger, RING protein	2.26	2.10	2.30
Os12g0640500	Na+/H+ antiporter-like protein	2.01	4.53	6.76
Os12g0427600	P69F protein	11.50	2.83	5.84

Short descriptions were annotated according to RAP-DB (Rice Annotation Project Database). Fold change in each gene is not expressed as log2. The P-value threshold of 0.05 was used for significant differential expression.

Table 7. Molecular function of the up DEGs.

Molecular function	Hits
Binding	12
Catalytic	12
Transporter	5
Molecular transducer	3
Electron carrier	2
Antioxidant	2
Enzyme regulator	2
Nutrient reservoir activity	2
Transcription factor	1
Translation regulator	1
Structural molecule	1
Unclassified	3

Hits refer to the number of DEGs clustered into certain functional groups.

Table 8. Biological process of the up DEGs.

Biological process	Hits
Cell process	14
Metabolic process	12
Response	10
Transport	5
Signaling	4
Protein modification	4
Oxidation reduction	3
DNA recombination	1
Microtubule-based process	1
Nuclear mRNA splicing, via spliceosome	1
Pollen development	1
Regulation of transcription	1
Translational elongation	1

Hits refer to the number of DEGs clustered into certain pathways.

6) showed that genes related to kinase, transporters, signals, resistance and so on are involved in response to ion-beam implantation.

Gene ontology terms and pathway analysis of the DEGs

In order to investigate the functional category enrichment of these DEGs, we analyzed the functional features of these DEGs according the GO terms using the SAS system (a web server). One transcript could be classified into more than one function catalog. Results showed that these 26 up-regulated DEGs were classified into 11 functional groups and one unclassified groups (Table 7), and were enriched into 13 biological processes (Table 8). The results also show an enrichment of signaling including kinase, transporter, transcription factor (TF) and so on, and these up-regulated DEGs were enriched in response process (38.5%, 10/26) (Table 8). It was indistinctly observed that genes related to antioxidant function and oxidation reduction process were involved in response to implantation, and this finding is coincident with many previous studies (Feng and Yu, 2006).

The probe Os07g0638400 was involved in three KEEG pathways listed in Table 9. These pathways are all associated with phenylpropanoid which are a group of plant secondary metabolites derived from phenylalanine and having a wide variety of functions both as structural and signaling molecules. So we considered that phenylpropanoid should be an import compounds responsive to implantation with ion beam.

It showed that the six down-regulated DEGs were classified into 8 functional groups and one unclassified groups according to molecular function GO term analysis (Table 10), and were enriched in 10 biological processes according to biological process GO term analysis (Table 11). It was observed that down-regulated genes also showed an enrichment of signals including protein kinase, transporter, receptor, and transcription factor. However, these six down-regulated DEGs were not enriched into any KEEG pathways.

Microarray technology has been used in many plants, and function as a powerful tool for high-thought screening of genes responsive to different abiotic stresses including

Table 9. KEEG pathway enrichment of the up-regulated DEGs.

Name (Category)	Hits	Enrichment test p value	Gene ID
Methane metabolism (Energy metabolism)	1	0.018	Os07g0638400
Phenylalanine metabolism (Amino acid metabolism)	1	0.018	Os07g0638400
Phenylpropanoid biosynthesis (Biosynthesis of secondary metabolites)	1	0.0215	Os07g0638400

Table 10. Molecular function of down DEGs.

Molecular function	Hits
Bingding	5
catalytic	4
protein kinase	1
Transcription factor	1
Transporter	1
Receptor	1
Molecular transducer	1
Solute: Hydrogen antiporter	1
Unclassified	1

Table 11. Biological process of down DEGs.

Description of biological process	Hits
Metabolic process	4
Cell process	4
Biological regulation	3
Regulation of biological process	2
Signal transduction	1
Regulation of transcription , DNA-dependent	1
Transport	1
Response	1
Protein modification	1
Proteolysis	1

salt, ABA (abscise acid), cold, heat and drought (Buchanan et al., 2005; Kawaura et al., 2008; Miyama and Tada, 2008; Rensink et al., 2005). However, little knowledge of the microarray for screening the genes responsive to implantation with low-energy ion beam in plant; even the molecular mechanism of the biological effects induced by ion-beam implantation is not enough illuminate. So it is necessary to carry out the microarray on high-thought screening of key genes in response to ion-beam implantation. A biological organism is a complex system; meanwhile, temporal and spatial changes in the biological structure greatly complicate the studies of the interactions between energetic ions and the living biological targets (Feng and Yu, 2006); this divergent physiology of each seeds could result in different response potential. In order to investigate the general-key genes responsive to ion-beam implantation, the overlapping DEGs are necessarily derived from the rice population in multiple ion-beam implantation experiments.

In present study, a total of 32 overlap DEGs, including 26 up-regulated and 6 down-regulated DEGs are observed, comprising 3.90% (32/821), 2.55% (32/1256), 2.81% (32/1136) of the total DEGs underlying three independent ion-fluence implantation respectively. This revealed that less than 10% transcripts were overlap differentially expressed. These 32 overlap DEGs will present target genes for the study on molecular mechanism of biological effects induced by implantation with low-energy ion-beam.

Stress-regulated proteins can be classified into two groups: proteins that take part in signal transduction and proteins that directly play a role in plant survival under stress conditions. Proteins of the first group include transcription factors, RNA-binding proteins, protein kinases and phosphatases (Xiong and Zhu, 2001). 10 out of 26 overlap up-regulated transcripts involves response process, and 5, 4, 4 out of the 26 up-regulated DEGs are related to transport, signaling, protein modification (including protein kinases and phosphatases) respectively. This finding suggested that rice responded to the implantation with ion beam by the unknown signals pathway.

Our microarray data on the different biological effects of the ion-beam implantation revealed the general and key genes responsive to stress of implantation with the low-energy ion beam during the rice germination. This suggests that the differentially expressed transcripts clustered into many groups were associated with the requirements of different events while adapting to the ion implantation. These data provide information on the candidate genes for further elucidation regarding the molecular mechanisms of the biological effects of ion-beam implantation and its use for improvement of corn.

Conflict of Interests

The author(s) have not declared any conflict of interests.

ACKNOWLEDGEMENTS

This work was supported by Program-funded Project for

Young Teachers in Universities of Henan Province (Grant No. 2010ggjs-168), National Natural Science Fund of China (Grant No.30800204) and The Key Project Science and Technology Research of the Education Department, Henan Province (Grant No. 12A180025).

REFERENCES

Buchanan CD, Lim S, Salzman RA, Kagiampakis I, Morishige DT, Weers BD, Klein RR, Pratt LH, Cordonnier-Pratt MM, Klein PE, Mullet JE (2005). Sorghum bicolor's transcriptome response to dehydration, high salinity and ABA. Plant Mol. Biol. 58:699-720. http://dx.doi.org/10.1007/s11103-005-7876-2; PMid:16158244

Feng HY, Liu XL, Yuan H, Kong MG, Wu LJ, Wu YJ, Yu ZL (2007). Utilizing low-energy ion beams to study living organisms. Surf. Coat. Technol. 201:8034-8038. http://dx.doi.org/10.1016/j.surfcoat.2006.09.318

Feng HY, Yu Zl (2006). Ion implantation of organisms. Mater. Sci. Eng. 54:49-120. http://dx.doi.org/10.1016/j.mser.2006.11.001

Jung KH, An G, Ronald PC (2008). Towards a better bowl of rice: Assigning function to tens of thousands of rice genes. Nat. Rev. Genet. 9:91-101. http://dx.doi.org/10.1038/nrm2343; PMid:18160965

Jwa NS, Agrawal GK, Tamogami S, Yonekura M, Han O, Iwahashi H, Rakwal R (2006). Role of defense/stress-related marker genes, proteins and secondary metabolites in defining rice self defense mechanisms. Plant Physiol. Biochem. 44:261-273. http://dx.doi.org/10.1016/j.plaphy.2006.06.010; PMid:16806959

Kawaura K, Mochida K, Ogihara Y (2008). Genome-wide analysis for identification of salt-responsive genes in common wheat. Funct. Integr. Genom. 8:277-286. http://dx.doi.org/10.1007/s10142-008-0076-9; PMid:18320247

Matsumoto T, Kanata S (2005). International Rice Genome Sequencing Project. The map based sequence of the rice genome. Nature 436(7052):793-800. http://dx.doi.org/10.1038/nature03895; PMid:16100779

Miyama M, Tada Y (2008). Transcriptional and physiological study of the response of Burma mangrove (Bruguiera gymnorhiza) to salt and osmotic stress. Plant Mol. Biol. 68:119-129. http://dx.doi.org/10.1007/s11103-008-9356-y; PMid:18568404

Rensink WA, Iobst S, Hart A, Stegalkina S, Liu J, Buell CR (2005). Gene expression profiling of potato responses to cold, heat, and salt stress. Funct. Integr. Genom. 5:201-207. http://dx.doi.org/10.1007/s10142-005-0141-6; PMid:15856349

Shimamoto K, Kyozuka J (2002). Rice as a model for comparative genomics of plants. Annu. Rev. Plant Biol. 53:399-419. http://dx.doi.org/10.1146/annurev.arplant.53.092401.134447; PMid:12221982

Tardif G, Kane NA, Adam H, Labrie L, Major G, Gulick P, Sarhan F, Laliberté J-F (2007). Interaction network of proteins associated with abiotic stress response and development in wheat. Plant Mol. Biol. 63:703-718. http://dx.doi.org/10.1007/s11103-006-9119-6, PMid:17211514

Walia H, Wilson C, Zeng L, Ismail AM, Condamine P, Close TJ (2007). Genome-wide transcriptional analysis of salinity stressed japonica and indica rice genotypes during panicle initiation stage. Plant Mol. Biol. 63:609-623. http://dx.doi.org/10.1007/s11103-006-9112-0; PMid:17160619 PMCid:PMC1805040

Wang JP, Bughrara SS (2007). Monitoring of gene expression profiles and identification of candidate genes involved in drought responses in Festuca mairei. Mol. Genet. Genom. 277:571-587. http://dx.doi.org/10.1007/s00438-007-0208-2; PMid:17323082

Xiong L, Zhu JK (2001). Abiotic stress signal transduction in plants: Molecular and genetic perspectives. Physiol. Plantarum 112:152-166. http://dx.doi.org/10.1034/j.1399-3054.2001.1120202.x ; PMid:11454221

Ya HY, Chen QF, Wang WD, Chen WG, Qin GY, Jiao Z (2012). Gene expression profiles in promoted-growth rice seedlings that germinated from the seeds implanted by low-energy N+ beam. J. Rad. Res. 53:558-569. http://dx.doi.org/10.1093/jrr/rrs008; PMid:22843621 PMCid:PMC3393346

Yu ZL (2007). Study on the interaction of low-energy ions with organisms. Surf. Coat. Technol. 201:8006-8013. http://dx.doi.org/10.1016/j.surfcoat.2006.09.316

Zhou J, Wang X, Jiao Y, Qin Y, Liu X, He K, Chen C, Ma L, Wang J, Xiong L, Zhang Q, Fan L, Deng XW (2007). Global genome expression analysis of rice in response to drought and high-salinity stresses in shoot, flag leaf and panicle. Plant Mol. Biol. 63:591-608. http://dx.doi.org/10.1007/s11103-006-9111-1; PMid:17225073 PMCid:PMC1805039

Zhu JK (2002). Salt and drought stress signal transduction in plants. Ann. Rev. Plant Biol. 53:247-273. http://dx.doi.org/10.1146/annurev.arplant.53.091401.143329; PMid:12221975 PMCid:PMC3128348

academicJournals

Vol. 9(9), pp. 407-409, 15 May, 2014
DOI: 10.5897/SRE2014.5920
Article Number: 82B4ACE44574
ISSN 1992-2248 © 2014
Copyright©2014
Author(s) retain the copyright of this article
http://www.academicjournals.org/SRE

Scientific Research and Essays

Short Communication

Study on the warp and weft direction conductivity of anti-radiation knitted fabric

Zhu Xiao Yu

College of Textile and Costume Design, Taiyuan University of Technology, Jinzhong 030600, China.

Received 29 March, 2014; Accepted 30 March, 2014

Measured by electrical experiments involving knitted warp and weft direction conductivity, we concrete analysis on the factors that affect electromagnetic shielding effectiveness of the knitted fabric. The influence factors of preventing electromagnetic radiation fabric shielding performance is associated with the organization structure and related parameters of knitted fabric. These include: organization type, the metal fiber content, the structure of the yarn or fabric, fabric horizontal (or vertical) electrical conductivity. It was found that the knitted fabric horizontal conductivity is different from the vertical conductivity, and the fabric transverse electrical conductivity is better than longitudinal. When knitted fabric electrical conductivity is good at the same condition, the shielding performance of the fabric is good.

Key words: Conductivity, knitted fabric, organization type, shielding effectiveness.

INTRODUCTION

The weave structure of knitted and woven fabric is obviously different. The two different kinds of fabric structure weaved by the same kind of metal fiber can also form a metal gate or metal mesh, and the electromagnetic shielding performance have obvious differences, and the fundamental reason comes down to its own weaving structure (Feng, 1986; Xie, 1996; Zhu et al., 2012).

Knitted fabric is braided by yarn along the lateral or vertical weaving string set of warp/weft, and woven fabric is composed of warp/weft yarns intertwined. If we analyze from the fabric structure, the knitted fabric weft have a yarn formed, and its lateral electrical conductivity is better. The knitted warp is only composed of a series of coil set between the yarn, and its longitudinal conductive performance is made up of string of suites coil resistance. The knitted warp and weft direction conductivity influencing its shielding effectiveness can be achieved by resistance experiments to further study them (Wang, 1986).

EXPERIMENT

Apparatus required

Stainless steel fiber and silver fiber, the knitted fabric, single-sided cloth, rib fabrics, and siping fabric; Laboratory equipment include: special conductive metal fixture, electricity use table DT9205 etc.

Methodology

First, a certain row and columns of fabric pieces were taken along the knitted fabrics weft and warp direction. Thereafter, the fabric

E-mail: 645479133@qq.com

Table 1. Siping knitted fabric resistance of stainless steel fiber.

Stainless steel fiber siping knitted fabric (resistance)							**Average**
Lateral (weft) resistance value ($K\Omega$)	50.5	47.5	46.8	46.2	45.7	49.1	47.6
Longitudinal (warp) resistance value ($M\Omega$)	13.5	13.1	12.65	13.7	18	14.3	14.2

Table 2. Siping knitted fabric resistance of stainless steel fiber.

Stainless steel fiber siping knitted fabric (resistance)							**Average**
Lateral(weft) resistance value ($\mathrm{K}\Omega$)	17.6	18.2	19.8	25.5	27	15.6	20.6
Longitudinal (warp) resistance value ($M\Omega$)	0.567	0.595	0.523	0.691	0.642	0.587	0.601

Table 3. Single-sided weft knitted fabric resistance of stainless steel fiber.

Single-sided weft knitted fabric resistance of stainless steel fiber							**Average**
Lateral(weft) resistance value ($K\Omega$)	27	26	24	29	30	31	27.8
Longitudinal (warp) resistance value ($M\Omega$)	0.5	0.8	0.7	1.3	1.1	0.9	0.88

was placed on both ends of the special fixture, clamping with zigzag bite, and tightly clamped at both ends of the knitted fabric. Finally, the knitted fabrics in the weft direction conductive resistance and warp conductive resistance were measured, averaging multiple measurements.

EXPERIMENTAL RESULTS AND ANALYSIS

This study was aimed at reporting the weft and warp direction conductivities of stainless steel fiber knitted fabric.

Experiment 1: Stainless steel fiber knitted fabric: siping organization; the weft density: 32/5 cm; the warp density: 51/5 cm.

The knitted lateral and longitudinal length: 17.5 × 6 cm; the knitted longitudinal and lateral length: 17.5 × 6 cm; the data results are shown in Table 1.

Experiment 2: stainless steel knitted fabric: siping organization: the lateral density: 32/5 cm; the longitudinal density: 51/5 cm; The knitted transverse and longitudinal length:6 × 6 cm; the data results are shown in Table 2.

The experimental data measured in Tables 1 and 2 are explicit. First, the knitted fabric of siping organization made of stainless steel is conductive fabric, which is the root cause that has the function of preventing electromagnetic radiation. Second, the fabric as conductive metal gate, the horizontal and vertical conductivity have obvious difference. Although the size of the two pieces of fabric is different, it is clear that the lateral resistance is far less than the longitudinal resistance, and the two different direction resistance value is not in an order of magnitude. Therefore, it can be seen that the knitting siping transverse conductivity is better than that of vertical conductivity of the organization. This feature confirms the characteristics of the knitted fabric horizontal weaving yarn namely along the horizontal knitting set into each other. Formed by a yarn knitted horizontally, the resistance is relatively small; between the longitudinal formed by the horizontal coil series, the series of flat coil connection is not quite close together, so resistance is larger, and lateral connectivity weak in fabric, namely cannot form effective metal gate, which is the important factor that affect the fabric shielding effectiveness. Third, the influence of the length of the fabric on the resistance value is not a simple serial or parallel relationship, in terms of the same fabric structure both transverse and longitudinal, the longer the fabric its resistance value will be bigger.

Experiment 3: Single-sided weft plain knitted fabric stainless steel fibers; Fabric size: 6 × 6 cm; the data is shown in Table 3.

Experiment 4: Stainless steel fiber rib organization; fabric size: 6 × 6 cm; the data is shown in Table 4.

When Tables 2 to 4 are viewed together, it can be seen that not only stainless steel fiber knitted fabric of horizontal and vertical conductivity are different, but also the conductivity of the different knitted fabric structures are different. The conclusion further confirmed from the perspective of conductive fabric that knitted fabric of the

Table 4. Rib organization fabric resistance of stainless steel fiber.

Rib organization fabric resistance of stainless steel fiber							Average
Lateral(weft) resistance value ($K\Omega$)	4.6	4.5	4.2	4.3	5.0	5.1	4.6
Longitudinal (warp) resistance value ($M\Omega$)	0.442	0.482	0.445	0.437	0.547	0.397	0.458

organization structure is the important factor that affects fabric shielding effectiveness. The knitted fabric resistance with different structure is unstable, so we must take more pieces of sample averaging measurement. Knitted fabric resistance value is the relationship with the structure of the fiber yarn and fabric structure. As for the knitted fabric of lateral resistance,

$$R_{single} = 27.8K\Omega > R_{siping} = 20.6K\Omega > R_{rib} = 4.6K\Omega .$$

As for the knitted fabric longitudinal resistance,

$$R_{single} = 0.88M\Omega > R_{siping} = 0.601M\Omega > R_{rib} = 0.458M\Omega ,$$

If knitted fabrics weaved by the same kind of fiber have different organizational structures, both in transverse electrical conductivity and longitudinal conductivity, then single-sided fabrics are weaker than siping fabric, siping weaker than rib, which are determined by the absolute content of metal fiber formed fabrics and which have close relationship with the fabric to form effective metal gate. Each coil is a small metal grid. A completely closed coil is the key that the knitted fabric forms an effective closed loop.

Conclusion

From fabric horizontal and vertical conductivity experiment we can draw some conclusion. Firstly, the transverse conductivity of ordinary stainless steel fiber knitted fabric is better than that of vertical electrical conductivity. As knitted fabric has better electrical conductivity at the same condition, the shielding performance of the fabric is better; the closer fabric knit between the coil set, the more fabric interwoven point contacting area between, the better electrical conductivity. Secondly, for the same fiber, different organization structures imply that the knitted fabric has different conductivity. The conductivity of the metal fiber is better, and knitted fabric of vertical and horizontal conductivity are also better; the smaller the difference between them, the better in shielding properties also.

Thirdly, the knitted fabric conductivity is associated with the type of fiber as well as with the fiber structure. The greater the absolute content of the metal fiber, the better the fabric conductivity, the better shielding effectiveness; the electrical conductivity of the metal fiber filament is better than that of short fibers.

In a word, to improve the electromagnetic shielding effectiveness and the knitted fabric metal fibre to continuous distribution, mutual conduction is an important factor. In order to further improve the shielding effectiveness of blended fabric, on the one hand, by improving the fabric tightness, increase in the density of the fabric articles as well as the stainless steel staple fiber with ordinary fibre mixing are ways to implement.

REFERENCES

Feng C (1986). Electromagnetic field. People's Education Press.

Wang X (1986). Electromagnetic field theory and application. Science Press.

Xie ZF (1996). The metal mesh for lightning transient magnetic field shielding Efficiency of the study.

Zhu X, Sun B, Li X (2012). Electromagnetic radiation on human function physical mechanism [J]. PRZEGLADELEKTROTECHNICZNY (Elect. Rev.) . R.88NR.2012.3.


Scientific Research and Essays
OPEN ACCESS